Dynamics and equilibration in integrable and solvable interacting models

विद्या वाचस्पति की
उपाधि की अपेक्षाओं की आंशिक पूर्ति में प्रस्तुत शोध प्रबंध

A thesis submitted in partial fulfillment of the requirements of the degree of Doctor of Philosophy

द्वारा / By
संदीपन मान्ना / Sandipan Manna
पंजीकरण सं. / Registration No.: 20202010

शोध प्रबंध पर्यवेक्षक / Thesis Supervisor:
डॉ. श्रीजीत जी. जे. / Dr. Sreejith G J

भारतीय विज्ञान शिक्षा एवं अनुसंधान संस्थान पुणे

INDIAN INSTITUTE OF SCIENCE EDUCATION AND RESEARCH PUNE

2026

To my elder sister,
Saheli.

Certificate

Certified that the work incorporated in the thesis entitled "*Dynamics and equilibration in integrable and solvable interacting models*", submitted by *Sandipan Manna* was carried out by the candidate, under my supervision. The work presented here or any part of it has not been included in any other thesis submitted previously for the award of any degree or diploma from any other university or institution.

Date: May 8, 2026

Dr. Sreejith GJ
Thesis Supervisor

Declaration

Name of Student: Sandipan Manna
Reg. No.: 20202010
Thesis Supervisor: Dr. Sreejith GJ
Department: Dept. of Physics, IISER Pune
Date of joining I-PhD program: 1st September, 2020
Date of starting of PhD program: August 1, 2022
Date of Pre-Synopsis Seminar: April 1, 2026
Title of Thesis: Dynamics and equilibration in integrable and solvable interacting models

I declare that this written submission represents my ideas in my own words and where others' ideas have been included, I have adequately cited and referenced the original sources. I declare that I have acknowledged collaborative work and discussions wherever such work has been included. I also declare that I have adhered to all principles of academic honesty and integrity and have not misrepresented or fabricated or falsified any idea/data/fact/source in my submission. I understand that violation of the above will be cause for disciplinary action by the Institute and can also evoke penal action from the sources which have thus not been properly cited or from whom proper permission has not been taken when needed.

The work reported in this thesis is the original work done by me under the guidance of Dr. Sreejith GJ.

Date: May 8, 2026

Sandipan Manna

Reg. No. 20202010

Acknowledgements

"We shall not cease from exploration, and the end
of all our exploring will be to arrive where we started
and know the place for the first time."
— T.S. Eliot, *Little Gidding*

I would like to begin by expressing my deepest gratitude to my advisor, Dr. Sreejith GJ, whose guidance has been the cornerstone of this work. His professionalism, intensity of focus, and an almost disarming dedication to the craft of research set a standard I can only aspire to carry into my own professional life. Whatever I have managed to achieve in these years is, in no small measure, a consequence of his encouragement, patience, and his quiet but persistent belief that the work was worth doing well.

I am deeply grateful to Prof. Deepak Dhar, from whom I learned much of what I know of graduate statistical mechanics. I would like to thank the members of my Research Advisory Committee, Dr. Bijay Kumar Agarwalla and Dr. Sachin Jain, for their valuable feedback at every stage. I also wish to thank Dr. Sthitadhi Roy and Dr. Tridib Sadhu, whose collaboration has been a genuine privilege. Their generosity in hosting me on multiple occasions at ICTS and TIFR respectively, and the many discussions we shared during those visits have enriched both this work and my understanding of physics considerably. I would like to acknowledge Prof. Manoj Sharan, whose guidance during my undergraduate internship gave me my first real experience of research, and played no small role in my choosing to pursue it further.

I am grateful to my labmates, past and present — Naveen, Abhishek, Ojasvi, and Anant. Abhishek has been there for both academic and non-academic advise since the first day, when I was just finding my footing, and I am grateful to him for all the things I learned from him spanning Physics to life. I wish to thank Ojasvi for useful discussion and collaborations in multiple projects. I wish her best for all the endeavor she takes in coming years.

I have been fortunate in my friends. Aakash, Mayank, and Amit kept me grounded, kept me laughing, and occasionally kept me from making poor decisions. I thank Bikirna for all the discussions on movies, games and everything in between. I want to thank Sagar, Sagnik, Katha, Jatin, Deep, Ajay, Rupesh, Ritam, Shreerang, and Nisarg, whose warmth and company made this time memorable in ways I did not expect. I will always cherish the time we shared. I would also like to mention Rajarshi, Sayanil, Sayan, and Abhijit, college friends who, despite the distance, were always just a call away whenever I needed advice or simply just to talk about anything under the sun.

Whatever I am, and whatever I hope to become, owes more to my family than I can adequately express here. My parents and sister have been unwavering in their support, their patience, and their quiet sacrifices. I carry that with me.

I am grateful to Nisha Kurkure and other members of IT Department for their diligent upkeep of the PARAM Brahma and other computational facilities that underpin much of this work. I acknowledge IISER Pune for a graduate research fellowship and Infosys Foundation for a travel grant.

This thesis stands, as all science does, on the shoulders of an enormous community of researchers whose curiosity and rigor contributed to the progress in our understanding. I am grateful to every researcher whose published work and openly shared code made this possible, and especially to the open-source communities.

Finally, I want to acknowledge the artists, educators, musicians, and storytellers whose work I sought refuge in during these years, most of whom I will never know personally. I have tried to learn from them as much as from anything else.

Sandipan Manna
IISER Pune
May, 2026

Contents

List of Publications

The following publications form the basis of this thesis:

1. **Sandipan Manna** and G. J. Sreejith, "*Thermal Drude weight in an integrable chiral clock model.*" *Phys. Rev. B* **108**, 054304 (2023).

2. **Sandipan Manna** and G. J. Sreejith, "*Full distribution and large deviations of local observables in an exactly solvable current carrying steady state of a strongly driven XXZ chain*", *Phys. Rev. E* **111**, 044139 (2025).

3. **Sandipan Manna**, Sthitadhi Roy and G. J. Sreejith, "*Projected ensemble in a system with conserved charges with local support*", *Phys. Rev. B* **111**, 144302 (2025).

4. G. J. Sreejith and **Sandipan Manna**, "*Signatures of quantum chaos and complexity in the Ising model on random graphs*", *Phys. Rev. B* **113**, 214322 (2026).

The following publication represent additional contributions of the author during the course of this thesis but are not included in this thesis:

1. Ojasvi Sharma, **Sandipan Manna**, Prashant Shekhar Rao and G. J. Sreejith. "*Group Convolutional Neural Network for the Low-Energy Spectrum in the Quantum Dimer Model*", *Phys. Rev. B* **114**, 014408 (2026).

Abstract

This thesis studies the dynamics and equilibration of interacting quantum systems in which integrability, or the structure of conserved charges, shapes the long-time behavior. The Introduction (Chapter 1) sets up machinery that the later chapters draw on: linear response and the fluctuation-dissipation theorem, large deviations and cumulant-generating functions, quantum state ensembles, and spectral diagnostics of chaos. With these in place, the four research chapters trace a single arc. They move from closed-system transport, to full counting statistics in boundary-driven steady states, to projected ensembles in systems with extensively many conserved charges, and finally to chaos diagnostics suited to near-term quantum hardware. The common technical thread is matrix product state methods (introduced in Chapter 2), combined with analytic input from (quasi-)local conserved quantities, to access regimes where integrability or solvability produces behavior outside the reach of generic thermalization arguments.

Chapter 3 applies time-dependent DMRG to thermal transport in a chiral $\mathbb{Z}_3$ clock chain tuned along an integrable, time-reversal symmetric line. The thermal current's finite overlap with a local conserved charge $Q^{(2)}$ obtained from the transfer matrix yields a Mazur bound that saturates the Drude weight at finite temperature, validated against a sum rule.

Chapter 4 studies the boundary-driven XXZ chain, whose non-equilibrium steady state under maximally polarising Lindblad operators admits an exact matrix product solution. In the XX limit we obtain closed-form spin correlators, entropy per site, and SCGFs of local observables. For $\Delta > 0$ a cosine of a rational multiple of π, the MPS yields numerically exact SCGFs and rate functions for the local z-magnetisation, with finite-size corrections decaying exponentially at a rate discontinuous in Δ. A double-peak structure in the x-magnetisation density for $\Delta \lesssim 1$ is suggestive of short-range ferromagnetic ordering.

Chapter 5 uses the projected ensemble—subsystem states conditioned on measurements of the complement, to probe deep thermalisation in systems with extensively many (quasi-)local conserved charges. In a Floquet spin chain deep in its MBL regime and the ℓ-bit model as a 1-local archetype, the late-time projected ensemble converges to a Scrooge ensemble *except* when the measurement operator aligns with the conserved charges, a behaviour we link to the emergence of Porter–Thomas bitstring statistics and justify with semi-analytical arguments.

Chapter 6 carries these diagnostics onto probes scalable on current quantum hardware, studying the mixed-field quantum Ising model on Erdős–Rényi graphs whose connectivity interpolates the dynamics between localized, chaotic, and permutation-symmetric integrable regimes–a crossover with implications for the trainability of variational algorithms such as QAOA. The regimes are characterized through convergence of the projected ensemble to Haar, a partial spectral form factor as a resource-efficient SFF proxy, and operator Krylov complexity, which is maximized in the chaotic regime. Taken together, the four chapters trace a path in which the role of conservation laws on quantum dynamics is investigated with progressively sharper probes.

1

Introduction

1.1 Overview

The collective behavior of interacting quantum particles is central to condensed matter physics, manifesting in phenomena ranging from superconductivity and magnetism to the topological order and the broader physics of strongly correlated electrons. None of these admits a description at the level of a single particle, and each emerges only when the cooperative dynamics of many degrees of freedom is taken into account. The theoretical understanding of such phenomena has developed in close contact with generations of experiment on bulk solids and quantum fluids, and it has been organized, for the most part, around two parallel routes of investigation. The first is the equilibrium state itself, characterized by its symmetries and correlations, order parameter, and ground state as well as low-energy excitations. The second is the linear response of that equilibrium state to a weak external perturbation, such as an applied electric or magnetic field, a temperature gradient, or a small mechanical strain, which determines measurable quantities such as electrical and thermal conductivities, magnetic susceptibilities, and spectroscopic line shapes [1, 2, 3]. Within the equilibrium and linear-response regime, theoretical frameworks such as Bardeen-Cooper-Schrieffer theory, Landau's theory of the Fermi liquid, the renormalization-group treatment of phase transitions and the Kondo problem, and the theories of topological order among others are tailored to questions of just this kind.

The conventional experimental probes are tied to bulk samples and to measurements of local expectation values and few-body correlations. Specific heat and magnetic susceptibility characterize the thermodynamics of the equilibrium state and can be obtained from partition function. Neutron and Raman scattering measure equilibrium correlation functions and the spectrum of low-energy excitations. In contrast, state-of-the-art qunatum simulators provide access to the quantities that are beyond few-body correlations. Such systems also allow partial measurements and reliable time evolution, which affords direct access to non-equilibrium dynamics e.g., quench protocols, thermalization and the build-up of entanglement in real time. Non-equilibrium physics has been conventionally probed through techniques like pump–probe spectroscopy and transport measurements. Quantum simulators add the ability to prepare a clean initial state, evolve it unitarily under a known Hamiltonian, and then obtain high-order

correlators, a degree of control that is difficult to match in bulk solid-state platforms. While the universal characteristics of equilibrium systems are by now reasonably well understood, the corresponding notion of universality out of equilibrium remains an active area of investigation.

Transport is the simplest drift away from the equilibrium setup. Yet at long times and long wavelengths it admits a universal description in terms of hydrodynamics, an effective theory whose form is fixed by the conservation laws of the underlying Hamiltonian [4]. In a generic many-body system with only a few local conservation laws, currents decay through many-body scattering and the late-time dynamics is diffusive, characterized by a finite diffusion constant. Integrable one-dimensional models occupy the opposite extreme. They are defined by the existence of an extensive set of mutually commuting local and quasi-local conserved quantities. In conventional experiments, inevitable interaction with environment (e.g., phonon-bath coupling) makes such conserved charges in fine-tuned integrable systems fragile. However, modern tunable quantum simulators make such systems experimentally realizable with reliable isolation from environmental effects. A typical current operator has finite overlap with the tower of conserved charges [5, 6] in integrable systems. A finite fraction of the current is therefore protected from decay, and this protected component appears in the dynamical conductivity as a singular contribution at zero frequency, the Drude weight, which remains finite at any temperature in a clean integrable system [7]. The simplest illustration is a gas of free electrons in a uniform electric field. With no scattering channel available, each electron accelerates indefinitely, the current never relaxes, and the entire conductivity collapses onto a delta function at zero frequency, a Drude weight in its purest form. Crucially, although transport is intrinsically a non-equilibrium phenomenon, in the linear-response regime it remains fully encoded in equilibrium correlation functions. By the fluctuation-dissipation theorem, transport coefficients such as diffusion constants and Drude weights can be extracted from the current-current correlator evaluated in the equilibrium ensemble [1]. We present an explicit computation of Drude weight for thermal conductivity in a strongly correlated system in Chapter 3.

Condensed matter experiments on most bulk samples characterize a many-body system through expectation values of local observables and low-order correlation functions, such as thermodynamic susceptibilities, scattering structure factors, and transport coefficients. These quantities are the ones constrained by the Eigenstate Thermalization Hypothesis (ETH) [8, 9] that provides the standard framework for understanding generic thermal quantum systems, asserting that individual energy eigenstates effectively act as their own thermal reservoirs. Under ETH, the local properties of a single eigenstate are indistinguishable from those of a thermal ensemble, which is usually represented by Gibbs ensemble or its generalizations. ETH places no constraint, however, on correlators whose support is comparable with the system size.

The development of programmable quantum platforms over the past two decades has brought these finer quantities into experimental reach. Repeated snapshots of a subregion in such setups reconstruct the full joint distribution of local observables on it, equivalent to n-point correlators with n scaling up to the size of the full system. The same platforms can be operated in driven configurations, where the system is coupled at its boundaries to reservoirs at different chemical potentials or temperatures and relaxes into a non-equilibrium steady state that sustains a finite current through the bulk [10, 11]. In such settings one interesting characterization of the state is

the full counting statistics (FCS) of the charge in a subsystem. Large-deviation rate function [12, 13] characterizes the probability of rare fluctuations in such quantities and exposes universal features [14, 15]. Obtaining such distribution of observables analytically in interacting system is challenging. Even numerical caluclation is limited to small system size, owing to the high-accuracy state description required for faithful estimation of FCS . Chapter 4 presents an exact computation of the FCS in a strongly driven boundary-coupled spin chain.

A complementary class of questions concerns the statistical structure of the quantum states themselves, rather than the values of observables computed in them. ETH, as discussed above, fixes the reduced density matrix of any small subsystem and thereby determines all few-body expectation values supported on it. It places no constraint, however, on the distribution of the qunatum states in the Hilbert space, which is a far stronger characterization of the system. Whether such state distributions exhibit universal behavior on Hilbert space is the central question of deep thermalisation [16, 17]. *Projected ensemble* acts as a natural protocol to obtain such an unravelling of qunuatum states in Hilbert space. In chaotic systems they are conjectured to converge to the Haar measure, the unique unitarily invariant distribution on Hilbert space, a form of randomness that can not be guranted with only few moments of observable or qunatum state distribution alone. Systems with extensively many conserved charges, such as integrable models or many-body localized systems where disorder arrests thermalization, are expected to converge instead to non-Haar universal ensembles whose form encodes the conservation-law structure directly. Identifying these universal ensembles in constrained settings remains a largely open problem. Chapter 5 addresses it in a setting combining strong disorder with strictly one-site conserved charges using numerical analysis assisted by semi-analytic justifications.

Current quantum devices are not restricted to regular geometries. Modern programmable platforms can realize systems with essentially arbitrary connectivity, including the irregular interaction graphs that arise naturally in practical quantum optimization problems. It is therefore natural to ask how the probes of quantum dynamics behave in this broader class of systems, where the regular geometric structure that underlies most analytical and numerical work no longer applies. From a more practical standpoint, one can also ask whether the nature of the dynamics carries any predictive information about the efficiency with which such devices can be operated. Chapter 6 addresses both questions through a detailed characterization of a random-graph spin system, with explicit consequences for quantum optimization.

In this introductory chapter we develop the foundational tools used across the thesis, establishing notation and theoretical framework. Concepts that are specific to a single chapter, such as the projected ensemble construction, Krylov complexity, the ℓ-bit Hamiltonian, and the quantum Mpemba effect, are introduced in the corresponding chapters and are only briefly mentioned here. We set $\hbar = k_B = 1$ throughout.

1.2 Linear Response Theory

The discussion in Sec. 1.1 emphasized that the symmetries and conservation laws of an integrable Hamiltonian leave a direct imprint on transport. Translating that statement into a calculation requires a framework that connects a microscopic Hamiltonian to the response of currents, susceptibilities, and spectral functions to a weak external probe. Linear response theory, in the

form developed by Kubo, supplies precisely this bridge: every transport coefficient is expressed as an equilibrium time-ordered correlator in the unperturbed system, with the external field entering only through its conjugate operator. We develop the formalism here, and specialize it in Sec. 1.3 to the Kubo formula for thermal conductivity used throughout Chapter 3. Much of the discussion in this section will follow Ref. [18].

Consider a quantum system described by a time-independent Hamiltonian H_0 in thermal equilibrium at inverse temperature $\beta = 1/T$, so that the equilibrium density matrix is $\rho_0 = e^{-\beta H_0}/Z$ where $Z = \mathrm{Tr}[e^{-\beta H_0}]$. At time t_0, a weak, time-dependent external perturbation $V(t)$ is applied, with $V(t) = 0$ for $t < t_0$, so that the full Hamiltonian becomes

$$H(t) = H_0 + V(t). \tag{1.1}$$

We write the perturbation in the general form

$$V(t) = -\sum_{\alpha} F_\alpha(t)\, B_\alpha \tag{1.2}$$

where $F_\alpha(t)$ are classical external fields and B_α are the conjugate Hermitian operators.

The time evolution of the density matrix in the interaction picture is governed by the von Neumann equation

$$\imath \frac{\partial \rho_I(t)}{\partial t} = [V_I(t),\, \rho_I(t)], \tag{1.3}$$

where $\rho_I(t) = e^{\imath H_0 t}\, \rho(t)\, e^{-\imath H_0 t}$ and $V_I(t) = e^{\imath H_0 t}\, V(t)\, e^{-\imath H_0 t}$. Iterating Eq. (1.3) with the initial condition $\rho_I(t_0) = \rho_0$ and retaining only the first-order correction gives

$$\rho_I(t) \approx \rho_0 - \imath \int_{t_0}^{t} dt'\, [V_I(t'),\, \rho_0]. \tag{1.4}$$

The change in the expectation value of an observable A from its equilibrium value $\langle A\rangle_0 = \mathrm{Tr}[\rho_0 A]$, to first order in V, is

$$\delta\langle A(t)\rangle = -\imath \int_{t_0}^{t} dt'\, \mathrm{Tr}\big(\rho_0\, [A_I(t),\, V_I(t')]\big). \tag{1.5}$$

To remove the dependence on the initial time t_0, we perform the *adiabatic switch-on* prescription: the perturbation is dressed by an exponential factor,

$$V(t) \;\longrightarrow\; V(t)\, e^{\eta t}, \qquad \eta \to 0^+, \tag{1.6}$$

and the lower limit of integration is sent to $t_0 \to -\infty$, with the $\eta \to 0^+$ limit taken at the end of the calculation. Physically this corresponds to the system having been in equilibrium in the distant past and the perturbation having been switched on infinitely slowly, so that no transient associated with the choice of turn-on time contaminates the response. With this prescription, Eq. (1.5) becomes

$$\delta\langle A(t)\rangle = \sum_{\alpha} \int_{-\infty}^{\infty} dt'\, \chi_{AB_\alpha}(t - t')\, F_\alpha(t'), \tag{1.7}$$

where the retarded response function (generalised susceptibility) is

$$\chi_{AB}(t-t') = \imath\,\theta(t-t')\,\langle[A(t),B(t')]\rangle_0, \tag{1.8}$$

and $A(t) = e^{\imath H_0 t} A\, e^{-\imath H_0 t}$ is the Heisenberg-picture operator. The Heaviside factor $\theta(t-t')$ encodes causality: the response of A at time t depends only on the field at earlier times $t' < t$. In frequency space this manifests as analyticity of $\chi_{AB}(\Omega)$ in the upper half of the complex Ω-plane, since the η in the switch-on shifts $\Omega \to \Omega + \imath\eta$ with $\eta > 0$. Upper-half-plane analyticity is precisely the input that yields the Kramers–Kronig relations developed in the next subsection. The central result of linear response theory is Eq. (1.7): every measurable linear transport coefficient is determined by an equilibrium time-ordered commutator of the unperturbed system [1, 18, 19].

1.2.1 Fourier-space representation and Kramers–Kronig relations

Experiments probe response at fixed frequency rather than in the time domain: optical conductivities, dynamical susceptibilities, and spectral functions are all measured as functions of Ω. Recasting Eq. (1.8) in frequency space therefore makes contact with observables, and as we now show, the upper-half-plane analyticity established above translates into a non-trivial constraint relating the dissipative and reactive parts of the response.

Taking the Fourier transform in time,

$$\chi_{AB}(\Omega) = \imath \int_0^\infty dt\; e^{\imath\Omega t}\,\langle[A(t),\,B(0)]\rangle_0. \tag{1.9}$$

Causality implies that $\chi_{AB}(\Omega)$ is analytic in the upper half of the complex Ω-plane, which yields the Kramers–Kronig relations [3]

$$\begin{aligned} \mathrm{Re}\,\chi_{AB}(\Omega) &= \frac{1}{\pi}\,\mathcal{P}\!\int_{-\infty}^{\infty} d\Omega'\;\frac{\mathrm{Im}\,\chi_{AB}(\Omega')}{\Omega'-\Omega}, \\ \mathrm{Im}\,\chi_{AB}(\Omega) &= -\frac{1}{\pi}\,\mathcal{P}\!\int_{-\infty}^{\infty} d\Omega'\;\frac{\mathrm{Re}\,\chi_{AB}(\Omega')}{\Omega'-\Omega}, \end{aligned} \tag{1.10}$$

where $\mathcal{P}$ denotes the Cauchy principal value. These relations connect the reactive (real) and dissipative (imaginary) parts of the response function and are a consequence of causality alone.

1.3 The KMS Condition and the Fluctuation-Dissipation Theorem

The retarded response function of the previous section is built from a commutator, $\langle[A(t),B(0)]\rangle_0$, whereas measured noise spectra and current-current autocorrelators are symmetric objects. For a system in thermal equilibrium these two are not independent: the Gibbs weight $e^{-\beta H_0}$ in ρ_0 relates them through an analytic continuation in time by the imaginary period $\imath\beta$. Making this relation precise is the content of the Kubo-Martin-Schwinger (KMS) condition, and its frequency-space corollary, the fluctuation-dissipation theorem, is what allows the Kubo formula of Sec. 1.2.1 to be written as a current-current correlator, the form actually computed by tDMRG in Chapter 3.

The Kubo–Martin–Schwinger (KMS) condition [1, 20] is a fundamental characterization of thermal equilibrium states. For a system at inverse temperature β, the KMS condition states that

$$\langle A(t)\, B(0)\rangle_\beta = \langle B(0)\, A(t+\imath\beta)\rangle_\beta, \tag{1.11}$$

for any pair of operators A and B. The proof follows from the cyclic property of the trace:

$$\begin{aligned}\langle A(t)\, B(0)\rangle_\beta &= \frac{1}{Z}\,\mathrm{Tr}[e^{-\beta H}\, e^{\imath H t}\, A\, e^{-\imath H t}\, B] \\ &= \frac{1}{Z}\,\mathrm{Tr}[B\, e^{-\beta H}\, e^{\imath H t}\, A\, e^{-\imath H t}] \\ &= \frac{1}{Z}\,\mathrm{Tr}[e^{-\beta H}\, B\, e^{\imath H(t+\imath\beta)}\, A\, e^{-\imath H(t+\imath\beta)}] = \langle B(0)\, A(t+\imath\beta)\rangle_\beta.\end{aligned} \tag{1.12}$$

In frequency space, defining the spectral functions $C^{\pm}_{AB}(\Omega) = \int_{-\infty}^{\infty} dt\; e^{\imath\Omega t}\, \langle A(t)\, B(0)\rangle^{\pm}_{\beta}$ where the $+$ and $-$ superscripts denote the two operator orderings, the KMS condition becomes

$$C^{+}_{AB}(\Omega) = e^{\beta\Omega}\, C^{-}_{AB}(\Omega). \tag{1.13}$$

The factor $e^{\beta\Omega}$ enforces detailed balance: transitions that increase energy are exponentially suppressed relative to those that decrease it. Haag, Hugenholtz, and Winnink [20] showed that any state satisfying Eq. (1.11) is a Gibbs state, establishing the equivalence between the KMS condition and the canonical ensemble.

1.3.1 Fluctuation-dissipation theorem

The fluctuation-dissipation theorem (FDT) [21, 1] is a direct consequence of the KMS condition. The imaginary part of the retarded response function is

$$\mathrm{Im}\,\chi_{AB}(\Omega) = \tfrac{1}{2}[C^{+}_{AB}(\Omega) - C^{-}_{AB}(\Omega)], \tag{1.14}$$

which, combined with Eq. (1.13), gives

$$C^{+}_{AB}(\Omega) = \frac{2\,\mathrm{Im}\,\chi_{AB}(\Omega)}{1 - e^{-\beta\Omega}}. \tag{1.15}$$

At high temperatures ($\beta\Omega \ll 1$) the prefactor reduces to T/Ω, connecting fluctuations linearly to temperature. The FDT is not merely a formal identity; it is the mechanism by which the Kubo formula for thermal conductivity (Sec. 1.3.3) reduces to a current–current correlator: the KMS condition introduces exactly the factor $(1 - e^{-\beta\Omega})$ that converts the antisymmetric commutator into the symmetric correlator. In Chapter 4, where the system is driven far from equilibrium, the KMS condition and FDT no longer hold, and the steady-state properties must be obtained from the exact solution of the Lindblad equation.

1.3.2 The Kubo formula: dynamical spin susceptibility

Before applying the formalism to thermal transport (which will be investigated in Chapter 3), where the coupling to the external probe is indirect, it is instructive to work through a setting of

spin-susceptibility where the conjugate operator appears directly in the perturbation. Consider applying a weak, spatially uniform, time-dependent magnetic field $h(t)$ in the z-direction to a spin chain in equilibrium. The perturbation is

$$V(t) = -h(t)\, M^z, \qquad M^z = \sum_j S^z_j, \tag{1.16}$$

so that M^z is itself the operator conjugate to the field, with no continuity equation or current to introduce. Linear response, Eq. (1.7), gives the induced magnetisation directly:

$$\delta\langle M^z(t)\rangle = \int_{-\infty}^{\infty} dt'\, \chi(t-t')\, h(t'), \tag{1.17}$$

with the dynamical susceptibility

$$\chi(t-t') = \imath\, \theta(t-t')\, \langle [M^z(t), M^z(0)]\rangle_0. \tag{1.18}$$

In frequency space, $\delta\langle M^z(\Omega)\rangle = \chi(\Omega)h(\Omega)$, and the imaginary part $\operatorname{Im}\chi(\Omega)$ governs the energy dissipated per cycle of the oscillating field. The corresponding symmetric correlator,

$$S(\Omega) = \int_{-\infty}^{\infty} dt\, e^{\imath\Omega t}\, \langle M^z(t)\, M^z(0)\rangle_\beta, \tag{1.19}$$

measures equilibrium magnetisation noise; the FDT (Eq. 1.15) then ties the two together,

$$S(\Omega) = \frac{2\operatorname{Im}\chi(\Omega)}{1-e^{-\beta\Omega}}, \tag{1.20}$$

so that knowledge of either object determines the other. This is the prototype Kubo relation: a transport coefficient (here $\operatorname{Im}\chi$) expressed as the Fourier transform of an equilibrium correlator of the operator conjugate to the external field.

Two features of this calculation are to be noted. First, the response function is built from a commutator $\langle [M^z(t), M^z(0)]\rangle_0$, which the FDT converts into the symmetric correlator that is actually computed by tDMRG or Bethe-ansatz methods. Second, the operator appearing in the response is the same one the field couples to. In thermal transport this second feature fails: a temperature gradient does not couple to a single Hamiltonian operator, and the appropriate response operator, the thermal current must be introduced indirectly through the continuity equation. We turn to that case next.

1.3.3 The Kubo formula : thermal conductivity

In Chapter. 3, we will explicitly compute thermal conductivity using two-point current-current correlator. Here, we illustrate the derivation for the required expression. The thermal current operator $\mathcal{I}$ is defined via the continuity equation for the local energy density H_i,

$$\dot{H}_i = \imath[H,\, H_i] = -(\mathcal{I}_{i+1} - \mathcal{I}_i), \tag{1.21}$$

where $\mathcal{I}_i$ is the energy current on the bond between sites i and $i{+}1$, and the total current is $\mathcal{I} = \sum_i \mathcal{I}_i$. Following Luttinger [2], a temperature gradient ∇T is represented as a fictitious gravitational potential conjugate to the local energy density, in exact analogy with the magnetic perturbation of Eq. 1.16. Let x_i denotes the position of site i. Writing the "heat polarization"

$$P_E \equiv \sum_i x_i H_i, \tag{1.22}$$

a uniform gradient ∇T corresponds to the perturbation

$$V(t) = -F(t)\, P_E, \qquad F(t) = \frac{\nabla T}{T}\, e^{-\imath\Omega t} e^{\eta t} \quad (\eta \to 0^+), \tag{1.23}$$

so that, exactly as in Eq. 1.17, linear response gives the induced current

$$\delta\langle I(t)\rangle = \int dt'\, \chi_{I,P_E}(t-t')\, F(t'), \qquad \chi_{I,P_E}(t) = \imath\,\theta(t)\,\langle [I(t), P_E(0)]\rangle_0. \tag{1.24}$$

The object in Eq. 1.24 still mixes a current with an energy density; the continuity equation, Eq. 1.21, lets us remove this asymmetry. Multiplying Eq. (1.21) by x_i and summing over sites,

$$\sum_i x_i \dot{H}_i = -\sum_i x_i (I_{i+1} - I_i), \tag{1.25}$$

and relabelling $i \to i-1$ in the first term on the right (an Abel summation, i.e. discrete integration by parts, dropping the boundary term under PBC or in the limit $L \to \infty$),

$$\sum_i x_i (I_{i+1} - I_i) = \sum_i (x_{i-1} - x_i)\, I_i = -\sum_i I_i, \tag{1.26}$$

one finds the operator identity

$$\dot{P}_E(t) = \sum_i x_i \dot{H}_i(t) = I(t). \tag{1.27}$$

This is the thermal analogue of $\dot{P} = J$ for charge transport: P_E plays the role of an energy dipole moment whose "velocity" is the total heat current.

Equation 1.27 converts χ_{I,P_E} into χ_{II}. Using $I(0) = \dot{P}_E(0)$ inside $\chi_{II}(t) = \imath\theta(t)\langle[I(t), I(0)]\rangle_0$ and Fourier transforming (the equal-time commutator $\langle[I, P_E]\rangle_0$, being the expectation of an anti-Hermitian operator, is purely imaginary and drops out of the combination below) gives the relation

$$\mathrm{Re}\,\chi_{I,P_E}(\Omega) = \frac{\mathrm{Im}\,\chi_{II}(\Omega)}{\Omega}. \tag{1.28}$$

Finally, identifying κ through $J_Q \equiv \delta\langle I\rangle/L = -\kappa(\Omega)\nabla T$ with $\nabla T = TF(\Omega)$, Eq. (1.24) gives $\kappa(\Omega) = -\chi_{I,P_E}(\Omega)/(TL)$; taking the dissipative (real) part and using Eq. (1.28),

$$\kappa_{\mathrm{reg}}(\Omega) = -\frac{\mathrm{Im}\,\chi_{II}(\Omega)}{T\Omega L}. \tag{1.29}$$

The imaginary part of the retarded correlator is then converted to a symmetric correlator using

the results of Sec. 1.3.1:

$$\begin{aligned}
\kappa_{\mathrm{reg}}(\Omega) &= \frac{-1}{T\Omega L}\cdot\tfrac{1}{2}\left[C^{+}_{\mathcal{I}\mathcal{I}}(\Omega)-C^{-}_{\mathcal{I}\mathcal{I}}(\Omega)\right] && \left[\text{Eq. (1.14)}\right]\\
&= \frac{1-e^{-\beta\Omega}}{2T\Omega L}\,C^{+}_{\mathcal{I}\mathcal{I}}(\Omega) && \left[C^{-}=e^{-\beta\Omega}C^{+},\ \text{Eq. (1.13)}\right]\\
&= \frac{1-e^{-\beta\Omega}}{T\Omega}\int_0^\infty e^{\imath\Omega t}\lim_{L\to\infty}\frac{\langle\mathcal{I}(t)\,\mathcal{I}(0)\rangle}{L}\,dt, && \left[C^{+}(\Omega)=2\,\mathrm{Re}\,\tilde{C}_{\mathrm{ret}}(\Omega),\ \mathcal{I}\ \text{time-reversal even}\right]
\end{aligned} \tag{1.30}$$

The prefactor $(1-e^{-\beta\Omega})/(T\Omega)$ encodes the asymmetry between absorption and emission at finite temperature and is precisely the ratio introduced by the FDT, Eq. (1.15). In the dc limit $\Omega\to 0$ it approaches β, and Eq. (1.30) reduces to the Einstein relation between the diffusion coefficient and the integrated current autocorrelation. The Drude term in Eq. (1.35) adds a separate $2\pi D_{\mathrm{th}}\,\delta(\Omega)$ contribution whose weight is set by the overlap of $\mathcal{I}$ with the conserved charges through the Mazur bound of Sec. 1.3.5.

The spin conductivity $\sigma^{s}(\Omega)$ takes an analogous form: it is obtained from Eq. (1.30) by replacing the thermal current $\mathcal{I}$ with the spin current operator $\mathcal{J}^{s}$, defined via the continuity equation for the local magnetisation density in place of Eq. (1.21).

1.3.4 Sum rules

A sum rule is an identity of the form

$$\int_0^\infty d\Omega\;\mathcal{S}_{AB}(\Omega)=\langle\mathcal{O}\rangle, \tag{1.31}$$

where $\mathcal{S}_{AB}(\Omega)$ is a spectral function built from a response function and $\mathcal{O}$ is an operator whose equal-time expectation value in the equilibrium ensemble is known. The left-hand side encodes the full Ω-dependence of the dynamics across the spectrum; the right-hand side is a single static quantity, computable from the ground state or the thermal ensemble alone with no reference to how the system evolves. The Thomas-Reiche-Kuhn f-sum rule is the prototype. For a non-relativistic electronic system, integration of the optical conductivity yields the total particle number,

$$\int_0^\infty d\Omega\;\mathrm{Re}\,\sigma(\Omega)=\frac{\pi e^{2}N}{2mV}, \tag{1.32}$$

a statement that follows from the canonical commutator $[x,p]=\imath\hbar$ and is therefore independent of the interactions. Sum rules of this kind are widespread. One prominent example is Luttinger's theorem, equating the volume enclosed by the Fermi surface of an interacting system to its particle density [22].

Sum rules are frequency-domain conservation laws that follow from the equations of motion alone and constrain the spectral weight distribution between the Drude peak and the regular part [23, 3]. The thermal conductivity satisfies

$$\int_0^\infty \mathrm{Re}\,\kappa(\Omega)\;d\Omega=\frac{\pi}{2TL}\,\langle\Theta\rangle, \tag{1.33}$$

where $\Theta = -\lim_{k\to 0}(d/dk)\,[\hat{\mathcal{I}}(k),\, \hat{H}(-k)]$ is the thermal stress operator [23], and the closely related spin sum rule reads [24]

$$\int_0^\infty \mathrm{Re}\,\sigma^s(\Omega)\; d\Omega = \frac{\pi}{2L}\left\langle -\frac{\partial^2 H}{\partial \phi^2}\right\rangle_{\phi=0}. \tag{1.34}$$

The right-hand side of each sum rule is an equal-time expectation value computable from the ground state or the thermal ensemble, independently of the dynamics.

1.3.5 Drude weight and ballistic transport

In integrable systems, the conductivity generically decomposes as

$$\kappa(\Omega) = 2\pi D_{\mathrm{th}}\,\delta(\Omega) + \kappa_{\mathrm{reg}}(\Omega). \tag{1.35}$$

where D_{th} is the thermal Drude weight and κ_{reg} is the regular part at finite frequency. A familiar example is as follows. Consider electrons in a perfectly clean crystal subjected to a constant electric field. In the absence of any mechanism that breaks momentum conservation, the electrons must accelerate indefinitely, and the DC conductivity diverges. This divergence is encoded in a delta function at zero frequency in the real part of the optical conductivity.

The Drude weight for conductivity is given by the long-time limit of the current–current correlator,

$$D_{\mathrm{th}}(T) = \lim_{t\to\infty}\lim_{L\to\infty}\frac{\langle \mathcal{I}(t)\,\mathcal{I}(0)\rangle}{2LT^2}. \tag{1.36}$$

A nonzero D_{th} signals ballistic transport: the system carries a persistent current without dissipation. The Mazur inequality [5, 6] provides a lower bound on D_{th} in terms of the overlap of the current with conserved charges. For a set of mutually orthogonal conserved charges $\{Q^{(k)}\}$ (with inner product $\langle A, B\rangle_\rho = \mathrm{Tr}[\rho\, A^\dagger B]$),

$$D_{\mathrm{th}}(T) \geq \lim_{L\to\infty}\frac{1}{2LT^2}\sum_k \frac{|\langle Q^{(k)},\, \mathcal{I}\rangle_\rho|^2}{\langle Q^{(k)},\, Q^{(k)}\rangle_\rho}, \tag{1.37}$$

with equality when $\{Q^{(k)}\}$ spans the full space of conserved charges [25]. This inequality is the key tool connecting integrability to macroscopic ballistic transport [7, 26, 27]. Substituting the decomposition Eq. (1.35) into Eq. (1.33) separates the contributions from the Drude peak and the regular part,

$$\pi D_{\mathrm{th}} + \int_0^\infty \mathrm{Re}\,\kappa_{\mathrm{reg}}(\Omega)\, d\Omega = \frac{\pi}{2TL}\,\langle\Theta\rangle, \tag{1.38}$$

so that knowledge of any two of the three quantities determines the third. In practice, D_{th} is obtained from the Mazur bound Eq. (1.37) and $\langle\Theta\rangle$ from an independent static calculation, making Eq. (1.38) the primary consistency check on the tDMRG spectral integration in Chapter 3.

1.4 The XXZ Spin Chain: Integrability, Bethe Ansatz, and Transport

The spin-$\frac{1}{2}$ XXZ chain serves as the prototype integrable model in which the preceding formalism can be made fully explicit. Its Hamiltonian on a chain of L sites with periodic boundary conditions is

$$H = J\sum_{j=1}^{L}(S_j^x S_{j+1}^x + S_j^y S_{j+1}^y + \Delta\, S_j^z S_{j+1}^z) \tag{1.39}$$

with $J > 0$ and anisotropy Δ. Writing $\Delta = \cos\eta$, the model is gapless for $|\Delta| < 1$ (Luttinger liquid), SU(2)-symmetric at $\Delta = 1$ (Heisenberg), and gapped for $\Delta > 1$ (Néel phase). ALternatively, J can be written as follows.

$$H = J\sum_{j=1}^{L}\frac{1}{2}(S_j^+ S_{j+1}^- + S_j^- S_{j+1}^+) + \Delta\, S_j^z S_{j+1}^z \tag{1.40}$$

1.4.1 Magnons, scattering, and the rapidity variable

Before introducing the algebraic machinery, we establish what is actually being computed. A convenient starting point is the fully polarised ferromagnetic state $|0\rangle = |\uparrow\uparrow\cdots\uparrow\rangle$, which is an exact eigenstate of H_{XXZ} with energy $E_0 = J\Delta L/4$. The simplest excitations above $|0\rangle$ are obtained by flipping a single spin. The state $|j\rangle = S_j^-|0\rangle$ is not an eigenstate—the hopping terms $S_j^+ S_{j+1}^-$ in Eq. (1.40) move the flipped spin to a neighboring site. Translational invariance tells us to diagonalize in momentum space, and the plane-wave combination

$$|k\rangle = \frac{1}{\sqrt{L}}\sum_{j=1}^{L} e^{\imath kj}\, S_j^-|0\rangle \tag{1.41}$$

is an exact eigenstate with dispersion

$$\varepsilon(k) = J(\cos k - \Delta). \tag{1.42}$$

This is a *magnon*: a single spin-flip excitation propagating coherently on the ferromagnetic background. It plays the role of a single-particle excitation for the chain, in the same way a phonon does for a crystal.

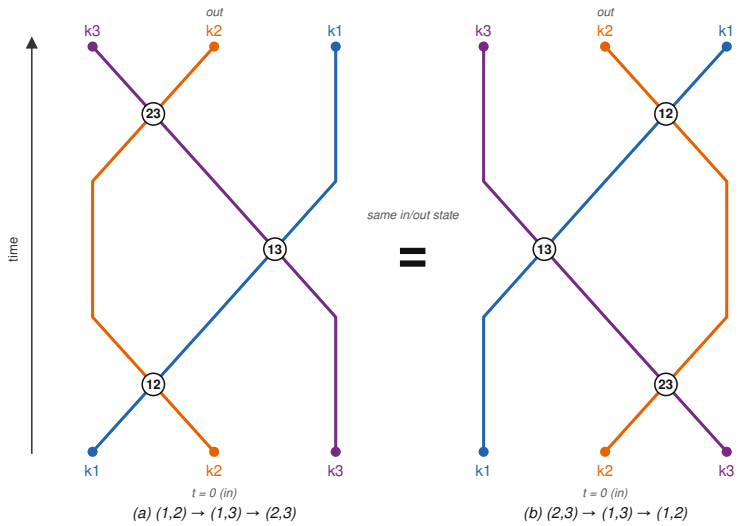

Figure 1.1: Two temporal orderings of the three pairwise collisions among magnons with momenta k_1, k_2, k_3, drawn as worldlines in space–time. In (a) the collisions occur in the sequence $(1,2) \to (1,3) \to (2,3)$; in (b), $(2,3) \to (1,3) \to (1,2)$. Both histories interpolate between the same incoming and outgoing momentum configuration, so the total scattering phase accumulated must be identical either way: $\Theta(k_1, k_2, k_3) = \theta_{12} + \theta_{13} + \theta_{23}$.

Two-magnon states and scattering. Flipping two spins gives a genuine interacting problem. Before asking what the interaction does, it is worth asking what it *can* do, given the constraints the Hamiltonian imposes. The XXZ chain conserves S^z_{tot} ($U(1)$ symmetry), so the number of down-spins is fixed: no magnons can be created or destroyed in a collision. Conservation of total momentum $k_1 + k_2$ and total energy $\varepsilon(k_1) + \varepsilon(k_2)$ further constrain the two-body problem. In one dimension these two conservation laws are already sufficient to fix the outgoing momenta: they must be either (k_1, k_2) (forward scattering, trivial) or (k_2, k_1) (exchange scattering, the only non-trivial option). Since the magnons are identical, forward and exchange scattering are physically indistinguishable and differ only by an overall complex phase $e^{\imath\theta(k_1,k_2)}$. The $\Delta\, S^z S^z$ term is the interaction that generates this phase; crucially, the block-diagonal structure imposed by $U(1)$ symmetry prevents it from mixing the two-magnon sector with any other. The exact two-magnon wavefunction therefore has the form

$$\Psi(j_1, j_2) \;\propto\; e^{\imath(k_1 j_1 + k_2 j_2)} + e^{\imath\theta(k_1,k_2)}\, e^{\imath(k_2 j_1 + k_1 j_2)}, \qquad j_1 < j_2, \tag{1.43}$$

an incoming plane wave plus an exchange-scattered one, with relative amplitude given by the two-body scattering phase $\theta(k_1, k_2)$. Such an interaction is called *elastic* and *non-diffractive*: kinematics alone, enforced by the $U(1)$ symmetry and one-dimensionality, ensure that the only effect of a collision is a phase shift.

Factorisation in the N-magnon sector. For a generic interacting model in one dimension, even if two-body scattering is elastic, an N-body collision would generate new amplitudes that cannot be written as a product of pairwise phases: the result of three particles colliding simultaneously is not the same as three successive two-body collisions. The XXZ chain is special precisely because this *is* the same. To see why, consider three magnons with momenta k_1, k_2, k_3.

In one dimension their world lines must cross pairwise, but the order in which the three crossings occur depends on the initial positions. There are two distinct orderings: collisions $(1,2)$, then $(1,3)$, then $(2,3)$; or collisions $(2,3)$, then $(1,3)$, then $(1,2)$. Since the in-state and the out-state are the same in both cases, consistency requires that the total accumulated phase is the same as well (Fig. 1.1). A Hamiltonian for which this consistency condition is satisfied is one in which the three-body amplitude genuinely factorises into pairwise pieces, and by induction the same holds for any N. The N-body scattering phase is therefore

$$\Theta(k_1, \dots, k_N) = \sum_{i<j} \theta(k_i, k_j), \tag{1.44}$$

and all dynamical information is compressed into the single two-body function θ. This factorisation is not a simplification one imposes; it is the precise statement of what "integrable" means in the present context. Most interacting models in one dimension do *not* satisfy this condition, which is why the XXZ chain, rather than being generic, is exceptional. When we recast the problem in the rapidity variable below, this consistency condition takes an especially clean operator form (the Yang–Baxter equation, Sec. 1.4.3) and becomes the starting point for the algebraic construction of the model.

A new variable: the rapidity. Written in the momentum variable k, the scattering phase $\theta(k_1, k_2)$ depends on both momenta in a complicated way. A change of variables $k \to \lambda$, defined through [28, 29]

$$e^{\imath k(\lambda)} = \frac{\sin\left(\frac{\lambda+\imath\eta}{2}\right)}{\sin\left(\frac{\lambda-\imath\eta}{2}\right)}, \qquad \Delta = \cos\eta, \tag{1.45}$$

linearises this dependence: the phase becomes a function only of the *rapidity difference*,

$$\theta(k_1, k_2) \;\longrightarrow\; \theta(\lambda_1 - \lambda_2). \tag{1.46}$$

The variable λ is called the *rapidity*. The analogy with special relativity is apt: just as a Lorentz boost acts additively on the relativistic rapidity but nonlinearly on the velocity, the scattering in the XXZ chain acts additively on λ but not on k. Choosing λ rather than k is thus not cosmetic; it is the choice that exposes the underlying symmetry of the scattering. Throughout what follows, quasiparticles are labelled by their rapidity, and the object that encodes the λ-dependence of scattering is the R-matrix, to which we now turn.

1.4.2 The R-matrix, the transfer matrix, and conserved charges

Integrability of the XXZ chain rests on a single algebraic object: the R-matrix. From the discussion of Sec. 1.4.1, we expect this object to encode the two-body scattering phase $\theta(\lambda_1 - \lambda_2)$ between magnons labelled by their rapidities, and to do so in a form that makes the factorisation property (1.44) manifest. The R-matrix does exactly this: it is the operator-valued two-body scattering amplitude acting on the internal (spin) degrees of freedom of the two colliding quasiparticles.

1.4.3 The R-matrix, the transfer matrix, and conserved charges

The algebraic backbone of Bethe-ansatz integrability is a single matrix-valued function of one complex variable, the R-matrix. Its role is to encode the two-body scattering of the magnons introduced in Sec. 1.4.1. Rather than postulate its form we construct it, in two steps: first by restricting its shape using the symmetries of the chain, then by solving the functional equation implied by scattering consistency.

Why scattering must be factorisable. Consider three magnons with rapidities $\lambda_1, \lambda_2, \lambda_3$ undergoing pairwise collisions in one dimension. In space–time, their world lines form three mutually crossing straight lines. Depending on the ordering of the collisions there are two distinct histories: (1–2) then (1–3) then (2–3), or (2–3) then (1–3) then (1–2). As space–time events these two histories correspond to the *same* asymptotic process; consistency requires that the accumulated scattering amplitudes agree. Writing the two-body scattering operator as $R(\lambda_i - \lambda_j)$ acting on the internal (spin) labels of the two colliding particles, this equality reads

$$R_{12}(\lambda_1 - \lambda_2)\, R_{13}(\lambda_1 - \lambda_3)\, R_{23}(\lambda_2 - \lambda_3) \;=\; R_{23}(\lambda_2 - \lambda_3)\, R_{13}(\lambda_1 - \lambda_3)\, R_{12}(\lambda_1 - \lambda_2), \tag{1.47}$$

the *Yang–Baxter equation* [30, 31, 32]. A solution of Eq. (1.47) is precisely a consistent factorised S-matrix: any N-body amplitude assembled from its two-body pieces is independent of the order in which collisions occur, and therefore depends only on the unordered set of rapidities $\{\lambda_i\}$. This is the content of "integrable" in the Yang–Baxter sense i.e., no genuine N-body scattering. Equation (1.47) is the condition that makes it possible.

Constructing the R-matrix from symmetry. For two spin-$\frac{1}{2}$ particles, $R_{ab}(\lambda)$ is a 4×4 matrix. Three physical inputs cut this down drastically.

First, the XXZ Hamiltonian commutes with S^z_{tot}, so magnons carry a conserved $U(1)$ charge. The two-body scattering must preserve this charge: $[R_{ab}(\lambda),\, S^z_a + S^z_b] = 0$. In the basis $(|\uparrow\uparrow\rangle, |\uparrow\downarrow\rangle, |\downarrow\uparrow\rangle, |\downarrow\downarrow\rangle)$ this forces R into block-diagonal form:

$$R_{ab}(\lambda) \;=\; \begin{pmatrix} a_+ & 0 & 0 & 0 \\ 0 & b & c & 0 \\ 0 & c' & b' & 0 \\ 0 & 0 & 0 & a_- \end{pmatrix}, \tag{1.48}$$

with six independent entries: the *six-vertex* structure [31].

Second, the Hamiltonian is symmetric under global spin flip $\prod_j \sigma^x_j$, which exchanges the two sectors $S^z_{\text{tot}} = \pm 1$. This identifies $a_+ = a_- \equiv a$ and $b = b'$. Third, parity invariance (interchange of the two auxiliary labels $a \leftrightarrow b$) gives $c = c'$. What survives are three weights:

$$R_{ab}(\lambda) \;=\; \begin{pmatrix} a(\lambda) & 0 & 0 & 0 \\ 0 & b(\lambda) & c(\lambda) & 0 \\ 0 & c(\lambda) & b(\lambda) & 0 \\ 0 & 0 & 0 & a(\lambda) \end{pmatrix}. \tag{1.49}$$

Feeding this ansatz into Eq. (1.47) gives, after expansion of the $8 \times 8 = 64$ component equations (the Yang–Baxter equation is an operator identity on $(\mathbb{C}^2)^{\otimes 3}$), a single nontrivial functional relation on the three weights. A direct computation [31, 32] shows that Yang–Baxter reduces to the requirement that the ratio

$$\Delta \;\equiv\; \frac{a(\lambda)^2 + b(\lambda)^2 - c(\lambda)^2}{2\,a(\lambda)\,b(\lambda)} \tag{1.50}$$

be the same number for all pairs of rapidities in the equation—equivalently, that it be *independent of* λ [31]. The parameter Δ plays the role of an integration constant for the functional equation; physically, it is the anisotropy of the XXZ chain. For $|\Delta| < 1$ one writes $\Delta = \cos\eta$ with $\eta \in (0, \pi)$, and the unique solution (up to an overall scalar) is the trigonometric parametrisation

$$a(\lambda) = \sin(\lambda + \eta), \qquad b(\lambda) = \sin\lambda, \qquad c(\lambda) = \sin\eta, \tag{1.51}$$

which gives the R-matrix

$$R_{ab}(\lambda) \;=\; \begin{pmatrix} \sin(\lambda+\eta) & 0 & 0 & 0 \\ 0 & \sin\lambda & \sin\eta & 0 \\ 0 & \sin\eta & \sin\lambda & 0 \\ 0 & 0 & 0 & \sin(\lambda+\eta) \end{pmatrix}. \tag{1.52}$$

The gapped regime $\Delta > 1$ uses the hyperbolic parametrisation $\Delta = \cosh\eta$ with $\sin \to \sinh$, and the free-fermion point $\Delta = 0$ is the rational limit. In all three regimes the anisotropy of the spin chain is the integration constant of the Yang–Baxter functional equation.

Checking Yang–Baxter. The content of Eq. (1.50) is trivial to verify for the trigonometric weights. Using standard identities,

$$\begin{aligned} a^2 + b^2 - c^2 &= \sin^2(\lambda+\eta) + \sin^2\lambda - \sin^2\eta \\ &= \cos\eta\,\big[\cos\eta - \cos(2\lambda+\eta)\big] \\ &= 2\cos\eta\;\sin(\lambda+\eta)\sin\lambda \\ &= 2\cos\eta\;a\,b, \end{aligned} \tag{1.53}$$

so that $(a^2 + b^2 - c^2)/(2ab) = \cos\eta$ independently of λ, as required. Yang–Baxter is therefore satisfied with the physical identification $\Delta = \cos\eta$.

Lax operator, monodromy, and transfer matrix. The R-matrix in Eq. (1.52) is a 4×4 matrix acting on the tensor product of two spin-$\frac{1}{2}$ spaces, $\mathbb{C}^2 \otimes \mathbb{C}^2$, corresponding to the two colliding particles. So far both copies have been on equal footing. The algebraic Bethe ansatz begins with a re-interpretation: we designate one copy as the physical spin at site j of the chain, and the other as an *auxiliary* space a, external to the chain and serving as a book-keeping device. Viewed this way, $R_{a,j}(\lambda)$ is a 2×2 matrix in the auxiliary space whose four entries are operators acting on site j; in this role we rename it the *Lax operator* $L_{a,j}(\lambda)$. The object itself has not changed — only the way we read its indices.

The usefulness of this rewriting is that 2×2 matrices can be multiplied. Taking the product along the chain with a *single* auxiliary line threaded through every site gives the *monodromy matrix*

$$M_a(\lambda) \;=\; L_{a,L}(\lambda)\, L_{a,L-1}(\lambda) \cdots L_{a,1}(\lambda) \;=\; \begin{pmatrix} A(\lambda) & B(\lambda) \\ C(\lambda) & D(\lambda) \end{pmatrix}_a . \tag{1.54}$$

The multiplication is ordinary 2×2 matrix multiplication in the auxiliary space, with the understanding that the operator-valued entries act on distinct physical sites and therefore commute among themselves across sites. The result is still a 2×2 matrix in auxiliary space, but its four entries A, B, C, D are now operators on the full 2^L-dimensional chain. Closing the auxiliary line into a loop i,e., tracing over the auxiliary space to eliminate it. This defines the *transfer matrix*

$$T(\lambda) \;=\; \mathrm{tr}_a\, M_a(\lambda) \;=\; A(\lambda) + D(\lambda), \tag{1.55}$$

which acts on the physical chain alone.

The Yang–Baxter equation (1.47) can be written in terms of R instead of M in a straightforward manner. Writing the YBE for three copies of $\mathbb{C}^2$ (two auxiliary labels a, b and one physical label j) and then iterating along the chain gives the *RTT relation*

$$R_{ab}(\lambda - \mu)\, M_a(\lambda)\, M_b(\mu) \;=\; M_b(\mu)\, M_a(\lambda)\, R_{ab}(\lambda - \mu). \tag{1.56}$$

For generic $\lambda - \mu$, the R-matrix is invertible; multiplying Eq. (1.56) on the left by $R_{ab}(\lambda - \mu)^{-1}$ gives

$$M_a(\lambda)\, M_b(\mu) \;=\; R_{ab}(\lambda - \mu)^{-1}\, M_b(\mu)\, M_a(\lambda)\, R_{ab}(\lambda - \mu). \tag{1.57}$$

Taking the trace over both auxiliary spaces and using the fact that M_a and M_b act on independent auxiliary factors, the left-hand side factorises as $\mathrm{tr}_{ab}[M_a(\lambda) M_b(\mu)] = T(\lambda) T(\mu)$. On the right-hand side, cyclicity of the trace moves the rightmost $R_{ab}(\lambda - \mu)$ to meet its inverse on the left, where they cancel, leaving $\mathrm{tr}_{ab}[M_b(\mu) M_a(\lambda)] = T(\mu) T(\lambda)$. Equating the two sides yields

$$\big[T(\lambda),\, T(\mu)\big] \;=\; 0 \qquad \text{for all} \quad \lambda, \mu \in \mathbb{C}. \tag{1.58}$$

The single-parameter family $T(\lambda)$ therefore shares a common eigenbasis at arbitrary rapidity, and any coefficient in its expansion about a chosen point of λ is a conserved operator on the chain.

The first two conserved charges. To extract *local* charges we expand about $\lambda = 0$, where from Eq. (1.52) one reads off $L_{a,j}(0) = \sin\eta\, P_{a,j}$ with $P_{a,j}$ the permutation of the auxiliary spin and the physical spin at site j. The monodromy at this point is a product of permutations,

$$M_a(0) \;=\; (\sin\eta)^L\, P_{a,L}\, P_{a,L-1} \cdots P_{a,1}, \tag{1.59}$$

and can be evaluated by acting on a basis state $|s\rangle_a \otimes |s_1 s_2 \cdots s_L\rangle$ and applying the permutations one at a time, right to left. Each $P_{a,j}$ swaps only the auxiliary slot with site j, leaving the other sites untouched. After the first swap the auxiliary slot holds s_1 and site 1 holds s; after the second, the auxiliary slot holds s_2, site 2 holds s_1, and site 1 still holds s; and soon. The auxiliary

label is handed forward one site at each step, so after all L swaps

$$M_a(0)\,|s\rangle_a \otimes |s_1 s_2 \cdots s_L\rangle \;=\; (\sin\eta)^L\,|s_L\rangle_a \otimes |s\, s_1 \cdots s_{L-1}\rangle. \tag{1.60}$$

Taking the trace over the auxiliary space with $\langle s|s_L\rangle_a = \delta_{s,s_L}$ replaces s by s_L in the chain and gives

$$T(0) \;=\; (\sin\eta)^L\,U, \tag{1.61}$$

where U is the one-site cyclic shift, $U\,|s_1 s_2 \cdots s_L\rangle = |s_L\, s_1 \cdots s_{L-1}\rangle$. Hence

$$Q_1 \;\equiv\; \ln T(0) - L\ln\sin\eta \;=\; \ln U \;=\; \imath P_{\mathrm{tot}}, \tag{1.62}$$

the total lattice momentum (up to an irrelevant c-number). This is the zeroth charge.

The first derivative of $\ln T(\lambda)$ at $\lambda = 0$ is, using the invertibility of $T(0)$,

$$\frac{d}{d\lambda}\ln T(\lambda)\Big|_{\lambda=0} \;=\; T(0)^{-1}\,T'(0) \;=\; \sum_{j=1}^{L} h_{j,j+1}, \tag{1.63}$$

with local density (sites $L+1 \equiv 1$)

$$h_{j,j+1} \;=\; \frac{1}{\sin\eta}\,P_{j,j+1}\,R'_{j,j+1}(0), \qquad R'(0) \;=\; \frac{\partial R}{\partial\lambda}\Big|_{\lambda=0}. \tag{1.64}$$

Only two ingredients are needed for the local algebra: the permutation and the derivative

$$R'(0) \;=\; \begin{pmatrix} \cos\eta & 0 & 0 & 0 \\ 0 & 1 & 0 & 0 \\ 0 & 0 & 1 & 0 \\ 0 & 0 & 0 & \cos\eta \end{pmatrix}. \tag{1.65}$$

Multiplying out and decomposing the result in Pauli operators on sites $j, j{+}1$,

$$P_{j,j+1}\,R'_{j,j+1}(0) \;=\; \tfrac{1}{2}\cos\eta\,\mathbb{I} \;+\; 2\big[S^x_j S^x_{j+1} + S^y_j S^y_{j+1} + \cos\eta\, S^z_j S^z_{j+1}\big], \tag{1.66}$$

so that, discarding the additive c-number,

$$\boxed{Q_2 \;\equiv\; \frac{\sin\eta}{2}\,\frac{d}{d\lambda}\ln T(\lambda)\Big|_{\lambda=0} \;=\; \sum_{j=1}^{L}\Big[S^x_j S^x_{j+1} + S^y_j S^y_{j+1} + \Delta\, S^z_j S^z_{j+1}\Big] \;=\; \frac{1}{J}\,H_{\mathrm{XXZ}},} \tag{1.67}$$

with $\Delta = \cos\eta$. The XXZ Hamiltonian is recovered exactly as the second charge in the tower, and the anisotropy Δ of the Hamiltonian is the same constant that labelled the R-matrix in Eq. (1.50).

The third charge and the energy current. The next member of the tower follows from the second derivative of $\ln T(\lambda)$. Since the monodromy is a product of L Lax operators (one per site), taking n derivatives of $T(\lambda)$ generates a sum of n local insertions at n sites along the chain. The logarithm then subtracts all *disconnected* contributions that are products of insertions at

non-overlapping sites. This leaves only *connected* strings in which the insertions share sites. At first order this gives a sum of bond densities $Q_2 = \sum_j h_{j,j+1}$; at second order, two insertions forced to share a site combine into the commutator

$$Q_3 \;=\; \sum_{j=1}^{L} \imath[h_{j-1,j},\, h_{j,j+1}]. \tag{1.68}$$

Q_3 is therefore strictly three-site: two overlapping bond densities share one common site (site j), with the outer sites $j-1$ and $j+1$ contributing trivially.

The equivalent algebraic statement is the *boost recursion* [33, 34, 35]

$$Q_{n+1} \;=\; [B,\, Q_n], \qquad B \;=\; -\imath \sum_j j\, h_{j,j+1}. \tag{1.69}$$

The boost operator B is the generator that systematically extracts connected overlapping strings: commuting it with Q_n multiplies each bond $h_{k,k+1}$ by the coordinate k, and the commutator then picks out precisely those pairs of bonds that overlap — the ones that survive the logarithm subtraction. Once $H = Q_2$ is known, Eq. (1.69) generates the entire tower algebraically, without any further reference to the R-matrix. Note that B itself is not conserved ($[B, H] \neq 0$); it is an auxiliary generator that maps charges to charges. The boost recursion captures the full local tower but does not generate the *quasilocal* charges that lie outside it and that become essential at root-of-unity anisotropy (Sec. 1.3.5).

Boost Formula for higher order derivatives

A short argument shows that Eq. (1.68) is genuinely equivalent to the second logarithmic derivative of $T(\lambda)$; we sketch it here to demystify the formula.

Expanding the Lax operator about the permutation point, $L_{a,j}(\lambda) = \sin\eta\, P_{a,j}\big[\mathbb{I} + \lambda\,\ell_j + \lambda^2\, m_j + O(\lambda^3)\big]$, the monodromy (1.54) becomes a telescoping product. Using $P_{a,j}\, X_j\, P_{a,j} = X_a$ to push permutations to the right and collecting powers of λ gives, after taking the auxiliary trace,

$$\ln T(\lambda) \;=\; \ln T(0) + \lambda\, Q_2 + \frac{\lambda^2}{2}\, Q_3 + O(\lambda^3), \tag{1.70}$$

with $Q_2 = \sum_j h_{j,j+1}$ as in Eq. (1.67) and a *second-order* piece that one must work out with care. The λ^2 coefficient of T itself is $\sum_j m_j + \sum_{j<k} h_{j,j+1}\, h_{k,k+1}$; the logarithm subtracts the square of the first-order piece, $\frac{1}{2}Q_2^2$, leaving

$$Q_3 \;=\; 2\sum_j m_j \;+\; \sum_{j<k} h_{j,j+1}\, h_{k,k+1} \;-\; \sum_{j,k} h_{j,j+1}\, h_{k,k+1}. \tag{1.71}$$

The double sum collapses to $-\sum_{j\geq k} h_{j,j+1} h_{k,k+1}$; the bulk of this double sum cancels against the m_j contributions (which are themselves quadratic in h on non-overlapping bonds), and the only terms that survive are those with j and k sharing a site—precisely $[h_{j-1,j},\, h_{j,j+1}]$. Restoring the overall factor gives Eq. (1.68).

The pattern generalises: at n-th order, non-overlapping products cancel between the contribution from the n-site Taylor coefficient of L and the n-fold product of Hamiltonian

densities produced by the logarithm, leaving only *connected* strings of overlapping commutators. This is the content of the boost recursion $Q_{n+1} = [B, Q_n]$ with $B = -\imath \sum_j j\, h_{j,j+1}$: the boost operator is the generator that systematically extracts these connected strings [33, 34].

For the XXZ chain, the commutator in Eq. (1.68) is evaluated by applying $[S^a_j, S^b_j] = \imath \epsilon_{abc} S^c_j$ at the site j shared by the two densities; contributions from the two outer sites commute trivially. A short calculation gives

$$\begin{aligned} \imath[h_{j-1,j},\, h_{j,j+1}] = \quad & \Delta\, S^z_{j-1}(\vec{S}_j \times \vec{S}_{j+1})^z \;+\; \Delta\, S^z_{j+1}(\vec{S}_{j-1} \times \vec{S}_j)^z \\ & -\; S^z_j(\vec{S}_{j-1} \times \vec{S}_{j+1})^z, \end{aligned} \tag{1.72}$$

so that $Q_3 = \sum_j j^E_j$ with j^E_j equal to the right-hand side of Eq. (1.72). At the isotropic point $\Delta = 1$, a vector identity collapses these three terms to the scalar chirality $Q_3\big|_{\Delta=1} = \sum_j \vec{S}_{j-1} \cdot (\vec{S}_j \times \vec{S}_{j+1})$, reproducing the familiar Heisenberg-chain energy current.

That Eq. (1.72) is genuinely the *energy current* rather than some arbitrary three-site operator that happens to be conservedfollows from an independent calculation. Writing the continuity equation for the local energy density,

$$\dot{h}_{j,j+1} = \imath[H,\, h_{j,j+1}] = -(j^E_{j+1} - j^E_j), \tag{1.73}$$

and noting that the only bonds of H that fail to commute with $h_{j,j+1}$ are its two overlapping neighbours, one reads off

$$j^E_j = \imath\big[h_{j-1,j},\, h_{j,j+1}\big], \tag{1.74}$$

exactly the summand of Eq. (1.68). The total thermal current is therefore *equal* to the third charge in the integrable tower, $\mathcal{J}^E = Q_3$, and is strictly locally conserved in the same sense as the Hamiltonian itself.

This coincidence, thermal current = an exact local charge is what makes thermal transport in the XXZ chain purely ballistic, with an infinite Drude weight at every finite temperature via the Mazur bound of Sec. 1.3.5. In Chapter 3 we shall see that the situation in the Z_3 chiral clock model is markedly different: the thermal current is *not* equal to any Q_n, but it retains a finite overlap with $Q^{(2)}$, producing a saturated Mazur bound rather than a trivial identification.

In Chapter 3 we apply the same transfer-matrix construction to the Z_3 chiral clock model, where the thermal current is *not* equal to any charge Q_n but has a finite overlap with $Q^{(2)}$, giving a saturated Mazur bound.

1.4.4 Bethe ansatz and thermodynamics

The coordinate Bethe ansatz [28, 29] constructs exact eigenstates as superpositions of plane waves with rapidity parameters λ_j. In the thermodynamic limit, the discrete rapidities become a continuum described by root density $\rho(\lambda)$ and hole density $\rho^h(\lambda)$, with total density $\rho^t = \rho + \rho^h$

satisfying the Bethe–Takahashi equation

$$\rho^t(\lambda) = \frac{1}{2\pi}\frac{dp}{d\lambda} + \int_{-\pi}^{\pi} \frac{d\mu}{2\pi}\, \varphi(\lambda-\mu)\, \rho(\mu) \tag{1.75}$$

where $\varphi(\lambda) = d\theta/d\lambda$ is the derivative of the scattering phase.

The filling fraction $\vartheta(\lambda) = \rho(\lambda)/\rho^t(\lambda)$ is determined by the thermodynamic Bethe ansatz (TBA) equations [29, 36],

$$\ln \frac{\rho^h(\lambda)}{\rho(\lambda)} = \beta\varepsilon(\lambda) - \int_{-\pi}^{\pi} \frac{d\mu}{2\pi}\, \varphi(\lambda-\mu)\, \ln\!\left(1 + \frac{\rho(\mu)}{\rho^h(\mu)}\right) \tag{1.76}$$

with bare energy $\varepsilon(\lambda) = J(\cos k(\lambda) - \cos\eta)$. All finite-temperature thermodynamic quantities follow from $\rho(\lambda)$.

Generalised hydrodynamics (GHD) [37, 38] provides an exact formula for the spin Drude weight in terms of the dressed quasiparticle velocity $v^{\mathrm{eff}}(\lambda) = (\varepsilon')^{\mathrm{dr}}/(p')^{\mathrm{dr}}$, obtained via the dressing equation $f^{\mathrm{dr}}(\lambda) = f(\lambda) + \int (d\mu/2\pi)\, \varphi(\lambda-\mu)\, \vartheta(\mu)\, f^{\mathrm{dr}}(\mu)$:

$$D_s = \frac{1}{2}\int_{-\pi}^{\pi} d\lambda\, \rho^t(\lambda)\, \vartheta(\lambda)\, (1-\vartheta(\lambda))\, \left[v^{\mathrm{eff}}(\lambda)\right]^2. \tag{1.77}$$

The factor $\vartheta(1-\vartheta)$ is the quasiparticle compressibility. The GHD formula agrees with Kohn-formula calculations [39], Mazur-bound estimates [26], and tDMRG results [40], and provides the analytical benchmark for the numerical transport calculations in this thesis.

1.5 Lindblad Dynamics and the Nonequilibrium Steady State

When a quantum system is weakly coupled to large Markovian reservoirs, integrating out the bath in the Born–Markov and secular approximations yields a closed equation of motion for the reduced density matrix ρ [41]. The result is the Lindblad master equation [10, 42]

$$\frac{\partial\rho}{\partial t} = \mathcal{L}\rho \equiv -\imath[H,\rho] + \sum_k \left(2L_k\,\rho\,L_k^\dagger - \{L_k^\dagger L_k,\,\rho\}\right), \tag{1.78}$$

where $\{L_k\}$ are Lindblad (jump) operators and $\mathcal{L}$ is the Liouvillian superoperator. Dissipation rate (usually referred to as γ) is absorbed in $\{L_k\}$ i.e. $L_k = \sqrt{\gamma}c_k$ where c_k is the bare jump operator. The Gorini–Kossakowski–Sudarshan–Lindblad theorem [42, 10] establishes that Eq. (1.78) is the most general generator of a completely positive, trace-preserving (CPTP) semigroup, so $\rho(t) = e^{\mathcal{L}t}\rho(0)$ remains a valid density matrix at all times. In the long-time limit the system relaxes to the NESS ρ_∞ satisfying $\mathcal{L}\rho_\infty = 0$.

1.5.1 Vectorisation and the Liouvillian spectrum

It is often convenient to flatten the density matrix onto the doubled Hilbert space $\mathcal{H}\otimes\mathcal{H}^*$ via $\rho = \sum_{ab}\rho_{ab}\,|a\rangle\langle b| \;\mapsto\; |\rho\rangle\!\rangle = \sum_{ab}\rho_{ab}\,|a\rangle\otimes|b\rangle$. In this representation $\mathcal{L}$ becomes an ordinary

(non-Hermitian) matrix,

$$\mathcal{L} = -\imath(H \otimes \mathbb{I} - \mathbb{I} \otimes H^T) + \sum_k (2\, L_k \otimes L_k^* - L_k^\dagger L_k \otimes \mathbb{I} - \mathbb{I} \otimes L_k^T L_k^*), \tag{1.79}$$

and the NESS is the right eigenvector of $\mathcal{L}$ with eigenvalue zero. The remaining spectrum $\{\Lambda_\alpha\}$ satisfies $\mathrm{Re}\,\Lambda_\alpha \leq 0$ by contractivity of the semi-group; the spectral gap $\Delta = -\max_{\alpha\neq 0} \mathrm{Re}\,\Lambda_\alpha$ sets the asymptotic relaxation rate, while the distribution of eigenvalues near the origin controls the approach to stationary state. The vectorized form in Eq. (1.79) is what makes matrix product operator ansätze a natural tool for open systems: the MPO is a variational approximation to the zero eigenvector of $\mathcal{L}$ on $\mathcal{H} \otimes \mathcal{H}^*$, treated on the same footing as an MPS on a chain of doubled local dimension.

1.5.2 Detailed balance versus boundary driving

If the jump operators are chosen so that $\mathcal{L}$ satisfies quantum detailed balance with respect to the Gibbs state [43],

$$\mathcal{L}^*[\rho_\beta^{1/2}\, A\, \rho_\beta^{1/2}] = \rho_\beta^{1/2}\, (\mathcal{L}^\dagger A)\, \rho_\beta^{1/2}, \tag{1.80}$$

then $\rho_\infty = \rho_\beta \propto e^{-\beta H}$ and the KMS condition of Sec. 1.3 is recovered at the steady state. A nontrivial NESS arises precisely when detailed balance is broken—either by coupling different portions of the system to reservoirs at different temperatures or chemical potentials, or by applying non-conservative jump operators at the boundaries.

For the boundary-driven XXZ chain studied in Chapter 4, the jump operators at the two ends pump spins in opposite directions ($L_1 = \sigma^+$, $L_N = \sigma^-$), producing a current-carrying steady state with a finite magnetisation gradient. Bulk conservation of S^z implies a local continuity equation $\dot{s}_i^z = -(j_{i+1}^s - j_i^s)$, and the NESS supports a uniform spin current $\langle j_i^s \rangle_\infty = \text{const}$ fixed by the boundary rates. The exact matrix product operator solution of Prosen [44] renders all local NESS properties analytically accessible.

In such a NESS, neither the KMS condition nor the FDT of Sec. 1.3.1 applies: detailed balance fails by construction, and fluctuations can no longer be inferred from linear response. Characterising the steady state therefore requires going beyond two-point correlators to the full probability distribution of local observables, which we describe next.

1.6 Full Counting Statistics and Large Deviations

The full probability distribution $P(m)$ of a spatially averaged local observable $\hat{m} = L^{-1}\sum_i \hat{o}_i$ is characterised by the moment generating function

$$Z(\lambda, L) = \mathrm{Tr}[e^{\lambda L \hat{m}}\, \rho], \tag{1.81}$$

where λ is the counting field conjugate to $\hat{m}$. For large systems, the relevant object is the scaled cumulant generating function (SCGF),

$$\mu(\lambda) = \lim_{L\to\infty} \frac{1}{L} \ln Z(\lambda, L), \tag{1.82}$$

whose derivatives at the origin give the cumulant densities $\kappa_n = d^n\mu/d\lambda^n|_{\lambda=0}$. The first two are the mean $\kappa_1 = \langle\hat{m}\rangle$ and the variance density $\kappa_2 = L\,\mathrm{Var}(\hat{m})$.

Under the conditions of the Gärtner–Ellis theorem [45]—essentially, that $\mu(\lambda)$ exists and is differentiable in a neighbourhood of the real axis—the probability of observing an atypical fluctuation $\hat{m} = m$ obeys a large-deviation principle,

$$P(\hat{m} = m) \asymp e^{-L\,I(m)}, \tag{1.83}$$

with rate function given by the Legendre–Fenchel transform of the SCGF,

$$I(m) = \sup_{\lambda}\big[\lambda m - \mu(\lambda)\big]. \tag{1.84}$$

Convexity of I follows automatically, as does $I(\langle\hat{m}\rangle) = 0$ and $I(m) \geq 0$ elsewhere. Near the mean, Taylor expansion reproduces the Gaussian regime

$$I(m) \approx \frac{(m - \langle\hat{m}\rangle)^2}{2\kappa_2}, \tag{1.85}$$

recovering the central limit theorem. The non-Gaussian tails of $I(m)$ are the genuinely new information encoded in full counting statistics: they probe the interaction-induced correlations that distinguish a quantum many-body steady state from L independent samples.

1.6.1 A tractable example: magnetisation of independent spins

The mechanics of Eq. (1.84) are most transparent in the simplest nontrivial setting: L uncorrelated spin-$\frac{1}{2}$ degrees of freedom in the maximally mixed state, with $\hat{m} = L^{-1}\sum_i \sigma_i^z$. Because the sites are independent and $\mathrm{Tr}[e^{\lambda\sigma^z}]/2 = \cosh\lambda$,

$$Z(\lambda, L) = [\cosh\lambda]^L \quad\Longrightarrow\quad \mu(\lambda) = \ln\cosh\lambda, \tag{1.86}$$

independently of L. The extremising condition $m = \mu'(\lambda) = \tanh\lambda$ inverts to $\lambda(m) = \frac{1}{2}\ln[(1+m)/(1-m)]$, and substituting into Eq. (1.84) yields the closed form

$$\boxed{I(m) = \frac{1+m}{2}\ln(1+m) + \frac{1-m}{2}\ln(1-m).} \tag{1.87}$$

This is the relative entropy of a biased coin with bias $(1+m)/2$ against the unbiased one. It vanishes at $m = 0$, grows logarithmically, and diverges as $m \to \pm 1$—the deterministic values the finite system can only attain with probability 2^{-L}. Expanding near the mean gives $I(m) \approx m^2/2$, consistent with $\kappa_2 = 1$ for uncorrelated spins.

The example is elementary but sets up the structure that recurs throughout FCS calculations: $\mu(\lambda)$ plays the role of a free energy density in a λ-biased ensemble, the counting field λ is the thermodynamically conjugate "force", and $I(m)$ is the entropy cost of constraining $\hat{m}$ to an atypical value. For the boundary-driven XXZ chain the ensemble is a NESS rather than a Gibbs state, and $Z(\lambda, L)$ is not a simple product: using the MPO solution of Sec. 1.5, $\mu(\lambda)$ is instead obtained as the logarithm of the largest eigenvalue of a λ-deformed transfer matrix [44].

Nonanalyticities in $\mu(\lambda)$ away from $\lambda = 0$ then signal dynamical phase transitions in the space of fluctuations—an effect strongly modulated by the anisotropy Δ, as developed in Chapter 4.

1.7 Eigenstate Thermalization and its Violations

We now turn from transport and steady states to the broader question of equilibration in closed quantum systems, which underlies Chapters 5 and 6.

1.7.1 The Eigenstate Thermalization Hypothesis

The eigenstate thermalization hypothesis (ETH) [8, 9, 46] asserts that in quantum-chaotic systems, the matrix elements of any local observable A in the energy eigenbasis $\{|n\rangle\}$ take the form

$$\langle m|A|n\rangle = A(\bar{E})\,\delta_{mn} + e^{-S(\bar{E})/2}\,f_A(\bar{E},\Omega)\,R_{mn} \tag{1.88}$$

where $\bar{E} = (E_m + E_n)/2$, $\Omega = E_m - E_n$, $S(\bar{E})$ is the microcanonical entropy, $f_A(\bar{E},\Omega)$ is a smooth function, and R_{mn} is a pseudo-random variable with zero mean and unit variance.

The diagonal part states that individual eigenstates encode thermal expectation values: $\langle n|A|n\rangle \approx A(E_n)$. For a generic initial state $|\psi_0\rangle = \sum_n c_n|n\rangle$ drawn from a narrow energy window, the late-time expectation value

$$\overline{\langle A(t)\rangle} = \sum_n |c_n|^2\,\langle n|A|n\rangle \approx A(\bar{E}) \tag{1.89}$$

reproduces the microcanonical average. The off-diagonal part governs dynamical correlations: the smooth envelope $f_A(\bar{E},\Omega)$ is directly related to the response function $\chi_{AA}(\Omega)$ of Sec. 1.2, connecting ETH to linear response theory.

The diagonal statement implies more than thermalisation of global observables. For a bipartition $\mathcal{H} = \mathcal{H}_A \otimes \mathcal{H}_{\bar{A}}$ with $|A|$ much smaller than the system, the reduced density matrix on A obtained from a single eigenstate $|n\rangle$ approaches the thermal reduced density matrix $\rho^A_{\rm th} = \mathrm{tr}_{\bar{A}}(e^{-\beta H}/Z)$ at the inverse temperature fixed by E_n [9, 46]. In this sense a pure eigenstate "is" a thermal state: no local measurement can distinguish it from the Gibbs ensemble.

1.7.2 Off-diagonal ETH and spectral functions

Whereas the diagonal part of Eq. (1.88) controls static expectation values, the off-diagonal envelope $f_A(\bar{E},\Omega)$ controls dynamics. Consider the thermal autocorrelator of a local observable A,

$$C_{AA}(t) = \langle A(t)\,A(0)\rangle_\beta = \frac{1}{Z}\sum_{m,n} e^{-\beta E_n}\,|\langle m|A|n\rangle|^2\,e^{i(E_n - E_m)t}. \tag{1.90}$$

Substituting the ETH ansatz and passing to the continuum, $\sum_n \to \int dE_n\, e^{S(E_n)}$, the pseudo-random variables R_{mn} self-average and the density-of-states factor $e^{S(E_m)+S(E_n)}$ cancels the $e^{-S(\bar{E})}$ in $|A_{mn}|^2$. Saddle-point evaluation on $\bar{E}$ fixes the thermal energy $\bar{E}_\beta$ through $S'(\bar{E}_\beta) = \beta$,

and one is left with a smooth integral over Ω alone:

$$S_{AA}(\Omega) \equiv \int_{-\infty}^{\infty} dt\, e^{\imath\Omega t}\, C_{AA}(t) \;\propto\; |f_A(\bar{E}_\beta, \Omega)|^2\, e^{\beta\Omega/2}, \tag{1.91}$$

up to corrections exponentially suppressed in the entropy [46, 47]. Combined with the FDT of Sec. 1.3.1, this determines the imaginary part of the response function up to thermal kinematic factors, so that $\mathrm{Im}\,\chi_{AA}(\Omega)$ is in the quantum-chaotic sector, entirely fixed by the ETH envelope.

The envelope f_A thus carries a dual interpretation. Statistically, $|f_A(\bar{E}, \Omega)|^2$ is the variance of off-diagonal matrix elements of A at energy $\bar{E}$ and energy transfer Ω, accessible in principle from numerical diagonalization. Dynamically, it is (up to kinematic factors) the spectral function that enters the Kubo formulas of Sec. 1.3.3: the thermal conductivity kernel in Eq. (1.30) is fixed by $f_{\mathcal{I}}$, the spin conductivity by $f_{\mathcal{J}^s}$, and so on. Hydrodynamic behavior is encoded in the small-Ω structure: a finite limit $|f_A(\bar{E}, 0)|^2 > 0$ signals ballistic transport, a vanishing $|f_A|^2 \sim \Omega$ diffusion, and conserved-charge structure constrains f_A at low frequencies. Off-diagonal ETH is in this sense the microscopic underpinning of the Kubo formalism of Sec. 1.3.3: the existence of a smooth envelope is what allows the entire machinery of linear response, FDT, and Drude-weight decomposition to transfer from the thermal ensemble to individual eigenstates.

1.7.3 Generalised Gibbs Ensemble

Integrable systems violate ETH because eigenstates at the same energy can differ in the eigenvalues of the conserved charges $\{Q^{(k)}\}$ (Sec. 1.4.3). The late-time steady state is the generalised Gibbs ensemble (GGE) [48, 49],

$$\rho_{\mathrm{GGE}} = \frac{1}{Z_{\mathrm{GGE}}} \exp\Big(-\sum_k \lambda_k\, Q^{(k)}\Big), \tag{1.92}$$

where the Lagrange multipliers $\{\lambda_k\}$ are fixed by the initial conditions. The GGE reduces to the Gibbs ensemble when only the Hamiltonian is conserved. This distinction manifests directly in transport: the GGE encodes the memory of conserved charges that protect currents from decaying, producing the nonzero Drude weight of Sec. 1.3.5.

Systems with strong quenched disorder can exhibit many-body localisation (MBL) [50, 51, 52], where all eigenstates are localised in Fock space and transport vanishes entirely. In the MBL phase, the system possesses an extensive set of local integrals of motion (LIOMs or ℓ-bits) $\{\tilde{\tau}_i^z\}$ with exponentially decaying mutual interactions [53, 54]. Despite the absence of thermalisation, MBL systems exhibit dephasing that drives the system toward a diagonal ensemble [55]. This dephasing is essential for the convergence of the projected ensemble to universal state designs, as studied in Chapter 5.

1.8 Quantum State Ensembles and k-Designs

The ETH describes thermalization at the level of the density matrix—the first moment of the ensemble of states accessible through measurement. A deeper question is whether the full statistical structure of the state ensemble also thermalises. This requires the language of quantum state designs, which we briefly introduce here; the specific constructions (projected ensemble,

Scrooge ensemble) are developed in Chapters 5 and 6.

1.8.1 Haar measure and random states

The natural notion of a uniformly random pure state in a D-dimensional Hilbert space is the Haar measure on $U(D)$. A Haar-random state $|\psi\rangle = \sum_i c_i|i\rangle$ has components c_i that are independent complex Gaussians (after normalisation), giving the measure [56]

$$P_{\text{Haar}}(\psi) = \int \delta\Big(\psi - \frac{\tilde{\Psi}}{\|\tilde{\Psi}\|}\Big) \prod_{i=1}^{D} \frac{D}{\pi}\, e^{-D|\tilde{\Psi}_i|^2}\, d^2\tilde{\Psi}_i. \tag{1.93}$$

Haar-random states in a bipartite system have nearly maximal entanglement when $D_B \gg D_A$ [57]—the volume-law scaling that makes them intractable for matrix product states (Chapter 2).

1.8.2 Approximate k-designs

An ensemble $\mathcal{E} = \{p_i, |\psi_i\rangle\}$ is a k-design if its k-th moment

$$\rho_{\mathcal{E}}^{(k)} = \sum_i p_i \left(|\psi_i\rangle\langle\psi_i|\right)^{\otimes k} \tag{1.94}$$

matches that of the Haar ensemble [58, 59]. A k=1 design reproduces the correct density matrix; a k=2 design additionally reproduces the purity fluctuations; higher k capture finer statistical structure. The proximity of two ensembles is quantified by the trace distance between their k-th moments,

$$\Delta^{(k)}(\mathcal{E}, \mathcal{E}') = \tfrac{1}{2}\,\mathrm{Tr}\sqrt{(\rho_{\mathcal{E}}^{(k)} - \rho_{\mathcal{E}'}^{(k)})^\dagger(\rho_{\mathcal{E}}^{(k)} - \rho_{\mathcal{E}'}^{(k)})}. \tag{1.95}$$

The convergence $\Delta^{(k)} \to 0$ with system size or time is the quantitative criterion for deep thermalization used in Chapters 5 and 6.

1.8.3 The Porter–Thomas distribution

The statistical fingerprint of Haar-random states in a fixed basis is the Porter–Thomas distribution [60]. For a Haar-random state, the measurement-outcome probabilities $p_i = |c_i|^2$ follow

$$P_{\text{PT}}(p) = (D-1)(1-p)^{D-2} \;\approx\; D\, e^{-Dp} \quad \text{for} \quad D \gg 1. \tag{1.96}$$

The Porter–Thomas distribution arises naturally from random matrix theory, where eigenstates of Gaussian unitary ensemble (GUE) matrices have independent Gaussian components [61]. In the context of quantum chaos, the emergence of this distribution in the measurement statistics of a time-evolved state is a signature that the dynamics has generated an effective k-design [16]. A useful characterization of this distribution is *anti-concentration*: the probability mass is spread over exponentially many outcomes, with no single bitstring carrying weight much greater than $O(1/D)$. This is the property that makes Porter–Thomas statistics a meaningful benchmark for randomness at all — a distribution concentrated on a small number of outcomes would be cheap to reproduce classically. This randomness is expected to emerge in quantum scrambling systems. Deviations from Porter–Thomas are therefore a sensitive diagnostic of the failure of

quantum chaos, a point exploited in Chapter 5 to probe the measurement-basis dependence of deep thermalization in MBL systems.

When the system possesses conserved charges, the appropriate reference ensemble is not the Haar ensemble but the Scrooge ensemble [62, 63]—the maximum-entropy ensemble of pure states subject to a fixed reduced density matrix. Its construction and role are discussed in Chapter 5.

1.9 Spectral Diagnostics of Quantum Chaos

Beyond the state-ensemble diagnostics above, quantum chaos can be probed through spectral correlations. The spectral form factor (SFF) is the Fourier transform of the two-point correlation of the density of states [61, 64],

$$\mathcal{K}(t) \;=\; \frac{1}{D^2}\,\overline{\left|\sum_n e^{-\imath E_n t}\right|^2}, \tag{1.97}$$

where the overline denotes an average over an ensemble (disorder realisations, random graphs, or time windows for a single sample). Expanding the square,

$$\mathcal{K}(t) \;=\; \frac{1}{D^2}\sum_{m,n}\overline{e^{-\imath(E_n-E_m)t}}, \tag{1.98}$$

exposes its content: $\mathcal{K}(t)$ is a sum over all pairs of energy levels, weighted by their spacing. Level *repulsion*, the defining spectral feature of random matrix theory, is therefore a direct statement about $\mathcal{K}(t)$.

In quantum-chaotic systems, $\mathcal{K}(t)$ exhibits a universal *dip–ramp–plateau* structure. At short times the sum in Eq. (1.98) is dominated by the smooth density of states and $\mathcal{K}(t)$ decays from unity (the "dip"). At intermediate times, correlations between distinct levels produce a linear-in-t "ramp" whose slope is fixed by the Wigner–Dyson ensemble of the symmetry class. At times larger than the Heisenberg time $t_{\mathrm{H}} \sim D/\bar{\rho}$ (with $\bar{\rho}$ the mean level density), the discreteness of the spectrum saturates the sum and $\mathcal{K}(t)$ reaches a plateau at $1/D$. The timescale at which the ramp begins, the *Thouless time* t_{Th} [65, 66], marks the onset of random-matrix universality and diverges at the transition out of the chaotic phase. In integrable systems, where energy levels are Poisson-distributed and uncorrelated, the ramp is absent and $\mathcal{K}(t)$ decays monotonically to the plateau.

A limitation of $\mathcal{K}(t)$ is that it is sensitive to eigenvalues alone: two Hamiltonians with identical spectra but different eigenvectors produce the same SFF. A refinement is the *partial* spectral form factor (pSFF) [67, 68], defined by restricting the trace to a subsystem A,

$$\mathcal{K}_A(t) \;=\; \frac{1}{D^2}\,\overline{\mathrm{tr}_A\left|\mathrm{tr}_{\bar{A}}\, e^{-\imath H t}\right|^2}. \tag{1.99}$$

Because $\mathcal{K}_A(t)$ involves partial traces of the evolution operator, it captures correlations among eigenvectors as well as eigenvalues; in particular, it is sensitive to the entanglement structure of individual eigenstates through its dependence on the bipartition. The pSFF has been measured directly in trapped-ion quantum simulators [67], motivating its use as a practical benchmark on

current hardware.

In Chapter 6 we employ both the SFF and the pSFF alongside the projected ensemble and Krylov complexity to characterise the chaos–integrability transition of the transverse-field Ising model on Erdős–Rényi graphs. The four diagnostics probe complementary aspects of chaos: the SFF tests spectral statistics, the pSFF tests eigenvector structure, the projected ensemble tests higher moments of the measurement distribution, and Krylov complexity tests operator spreading. Agreement across the four provides a stringent test that the transition is a genuine chaos–integrability crossover rather than a feature of any single diagnostic.

1.10 Outline of the Thesis

Chapter 2: Tensor Network Methods. We develop the MPS formalism and the tDMRG algorithm that provides the numerical backbone for Chapters 3 and 4.

Chapter 3: Thermal Transport in the Integrable Chiral Clock Model. The thermal Drude weight is computed by tDMRG and shown to be saturated by the Mazur bound from a single transfer-matrix charge $Q^{(2)}$. The sum rules of Sec. 1.3.4 validate the numerics.

Chapter 4: Full Counting Statistics in the Boundary-Driven XXZ Chain. We exploit the exact MPO solution of the NESS (Sec. 1.5) to compute the SCGF and rate function (Sec. 1.6) for several local observables in the thermodynamic limit.

Chapter 5: Projected Ensemble with Locally Conserved Charges. We study deep thermalization in MBL systems using the ℓ-bit Hamiltonian (Sec. 1.7), showing convergence of the projected ensemble to the Scrooge ensemble and connecting deviations to the Porter–Thomas distribution (Sec. 1.8.3).

Chapter 6: Quantum Chaos on Random Graphs. We deploy the projected ensemble, pSFF (Sec. 1.9), Krylov complexity, and the quantum Mpemba effect to characterise the chaos–integrability transition in the Ising model on Erdős–Rényi graphs.

2

Tensor Network Approach to Strongly Correlated Systems

STRONGLY correlated quantum systems rarely yield to exact analytical methods. The Hilbert space grows exponentially with system size making brute-force approaches limited to small systems. The strong interactions that make these systems interesting in the first place render perturbative treatments unreliable. Mean-field approaches fare no better at capturing the intricate phase structure across dynamical regimes. Efficient numerical methods play a crucial role in studying these systems. For the one-dimensional systems that form the subject of this thesis, the tool of choice is the matrix product state (MPS), and this chapter develops the formalism and algorithmic machinery needed for the chapters that follow. This chapter is not intended as a comprehensive introduction to tensor networks. We focus on the specific tools required for the calculations presented in later chapters and refer the reader to Refs. [69, 70, 71] for a more complete treatment.

2.1 Overview

The quantum many-body problem, at its core, is a problem of representation. A system of L spin-$\frac{1}{2}$ particles lives in a Hilbert space of dimension 2^L, so that specifying an arbitrary state requires 2^L complex amplitudes. For even moderate system sizes (e.g., $L \sim 100$), this already exceeds feasible classical information storage capacity.[1].

The states of primary physical interest are generally the low-energy eigenstates: they control equilibrium properties and determine the phases of matter accessible to experiment. For the systems studied in this thesis (except in Chapter 6), the Hamiltonians have spatial locality i.r., each constituent term in H acts on only a few neighboring sites, and this locality places strong constraints on the entanglement structure of these low-lying states. For a bipartition of the

[1]For concreteness, storing the state vector of $L = 100$ spin-$\frac{1}{2}$ particles at double precision (16 bytes per complex amplitude) would require roughly 2×10^{31} bytes, or about 2×10^{13} exabytes, exceeding the total estimated global data storage capacity ($\sim 10^{23}$ bytes) by eight orders of magnitude.

system into complementary subsystems A and B, the von Neumann entropy

$$S_A = -\mathrm{Tr}[\rho_A \log \rho_A], \qquad \rho_A = \mathrm{Tr}_B \, |\psi\rangle\langle\psi|, \tag{2.1}$$

quantifies the degree of quantum entanglement between the two parts. A generic state in the Hilbert space, one drawn uniformly at random (Formally, sampled from the Haar ensemble introduced in Chapter 1), obeys the *volume law*, $S_A \propto |A|$, with entanglement scaling as the size of the subsystem itself. Ground states of gapped, local Hamiltonians in one dimension obey a qualitatively different scaling: the *area law*,

$$S_A \leq \text{const}, \tag{2.2}$$

where the entropy is bounded by a quantity that scales with boundary of the subsystem [72]. This result, proved rigorously for one-dimensional gapped systems, implies that ground states occupy a small and structured corner of the full Hilbert space, that can be parameterized efficiently without ever confronting the full 2^L-dimensional Hilbert space. For one-dimensional system, this area law scaling implies a constant bound.

The matrix product state (MPS) formalism is designed to exploit this entanglement structure. Rather than representing the wavefunction as a single exponentially large tensor, MPS decomposes it into a chain of local tensors connected by bonds of finite dimension D, dentoted as the *bond dimension*. The area law guarantees that for gapped ground states, a modest D suffices for an accurate representation, reducing the cost of storing and manipulating the state from exponential to polynomial in system size. Understanding when and why this compression is faithful and where it breaks down is not merely a technical question. It is directly tied to the physics of entanglement growth, quantum criticality, and thermalization that underlies much of what is studied in this thesis. In the following sections, we will go through the systemetic construction of MPS and its properties. We will start with the definition of MPS and its properties, and then we will discuss the algorithms for constructing and manipulating MPS. Before discussing the contruction of MPS and it smanipulation to capture qunatum states, we start with the building bock of the tensor network mwthods i.e. tensors.

2.2 Tensors and Tensor Networks

The algorithms in this chapter are most naturally described using a diagrammatic language that we now introduce. A rank-k tensor is an array of complex numbers carrying k discrete indices, each running over a finite range. Some familiar physical quantities fit into this framework immediately. A scalar $s \in \mathbb{C}$ has no indices and is therefore a rank-0 tensor. A vector v_i with $i = 1, \ldots, d$ carries one index and is rank 1, while a matrix M_{ij} carries two indices and is rank 2. The complex conjugate of a vector, written v_i^*, is obtained by conjugating every entry. In the diagrammatic notation used throughout this thesis, each tensor is drawn as a filled shape with one protruding line (or "leg") per index. A scalar has no legs, a vector has one, and a matrix has two. For the dual vector v_i^* the leg is conventionally drawn on the opposite side to distinguish it from the ket. These conventions are illustrated in Fig. 2.1.

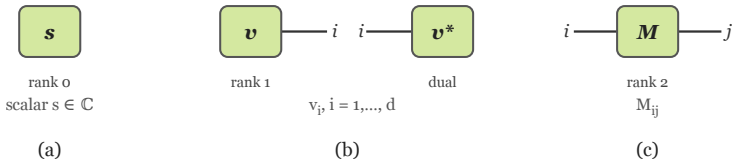

Figure 2.1: (a) A scalar s is a rank-0 tensor with no legs. (b) A vector v_i is a rank-1 tensor with one leg; its dual v_i^* has the leg flipped.(c) A matrix M_{ij} is a rank-2 tensor with two legs.

Tensors can be combined through contraction, which amounts to summing over a shared index. The simplest example is matrix-vector multiplication. Multiplying a matrix M_{ij} by a vector u_j sums over the index j and produces a vector $v_i = M_{ij}\, u_j$. Similarly, two matrices A_{ij} and B_{jk} can be multiplied by summing over the common index j, yielding a matrix $C_{ik} = A_{ij}\, B_{jk}$ (following the Einstein summation convention throughout). In the diagrammatic picture, contraction corresponds to connecting the legs of two tensors that share an index. The connected leg disappears from the result and the remaining free legs become the indices of the output tensor. This graphical rule extends to networks of many tensors and is what makes the diagrammatic notation so useful for the MPS constructions that follow. The pictorial representations of matrix-vector and matrix-matrix multiplication are shown in Fig. 2.2.

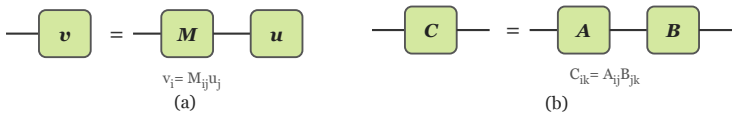

Figure 2.2: (a) Matrix-vector multiplication: the shared index j is contracted (connected legs). (b) Matrix-matrix multiplication: $C_{ik} = A_{ij} \cdot B_{jk}$; the contracted index j disappears from the result.

2.3 Singular Value Decomposition

Several of the algorithms developed in this chapter rely on a controlled way of factorising matrices, and the tool that makes this possible is the singular value decomposition (SVD). We summarise its key properties here, as they are invoked at nearly every step of the constructions that follow.

Given any complex matrix M of dimensions $N_A \times N_B$, there exist matrices U, S, and V such that

$$M = U\, S\, V^\dagger. \tag{2.3}$$

The three factors satisfy the following properties.

- S is a diagonal matrix of size $\lambda \times \lambda$ with $\lambda = \min(N_A, N_B)$. Its entries are real and non-negative, and when arranged in decreasing order they are called the singular values of M.
- U and V have dimensions $N_A \times \lambda$ and $N_B \times \lambda$ respectively. Both have orthonormal columns, meaning $U^\dagger U = V^\dagger V = \mathbb{I}_\lambda$.

The decomposition is unique up to phases when all singular values are distinct. Pictorially this can be shown as follows.

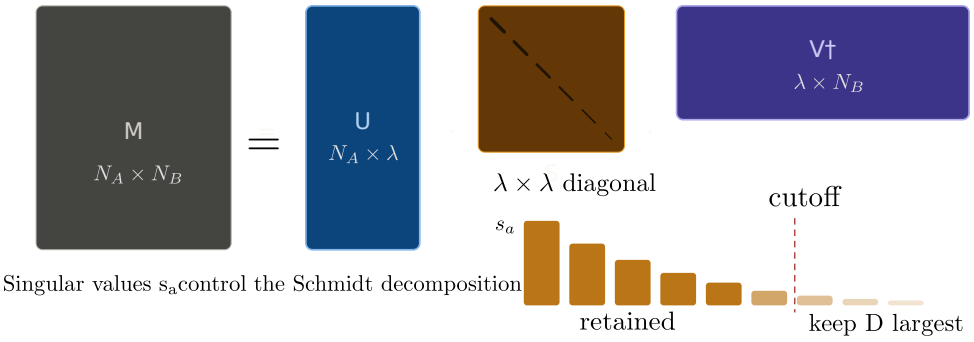

The connection between SVD and entanglement is worth spelling out, as it underpins nearly every algorithm discussed in this chapter. Consider a bipartite pure state $|\psi\rangle$ written in some product basis $|i\rangle_A |j\rangle_B$. The coefficient matrix Ψ_{ij} can be decomposed via SVD as $\Psi = U\,S\,V^\dagger$, which immediately yields the Schmidt decomposition

$$|\psi\rangle = \sum_{a=1}^{r} s_a \, |a\rangle_A \, |a\rangle_B \,, \tag{2.4}$$

where s_a are the singular values, $|a\rangle_A$ and $|a\rangle_B$ are orthonormal bases for the left and right partitions respectively, and $r = \min(D_A, D_B)$ is the Schmidt rank. The eigenvalues of the reduced density matrix are simply $w_a = s_a^2$, so the von Neumann entropy can be computed directly from the singular values:

$$S = -\sum_a w_a \log_2 w_a. \tag{2.5}$$

For a ground state obeying the area law, the singular values fall off rapidly, which means that truncating to a modest number D of Schmidt states introduces only an exponentially small error. This is the reason why MPS (which are built by successive SVDs, as we shall see next) can efficiently capture the physics of such states.

2.4 Matrix Product States

An MPS represents the exponentially large coefficient tensor $c_{\sigma_1\sigma_2\ldots\sigma_L}$ as a product of L small tensors, one per site, contracted along a one-dimensional chain. The factorization is achieved by applying SVD repeatedly, peeling off one site at a time from left to right. If no singular values are discarded, the factorization is exact and the product of the local tensors recovers $c_{\sigma_1\sigma_2\ldots\sigma_L}$ identically. If the smallest singular values are truncated at each step, the result is an approximation whose accuracy is controlled by the number of singular values retained.

The MPS as a tensor factorization. From a computational point of view, this is a particular form of *tensor decomposition*: the coefficient tensor is written as a *tensor train* [73], which is the name under which MPS are known in the applied mathematics and machine learning. Just as a large matrix can be compressed by its truncated SVD, a large tensor can be compressed by its tensor train decomposition. The key parameter controlling the accuracy of this compression is the

bond dimension D, which plays a role analogous to the rank in a low-rank matrix approximation.

For a spin chain of L spins with open boundary conditions, the MPS representation of the coefficient $c_{\sigma_1\sigma_2\ldots\sigma_L}$ of any arbitrary pure state $|\psi\rangle$ is given by

$$c_{\sigma_1\sigma_2\ldots\sigma_L} = \sum_{\alpha} T^{\sigma_1}_{\alpha_1}\, T^{\sigma_2}_{\alpha_1,\alpha_2} \cdots T^{\sigma_{L-1}}_{\alpha_{L-2},\alpha_{L-1}}\, T^{\sigma_L}_{\alpha_{L-1}} \tag{2.6}$$

where the summation over α denotes summation over all internal (bond) indices α_i, $i = 1, \ldots, N-1$. For each fixed value of the physical index σ_i, the local tensor T^{σ_i} is a matrix of dimension at most $D \times D$. The coefficient $c_{\sigma_1\sigma_2\ldots\sigma_N}$ is therefore a product of L such matrices (with the first and last being a row and column vector respectively), hence the name "matrix product state."

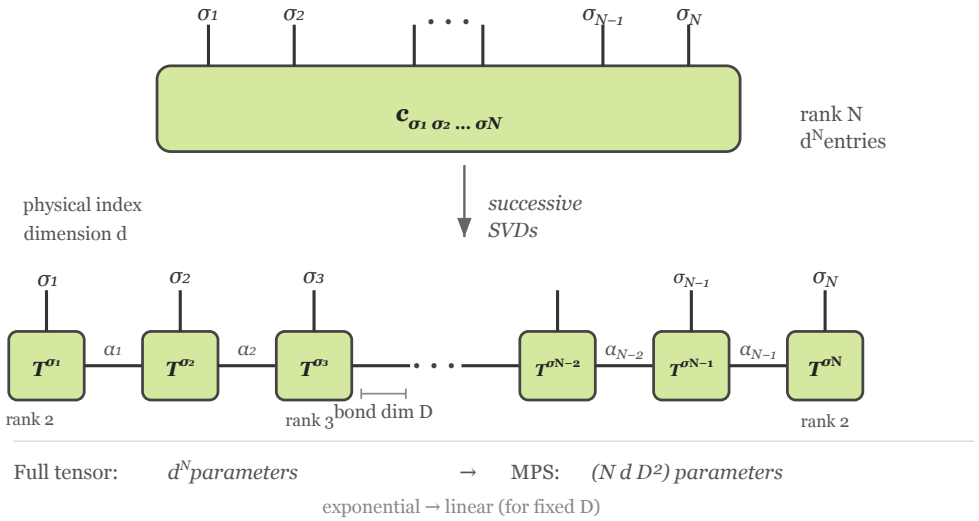

Figure 2.3: The MPS decomposition of the coefficient tensor $c_{\sigma_1\sigma_2\ldots\sigma_N}$. The rank-$N$ tensor (top), which requires d^N complex entries to store, is factorised into a chain of local tensors T^{σ_i} by successive SVDs. Each local tensor has one physical index σ_i of dimension d (vertical leg) and up to two bond indices α_i of dimension D (horizontal legs). The first and last tensors are rank 2 while all bulk tensors are rank 3. The total number of parameters reduces from d^N to $\mathcal{O}(N\,d\,D^2)$ for a fixed bond dimension D.

How the decomposition works. We illustrate the procedure for a chain of three spins, shown step by step in Fig. 2.4.

1. *Reshape.* Group the indices of the coefficient tensor $c_{\sigma_1\sigma_2\sigma_3}$ into a $d \times d^2$ matrix $c_{\sigma_1,(\sigma_2\sigma_3)}$.
2. *SVD.* Decompose $c_{\sigma_1,(\sigma_2\sigma_3)} = U_{\sigma_1,\alpha_1}\, S_{\alpha_1,\alpha_1}\, V^{\dagger}_{\alpha_1,\sigma_2\sigma_3}$. The columns of U, rearranged, give the first site tensor $T^{\sigma_1}_{\alpha_1}$. The remainder $Q_{\alpha_1,(\sigma_2\sigma_3)} = S\,V^{\dagger}$ is carried forward.
3. *Reshape and repeat.* Regroup Q as $Q_{(\alpha_1\sigma_2),\sigma_3}$ and perform a second SVD. This yields $T^{\sigma_2}_{\alpha_1,\alpha_2}$ from U and $T^{\sigma_3}_{\alpha_2}$ from $S\,V^{\dagger}$.

Each SVD peels off one site from the left end of the remaining tensor. For a general chain of N sites, the procedure is repeated $N-1$ times, sweeping from left to right.

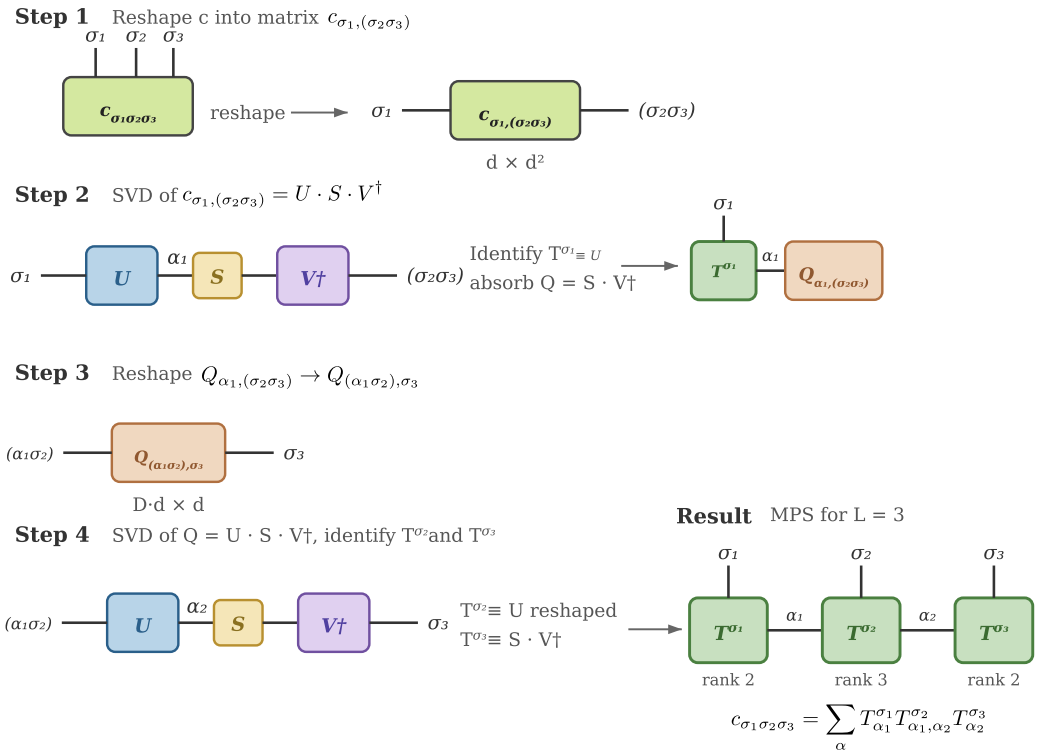

Figure 2.4: Illustration of decomposing a rank-3 tensor to an MPS

At each step, the SVD can be truncated to retain only the D largest singular values. Without truncation, the bond dimension at the k^{th} bond grows as $\min(d^k, d^{N-k})$, reaching its maximum in the middle of the chain and recovering the exact state. For states satisfying the area law, the singular values decay rapidly, so a modest D already yields an excellent approximation. More precisely, for a product state $D = 1$ suffices for an exact representation, while for area-law states the required D remains bounded as the system size increases, i.e. $D = \mathcal{O}(1)$ with respect to N. It is in this sense that the MPS representation efficiently exploits the area law scaling of entanglement.

For periodic boundary conditions, the MPS representation modifies to

$$c_{\sigma_1\sigma_2\ldots\sigma_N} = \sum_\alpha T^{\sigma_1}_{\alpha_0,\alpha_1} T^{\sigma_2}_{\alpha_1,\alpha_2} \cdots T^{\sigma_N}_{\alpha_{N-1},\alpha_0} = \mathrm{Tr}(T^{\sigma_1} T^{\sigma_2} \cdots T^{\sigma_N}) \ . \tag{2.7}$$

The difference between the two lies at the boundaries: in the open case, the first and last tensors are rank 2, while in the periodic case, all tensors are rank 3 and the first and last bond indices are traced over. In this thesis we deal primarily with open boundary conditions.

Counting parameters. The MPS representation reduces the number of variational parameters drastically for low-entanglement states. The full coefficient tensor in Eq. (2.6) has d^L entries, which grows exponentially with the system size. In the MPS representation, we have roughly L tensors of rank three, each with one physical index of dimension d and two bond indices of dimension $\mathcal{O}(D)$, giving $\mathcal{O}(L\, d\, D^2)$ parameters in total. For fixed D, this is *linear* in the system size.

To put this in concrete terms: a chain of $L = 100$ spin-$\frac{1}{2}$ particles has a Hilbert space of dimension $2^{100} \approx 10^{30}$. An MPS with bond dimension $D = 100$ requires only about $100 \times 2 \times 100^2 = 2 \times 10^6$ parameters — a compression ratio of some 10^{24}. Of course, not every state admits such a compact representation. The bond dimension D can itself grow exponentially with L for highly entangled states such as volume-law states, and in that case the MPS representation does not reduce the complexity of state representation. The class of states that *are* efficiently representable i.e., those in the "physical corner" of the Hilbert space discussed in Sec. 2.1, is the class for which D remains manageable.

MPS as a computational data structure. It is useful to think of an MPS not merely as a mathematical decomposition but as a *data structure* that supports a rich set of efficient operations. Given an MPS with bond dimension D:

- *Inner products* $\langle\phi|\psi\rangle$ between two MPS can be computed in $\mathcal{O}(L\,d\,D^3)$ time by sequential contraction from one end (Known as zipper method).
- *Local expectation values* $\langle\psi|\hat{O}_i|\psi\rangle$ cost $\mathcal{O}(d^2\,D^2)$ when the MPS is in the appropriate canonical form (Discussed in the next section).
- *Addition* of two MPS (to form $|\psi\rangle + |\phi\rangle$) is exact and produces an MPS whose bond dimension is the sum of the two input bond dimensions.
- *Application of an MPO* (Sec. 2.5) to an MPS produces an MPS whose bond dimension is the product $D \cdot D_W$, where D_W is the bond dimension of the MPO.

The last two operations increase the bond dimension, which must then be brought back to a manageable value by *compression* (e.g., SVD, Sec. 2.3). This compress-after-operate pattern is the computational backbone of MPS algorithms for time evolution and more.

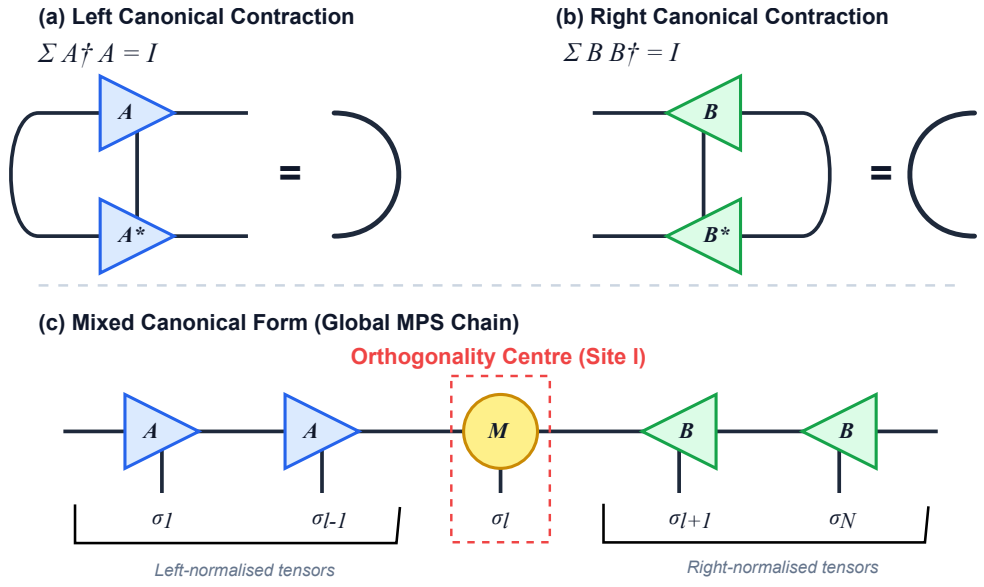

Figure 2.5: MPS canonical forms. (a, b) Contraction rules showing how left-normalized (A) and right-normalized (B) tensors evaluate to the identity. (c) A mixed canonical MPS centered at site l. This arrangement simplifies calculations because the left and right environments effectively cancel out.

2.4.1 Gauge degrees of freedom and canonical forms

The MPS representation of a pure state has a large gauge degree of freedom. Under the transformation

$$\tilde{T}^{\sigma_i}_{\beta_{i-1},\beta_i} = (X^{-1})^{(i)}_{\beta_{i-1},\alpha_{i-1}}\, T^{\sigma_i}_{\alpha_{i-1},\alpha_i}\, X^{(i+1)}_{\alpha_i,\beta_i} \tag{2.8}$$

for any choice of $\{X^{(1)}, \ldots, X^{(N-1)}\}$ invertible matrices with suitable dimensions, the physical state $|\psi\rangle$ remains unchanged. In the tensor diagram, this is visible as the insertion of $X^{(i+1)}\big(X^{(i+1)}\big)^{-1} = \mathbb{I}$ on the bond between sites i and $i+1$, which is an identity operation.

From a computational perspective, the gauge freedom means that the mapping from physical states to MPS representations is many-to-one: infinitely many different MPS tensors can describe the same quantum state. For a given state $|\psi\rangle$, all the possible MPS representations form a manifold. To make the representation unique (up to phases) and computationally convenient, we fix the gauge by imposing *normalisation conditions* on the local tensors, arriving at what are called *canonical forms*. This is analogous to putting a matrix in a normal form (such as row echelon form or Jordan form) to make subsequent computations easier and more numerically stable. We describe these canonical forms below.

Left canonical form. In this representation,

$$c_{\sigma_1\sigma_2\ldots\sigma_N} = \sum_{\alpha} A^{\sigma_1}_{\alpha_1}\, A^{\sigma_2}_{\alpha_1,\alpha_2} \cdots A^{\sigma_{N-1}}_{\alpha_{N-2},\alpha_{N-1}}\, A^{\sigma_N}_{\alpha_{N-1}}\,, \tag{2.9}$$

where the tensors A are "left-normalised" and satisfy

$$\sum_{\sigma_i}\sum_{\alpha_{i-1}} A^{\sigma_i\dagger}_{\alpha_{i-1},\alpha_i'}\, A^{\sigma_i}_{\alpha_{i-1},\alpha_i} = \delta_{\alpha_i,\alpha_i'}\,. \tag{2.10}$$

Diagrammatically, this means that contracting a left-normalised tensor with its conjugate over the physical index and the left bond index produces an identity on the right bond index, as shown in Fig. 2.5(a). From a linear algebra perspective, the condition says that for each site i, the matrix formed by stacking the d matrices $A^{\sigma_i=1}, A^{\sigma_i=2}, \ldots, A^{\sigma_i=d}$ vertically has orthonormal columns. This is the property guaranteed by the "thin U" factor of an SVD.

Right canonical form. Analogously,

$$c_{\sigma_1\sigma_2\ldots\sigma_N} = \sum_{\alpha} B^{\sigma_1}_{\alpha_1}\, B^{\sigma_2}_{\alpha_1,\alpha_2} \cdots B^{\sigma_{N-1}}_{\alpha_{N-2},\alpha_{N-1}}\, B^{\sigma_N}_{\alpha_{N-1}}\,, \tag{2.11}$$

with right-normalised tensors B satisfying

$$\sum_{\sigma_i}\sum_{\alpha_i} B^{\sigma_i\dagger}_{\alpha_{i-1}',\alpha_i}\, B^{\sigma_i}_{\alpha_{i-1},\alpha_i} = \delta_{\alpha_{i-1}',\alpha_{i-1}}\,. \tag{2.12}$$

Mixed canonical form. This is the form most commonly used in practice. We pick a particular site l called the *orthogonality centre*. All tensors to the left of site l are brought into left-canonical

form, and all tensors to the right are brought into right-canonical form:

$$c_{\sigma_1\sigma_2\ldots\sigma_N} = \sum_{\alpha} A^{\sigma_1}_{\alpha_1} \cdots A^{\sigma_l}_{\alpha_{l-1},\alpha_l} \, B^{\sigma_{l+1}}_{\alpha_l,\alpha_{l+1}} \cdots B^{\sigma_N}_{\alpha_{N-1}} \,. \tag{2.13}$$

The name "orthogonality centre" comes from the fact that the Schmidt bases for the bipartition at any bond touching site l are automatically orthonormal, thanks to the normalisation conditions (2.10) and (2.12). This has practical utility. When computing the norm $\langle\psi|\psi\rangle$, all left-normalised tensors contract to identity on the left and all right-normalised tensors contract to identity on the right, leaving only the contraction at the orthogonality centre. Similarly, computing a local observable at site l requires work only at that site (as we discuss in Sec. 2.5.2).

Constructing the canonical form. The procedure is an iterative application of SVD (or QR decomposition, which is cheaper when the singular values are not needed). Starting from site 1, one reshapes the local tensor, performs a QR decomposition, and absorbs the upper-triangular factor R into the tensor at the next site. Repeating this sweep from left to right brings all tensors into left-canonical form. Right-canonicalisation works analogously from site N to the left. A mixed canonical form centred at site l is obtained by left-canonicalising from site 1 to site $l-1$ and right-canonicalising from site N to site $l+1$. The cost of a full canonicalisation sweep is $\mathcal{O}(N\,d\,D^3)$.

Using a suitable gauge, any MPS representation can be converted to any of the three canonical forms. The choice of which form to use is dictated by the algorithm at hand: DMRG and TDVP sweep the orthogonality centre through the chain, while Trotter time evolution typically works with a globally canonical state and re-canonicalises after each time step.

2.5 Matrix Product Operators

The idea of MPS can be straightforwardly generalised to operators, and the analogous construction for operators is called Matrix Product Operators (MPO). Where an MPS has one physical index per site (the ket index), an MPO has *two* — one for the incoming (bra) index σ'_i and one for the outgoing (ket) index σ_i. A general operator $\hat{O}$ can be written in MPO form as

$$\hat{O} = \sum_{\sigma,\sigma'} W^{\sigma_1\sigma'_1}_{[1]\beta_1} \, W^{\sigma_2\sigma'_2}_{[2]\beta_1,\beta_2} \cdots W^{\sigma_N\sigma'_N}_{[N]\beta_{N-1}} \, |\sigma_1\sigma_2\ldots\sigma_N\rangle\langle\sigma'_1\sigma'_2\ldots\sigma'_N| \,. \tag{2.14}$$

The diagrammatic representation of an MPO is shown in Fig. 2.6. Each local tensor $W_{[i]}$ now has four indices: two horizontal (bond) indices connecting to the neighbours and two vertical (physical) indices for σ_i and σ'_i.

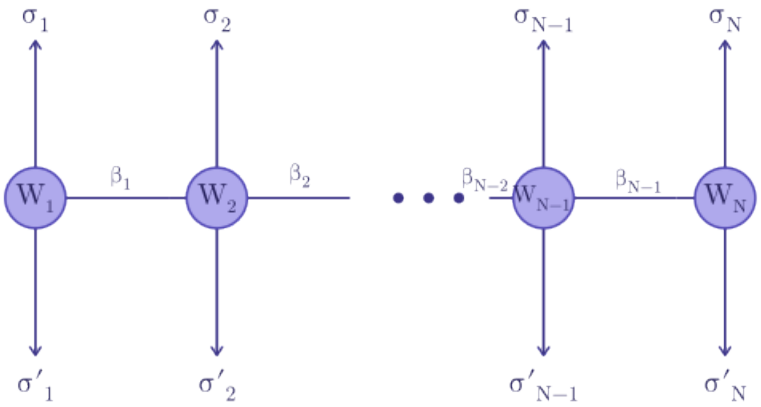

Figure 2.6: Diagrammatic representation of an MPO for a chain of N sites. Each tensor $W_{[i]}$ carries four indices: ket (σ_i, upward), bra (σ'_i, downward), and two horizontal bond indices β_{i-1}, β_i; boundary tensors are rank 3. Arrows indicate the direction of operator action, consistent with Eq. (2.14). The MPO bond dimension D_W controls operator complexity; see main text.

Another way to think of the MPO is that the W's are rank-2 tensors whose entries are themselves operators acting on the local Hilbert space (i.e., $d \times d$ matrices). In this manner of thinking, the local tensors of an MPS have vector-valued entries, while the local tensors of an MPO have matrix-valued (operator-valued) entries.

The MPO bond dimension. Just as the MPS bond dimension D controls how much entanglement the state can carry, the MPO bond dimension D_W controls the complexity of the operator. For a nearest-neighbour Hamiltonian, D_W is a small constant (typically $\mathcal{O}(5)$ to $\mathcal{O}(10)$, depending on the number of distinct coupling terms). For Hamiltonians with longer-range interactions, D_W can grow, but techniques exist to compress it. For example, by approximating a power-law coupling $J(r) = r^{-\alpha}$ as a sum of m exponentials, $J(r) \approx \sum_{k=1}^{m} c_k \, \lambda_k^r$, which yields an MPO bond dimension of $D_W = m + 2$ regardless of the system size [74, 75, 76]. The central role of MPOs in practice is that they act on MPS by contraction: given a state $|\psi\rangle$ in MPS form with bond dimension D, applying $\hat{O}$ produces a new MPS whose bond dimension grows to $D\,D_W$. Each site contraction costs $\mathcal{O}(D^2 D_W d^2)$ operations, where d is the local Hilbert space dimension. This is the operation performed at every step of time-evolution algorithms (Sec. 2.7) and at every Lanczos iteration in ground-state search; keeping D_W small is therefore as important as keeping D small for numerical tractability.

2.5.1 Constructing the MPO: the chiral clock Hamiltonian as a finite state automaton

Rather than simply writing down the MPO tensor for a given Hamiltonian, it is instructive to see how it can be *constructed* systematically. The key idea, due to Crosswhite and Bacon [77], is to think of the MPO as a *finite state automaton* (FSA), a concept from theoretical computer science. We illustrate this by building the MPO for the chiral clock Hamiltonian, which appears

in Chapter 3 of this thesis:

$$H = -J \sum_{i=1}^{N-1} (e^{i\theta}\, \sigma_i \sigma_{i+1}^{\dagger} + e^{-i\theta}\, \sigma_i^{\dagger} \sigma_{i+1}) - \sum_{i=1}^{N} (f\, e^{i\phi}\, \tau_i + f\, e^{-i\phi}\, \tau_i^{\dagger})\,. \tag{2.15}$$

Here σ and τ are the $\mathbb{Z}_n$ clock operators satisfying $\sigma^n = \tau^n = \mathbb{I}$ and $\sigma\tau = \omega\,\tau\sigma$ with $\omega = e^{2\pi i/n}$, θ is the chiral parameter for the coupling, and ϕ controls the transverse field direction.

Operator strings. The starting point is to write each term of H in tensor product notation. Every term becomes a string of local operators, one per site, drawn from the alphabet $\{\mathbb{I}, \sigma, \sigma^{\dagger}, \tau, \tau^{\dagger}\}$. For instance, the coupling $-Je^{i\theta}\,\sigma_2\sigma_3^{\dagger}$ on a five-site chain becomes the string $\mathbb{I} \otimes \sigma \otimes \sigma^{\dagger} \otimes \mathbb{I} \otimes \mathbb{I}$. The full Hamiltonian is the sum of all such strings. Our task is to construct an automaton that generates every string exactly once with the correct coefficient.

States of the automaton. We read each string from right to left and introduce a "state" to track how far along the chain we are. For the chiral clock Hamiltonian, the nearest-neighbour coupling involves exactly two operators, so we need to track three stages (see Fig. 2.7):

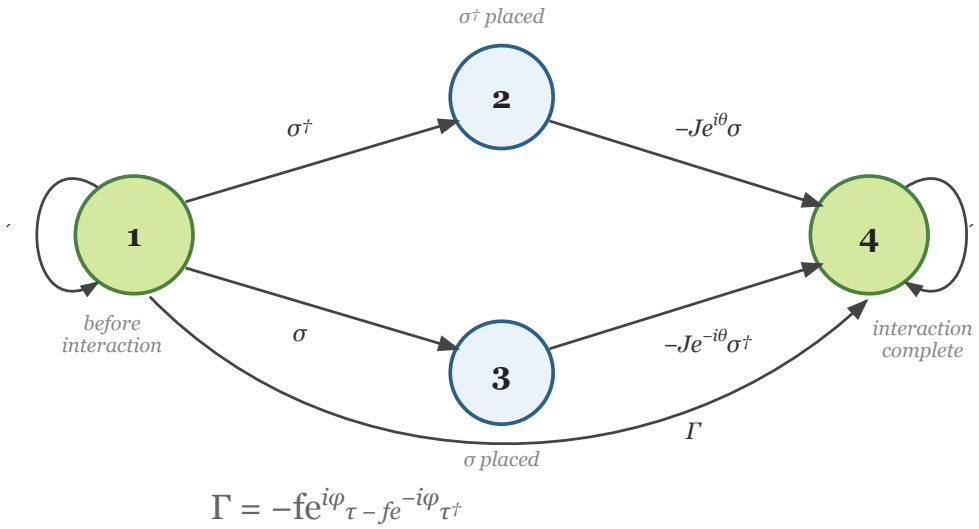

Figure 2.7: Finite state automaton for the MPO of the chiral clock Hamiltonian (Eq. 2.15). Each node is an automaton state, and each directed edge is labeled by the operator emitted during the transition. The two coupling channels ($\sigma\sigma^{\dagger}$ and $\sigma^{\dagger}\sigma$) pass through states 2 and 3 respectively, while the on-site field Γ corresponds to a direct transition from state 1 to state 4. The transition matrix of this automaton is the bulk MPO tensor $W_{[i]}$ in Eq. (2.16), with bond dimension $D_W = 4$.

1. *Before the interaction* (state 1). Reading from the right, we have seen only $\mathbb{I}$ so far. The automaton remains in state 1 as long as it emits $\mathbb{I}$.

2. *First operator placed* (states 2 and 3). The automaton encounters the right-hand operator of a two-body coupling term. There are two possibilities: if the term is $e^{i\theta}\sigma_i\sigma_{i+1}^{\dagger}$, then the right-hand operator is $\sigma^{\dagger}$ and we enter state 2; if the term is $e^{-i\theta}\sigma_i^{\dagger}\sigma_{i+1}$, then the right-hand operator is σ and we enter state 3.

3. *Interaction complete* (state 4). At the next site, the automaton places the matching left-hand operator with the appropriate coupling: $-Je^{i\theta}\sigma$ (completing the path through state 2) or $-Je^{-i\theta}\sigma^\dagger$ (completing the path through state 3). The automaton then enters state 4 and emits $\mathbb{I}$ for all remaining sites to the left.

The transverse field is a one-body term that requires no intermediate state. Writing $\Gamma = -f\,e^{i\phi}\,\tau - f\,e^{-i\phi}\,\tau^\dagger$ for the on-site field operator, this corresponds to a direct transition from state 1 to state 4, bypassing the intermediate states entirely.

Altogether we need four automaton states, so the MPO bond dimension is $D_W = 4$. This can be Compared this with the five states needed for the Heisenberg model, which has three distinct coupling channels (σ^x, σ^y, σ^z) instead of two.

From automaton to MPO tensor. The transition diagram is shown in Fig. 2.7. Each directed edge carries the operator emitted during the transition. The bulk MPO tensor $W_{[i]}$ is the *transition matrix* of this automaton. The entry $(W_{[i]})_{\beta,\beta'}$ is the operator emitted when transitioning from state β' to state β:

$$W_{[i]} = \begin{pmatrix} \mathbb{I} & 0 & 0 & 0 \\ \sigma^\dagger & 0 & 0 & 0 \\ \sigma & 0 & 0 & 0 \\ \Gamma & -Je^{i\theta}\sigma & -Je^{-i\theta}\sigma^\dagger & \mathbb{I} \end{pmatrix}. \tag{2.16}$$

The rows and columns are indexed by the four automaton states. The structure mirrors the transition diagram directly: the self-loops on states 1 and 4 appear as $\mathbb{I}$ on the diagonal, the two intermediate transitions fill the first column (rows 2 and 3), their completions fill the last row (columns 2 and 3), and the on-site field Γ occupies the $(4,1)$ entry.

The boundary tensors are fixed by the requirement that the automaton starts in state 1 (right boundary) and ends in state 4 (left boundary). Extracting the last row and first column:

$$W_{[1]} = \begin{pmatrix} \Gamma & -Je^{i\theta}\sigma & -Je^{-i\theta}\sigma^\dagger & \mathbb{I} \end{pmatrix}, \qquad W_{[N]} = \begin{pmatrix} \mathbb{I} \\ \sigma^\dagger \\ \sigma \\ \Gamma \end{pmatrix}. \tag{2.17}$$

Verification. We check the construction on a three-site chain. Consider the path $1 \xrightarrow{\sigma^\dagger} 2 \xrightarrow{-Je^{i\theta}\sigma} 4$ through the automaton. At site 3 the automaton is in state 1 and emits $\sigma^\dagger$; at site 2 it transitions to state 4 emitting $-Je^{i\theta}\sigma$; at site 1 it remains in state 4 and emits $\mathbb{I}$. The resulting operator string is $\mathbb{I} \otimes (-Je^{i\theta}\sigma) \otimes \sigma^\dagger = -Je^{i\theta}\,\sigma_2\sigma_3^\dagger$, which is indeed a term in Eq. (2.15). The conjugate path through state 3 produces $-Je^{-i\theta}\,\sigma_2^\dagger\sigma_3$, and the direct $1 \to 4$ paths at each site produce the on-site field terms. Summing over all paths recovers H.

The FSA approach provides a constructive recipe that works for any Hamiltonian expressible as a sum of products of local operators. One identifies the minimal set of automaton states needed to track the progress of each interaction term, writes down the transition rules with the

appropriate operator weights, and reads off the MPO tensor as the transition matrix. The MPO bond dimension equals the number of automaton states. =For Hamiltonians with longer-range interactions, the number of intermediate states grows (since the automaton must "remember" an operator placement for more than one step), but the resulting MPO can often be compressed to a smaller effective D_W [78, 79]. From a computational standpoint, the connection runs deeper. The set of operator strings that contribute to a Hamiltonian forms a *regular language*, and the MPO is the linear-algebraic encoding of the finite automaton that recognises this language. The MPO bond dimension is bounded by the number of states in the minimal automaton.

2.5.2 Expectation values and orthogonality

Computing the expectation value of a local or global operator is one of the most frequent operations in any MPS-based calculation. The naive approach, contracting the full bra $\langle\psi|$, the operator $\hat{O}$, and the ket $|\psi\rangle$ as a single tensor network scales exponentially in N and is therefore infeasible s in practice. The key insight is that the canonical form of the MPS, introduced in Sec. 2.4.1, reduces this contraction to a procedure that is linear in L and polynomial in D.

The overlap and the norm. Before treating operators, consider the simpler problem of computing the inner product $\langle\phi|\psi\rangle$ of two MPS. Writing both states in the form of Eq. (2.6), the overlap is

$$\langle\phi|\psi\rangle = \sum_{\{\sigma\}} (A^{\sigma_1})^\dagger \cdots (A^{\sigma_N})^\dagger \, B^{\sigma_1} \cdots B^{\sigma_N}, \tag{2.18}$$

where A^{σ_i} and B^{σ_i} are the site tensors of $|\phi\rangle$ and $|\psi\rangle$ respectively. This is evaluated by building a *transfer matrix* $\mathcal{T}$ that contracts the bra and ket layers site by site from left to right. The left boundary vector is initialised as the 1×1 identity, and at each site i the environment is updated as

$$\overline{L}^{[i]}_{\alpha,\alpha'} = \sum_{\sigma_i,\beta,\beta'} (A^{\sigma_i}_{\alpha,\beta})^* \, B^{\sigma_i}_{\alpha',\beta'} \, \overline{L}^{[i-1]}_{\beta,\beta'}, \tag{2.19}$$

with the norm recovered as $\langle\psi|\psi\rangle = \mathrm{Tr}(\overline{L}^{[N]})$. Each update costs $\mathcal{O}(D^3 d)$, so the total cost of the overlap is $\mathcal{O}(LD^3 d)$.

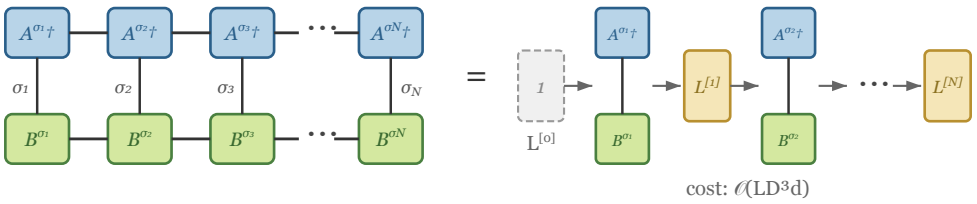

Figure 2.8: Overlap computation of two MPS through the transfer matrix $\overline{L}$.

Why orthogonality matters. For a general (non-canonical) MPS, every site contraction in Eq. (2.19) contributes a nontrivial matrix to the environment. In contrast, recall that a left-canonical MPS satisfies the isometry condition

$$\sum_{\sigma} (A^\sigma)^\dagger A^\sigma = \mathbf{1}, \tag{2.20}$$

and analogously for right-canonical tensors B^σ. When $|\psi\rangle = |\phi\rangle$ and every tensor is left-canonical, the left environment satisfies $\overline{L}^{[i]} = \mathbb{I}$ for all i, collapsing the full overlap to a single boundary contraction. This is the diagrammatic statement that all tensors to the left of any cut contribute only an identity to the reduced density matrix of the right half. This is a direct consequence of the Schmidt decomposition across that cut [69].

Single-site expectation values. For a single-site operator $\hat{o}_j$ acting at site j, we place the MPS in *mixed-canonical form* centred on j: tensors $\{A^{\sigma_i}\}_{i<j}$ are left-canonical and tensors $\{B^{\sigma_i}\}_{i>j}$ are right-canonical, with a single non-isometric centre tensor C^{σ_j}. In this gauge the expectation value reduces to

$$\langle \hat{o}_j \rangle = \sum_{\sigma_j, \sigma_j'} \sum_{\alpha, \alpha'} (C^{\sigma_j}_{\alpha,\alpha'})^* \; o_j^{\sigma_j, \sigma_j'} \; C^{\sigma_j'}_{\alpha,\alpha'}, \tag{2.21}$$

because the isometry conditions ensure that all environments left of j and right of j evaluate to identity matrices. The cost is $\mathcal{O}(D^2 d^2)$, independent of L once the canonical form has been established.

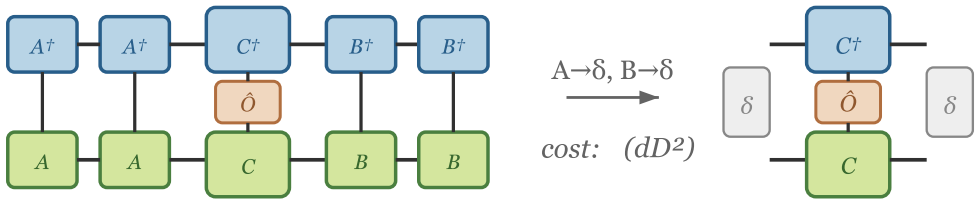

Figure 2.9: Expectation value of a single-site operator in mixed-canonical MPS.

Global operators and the MPO sandwich. For a global operator $\hat{O}$ written in MPO form with bond dimension D_W (Sec. 2.5), the expectation value

$$\langle \hat{O} \rangle = \langle \psi | \hat{O} | \psi \rangle = \sum_{\{\sigma, \sigma'\}} \langle \psi | \sigma' \rangle \, \langle \sigma' | \hat{O} | \sigma \rangle \, \langle \sigma | \psi \rangle \tag{2.22}$$

is evaluated by sweeping through the three-layer bra–MPO–ket network from left to right. At each site the environment tensor is a rank-3 object $F^{[i]}_{\alpha,\beta,\gamma}$ with one index for each layer, and the update rule is

$$F^{[i]}_{\alpha,\beta,\gamma} = \sum_{\sigma,\sigma'} \sum_{\alpha',\beta',\gamma'} (A^{\sigma}_{\alpha',\alpha})^* \; W^{\sigma\sigma'}_{\beta',\beta} \; A^{\sigma'}_{\gamma',\gamma} \; F^{[i-1]}_{\alpha',\beta',\gamma'}, \tag{2.23}$$

where $W^{\sigma\sigma'}$ is the MPO tensor at site i. The expectation value $\langle \psi | \hat{O} | \psi \rangle$ is computed by sweeping through the chain and building up the left (or right) environment tensor at each step. The environment tensor has dimensions $D \times D \times D_W$ (where D_W is the MPO bond dimension) and the cost of updating it at each site is $\mathcal{O}(D^3 D_W d)$. The total cost for the full chain is $\mathcal{O}(L\, D^3 D_W\, d)$. This environment-building procedure is shared by nearly every MPS algorithm discussed in this thesis. It reappears in the ground state search (DMRG) and in the TDVP time evolution.

Cost summary. Table 2.1 collects the scaling of the principal MPS operations discussed in this chapter. The linear-in-N prefactor is a direct consequence of the one-dimensional tensor network structure: each site is visited once, and the boundary environments propagate sequentially. This is the computational advantage that MPS methods exploit, and it breaks down when the entanglement of the state requires D to grow exponentially with N — the fundamental limitation discussed in Sec. 2.1.

Operation	Cost	Notes
Norm $\langle\psi\|\psi\rangle$	$\mathcal{O}(ND^3d)$	Transfer matrix sweep
Single-site expectation value $\langle\hat{o}_j\rangle$	$\mathcal{O}(D^2d^2)$	Mixed-canonical form required
MPO expectation value $\langle\hat{O}\rangle$	$\mathcal{O}(ND^3D_Wd^2)$	Three-layer contraction
MPS–MPO product $\hat{O}\|\psi\rangle$	$\mathcal{O}(ND^2D_Wd^2)$	Bond dimension grows to DD_W

Table 2.1: Computational cost of principal MPS operations. N: system size; D: MPS bond dimension; D_W: MPO bond dimension; d: local Hilbert space dimension.

2.6 Ground state search: the DMRG algorithm

Having assembled the machinery of MPS, MPO, and canonical forms, we are now in a position to describe the density matrix renormalization group (DMRG) algorithm [80, 69]. Originally formulated in the language of target states and truncated density matrices, DMRG is now understood as a *variational optimisation over the MPS manifold*. We seek the MPS of bond dimension D that minimises the energy

$$E[|\psi\rangle] = \frac{\langle\psi|\hat{H}|\psi\rangle}{\langle\psi|\psi\rangle}\,. \tag{2.24}$$

Attempting this optimisation in all tensors simultaneously is a non-convex and highly non-linear problem. Instead, DMRG solves a sequence of small local problems by sweeping through the chain, updating one or two tensors at a time. This *divide-and-conquer* strategy is what makes the algorithm practical.

We describe the two-site variant of DMRG, which is the most commonly used in practice and the one employed in the calculations of this thesis. The procedure at each bond is summarised in Fig. 2.6.1.

2.6.1 The algorithm

We start with an initial MPS $|\psi\rangle$ in mixed canonical form, with the orthogonality centre at site 1. The environments $\overline{L}^{[i]}$ and $\overline{R}^{[i]}$, the partial contractions of the bra, MPO, and ket layers from the left and right respectively, are pre-computed and stored. A single left-to-right sweep then visits each bond $(l, l+1)$ for $l = 1, 2, \ldots, N-1$ and performs the following steps.

Step 1 — Build the effective Hamiltonian. At the current bond we form the two-site tensor

$$\Theta^{\sigma_l\sigma_{l+1}}_{\alpha_{l-1},\alpha_{l+1}} = \sum_{\alpha_l} C^{\sigma_l}_{\alpha_{l-1},\alpha_l}\, C^{\sigma_{l+1}}_{\alpha_l,\alpha_{l+1}}\,, \tag{2.25}$$

by contracting the two neighbouring site tensors over their shared bond. This Θ plays the role of a local variational parameter. The *effective Hamiltonian* acting on Θ is obtained by contracting the stored environments with the two MPO tensors:

$$(\mathcal{H}_{\text{eff}})^{\sigma_l \sigma_{l+1},\, \sigma'_l \sigma'_{l+1}}_{\alpha_{l-1}\alpha_{l+1},\, \alpha'_{l-1}\alpha'_{l+1}} = \sum_{\beta_{l-1},\beta_l,\beta_{l+1}} L^{[l-1]}_{\alpha_{l-1},\alpha'_{l-1},\beta_{l-1}}\, W^{\sigma_l \sigma'_l}_{\beta_{l-1},\beta_l}\, W^{\sigma_{l+1}\sigma'_{l+1}}_{\beta_l,\beta_{l+1}}\, R^{[l+2]}_{\alpha_{l+1},\alpha'_{l+1},\beta_{l+1}}\,. \tag{2.26}$$

Viewed as a matrix acting on Θ reshaped into a vector, $\mathcal{H}_{\text{eff}}$ has dimensions $(d^2D^2)\times(d^2D^2)$.

Step 2 — Solve the local eigenvalue problem. Because the MPS is in mixed canonical form centred at the active bond, the normalisation matrix is the identity and the generalised eigenvalue problem reduces to a standard one:

$$\mathcal{H}_{\text{eff}}\,\Theta = E\,\Theta\,. \tag{2.27}$$

We solve this iteratively using a Krylov-subspace method such as Lanczos or Jacobi–Davidson, which requires only the ability to compute the action of $\mathcal{H}_{\text{eff}}$ on a vector. The explicit matrix is never formed. Instead, each matrix-vector product contracts the four-tensor network $L\cdot W\cdot W\cdot R$ with Θ on the fly at cost $\mathcal{O}(D^3 D_W d^2 + D^2 D_W^2 d^2)$. A good initial guess (usually the Θ from the previous iteration) accelerates convergence substantially. The eigenvalue E is the current estimate of the ground state energy, which decreases monotonically as the sweep progresses.

Step 3 — SVD and truncation. The updated Θ is reshaped as a $(dD)\times(dD)$ matrix by grouping the left physical and left bond indices on one side and the right physical and right bond indices on the other. An SVD yields

$$\Theta_{(\sigma_l\alpha_{l-1}),\,(\sigma_{l+1}\alpha_{l+1})} = \sum_{\alpha_l} U_{(\sigma_l\alpha_{l-1}),\,\alpha_l}\; s_{\alpha_l}\; V^{\dagger}_{\alpha_l,\,(\sigma_{l+1}\alpha_{l+1})}\,. \tag{2.28}$$

We truncate by keeping only the D largest singular values $\{s_{\alpha_l}\}$. The truncation error at this bond is $\epsilon = \sum_{a>D} s_a^2$ and should be monitored throughout the sweep, if it exceeds a preset tolerance, D is too small. The new left-canonical tensor is $A^{\sigma_l}_{\alpha_{l-1},\alpha_l} = U_{(\sigma_l\alpha_{l-1}),\alpha_l}$ (after reshaping), and the remainder $s\,V^{\dagger}$ is absorbed into the next-site tensor as the new orthogonality centre C_{l+1}.

Step 4 — Update the environment and advance. Having fixed A^{σ_l} in left-canonical form, we update the left environment by one site:

$$L^{[l]}_{\alpha_l,\alpha'_l,\beta_l} = \sum_{\alpha_{l-1},\alpha'_{l-1},\beta_{l-1},\sigma_l,\sigma'_l} (A^{\sigma_l})^{*}_{\alpha_{l-1},\alpha'_l}\, W^{\sigma_l\sigma'_l}_{\beta_{l-1},\beta_l}\, A^{\sigma'_l}_{\alpha'_{l-1},\alpha_l}\, L^{[l-1]}_{\alpha_{l-1},\alpha'_{l-1},\beta_{l-1}}\,. \tag{2.29}$$

The orthogonality centre is now at site $l+1$, and we proceed to the next bond $(l+1, l+2)$, repeating Steps 1–4.

At the right end of the chain, the sweep direction reverses and we sweep from right to left, building right-canonical tensors B^{σ_l} and updating right environments $R^{[l]}$ instead. Alternating forward

and backward sweeps continue until the energy converges; convergence is typically declared when the energy change between successive sweeps falls below a chosen threshold, or when the variance $\langle\psi|\hat{H}^2|\psi\rangle - \langle\psi|\hat{H}|\psi\rangle^2$ is sufficiently small. The entire procedure is diagramatically illustrated below.

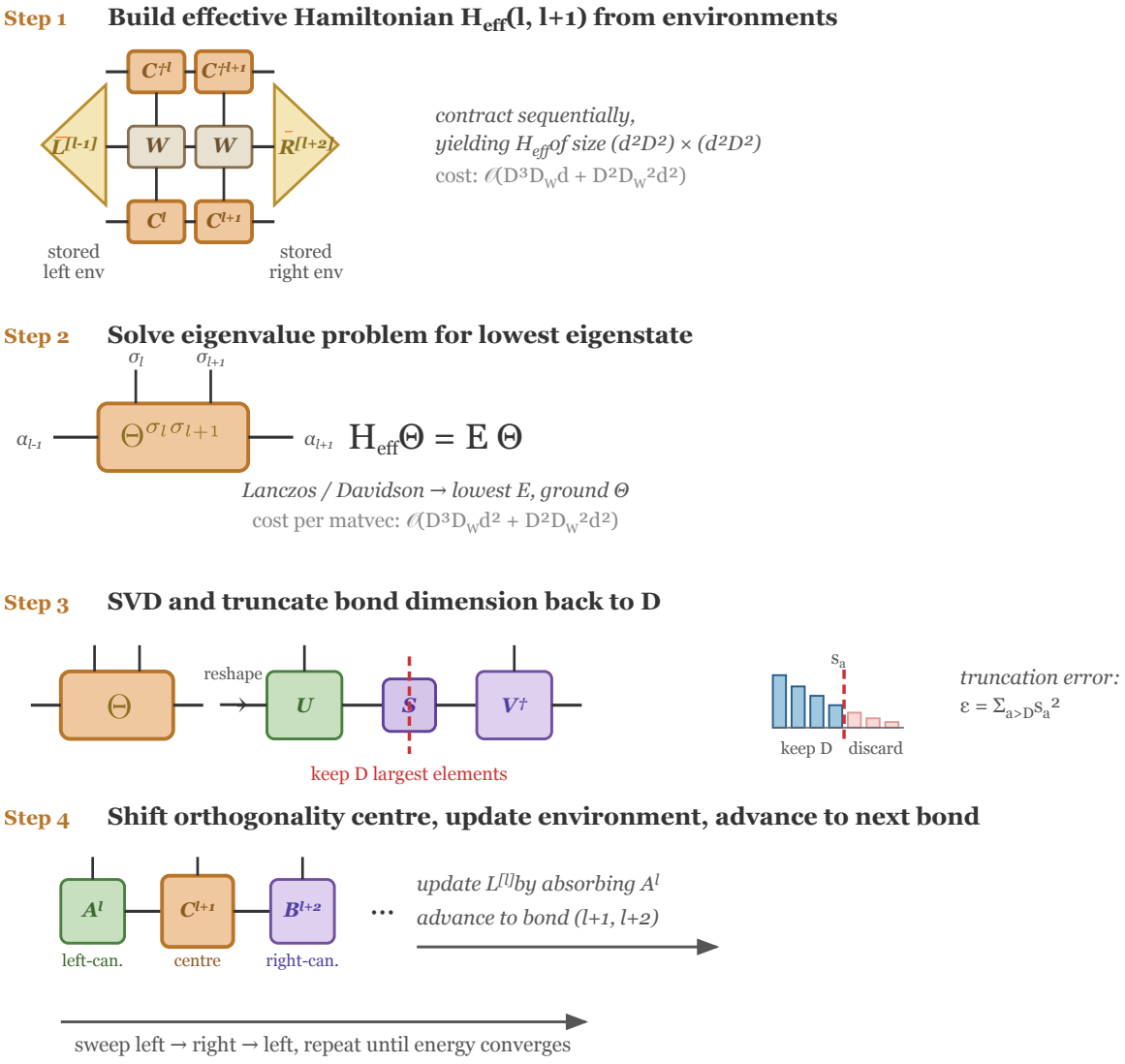

2.6.2 Caveats and practical considerations

Several subtleties determine whether a DMRG calculation succeeds or fails in practice. We collect the most important of these here.

Local minima and the single-site trap. Although the two-site variant is generally robust, the single-site version of DMRG, in which only one tensor is optimised at a time, stuck in local minima. The reason is structural: neither the localeigensolve nor the subsequent SVD can introduce *new quantum number sectors* or increase the bond dimension within a given sector. If the initial MPS happens to lack a sector that is important for the ground state, single-site DMRG has no mechanism to recover it. The two-site variant circumvents this by optimising on a larger local Hilbert space (dimension d^2D^2 rather than dD^2), which allows the SVD to redistribute

bond dimension across sectors. For problems where single-site DMRG is preferred for reasons of cost or compatibility with subspace methods, *subspace expansion* provides an alternative: the bond space is artificially enlarged using a perturbation derived from the MPO [81], enabling the algorithm to escape local minima.

Choice of initial state. A random initial MPS with appropriate quantum numbers usually suffices for small systems, but for larger or harder problems a good starting point can make a significant difference. Common choices include a classical product state respecting the target symmetry sector, or the ground state obtained for a simpler Hamiltonian in the same phase. A poor starting point may require many more sweeps, or may lead to convergence onto a low-lying excited state rather than the ground state.

Bond dimension and truncation error. The bond dimension D is the central control parameter of the algorithm. Too small a D underresolves the entanglement of the true ground state and introduces a systematic error; too large a D wastes computational resources. In practice, one performs a sequence of calculations at increasing D and extrapolates physical observables against the truncation error ϵ. A healthy DMRG calculation has ϵ decaying smoothly with D; a stagnating ϵ signals a problem such as a missing quantum number sector or entanglement scaling that exceeds the area law (as happens at critical points or for two-dimensional systems).

Exploiting symmetries. When the Hamiltonian commutes with a set of global charges, building these symmetries explicitly into the MPS results in simgnificant improvement: the block-diagonal structure of the site tensors reduces the cost of the local eigensolve by a large factor and guarantees that the algorithm stays within the target sector throughout.

Open versus periodic boundary conditions. The MPS representation is natural for open boundary conditions but less so for periodic ones, where the tensor network acquires a ring topology and the canonical form has no clean analogue. For periodic systems, one can either use a ring-shaped MPS (at substantially increased cost, $\mathcal{O}(D^5)$ per Lanczos step) or impose open boundaries and treat finite-size effects separately.

Computational cost summary. Per bond update, the dominant costs are the environment contractions in building $\mathcal{H}_{\text{eff}}$ and the Lanczos matrix-vector products, both scaling as $\mathcal{O}(D^3 D_W d)$. One full sweep therefore costs $\mathcal{O}(N D^3 D_W d)$. The memory footprint is dominated by storing the N environment tensors, each of size $D^2 D_W$. These scalings make DMRG extremely efficient for one-dimensional gapped systems, where D need not grow with system size; for two-dimensional systems approximated as ladders, D must grow exponentially with the ladder width, which is the primary obstacle to applying the method in higher dimensions.

From ground states to dynamics

The DMRG algorithm just described is tailored to obtain the lowest-energy eigenstate of a time-independent Hamiltonian. Much of the physics studied in this thesis, however, concerns

dynamics. It is tempting to imagine that time evolution is a minor variation on ground state search. The catch is that evolving a state away from the ground state or any atypical states typically generates entanglement that grows linearly in time, so the bond dimension required to represent $|\psi(t)\rangle$ faithfully grows exponentially [82].

Two families of algorithms are primarily designed to address this problem of time-evolution of quantum states. The *Suzuki–Trotter* approach (Sec. 2.8) approximates the evolution operator $e^{-i\hat{H}\delta t}$ as a product of local gates and applies them to the MPS one at a time; the bond dimension grows at each step and is then truncated back. The *time-dependent variational principle* (TDVP), which we describe next, takes a different route: rather than approximating the operator, it projects the Schrödinger equation onto the tangent space of the MPS manifold, producing an exact evolution *within* the manifold of fixed bond dimension. The two approaches have complementary strengths. Trotter is conceptually simple and mirrors the experimental protocols. TDVP is unitary by construction and handles long-range interactions without modification.

2.7 Time evolution: the TDVP algorithm

The time-dependent variational principle (TDVP) [83, 84] is closely related to DMRG. It is a variational algorithm that sweeps through the chain, solving small local problems at each site. Where DMRG minimises an energy functional by solving a local eigenvalue problem, $\mathcal{H}_{\text{eff}}\,\Theta = E\,\Theta$, TDVP integrates a Schrödinger equation by solving a local *initial value problem*, $i\,\partial_t C = \mathcal{H}_{\text{eff}}\,C$. The effective Hamiltonian, the environments, and the sweep structure are all inherited directly from the DMRG toolbox.

The set of MPS of bond dimension D forms a smooth manifold $\mathcal{M}_D$ inside the full Hilbert space; exact time evolution generally takes the state off this manifold, so TDVP projects the right-hand side of the Schrödinger equation onto the tangent space of $\mathcal{M}_D$ at the current state,

$$i\,\frac{d}{dt}|\psi[M](t)\rangle = \hat{P}_{T_{|\psi\rangle}\mathcal{M}_D}\,\hat{H}\,|\psi[M](t)\rangle\,. \tag{2.30}$$

The tangent space projector $\hat{P}_{T_{|\psi\rangle}\mathcal{M}_D}$ decomposes into a sum of local pieces, one per site and one per bond, and this decomposition is the reason TDVP can be implemented as a sweep.

We describe the single-site variant of TDVP here. The procedure at each site is summarised in Fig. 2.7.1 and parallels the DMRG sweep steps.

2.7.1 The algorithm

We start with an initial MPS $|\psi(0)\rangle$ in mixed canonical form centred at site 1, with left and right environments pre-computed and stored. One left-to-right sweep advances the state by a time step δt. At each site $l = 1, 2, \ldots, N$ the procedure is as follows.

Step 1 — Build the single-site effective Hamiltonian. Exactly as in DMRG, we form

$$(\mathcal{H}(l))^{\sigma_l,\,\sigma_l'}_{\alpha_{l-1}\alpha_l,\,\alpha_{l-1}'\alpha_l'} = \sum_{\beta_{l-1},\beta_l} \overline{L}^{[l-1]}_{\alpha_{l-1},\alpha_{l-1}',\beta_{l-1}}\, W^{\sigma_l\sigma_l'}_{\beta_{l-1},\beta_l}\, \overline{R}^{[l+1]}_{\alpha_l,\alpha_l',\beta_l}\,, \tag{2.31}$$

by sandwiching the MPO tensor at site l between the stored left and right environments. This is the *same* object that drives the local eigenvalue problem in DMRG - the only difference is what we do with it.

Step 2 — Evolve the site tensor forward. We integrate the local Schrödinger equation

$$i\,\frac{d}{dt}\,C_l(t) = \mathcal{H}(l)\,C_l(t) \tag{2.32}$$

over a time step δt, which amounts to applying the matrix exponential:

$$C_l(t+\delta t) = e^{-i\,\mathcal{H}(l)\,\delta t}\,C_l(t)\,. \tag{2.33}$$

Exponentiating $\mathcal{H}(l)$ explicitly is out of the question as the matrix is of size $(dD^2)\times(dD^2)$, so we use a Krylov-subspace method (the Lanczos algorithm applied to the matrix exponential rather than to the eigenvalue problem). As in DMRG, only the action of $\mathcal{H}(l)$ on a vector is required, computed on the fly by contracting the four-tensor environment-MPO-C network. Crucially, the bond dimension of the MPS does not change at this step: the tensor network that represents $|\psi\rangle$ is the same before and after the update, with only the numerical entries of C_l changing.

Step 3 — Decompose and prepare to shift. To move the orthogonality centre to site $l+1$, we factor the updated C_l as

$$C_l = A_l\,D_l\,, \tag{2.34}$$

where A_l is left-canonical and D_l is a small bond matrix. This can be done with a QR decomposition (cheaper than SVD when singular values are not needed). Note that *no truncation is performed* here: the decomposition is exact, and the bond dimension is preserved.

Step 4 — Evolve the bond matrix backward. The Lie-Trotter splitting of the tangent space projector produces a second, less familiar piece of the evolution: an equation of motion for the bond matrix D_l, driven by a *zero-site* effective Hamiltonian,

$$\left(\mathcal{K}(l)\right)_{\alpha_l,\alpha_l',\tilde{\alpha}_l,\tilde{\alpha}_l'} = \sum_{\beta_l} \overline{L}^{[l]}_{\alpha_l,\tilde{\alpha}_l,\beta_l}\,\overline{R}^{[l+1]}_{\alpha_l',\tilde{\alpha}_l',\beta_l}\,, \tag{2.35}$$

obtained by contracting the updated left environment $\overline{L}^{[l]}$ (which now includes A_l) with the right environment $\overline{R}^{[l+1]}$ across the bond. Unlike $\mathcal{H}(l)$, the tensor $\mathcal{K}(l)$ has no physical leg — hence "zero-site." The bond matrix is evolved

$$D_l(t+\delta t) = e^{+i\,\mathcal{K}(l)\,\delta t}\,D_l(t)\,, \tag{2.36}$$

where the crucial detail is the *plus* sign in the exponent: D_l is propagated *backward* in time by δt. This is not an error. The forward evolution of C_l in Step 2 overcounts the bond content between sites l and $l+1$ as the projector $\hat{P}_{T\mathcal{M}}$ has a double-counting structure, visible in its decomposition as a sum over sites minus a sum over bonds. The backward

step on D_l exactly compensates, and the overall evolution is consistent.

Step 5 — Absorb and advance. The evolved bond matrix $D_l(t+\delta t)$ is absorbed into the orthogonality-centre tensor at the next site, $C_{l+1} \to D_l\, C_{l+1}$. We advance the orthogonality centre to site $l+1$ and repeat Steps 1–5.

At the right end of the chain, the sweep reverses and we sweep back from right to left. One complete forward-plus-backward sweep advances the state by δt with first-order accuracy; a symmetric version (half sweep forward with $\delta t/2$, half sweep backward with $\delta t/2$) yields a second-order integrator, which is the standard choice in practice. The tensor diagramatic illustarton of each step is provided below.

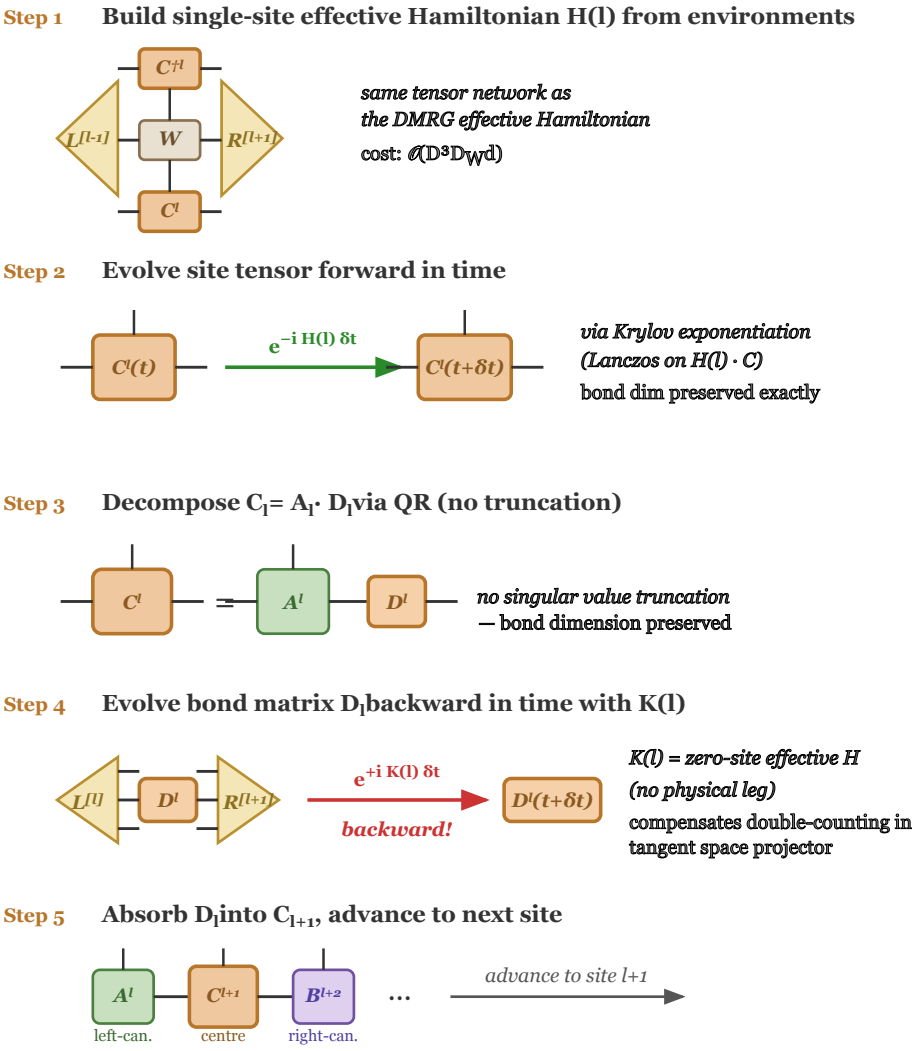

2.7.2 Caveats and practical considerations

The structural parallel with DMRG makes it easy to think of TDVP as "DMRG with an exponential instead of an eigensolve." The analogy is useful, but some aspects are genuinely different and deserve attention.

Fixed bond dimension, projection error. Unlike DMRG, where the bond dimension can be dialled up until the truncation error is acceptable, TDVP evolves the state *within* the manifold

$\mathcal{M}_D$. There is no truncation error; instead, the component of $\hat{H}|\psi\rangle$ perpendicular to the tangent space is discarded at every instant, producing a *projection error*. The size of this error depends on how closely the true dynamics can be approximated by an MPS of bond dimension D. For weakly entangled early-time dynamics, the projection error is tiny. As entanglement grows and the true state drifts away from $\mathcal{M}_D$, the projection error grows accordingly.

Unitarity and energy conservation. The projected evolution in Eq. (2.30) is generated by a Hermitian operator, so the integrator preserves the norm exactly (up to round-off). Energy is also conserved to high accuracy, which is a useful diagnostic: a drifting energy signals that δt is too large or that D is insufficient. This is in contrast to the Suzuki–Trotter approach, where the MPO-MPS truncation breaks unitarity step by step.

The single-site trap. Single-site TDVP inherits the local-minimum pathology of single-site DMRG: the algorithm cannot increase the bond dimension on its own or introduce new quantum number sectors. If the initial bond dimension is too small to accommodate the growing entanglement of the time-evolved state, the dynamics stagnates in the wrong subspace. This is usually addressed by executing the first few TDVP steps using a two-site variant of TDVP, which can grow the bond imension of MPS att the cost of introducing truncation error. Another approach is to use subspace expansion method [85].

Choice of time step. The time step δt plays a role analogous to the bond dimension in DMRG: smaller is more accurate, but more expensive. A practical choice is $\delta t \sim 0.01$–0.1 in units of the Hamiltonian scale. The Lie-Trotter splitting introduces an error of $\mathcal{O}(\delta t^3)$ per step for the second-order integrator, which accumulates linearly in t.

Long-range interactions. TDVP has a practical advantage over Suzuki–Trotter for Hamiltonians with long-range couplings. The Trotter approach requires decomposing $\hat{H}$ into groups of mutually commuting terms; for power-law or infinite-range interactions, this decomposition gets complicated and the number of Trotter layers per step grows quickly. TDVP, by contrast, enters the Hamiltonian only through its MPO representation, so long-range couplings are handled automatically as long as they admit a compact MPO (Sec. 2.5).

The entanglement barrier, once more. Neither truncation-free evolution nor unitarity avoids the entanglement barrier. For dynamics that generates entanglement linearly in time, the bond dimension D required to keep the projection error small grows exponentially, and TDVP (like Suzuki–Trotter) eventually fails. The maximum accessible time scales as $t_{\max} \sim \alpha^{-1} \log D$ [86], where α is the entanglement growth rate. Techniques such as density matrix truncation (DMT) [87] can extend the accesible timescale for thermalising systems, at the cost of giving up fidelity to the global state.

Computational cost summary. Per sweep, the dominant costs are the Krylov exponentiations in Steps 2 and 4, each of which requires a handful of matrix-vector products scaling as $\mathcal{O}(D^3 D_W d +$

$D^2 D_W^2 d^2$). This is the same scaling as the DMRG local eigensolver. One complete second-order TDVP sweep therefore costs $\mathcal{O}(ND^3 D_W d)$, comparable to one DMRG sweep.

2.8 Time evolution: the tDMRG algorithm

The TDVP approach of the previous section addressed the time evolution problem by projecting the Schrödinger equation onto the tangent space of the MPS manifold. Another widely used (and closer to experimental implementation) approach is to work at the level of the evolution operator itself. If we can approximate $e^{-i\hat{H}\delta t}$ as a product of operators that each act on only a few sites, then each factor is small enough to be applied to the MPS explicitly, and the full time evolution becomes sequence of such local applications. This is the philosophy behind the time-dependent DMRG algorithm (tDMRG) [88, 89, 90]. ANother closely related method is TEBD(time-evolving block decimation) which will not be discussed in this thesis.

The Suzuki–Trotter decomposition. The Hamiltonian, $\hat{H} = \sum_i h_i$ is a sum of many non-commuting local terms, so the exponential $e^{-i\hat{H}\delta t}$ does not factorise. For a local Hamiltonian with nearest-neighbour interactions, however, we can split the terms into two groups that each consist of mutually commuting operators:

$$\hat{H} = \hat{H}_{\text{odd}} + \hat{H}_{\text{even}}\,, \qquad \hat{H}_{\text{odd}} = \sum_{l\ \text{odd}} h_{l,l+1}\,, \quad \hat{H}_{\text{even}} = \sum_{l\ \text{even}} h_{l,l+1}\,. \tag{2.37}$$

All terms in $\hat{H}_{\text{odd}}$ commute with each other (they act on disjoint pairs of sites), and likewise for $\hat{H}_{\text{even}}$. The Baker–Campbell–Hausdorff formula gives

$$e^{-i(\hat{H}_{\text{odd}}+\hat{H}_{\text{even}})\,\delta t} = e^{-i\hat{H}_{\text{odd}}\delta t}\, e^{-i\hat{H}_{\text{even}}\delta t}\, e^{-\frac{1}{2}\delta t^2\,[\hat{H}_{\text{odd}},\,\hat{H}_{\text{even}}]+\cdots}\,. \tag{2.38}$$

Dropping the commutator correction gives the first-order Suzuki–Trotter approximation [91, 92]:

$$U_1(\delta t) = e^{-i\hat{H}_{\text{odd}}\delta t}\, e^{-i\hat{H}_{\text{even}}\delta t} = e^{-i\hat{H}\delta t} + \mathcal{O}(\delta t^2)\,. \tag{2.39}$$

A symmetrised version eliminates the $\mathcal{O}(\delta t^2)$ error by splitting the odd evolution in half:

$$U_2(\delta t) = e^{-i\hat{H}_{\text{odd}}\delta t/2}\, e^{-i\hat{H}_{\text{even}}\delta t}\, e^{-i\hat{H}_{\text{odd}}\delta t/2} = e^{-i\hat{H}\delta t} + \mathcal{O}(\delta t^3)\,. \tag{2.40}$$

This is the second-order Trotter formula. Higher-order schemes can be constructed recursively from U_2 [93]; they reduce the per-step error further at the cost of more factors per step, a trade-off we return to in the caveats below.

The key feature of Eqs. (2.39) and (2.40) that makes them useful for MPS is that each exponential factorises:

$$e^{-i\hat{H}_{\text{odd}}\delta t} = \prod_{l\ \text{odd}} e^{-i\,h_{l,l+1}\,\delta t} = \prod_{l\ \text{odd}} U_{l,l+1}(\delta t)\,, \tag{2.41}$$

and similarly for the even part. Each $U_{l,l+1}$ is a two-site unitary gate, which is a $d^2 \times d^2$ matrix that can be precomputed once by direct exponentiation of the local term $h_{l,l+1}$. One Trotter step

of $U_2(\delta t)$ therefore reduces to applying three layers of two-site gates, arranged in a *brick-wall* pattern: odd-bond gates for time $\delta t/2$, then even-bond gates for time δt, then odd-bond gates for time $\delta t/2$.

From gates to an MPS algorithm. Suzuki–Trotter decomposition provides a concrete, finite set of operations that implement $e^{-i\hat{H}\delta t}$: a sequence of $\mathcal{O}(N)$ two-site gates. Each gate acts on only two neighbouring sites of the MPS, so it is tractable to apply directly i.e., contract the two site tensors, apply the gate on the physical indices, and factorise the result back into two tensors. This factorisation uses SVD and introduces a truncation back to bond dimension D, just as in DMRG. The algorithm that carries out this procedure gate-by-gate is tDMRG.

The structural parallel with our earlier sections is useful. DMRG (Sec. 2.6) sweeps through the chain solving a local eigenvalue problem at each bond; TDVP (Sec. 2.7) sweeps through the chain solving a local initial value problem at each site; tDMRG sweeps through the chain *applying a local gate and truncating* at each bond. The three algorithms share the same essential recipe a sweep, a local update, a reshape-and-decompose step and differ in what the ingredient, "local update" means.

2.8.1 The algorithm

We start with an initial MPS $|\psi(t)\rangle$ in mixed canonical form with the orthogonality centre at the left boundary. One Trotter step advances the state by δt. We use the second-order scheme $U_2(\delta t)$ throughout, since it is the simplest useful case.

Step 1 — Precompute the two-site gates. At the start of the simulation (not once per step), compute the two-site gate $U_{l,l+1}(\tau) = e^{-ih_{l,l+1}\tau}$ for each distinct local term $h_{l,l+1}$ and for each of the time steps used in the Trotter formula. For the second-order scheme this means two gates per distinct bond type: one for $\tau = \delta t$ (used in the even-layer application) and one for $\tau = \delta t/2$ (used in the two odd-layer applications). Each gate is a $d^2 \times d^2$ matrix, small enough to exponentiate by direct diagonalisation. Translationally invariant Hamiltonians need only a single gate per layer, which is reused at every bond.

Step 2 — Apply a single two-site gate. Consider applying one gate $U_{l,l+1}(\tau)$ at bond $(l, l+1)$, with the orthogonality centre already positioned there. Contract the two neighbouring site tensors into a single four-leg tensor

$$\Theta^{\sigma_l\sigma_{l+1}}_{\alpha_{l-1},\alpha_{l+1}} = \sum_{\alpha_l} C^{\sigma_l}_{\alpha_{l-1},\alpha_l}\, C^{\sigma_{l+1}}_{\alpha_l,\alpha_{l+1}}\,, \tag{2.42}$$

and then apply the gate on its physical indices:

$$\tilde{\Theta}^{\sigma_l\sigma_{l+1}}_{\alpha_{l-1},\alpha_{l+1}} = \sum_{\sigma'_l,\sigma'_{l+1}} \left[U_{l,l+1}(\tau)\right]^{\sigma_l\sigma_{l+1},\,\sigma'_l\sigma'_{l+1}}\, \Theta^{\sigma'_l\sigma'_{l+1}}_{\alpha_{l-1},\alpha_{l+1}}\,. \tag{2.43}$$

Before the SVD in the next step, $\tilde{\Theta}$ is a $(dD) \times (dD)$ matrix i.e., the bond between sites l and $l+1$ has temporarily grown from D to dD.

Step 3 — SVD and truncation. Reshape $\tilde{\Theta}$ by grouping the left physical index with the left bond index and similarly on the right, then perform an SVD:

$$\tilde{\Theta}_{(\sigma_l \alpha_{l-1}),\,(\sigma_{l+1} \alpha_{l+1})} = \sum_{\alpha_l} U_{(\sigma_l \alpha_{l-1}),\,\alpha_l}\, s_{\alpha_l}\, V^{\dagger}_{\alpha_l,\,(\sigma_{l+1} \alpha_{l+1})}\,. \tag{2.44}$$

Keeping only the D largest singular values compresses the bond back down. The reshaped factor $A^{\sigma_l}_{\alpha_{l-1},\alpha_l} \equiv U$ is left-canonical, and $sV^{\dagger}$ is absorbed into the next-site tensor as the new orthogonality centre C_{l+1}. The truncation error $\epsilon_l = \sum_{a>D} s_a^2$ is the key diagnostic at this bond. This step is structurally identical to the SVD-and-truncate step of two-site DMRG (Sec. 2.6, Step 3), the difference is only in what produced $\tilde{\Theta}$.

Step 4 — Sweep through the chain ("zipper"). With the orthogonality centre now at site $l+1$, proceed to the next bond in the current Trotter layer and repeat Steps 2–3. For the odd layer, the gates live on disjoint bonds $(1,2),(3,4),\ldots$, so the sites involved do not overlap; we sweep through them in order, moving the orthogonality centre two sites at a time. Once the odd layer is complete, we reverse direction and apply the even-layer gates, then the second odd layer with $\delta t/2$. At the end of this three-layer zipper, the state has been advanced by δt.

Step 5 — Iterate in time. Repeat Steps 2–4 with the same δt until the desired final time is reached. Measurements are performed between Trotter steps, using the canonical form to compute expectation values as in Sec. 2.5.2.

The procedure for one Trotter step is illustrated below through tensor diagrams.

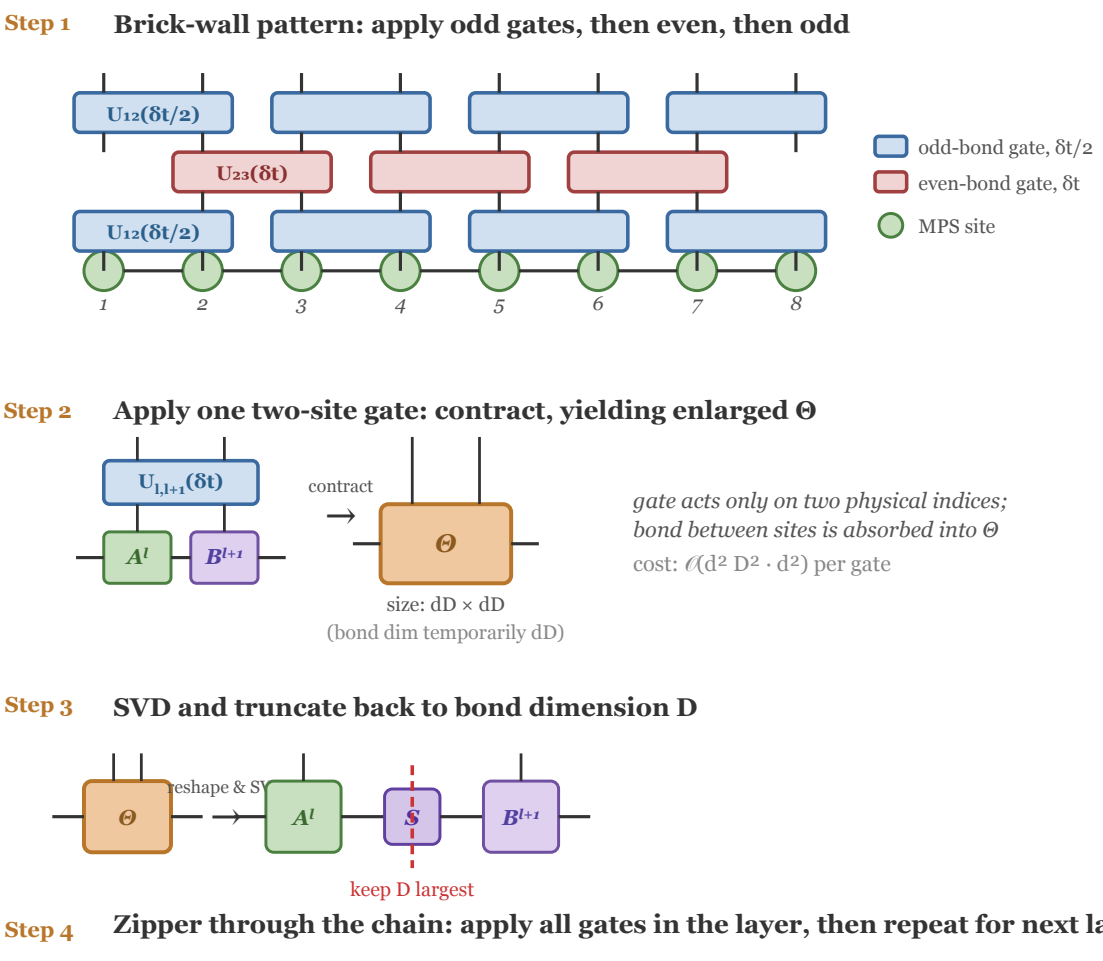

Figure 2.10:

2.8.2 Caveats and practical considerations

Trotter error and the choice of order. The error per step of the second-order scheme is $\mathcal{O}(\delta t^3)$, accumulating to $\mathcal{O}(\delta t^2 \cdot t_{\text{final}})$ over a total time t_{final}. The fourth-order scheme reduces this to $\mathcal{O}(\delta t^4 \cdot t_{\text{final}})$ but requires five second-order substeps per step, and therefore five times as many gate applications. The trade-off is not always in favour of the higher-order scheme: each gate application incurs a truncation, and more gates means more truncation errors. In practice, the second-order scheme with a modestly small δt strikes the best balance for most problems studied in this thesis.

Truncation error accumulation. Unlike DMRG, where the truncation error is a property of the final (static) state, in tDMRG the truncation at every gate contributes a small perturbation to the state, and these perturbations accumulate over time. Monitoring the per-step truncation $\epsilon = \sum_l \epsilon_l$ is essential; when ϵ exceeds a tolerance ($\sim 10^{-8}$ for reliable long-time results), the bond dimension should be increased. A runaway growth of ϵ with time is the signature of the entanglement barrier encroaching on the simulation.

Long-range interactions. The Trotter decomposition in Eq. (2.40) works cleanly only for nearest-neighbour Hamiltonians. For longer-range couplings, one must either (i) use SWAP gates to bring distant sites together before applying the gate and swap them back, (ii) use a different splitting based on the geometry of the interactions, or (iii) switch to MPO-based time evolution such as $W^{I,II}$ [94] or TDVP (Sec. 2.7). For the models studied in this thesis, (i) and (ii) suffice.

Unitarity. Each two-site gate $U_{l,l+1}$ is exactly unitary, but the SVD truncation that follows is not: it projects the state onto a lower-dimensional submanifold, which reduces the norm unless explicitly renormalised. In practice the state is renormalised after each truncation, but the underlying non-unitarity means that conserved quantities can drift over long times, more so than in TDVP, which is unitary by construction. Energy conservation is a good diagnostic.

Open versus periodic boundaries. The zipper structure relies on the chain having open ends. For periodic systems, either a ring-shaped MPS (with higher cost) or a large open chain with the quantity of interest measured in the bulk is used. All dynamics calculations in this thesis use open boundaries.

Parallelism. Within a single Trotter layer, the gates act on disjoint bonds and can in principle be applied in parallel. In MPS practice, the need to maintain the canonical form serialises the gate applications as the orthogonality centre must be moved sequentially, so the in-principle parallelism is not easily exploited.

Relation to TDVP. The tDMRG and TDVP algorithms produce different approximations to $|\psi(t)\rangle$, and the differences can be instructive. Trotter errors in tDMRG are commutator terms $[\hat{H}_{\text{odd}}, \hat{H}_{\text{even}}]$; projection errors in TDVP are components of $\hat{H}|\psi\rangle$ orthogonal to the tangent space. Truncation errors are present in tDMRG but absent in single-site TDVP. For short times, the two methods agree within their respective errors; for long times, the entanglement barrier limits both. Benchmarking a simulation against both methods is a standard consistency check.

Computational cost summary. Each two-site gate application costs $\mathcal{O}(d^3D^3)$ for the gate application plus $\mathcal{O}(d^3D^3)$ for the SVD, so $\mathcal{O}(d^3D^3)$ per gate. With $\mathcal{O}(N)$ gates per Trotter layer and three layers per second-order step, one Trotter step costs $\mathcal{O}(Nd^3D^3)$. This is roughly comparable to one DMRG or TDVP sweep, with the important caveat that accurate dynamics typically demand many more sweeps i.e., one per time step of size δt than a ground state calculation.

2.8.3 Finite-temperature states via ancilla purification

A thermal density matrix $\rho_\beta = e^{-\beta H}/Z$ is mixed and cannot be directly represented as a pure matrix product state. The standard approach is *purification* [95]. One approach to address density matrices using MPS formalism is to double the Hilbert space by attaching L ancilla sites, one for each physical site, and constructs a pure state $|\psi_\beta\rangle$ on the combined $2L$-site system

whose partial trace recovers the Gibbs state,

$$\mathrm{Tr}_{\mathrm{anc}}\left[|\psi_\beta\rangle\langle\psi_\beta|\right] = \rho_\beta. \tag{2.45}$$

The construction starts at $\beta = 0$, where the purification is simply a product of maximally entangled states between each physical site p_i and its ancilla partner a_i:

$$|\psi_0\rangle = \bigotimes_{i=1}^{L} \frac{1}{\sqrt{d}} \sum_{s=0}^{d-1} |s\rangle_{p_i} |s\rangle_{a_i}, \tag{2.46}$$

with $d = 3$ for the clock model discussed earlier (See. Sec 2.5.1). The finite-β state is reached by imaginary-time evolution acting on the physical sites only,

$$|\psi_\beta\rangle \propto \left(e^{-\beta H_{\mathrm{phy}}/2} \otimes \mathbb{I}_{\mathrm{anc}}\right)|\psi_0\rangle, \tag{2.47}$$

implemented as a sequence of Trotter steps in the MPO representation of $e^{-\delta\tau H}$ [96].

The purification is non-unique: ρ_β is invariant under any unitary U_{anc} acting solely on the ancilla subsystem. This gauge freedom can be exploited to slow entanglement growth during the subsequent real-time evolution(See Chapter 3 also, [97, 40]). One such choice is,

$$U_{\mathrm{anc}}(t) = \mathbb{I}_{\mathrm{phy}} \otimes e^{+iH_{\mathrm{anc}}t}, \tag{2.48}$$

where H_{anc} has the same form as H_{phy} but acts on the ancilla sites. This setup will be utilized in the next chapter. The schematic tensor network is outlined below,

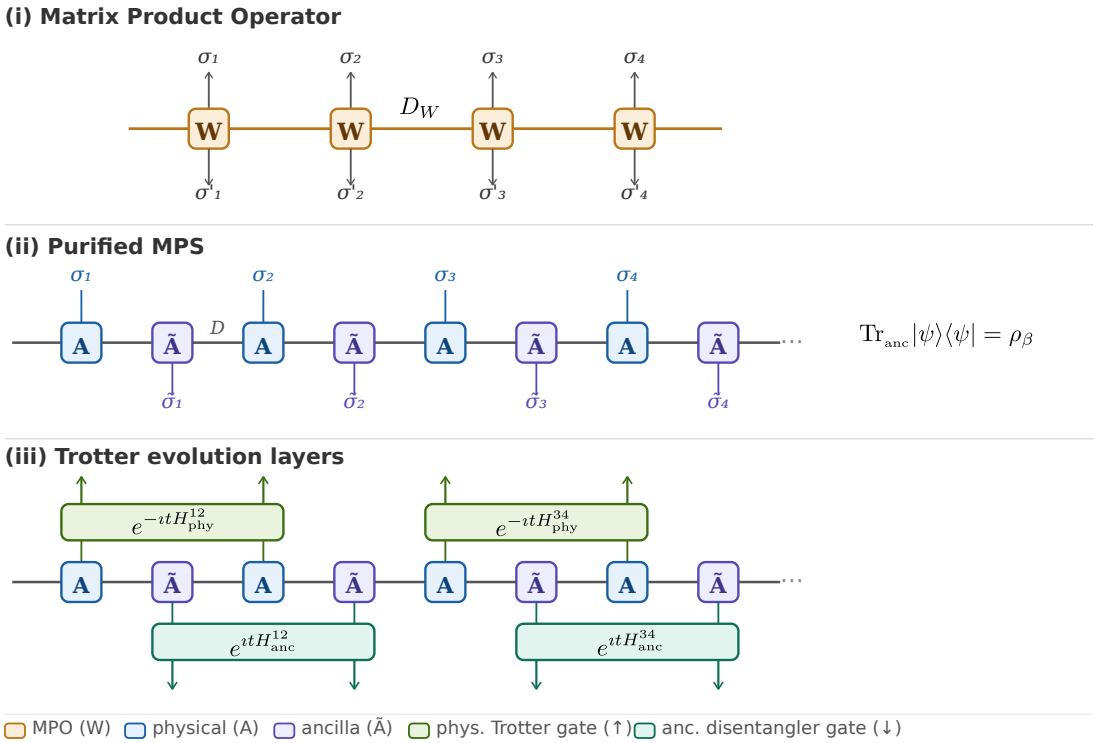

2.9 Conclusion

The methods developed in this chapter form the complete numerical toolkit deployed in the remainder of the thesis. The MPS ansatz compresses many-body states into a tractable sequence of local tensors, with canonical forms keeping the representation orthogonal and computationally stable. Ground states are obtained by DMRG-style sweeping, solving a local eigenvalue problem at each site and updating the bond space via subspace expansion when needed. For dynamics, the Trotter decomposition translates the time-evolution operator into a brick-wall circuit of local MPO gates, while TDVP projects the evolution directly onto the MPS tangent space, preserving unitarity without inflating the bond dimension. Finally, the ancilla purification scheme embeds the thermal state ρ_β into a pure $2L$-site MPS, and the ancilla disentangler keeps entanglement growth localised during real-time evolution, making long-time correlators numerically accessible. The following chapter applies each of these tools to compute the thermal Drude weight in the integrable chiral clock model.

3

Thermal Transport in an Integrable Chiral Clock Model

THE preceding chapters established the two pillars on which the discussion in this chapter rests: the Kubo formula and linear response theory, which reduce the problem of experimentally measurable transport to equilibrium current fluctuations in the isolated system (Chapter 1). The tensor network methods provide a controlled numerical route to those fluctuations in large one-dimensional systems (Chapter 2) at late times. We now deploy both to address a sharper question: what does integrability imply for the phenomena of thermal transport?

In a generic quantum many-body system, conservation of energy alone is sufficient to permit diffusive thermal transport. In an integrable system, however, the existence of an extensive set of local conserved charges in involution places far stronger constraints on dynamics — suppressing thermalization and generically producing a nonzero Drude weight, a delta-function singularity at zero frequency in the dynamical conductivity that signals presence of ballistic energy transport. The precise mechanism by which conserved charges give rise to this anomalous contribution is captured by the Mazur inequality, which bounds the Drude weight from below through the overlap of the current operator with each conserved charge. Whether this bound is tight, and which charges are responsible, depends sensitively on the model — and remains largely unexplored outside the extensively studied XXZ family .

In this chapter, we calculate the finite temperature thermal conductivity of a time-reversal invariant chiral $\mathbb{Z}_3$ clock model along an integrable line in the parameter space using the time-dependent density matrix renormalization group. The thermal current itself is not a conserved charge, unlike in the case of XXZ model, but has a finite overlap with a local conserved charge $Q^{(2)}$ obtained from the transfer matrix. We find that the Drude weight is finite at nonzero temperature, and the Mazur bound from $Q^{(2)}$ saturates the Drude weight, allowing us to obtain an asymptotic expression for the Drude weight at high temperatures. The numerical estimates of the conductivity are validated using a sum rule for thermal conductivity. On the computational side,

This chapter is adapted from the publication: **Sandipan Manna** and G. J. Sreejith, "Thermal Drude weight in an integrable chiral clock model," *Phys. Rev. B* **108**, 054304 (2023).

we also explore the effectiveness of the ancilla disentangler in the integrable and nonintegrable regimes of the model. We find that at high temperature, the disentangler helps by localizing the entanglement growth around the quench location allowing us to obtain the Drude weight in the integrable model. The improvement is insufficient to extract the asymptotic value of the correlator in the nonintegrable regime. The ancilla disentangler also provides no additional advantage at low temperatures.

3.1 Introduction

One-dimensional quantum systems host many experimentally realizable and theoretically tractable models that exhibit a rich set of quantum phenomena, including phase transitions, quantum transport, Luttinger liquids, etc. Transport setups that measure energy, spin or charge currents generated in response to weak external field gradients are widely used in characterization of such systems. Related questions of dynamics in weakly non-equilibrium situations have garnered considerable theoretical interest [98] and inspired the development of efficient algorithms [99, 100, 101, 96] for their study. The spin-1/2 XXZ chain is an analytically tractable model that can be realized in certain one-dimensional quantum magnets [102, 103]. Attempts to understand their measured transport properties led to many early works on isolated XXZ chains and closely related bosonic and fermionic models. These studies have revealed a connection between integrability and anomalous transport applicable not just in magnets but also in experimentally realizable bosonic and fermionic systems [104, 105, 106, 107].

Based on the seminal works by Mazur and Suzuki which relate the time-averaged correlations with overlaps of operators and conserved charges [5, 6], it was argued [7] that the conductivity of integrable systems such as the XXZ chain should have an anomalous zero frequency singularity (Drude weight). XXZ model is associated with two physically accessible conserved charges - namely energy and total spin quantum number along the z direction. The possibility of a finite Drude weight for thermal and spin conductivity, as well as broader features of associated transport, have been investigated in the XXZ model and its variants (including the cases with impurity [108, 109] or noise [110]) over the past several decades [111, 112, 40, 113, 114, 115].

In the gapless phase of the XXZ model, corresponding to the easy plane anisotropic case, early studies using Bethe ansatz suggested a finite zero temperature spin Drude weight which monotonically decreases with temperature [39]. The spin Drude weight decreases towards zero at all temperatures as the isotropic Heisenberg point is approached [116]. Numerical studies using exact diagonalization and a finite temperature generalization of the Kohn's formula [24, 25, 117] hints at vanishing spin Drude weight at finite temperatures in gapped phase when the system has net zero magnetization [118, 119, 120, 121]. Results using generalized hydrodynamics and thermodynamic Bethe ansatz approach also indicate zero spin Drude weight in the gapped phase and finite spin-Drude weight in the gapless phase [116]. Broadly the results also agree with tDMRG calculations which can access large finite size system sizes [40]. These results pertain to the zero magnetization ensembles; the spin Drude weight is finite in ensembles with finite magnetization even in the gapped phase [119]. Though the spin Drude weight has been found to be finite in the gapless phase, contrary to the expectation, the spin current operator is orthogonal to all local conserved charges obtained from the transfer matrix [35, 7]. The finite Drude weight

has been understood in terms of the Mazur bound related to the overlap of the spin current with certain additional quasi-local conserved charges [26, 122].

The thermal current operator in the XXZ model is a conserved charge [7], and consequently the dynamical thermal conductivity has no finite frequency contribution. For the gapped phase, numerics and Bethe ansatz [123, 7, 124] approaches reveal a power-law decay with temperature of thermal Drude weight at high temperatures and an exponential decay with $1/T$ at low temperatures, separated by a finite maximum. The trend is similar for the gapless regime, but the low temperature behavior[125] is linear in T.

Besides the calculation of the Drude weight, other related aspects of ballistic transport have also been explored. These include studies on Fourier's law violations in non equilibrium steady state currents generated in response to a potential gradient [99, 126, 127, 128, 129, 130, 108, 109], studies of currents in ray-dependent steady states after quench from a bipartitioned system [131, 132, 133, 134, 135, 136, 137], and studies on the nature of spread of initial spin or energy packets [114, 138, 139, 140]. Breaking the integrability in such models, for instance, by next nearest neighbor interactions or noise, results in vanishing of the Drude weight and transfer of the conductivity weight to finite frequencies [141, 142, 110, 143, 120].

While the XXZ model and equivalent fermionic and bosonic models have been explored in great detail, not much has been systematically explored in other models [144]. In this chapter, we investigate the $\mathbb{Z}_3$ chiral clock model with a spatial chirality [145, 146, 147, 148]. The model hosts a rich phase diagram [149] and exhibits dynamics [150, 151, 131] of interest in Rydberg atom systems [152]. More importantly, for our current interest, in parameter regime the model is integrable [153].

We numerically calculate the dynamical thermal conductivity in the integrable regime using techniques developed and applied successfully in the XXZ model and characterize the Drude weight as a function of the temperature and model parameters. The Drude weight is found to be finite at all temperatures and the temperature dependence qualitatively matches that of the thermal Drude weight in the gapped phase of the XXZ model. We then borrow results on the transfer matrix of the classical chiral clock model [153] to construct local conserved charges for the quantum model. The Mazur bound from the simplest among these charges $Q^{(2)}$ is found to saturate the numerically calculated Drude weight, which indicates that the current has a finite overlap only with $Q^{(2)}$. This allows us to obtain an asymptotically exact expression for Drude weight in the large temperature limit. The thermal current is not a conserved quantity, unlike the XXZ model and has a component that is not conserved and therefore orthogonal to all other conserved charges, we expect this to result in coexistence of diffusive and ballistic components in the dynamics of energy packets in this model.

In the past, several numerical techniques have been utilised to address the questions on transport phenomena in interacting quantum systems. Exact diagonalization techniques can estimate correlator of local observables with high accuracy but suffers from severe finite-size effect making the results unreliable in thermodynamic limit [154, 121, 155, 156, 157, 119, 120]. Tensor network based tDMRG method have also been used to investigate large system sizes and therefore, practically approaching thermodynamic limit with tunable error and computation cost [96, 69]. A modified tDMRG approach based on the ancilla purification is found to be able to

significantly reduce the computational cost of the simulation [158, 40]. We use the latter in our calculation of the relevant correlators.

This chapter is organized as follows. In Sec. 3.2, we introduce the model. Next, in Sec. 3.3, we present the expressions for the energy density and energy current; and introduce the relation between the conductivity and the current-current correlator which we use in the numerical calculations. We also discuss constraints satisfied by the thermal conductivity namely the sum rules and Kramers-Kronig like relation which we use in subsequent sections to validate our numerical results. We discuss the Mazur bound and the conserved charges in Sec. 3.3.4. Derivation of the conserved charges from the transfer matrix is presented in the Appendix 3.A. In Sec. 3.4, we outline the tDMRG method that was used to obtain the numerical results. Finally, in Sec. 3.5, we present our key results including the Drude weights as a function of temperature and parameters and comparison with estimates from Mazur bound. This section also discusses the frequency content of the regular part of the dynamical thermal conductivity. In Sec. 3.5.4, we present our empirical observations regarding the efficiency of the ancilla disentangler used in tDMRG calculations and conclude in Sec 3.6.

3.2 The quantum $\mathbb{Z}_3$ chiral clock model

In this section, we introduce the $\mathbb{Z}_3$ symmetric quantum chiral clock model in one spatial dimension [145, 147, 148]. We assume open boundary conditions throughout unless mentioned otherwise. The model can be motivated as a generalization of the $\mathbb{Z}_2$ symmetric transverse-field Ising model [146]. The Hamiltonian is given by

$$H = -\sum_{j=1}^{L} [\bar{\alpha}_1 \tau_j + \bar{\alpha}_2 \tau_j^\dagger + \alpha_1 \sigma_j \sigma_{j+1}^\dagger + \alpha_2 \sigma_j^\dagger \sigma_{j+1}] \tag{3.1}$$

where the operators τ and σ satisfy the following algebra,

$$\tau^3 = \sigma^3 = \mathbb{I}; \quad \tau^\dagger = \tau^{-1}; \quad \sigma^\dagger = \sigma^{-1}; \quad \sigma\tau = \omega\tau\,\sigma.$$

and $\omega \equiv \exp\left(\frac{2\pi\imath}{3}\right)$. These can be explicitly represented by the following matrices.

$$\sigma = \begin{pmatrix} 1 & 0 & 0 \\ 0 & \omega & 0 \\ 0 & 0 & \omega^2 \end{pmatrix}, \quad \tau = \begin{pmatrix} 0 & 0 & 1 \\ 1 & 0 & 0 \\ 0 & 1 & 0 \end{pmatrix}. \tag{3.2}$$

The algebra of the operators σ and τ generalizes that of the Pauli matrices S_z and S_x which appear in the Ising model.

The Hamiltonian is parameterized by complex scalar parameters α_1 and $\bar{\alpha}_1$, whose complex conjugates are denoted by α_2 and $\bar{\alpha}_2$ respectively. We emphasize that the bar does not indicate complex conjugates and the convention follows the one that has been used in literature [153].

Alternatively, we can use the following parametrization.

$$\alpha_1 = Je^{\imath\theta},\ \alpha_2 = Je^{-\imath\theta}$$
$$\bar{\alpha}_1 = fe^{\imath\phi},\ \bar{\alpha}_2 = fe^{-\imath\phi} \tag{3.3}$$

where $f \geq 0$ is local Zeeman field and $J \geq 0$ is nearest neighbor coupling. θ is a scalar parameter that governs the chirality. ϕ breaks the time-reversal symmetry.

In the $\mathbb{Z}_3$ ordered phase, the order parameter cycles through three values $(1, \omega, \omega^2)$, so a domain wall separating two ordered domains can wind in one of two directions, distinguished as left- and right-moving (or opposite chirality) walls. For $\theta = 0$ these two wall types are degenerate, but the chiral coupling ($\theta \neq 0$) breaks the spatial left-right symmetry of the Hamiltonian, making the two wall energies inequivalent: one type has a strictly lower gap than the other. This asymmetry is the origin of the model's "spatial chirality."

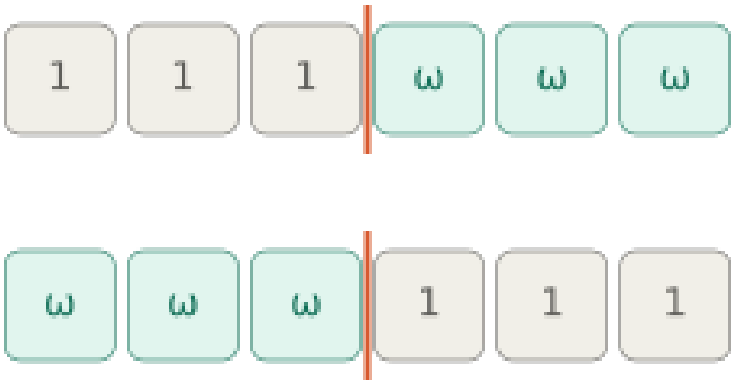

Depending on the parameters θ, ϕ, the model can have discrete symmetries e.g. charge conjugation ($\sigma \leftrightarrow \sigma^\dagger, \tau \leftrightarrow \tau^\dagger$), spatial parity($j \leftrightarrow L - j + 1$) and time-reversal ($H \leftrightarrow H^*$) symmetry. In this chapter, we focus on $\theta \neq 0$ and $\phi = 0$ regime (i.e. $\bar{\alpha}_1 = \bar{\alpha}_2 = f \in \mathbb{R}$) where the model exhibits time-reversal symmetry. The model has a spatial chirality in this regime as the energy of left and right domain walls are not equal. The $\mathbb{Z}_3$ chiral clock model has a phase diagram with a disordered ($f \gg J$) phase and a $\mathbb{Z}_3$ symmetry broken ordered phase ($J \gg f$); the latter contains a topological regime [149, 159, 160]. The phases are separated by a surface of second order quantum phase transition points that passes through the critical three state Potts model at $J = f$, $\theta = \phi = 0$ [161].

The model is integrable along the line [153]

$$f\cos(3\phi) = J\cos(3\theta) \tag{3.4}$$

and superintegrable when $\theta = \phi = \frac{\pi}{6}$ [162, 163]. This chapter aims to understand aspects of the model along the integrable line. For simplicity we consider only the time reversal invariant models and study the properties as θ varies keeping ϕ to be 0, leaving the calculations in the finite ϕ regime for a future work.

3.3 Energy density,Thermal current operator and Drude weight

A key signature of an integrable model is the non-zero Drude weight which refers to a zero frequency delta function peak in the conductivity. In this chapter, we explicitly calculate the Drude weight in thermal conductivity as a function of temperature and Hamiltonian parameters. In the following subsections, we present the expressions for the energy density, thermal currents, conductivity and its Drude weight.

3.3.1 Local energy density and thermal current operator

In order to calculate the Drude peak (and dynamical thermal conductivity in general), we study the two-point correlator for the thermal current whose definition depends on the choice of the form of the local energy density operator. We choose the local energy density as a 3-site operator,

$$H_i = -\frac{\alpha_1}{2}(\sigma_{i-1}\sigma_i^\dagger + \sigma_i\sigma_{i+1}^\dagger) - \bar{\alpha}_1\tau_i + h.c \tag{3.5}$$

The thermal current operator, I_i acting on the bond between site i and site $i+1$ can be inferred from continuity equation as $\dot{H}_i = \imath[H, H_i] = -\{I_{i+1} - I_i\}$. The local current operator I_i has the form

$$I_i = \imath\frac{\bar{\alpha}\alpha_1}{2}(I_i^{(1)} + I_i^{(2)}) + h.c \tag{3.6}$$

where

$$\begin{aligned} I_i^{(1)} &= (\omega^2 - 1)\sigma_i(\tau_i + \tau_{i+1})\sigma_{i+1}^\dagger \\ I_i^{(2)} &= (\omega - 1)\sigma_i(\tau_i^\dagger + \tau_{i+1}^\dagger)\sigma_{i+1}^\dagger. \end{aligned} \tag{3.7}$$

The total current operator is defined as $I = \sum_{i=1}^{L} I_i$. Symmetry considerations imply that the current operator has zero expectation value in any thermal state [130].

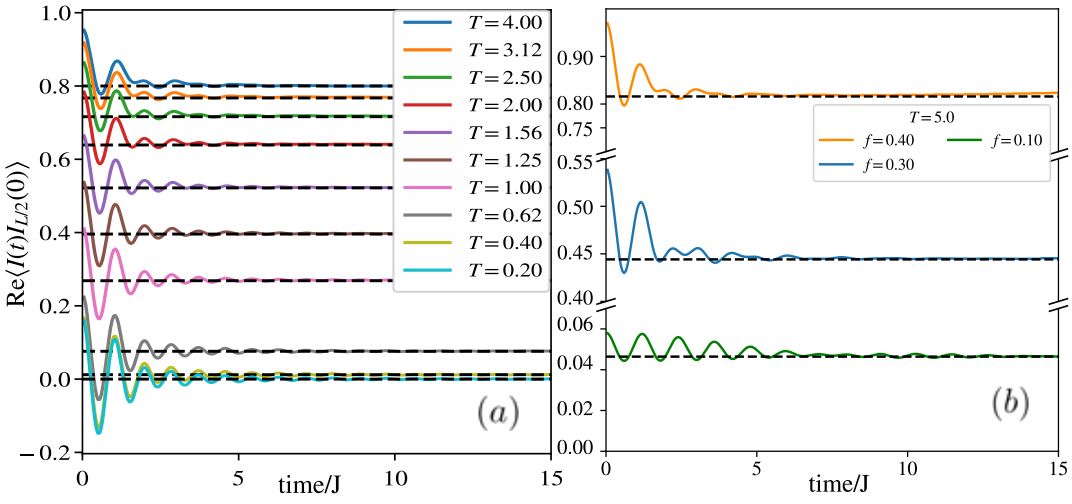

Figure 3.1: (a) Evolution of the current-current correlator. The dotted lines are lower bound on current-current correlator at different temperatures obtained from Mazur bound. The maximum bond dimension for MPS is kept at 900-1200 with a cutoff for truncation $\sim 10^{-9} - 10^{-10}$. $J = 1, f = 2/5, \theta = \frac{1}{3}\cos^{-1}(2/5)$. (b) Evolution of the current-current correlator for different f along the integrable line at $T = 5$. Cutoff for truncation, $\epsilon \sim 10^{-9} - 10^{-12}$.

3.3.2 Thermal conductivity and sum rule

Here, we briefly recap the expression of thermal conductivity obtained in Chapter 1. Fourier transform of thermal conductivity in the linear response regime is given by [2, 1]

$$\kappa(k,\Omega_+) = \frac{1}{\hbar T k L}\int_{-\infty}^{0} e^{-\imath\Omega_+ t}\langle[\hat{I}(k,0),\hat{H}(-k,t)]\rangle\,\mathrm{d}t \tag{3.8}$$

where operators with hat ($\hat{I}$ and $\hat{H}$) represent the corresponding spatial Fourier transformed form, $\Omega_+ = \Omega + \imath 0^+$, T is temperature, L is the number of sites. Integrating Eq. 3.8 by parts and subsequently using continuity equation and the KMS condition [20] on the resulting expression, the thermal conductivity in the long wavelength limit ($k \to 0$) reduces to

$$\kappa(\Omega) = \frac{1-e^{-\beta\Omega}}{T\Omega}\int_0^\infty e^{\imath\Omega t}\lim_{L\to\infty}\frac{\langle I(t)I(0)\rangle}{L}\,\mathrm{d}t \tag{3.9}$$

which can be used to numerically evaluate the thermal conductivity (hereafter we use thermal conductivity to refer to its long wavelength limit only). The current-current correlator is directly accessible in the numerical time evolution which we implement using finite temperature tDMRG methods [69, 40, 101, 139, 132, 97].

As shown in Ref. [23] thermal conductivity satisfies the following sum rule:

$$\int_0^\infty \mathrm{Re}\,\kappa(\Omega)\,\mathrm{d}\Omega = \lim_{L\to\infty}\frac{\pi}{2\hbar T L}\langle\Theta\rangle \tag{3.10}$$

which we can user to validate the results of the numerically estimated conductivity. We set $\hbar = 1$ throughout this chapter. Here Θ is called the thermal operator for which an exact expression is given by,

$$\Theta = -\lim_{k\to 0}\frac{\mathrm{d}}{\mathrm{d}k}[\hat{I}(k),\hat{H}(-k)]. \tag{3.11}$$

The expectation value in Eq. 3.10 is calculated in the thermal ensemble. For the specific choice of current and energy operator, Θ can be expressed in terms of local real space operators as follows.

$$\Theta = \frac{\imath}{2}\sum_i [I_i, -3H_{i-1} - H_i + H_{i+1} + 3H_{i+2}] \tag{3.12}$$

3.3.3 Drude weight

The extensive number of conservation laws in the integrable model can result in a non-zero value for the current-current correlator at asymptotically large time, resulting in a divergent zero frequency contribution to the thermal conductivity. The conductivity in the Fourier space has the following decomposition:

$$\kappa(\Omega) = 2\pi D_{\mathrm{th}}\delta(\Omega) + \kappa_{\mathrm{reg}}(\Omega) \tag{3.13}$$

where,

$$D_{\mathrm{th}}(T) = \lim_{t\to\infty}\lim_{L\to\infty}\frac{\langle I(t)I(0)\rangle}{2LT^2} = \lim_{t\to\infty}\lim_{L\to\infty}\frac{\langle I(t)I_{L/2}(0)\rangle}{2T^2} \tag{3.14}$$

We have invoked spatial translation invariance in the second equality. This can be directly evaluated in tDMRG calculations.

As shown in Ref. [158], thermal conductivity can be calculated from the real or the imaginary part of the current-current correlator; and the difference between the two can be used as an estimate of the error in the calculated Drude weight. First, the real regular part of the dynamical thermal conductivity (Eq. 3.13) can be obtained directly from Eq. 3.9. Moreover, thermal conductivity Re $\kappa_{\rm reg}(\Omega)$ can also be estimated using

$$\text{Re } \kappa_{\rm reg}(\Omega) = -\frac{2}{T\Omega}\text{Im}\int_0^\infty e^{\imath\Omega t}\,\text{Im}\left[\lim_{L\to\infty}\frac{\langle I(t)I(0)\rangle_{\rm reg}}{L}\right]\,\mathrm{d}t \tag{3.15}$$

In addition to the sum rule, discussed in the previous section, we use this to estimate error in the calculated conductivity and Drude weights (See Appendix 3.D).

3.3.4 Mazur bound

The Drude weight is related to conserved charges of the integrable model through Mazur's inequality [5, 6]. Assuming that the correlator has a steady asymptotic value, we can express this as the long time average of current-current correlator expectation value. For averages over a sufficiently large time window, the fluctuating contributions vanish from the spectral expansion, and we get [164]

$$\lim_{\Lambda\to\infty}\frac{1}{\Lambda}\int_0^\Lambda dt\langle I(t)I(0)\rangle = \sum_{\substack{m,n\\E_n=E_m}}\frac{e^{-\beta E_n}}{Z}|\langle n|I|m\rangle|^2 \tag{3.16}$$

where $Z=\text{Tr}[\rho]$, $\rho=e^{-\beta H}$ and E_m denotes the energy of the m^{th} eigenstate, $|m\rangle$ and $\beta=\frac{1}{T}$ is the inverse temperature.

We denote the extensive set of Hermitian local conserved charges by $\{Q^{(j)} : [Q^{(j)}, H] = 0\}$. The conserved charges can always be made orthogonal (under the operator inner product $\langle A, B\rangle_\rho = \text{Tr}[\rho A^\dagger B]$) *i.e.* $\langle Q^{(j)}, Q^{(k)}\rangle \propto \delta_{jk}$.

Any operator that is diagonal in the energy basis must be a conserved charge for the Hamiltonian. This implies in particular that the diagonal part of current operator, I is a constant of motion. Consequently, the total current operator, I can be expanded as

$$I = \sum_{k=1} a_k Q^{(k)} + I' \tag{3.17}$$

where

$$a_k = \frac{\langle Q^{(k)}, I\rangle_\rho}{\langle Q^{(k)}, Q^{(k)}\rangle_\rho}$$

and I' is a purely off-diagonal matrix in any energy eigenbasis *i.e.* $\langle m|I'|n\rangle = 0$ if $E_m = E_n$. Using the expression for I from Eq. 3.17 in Eq. 3.16, we obtain the following expression for the

asymptotic value for the current-current correlator

$$\lim_{\Lambda\to\infty}\frac{1}{\Lambda}\int_0^\Lambda \mathrm{d}t\langle I(t)I(0)\rangle = \sum_k \frac{|\langle Q^{(k)}, I\rangle_\rho|^2}{\langle Q^{(k)}, Q^{(k)}\rangle_\rho} \tag{3.18}$$

where sum is over conserved charges. Equation 3.18 can be used to get the following expression for the Drude weight in terms of overlap of current operator and conserved charges:

$$D_{\mathrm{th}}(T) = \lim_{L\to\infty}\frac{1}{2LT^2}\sum_k \frac{|\langle Q^{(k)}, I\rangle_\rho|^2}{\langle Q^{(k)}, Q^{(k)}\rangle_\rho} \tag{3.19}$$

The right hand side is a sum of non-negative terms, and in the absence of a complete set of conserved charges the expression still provides a lower bound to the Drude weight.

There exists a one parameter family of 3^L dimensional transfer matrices $T(u)$ [153] parametrized by u for the classical chiral Clock model in periodic boundary conditions. For parameters that satisify Eq. 3.4, T commutes with the quantum Hamiltonian as well as with each other (*i.e.* $[T(u), T(u')] = 0$).

An extensive number of local conserved charges for the quantum model can be obtained from a formal Taylor expansion of $\ln(T)$ in powers of u (see for instance Ref [165]):

$$\ln T(u) = \sum_{j=1}^{\infty} Q^{(j)} u^j \tag{3.20}$$

The simplest conserved charge $Q^{(1)}$ is the quantum Hamiltonian. The next term in the expansion namely $Q^{(2)}$ is a 3-local conserved charge with the following form.

$$Q^{(2)} = \sum_k I_k + \imath\left(\frac{1}{2}+\omega\right)\left(\frac{\alpha_1^2\bar{\alpha}}{\alpha_2} - \bar{\alpha}^2\right)\tau_k + \imath\left(\frac{1}{2}+\omega^2\right)\left(\frac{\alpha_1^2\bar{\alpha}}{\alpha_2} - \bar{\alpha}^2\right)\tau_k^\dagger \tag{3.21}$$

Expression for $Q^{(3)}$ is presented in the Appendix 3.A.

The thermal current has a finite overlap with $Q^{(2)}$ and zero overlap with $Q^{(3)}$; this can be explicitly computed for the infinite temperature ensemble, and numerically seen to hold at all finite temperatures. This is similar to the case of the XXZ model [7]. Further, the numerical results in the subsequent sections show that the thermal current has a finite overlap only with $Q^{(2)}$ as the bound to the Drude weight calculated from only $Q^{(2)}$ using Eq. 3.19 saturates the Drude weights calculated from asymptotic value of the finite temperature current-current correlator. However, unlike the XXZ model, the thermal current is not a conserved quantity in itself and $Q^{(2)}$ is not proportional the current. Only at critical point ($\alpha_1 = \alpha_2 = \bar{\alpha}$), conserved charge $Q^{(2)}$ coincide with the thermal current operator (Eq. 3.21).

3.4 Numerical Method

To calculate the dynamical current-current correlator in Eq. 3.14, we employ a time-dependent DMRG method (tDMRG) implemented using matrix product states. We realize the finite temperature system as the subsystem of a bigger system containing the L physical and L ancilla

degrees of freedom in a pure entangled state ψ_β such that reduced density matrix of the physical degrees of freedom is $e^{-\beta H_{\text{phy}}}/Z$ [95]. H_{phy} is the Hamiltonian in Eq. 6.1 applied only on the subsystem of physical sites. To prepare the state ψ_β we start with a state where each physical site is maximally entangled with one neighbouring ancilla, representing the purification ψ_0 of an infinite temperature physical system. The purification of the physical system at inverse temperature β is obtained through an imaginary time evolution of the initial state: $|\psi_\beta\rangle \propto e^{-\frac{\beta}{2}H_{\text{phy}}} \otimes \mathbb{I}_{\text{anc}} |\psi_0\rangle$. Both imaginary and subsequent real time evolutions are implemented through a fourth-order Trotter decomposition [96]. The real-time evolution results in exponential growth of bond dimension in the MPS.

To slow down the bond dimension growth and access the largest possible time-scale, we exploit the fact that purification is not unique as outlined in Ref. [40], due to the invariance of the reduced density matrix of the physical system under arbitrary unitary transformations of the ancilla subsystem. Entanglement growth can be slowed down by applying a suitable disentangler unitary on the ancilla. For XXZ model, $U = \mathbb{I}_{\text{phys}} \otimes e^{+\imath H_{\text{anc}} t}$ where H_{anc} is the same as the Hamiltonian for the physical system (H_{phy}) but, acting instead on the ancilla subsystem (See Ref [97, 40, 166] for details).

In this model (Eq. 6.1) as well, we observe empirically that, within a restricted class of unitaries considered, the above unitary is optimal (See Appendix 3.C). This particular choice of U_{anc} makes time-evolution of thermal state $|\psi_\beta\rangle$ nearly trivial and for the quenched state (the thermal state perturbed by the operator *i.e.* $I_{L/2} |\psi_\beta\rangle$ in the present case), entanglement buildup gets confined in the vicinity of the site where the current operator is applied. We found that for our calculations it was sufficient to use a maximum bond dimension of χ of 900-1200 and a singular value cut-off (ϵ) of $10^{-9} - 10^{-12}$ for truncation to get results with sufficient convergence. We repeated the calculation for multiple system sizes, cutoff bond dimensions (χ) and truncation weight cutoffs (ϵ) to confirm the convergence of our results (See Appendix 3.B).

One further optimization often carried out in such numerical calculations of correlators is to exploit the time translation invariance in correlator where we write $\langle A(t)B(0)\rangle$ as $\langle A(-t/2)B(t/2)\rangle$ [167]. Unlike the case for the two-point correlator between a pair of *local* observables, we have a task of evaluating a correlator of the form $\langle I(t) I_{\frac{L}{2}}(0)\rangle$ where one of the two operators is a *sum of local* observables. The alternate strategy of calculating the required correlator as the sum of correlators of local objects $\langle I_i(t/2) I_{\frac{L}{2}}(-t/2)\rangle$ has a cost that is typically higher [168, 167].

All the numerical calculations in the following section were carried out using code built on ITensor [169, 170].

3.5 Numerical results

In this section, we present the results from the numerical calculations using methods discussed in the previous section. All the results presented in the main text are for a system of $L = 60$ physical sites. This section is organized as follows. The general features of the dynamical current-current correlations and thermal conductivity are presented in Sec. 3.5.1 and verification of the sum rule is discussed in Sec. 3.5.2. The main results of the chapter namely the variation of Drude weight with temperature and parameters as well as a comparison with the Mazur bound are described in Sec. 3.5.3. Lastly, we present an analysis of the efficiency of the disentangler unitary that

we chose in subsection 3.5.4. Except in the last subsection, we consider only the integrable line, along which the chirality θ is fixed by the integrability condition (Eq. 3.4); as f increases from 0 to 1, θ decreases from $\pi/6$ to 0.

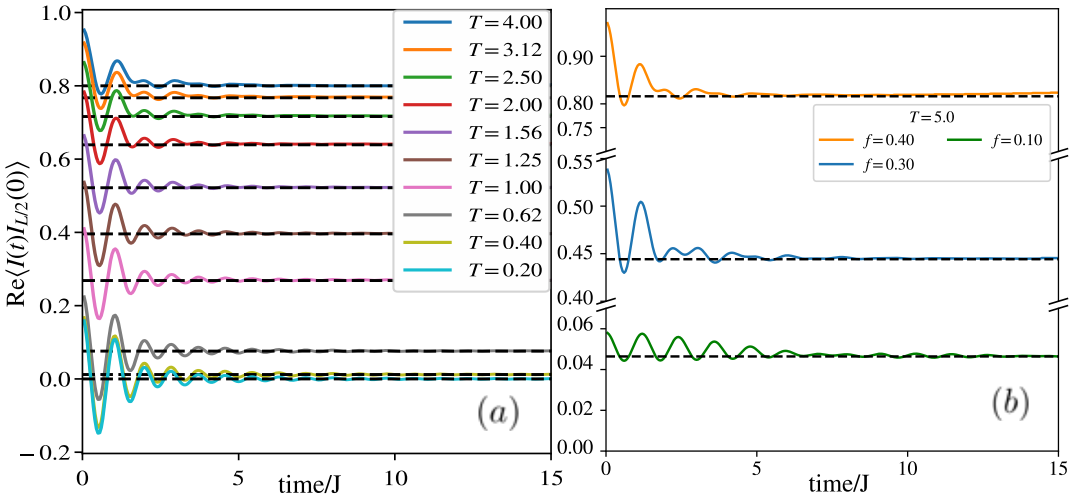

Figure 3.2: (a) Evolution of the current-current correlator. The dotted lines are lower bound on current-current correlator at different temperatures obtained from Mazur bound. The maximum bond dimension for MPS is kept at 900-1200 with a cutoff for truncation $\sim 10^{-9} - 10^{-10}$. $J = 1, f = 2/5, \theta = \frac{1}{3}\cos^{-1}(2/5)$. (b) Evolution of the current-current correlator for different f along the integrable line at $T = 5$. Cutoff for truncation, $\epsilon \sim 10^{-9} - 10^{-12}$.

3.5.1 Current-current correlator and thermal conductivity

Fig. 3.2(a) shows the time dependence of the real part of the current-current correlator for a range of temperatures at a fixed Hamiltonian parameter $f = 2/5$. The dotted lines show the estimates from the Mazur bound (Eq. 3.18). The calculated current-current correlator is in excellent agreement with the Mazur bound. Generally the time taken to reach the asymptotic value is larger at lower temperatures. Time dependence of the real part of the current-current correlator at a fixed temperature $T = 5$ and different points along the integrable line is shown in Fig. 3.2(b). We find that the current-current correlator reaches its asymptotic value faster at larger f. We note that in the time series plot shown in Fig. 3.2(a,b) or the Fourier transforms presented below, we have not used any extrapolation on the time series data [171] obtained from tDMRG. All the data shown are from the actual tDMRG evolution. We did not find any qualitative changes to the results upon using the extrapolated data.

Fourier transform of the conductivity can be calculated from the current-current correlator using Eq. 3.9. Fig 3.3(a) shows the variation of the regular part of the thermal conductivity as a function of Ω across a range of Hamiltonian parameter f. As f increases from 0 to 1 (simultaneously θ varies from $\pi/6$ to 0), the peak broadens but for f close to 1 the peak rapidly decreases in height and vanishes at $f = 1$. In particular the κ_{reg} is exactly 0 for all frequencies at the critical Potts model point ($f = 1, \theta = 0$).

$\kappa(\Omega)$ has a delta function peak arising from the Drude weight, the remaining regular part κ_{reg} of the conductivity as a function of the frequency is shown in Fig. 3.3(b). κ_{reg} is near zero

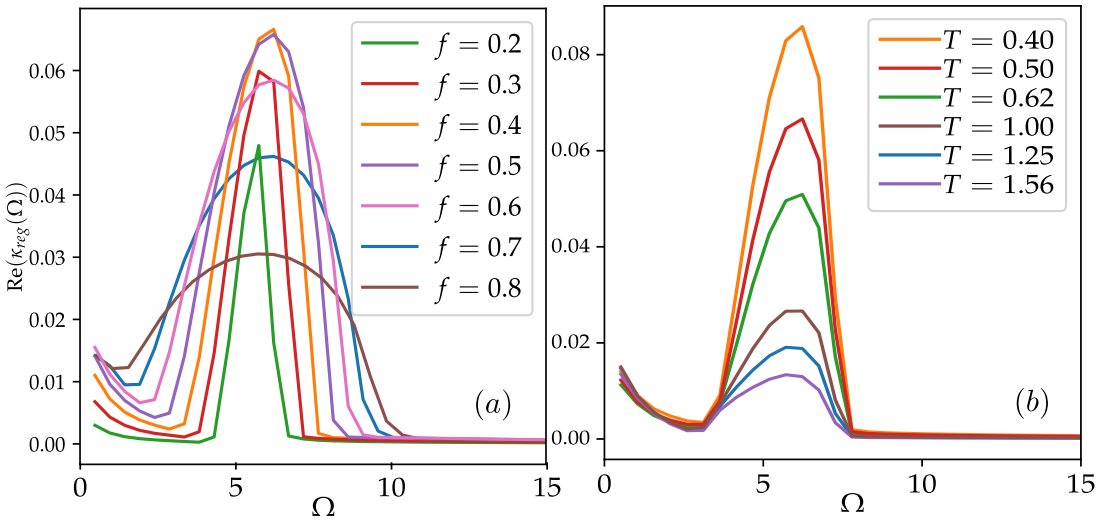

Figure 3.3: (a) Real part of Fourier transformed regular thermal conductivity $T = 0.5$ as a function of Ω. Different lines correspond to different values of Hamiltonian parameter f along the integrable line. (b) Similar to (a) but for different values of temperature (T). Results shown are for $J = 1$, $f = 2/5$, $\theta = \frac{1}{3}\cos^{-1}(2/5)$, $\phi = 0$.

at the highest accessible frequency and is finite for $\Omega \to 0$. This finite DC value indicates a finite diffusive part to the energy transport in addition to the ballistic part. Due to errors arising from finite time data (See Appendix 3.D) we are not able to detect the temperature dependence of $\kappa_{\mathrm{reg}}(\Omega \to 0)$. At an intermediate range of frequencies (3.0 to 7.5 in this case) there is a finite peak whose height decreases with increasing temperature. The frequency range is independent of the temperature.

Now we consider the location of the peak in relation to the spectral gap. For the value of f considered in Fig. 3.3, the gap above the ground state is $\Delta = 1.2551$ (calculated using DMRG in a system of size 60). This should correspond to the lowest energy domain wall quasiparticle. Energy of the domain wall with the opposite chirality should be higher due to finite chirality θ [150]. Insertion of the current operator $I_{L/2}$ is expected to generate a pair of opposite chirality domain walls (τ operators in Eq. 3.7 flips a single spin, generating a pair of domain walls around it) whose energy should be more than $\sim 2\Delta$ consistent with the low frequency end Ω_{low} of the peak. An alternate possibility is that a chain of three domain walls $|...11...\omega\omega...\omega^2\omega^2...11...\rangle$ of same chirality costing an energy of $\sim 3\Delta$ determines the location of low frequency end. Within the resolution possible for Ω_{low} the two scenarios cannot be distinguished. As the critical point is approached, $f \to 1$, $\theta \to 0$, the spectral gap vanishes, which is consistent with vanishing Ω_{low} in Fig. 3.3(a).

3.5.2 Sum rule

We now verify the sum rule for thermal conductivity following Eq.3.10. Fig. 3.4 shows the integrated value of (numerically calculated) real part of thermal conductivity, Re $\kappa(\Omega)$ (LHS of Eq. 3.10 shown as dots in the figure) compared with the expected sum (RHS of Eq. 3.10 shown as continuous line) as a function of temperature. We find good agreement between the two, implementing a partial check on the current-current correlators calculated numerically.

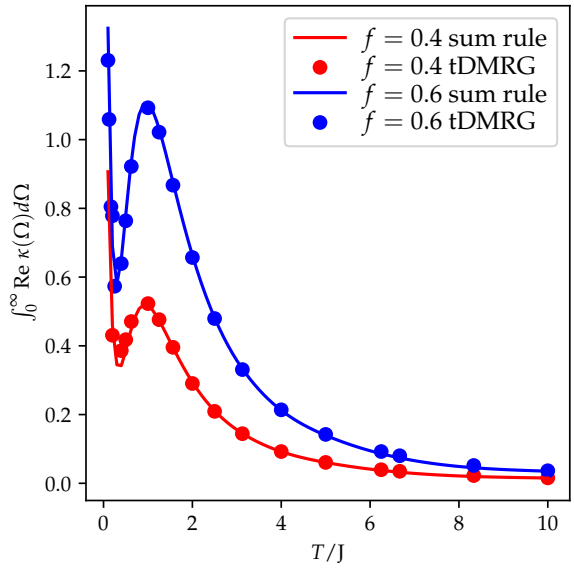

Figure 3.4: Verification of the sum rule by comparing RHS of Eq. 3.10 (solid line) where the expectation value of Θ is calculated numerically using Eq.3.12 . The dots indicate the integral of real part of Eq. 3.9 obtained from real time correlatlor $\langle I(t) I_{\frac{L}{2}} \rangle$ evaluated using tDMRG. The different lines show results for different points on the integrable line.

The T in denominator of Eq. 3.10 results in the divergence at low temperature in Fig. 3.4. The sharp increase in integrated thermal conductivity at low temperature arises from the intermediate frequency peak in Fig. 3.3 that gets more significant at low temperatures. The finite temperature peak in the sum rule arises from the singular, zero frequency part *i.e.* Drude weight of the thermal conductivity. Fig. 3.4 has a similar trend as in Fig. 3.6 at intermediate and high temperature.

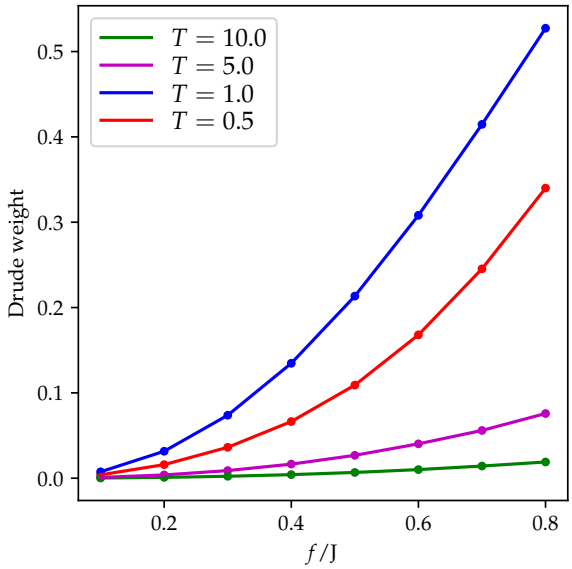

Figure 3.5: Drude weight calculated from tDMRG as a function of f showing the monotonic increase of Drude weight with increasing f. θ is chosen accoding to f along integrable line. The solid line is a linear interpolation between data shown as a guide to the eye.

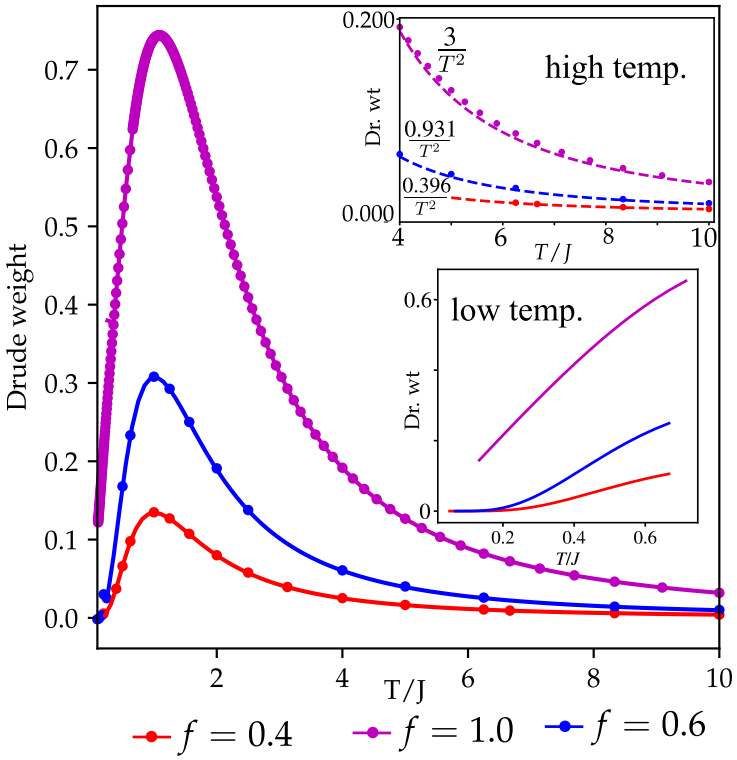

Figure 3.6: Variation of the Drude weight with temperature for different values of f. The solid lines show the Mazur bound (Eq. 3.19). Dot markers show the Drude weight estimated from tDMRG data (Eq.3.14). Temperature axis starts from $T = 0.1$. (Inset) High temp: Asymptotic expression for Drude weight is represented by the dashed lines (Eq. 3.22). The dots are from tDMRG estimates. Low temp: Drude weight from Mazur Bound in the low temperature regime. Behavior for the critical point is consistent with a linear scaling with T while for the gapped phase the trend is consistent with $e^{-\frac{\delta}{T}}$.

3.5.3 Variation of Drude weight with temperature and Hamiltonian parameters

In this section, we present the results for the numerically calculated Drude weights as a function of the temperature and comparison with the Mazur bound. Fig 3.5 shows the Drude weight computed from tDMRG as a function of the f for different temperatures showing a monotonic (nearly quadratic at small f) increase with f. Drude weight changes non-monotonically with temperature as can be inferred from comparing the plots for $T = 0.5, 1, 5.0$.

Fig. 3.6 shows the Drude weight numerically computed using tDMRG (dots in the figure) as a function of temperature for different values of f; and as mentioned before, the temperature dependence is non-monotonic. The solid line shows the Mazur bound calculated numerically using Eq. 3.19 considering only the $Q^{(2)}$ charge (See discussion in Sec 3.3.3 and Appendix 3.A). The Mazur bound from $Q^{(2)}$ saturates the estimated Drude weight indicating that the thermal current has no overlap with any other conserved charge.

Drude weight is found to be zero at zero temperature and increases rapidly as temperature is increased till it reaches a finite temperature peak around $T = 1$. The high temperature asymptotic behavior of the Mazur bound from charge $Q^{(2)}$ can be estimated to be

$$D_{\text{th}}(T = \infty) = \frac{1}{2T^2} \frac{\langle I, Q_i^{(2)} \rangle_{\rho=\mathbb{I}}}{\langle Q_i^{(2)}, Q_i^{(2)} \rangle_{\rho=\mathbb{I}}} = \frac{1}{2T^2} \frac{24f^2}{5 - f^2}. \tag{3.22}$$

For $f \ll 1$, the above expression suggests a quadratic variation with f consistent with Fig. 3.5. Figure 3.6(inset : high temp) shows the agreement (asymptotically) of Eq. 3.22 with data obtained from tDMRG at high temperature.

In the low temperature (inset:low temp) regime, Drude weight decays linearly with T for the critical system. The behaviour is qualitatively different in the gapped system ($f \neq 1$) where we observe a decay to 0 as $e^{-\frac{\delta}{T}}$. We can extract δ by fitting this to our data. For the two cases we considered here, $f = 0.4$ and 0.6, we find $\delta \sim 1.19$ and 0.98 which are close to the corresponding spectral gap 1.25 and 0.95 above the ground state respectively.

3.5.4 Efficiency analysis of the tDMRG with ancilla disentangler

The results presented in the previous sections were achieved using a disentangler unitary (See Sec. 3.4) on the ancilla subsystem in the tDMRG calculations. The disentangler slows down entanglement growth in general and makes accessing longer time scales possible. The effectiveness of this approach however varies with the parameter and temperature regimes; qualitatively similar to what was found in the case of XXZ model [97]. In this section, we present our empirical observations along with some quantitative data on the efficacy of the disentangler approach across model parameters and temperature for the model studied here.

In Fig. 3.7 (a) and (b) we show the variation of the maximum bond dimension after time-evolution of the quenched ($I_{\frac{L}{2}}|\psi_\beta\rangle$) and thermal ($|\psi_\beta\rangle$) states respectively. In each case we compare the bond-dimension growth with and without disentanglers applied to the ancilla. From panel (a), we observe that the maximum bond-dimension of the quenched MPS grows much faster (up to 2.5 times) for tDMRG without disentangler (dotted line) in contrast to the tDMRG

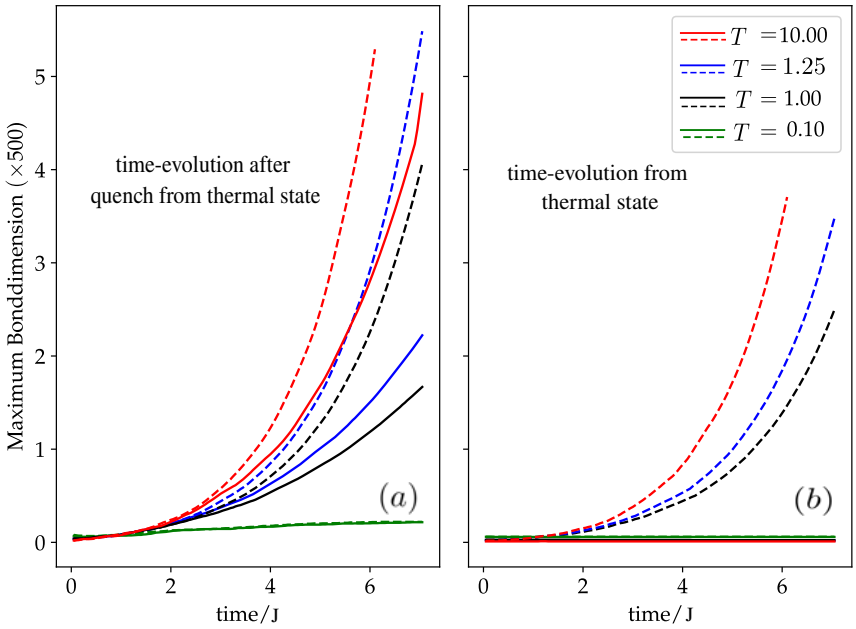

Figure 3.7: (a)Growth of maximum bond dimension under real time evolution for the MPS quenched from thermal state at different values of β. The dotted line indicates tDMRG without application of disentangler and the solid line is for disentangled tDMRG. (b) Same as panel a but, for time-evolution of thermal MPS without any quench.The parameters for the Hamiltonian are $J = 1$, $f = 2/5$, $\theta = \frac{1}{3}\cos^{-1}(2/5)$, $\phi = 0$ (integrable point). The truncation cutoff,$\epsilon = 10^{-9}$.

with disentangler (solid line). At low temperatures, on the other hand, both methods show almost similar growth in maximum bond dimension with time. In Fig. 3.7 (b), we see that the tDMRG with disentangler almost fully eliminates bond dimension growth of the thermal MPS under unitary evolution. In contrast, unitary evolution of thermal MPS ($|\psi_\beta\rangle$) implemented using tDMRG without disentangler shows rapid growth of maximum bond dimension with time.

In Fig. 3.8, we show the bond dimension of the time evolved states, as a function of the bond position contrasting the cases with and without disentangler. We notice a uniform growth of bond dimension throughout the system in the state that evolved without the ancilla disentangler in contrast to localized growth of bond dimensions near the quench site in case of tDMRG with disentangler. The spatial support of the operator is expected to spread linearly with time evolution; this increase is manifested in the excess growth of entanglement around the quench site (center in our case). Without disentangler, however there is an additional uniform buildup of entanglement everywhere in the system. In Fig. 3.9, we show local bond dimension at low temperature. Here, in both cases (tDMRG with and without disentangler unitary), local bond dimension shows similar behaviour indicating no significant gain in efficiency from application of ancilla disentangler.

We, so far, focused on the local bond dimension growth. However, time evolution calculations are dominated by matrix multiplications and SVD operations which have a computational complexity of $O(d^3)$ where d is the dimension of the matrices involved. Denoting the local bond dimension at site i of the MPS by M_i, the computational cost can be quantified by $\sum_i M_i^3$ [97]. In Fig. 3.10, we provide a contour plot showing the variation of the computational cost $\sum_i M_i^3$ with inverse temperature β and time, while keeping the truncation cutoff fixed at 10^{-9}.

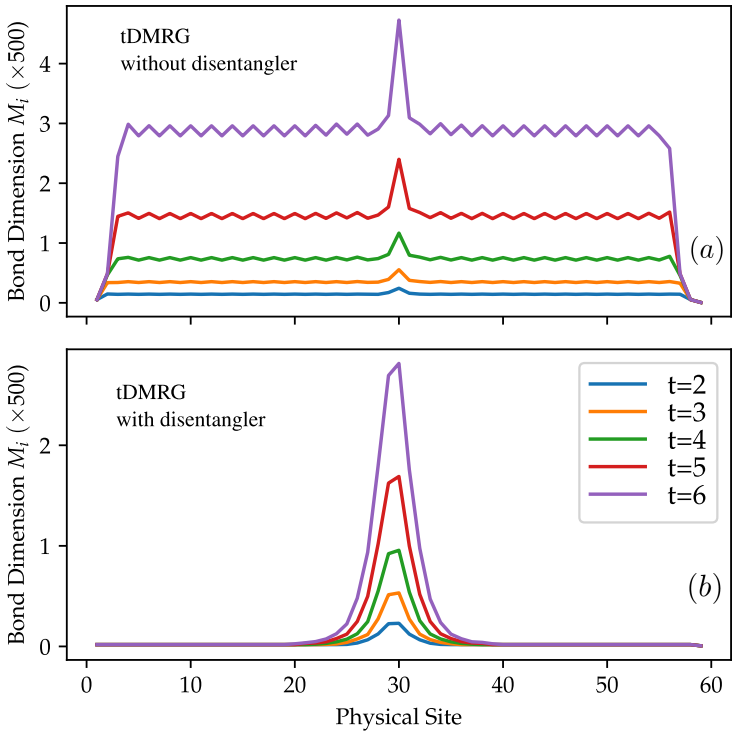

Figure 3.8: Bond dimension as a function of bond position for the state quenched from a high temperature ($T = 6.25J$) thermal state. Panel (a) data for tDMRG without disentangler and panel (b) shows data for tDMRG with disentangler. Different lines correspond to different times. The MPS bond dimension growth is localised about the quench site in case of tDMRG with disentangler. Results shown are for the integrable point $J = 1, f = 2/5, \theta = \frac{1}{3}\cos^{-1}(2/5), \phi = 0$. The truncation cutoff, $\epsilon = 10^{-9}$.

We first compare Fig. 3.10(a) and (b) where we show the contour plot for integrable point. We observe that the tDMRG with disentangler affords us an improvement in the accessible timescale - the same computational cost (the contour lines) is reached at a later time if the disentangler is applied, as compared to the case without the disentangler. However the improvement is most significant at higher temperatures, where the bond dimensions growth is generally much faster and is therefore a relevant consideration. At low temperature where the bond dimension growth is a lesser issue, the disentangler performs slightly worse. These observations are consistent with Fig. 3.8 and Fig. 3.9.

Finally, we discuss Fig. 3.10(c) and (d) where we study a non-integrable point. The plots suggest a minor gain in accessible time scales from ancilla disentangler. However, at non-integrable points, we find that the timescales required for the transients in the current-current correlaters to decay away is much larger compared to the integrable points; the improvements afforded by the disentangler is not sufficient for us to reach these time scales.

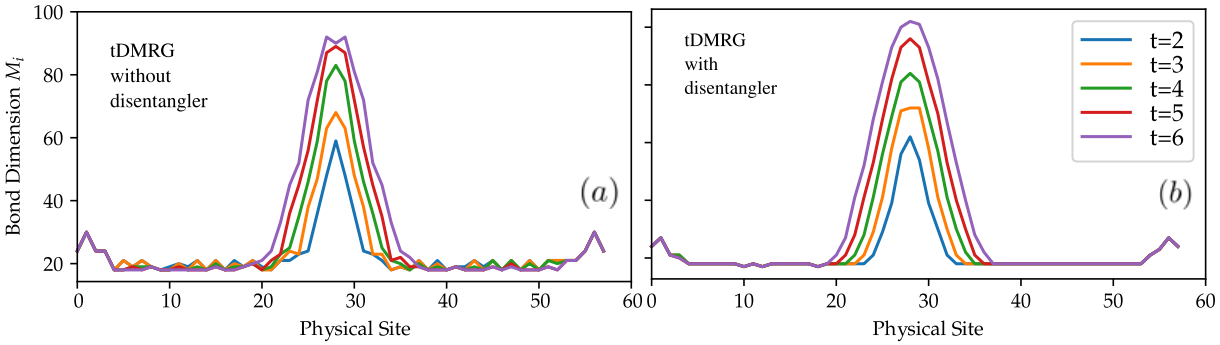

Figure 3.9: Similar to Fig. 3.8, this plot shows the spatial distribution of bond dimension but at a low temperature point $T = 0.1$ (in unit of J). The parameters for Hamiltonian are $J = 1$, $f = 2/5$, $\theta = \frac{1}{3}\cos^{-1}(2/5)$, $\phi = 0$. The truncation cutoff is $\epsilon = 10^{-9}$.

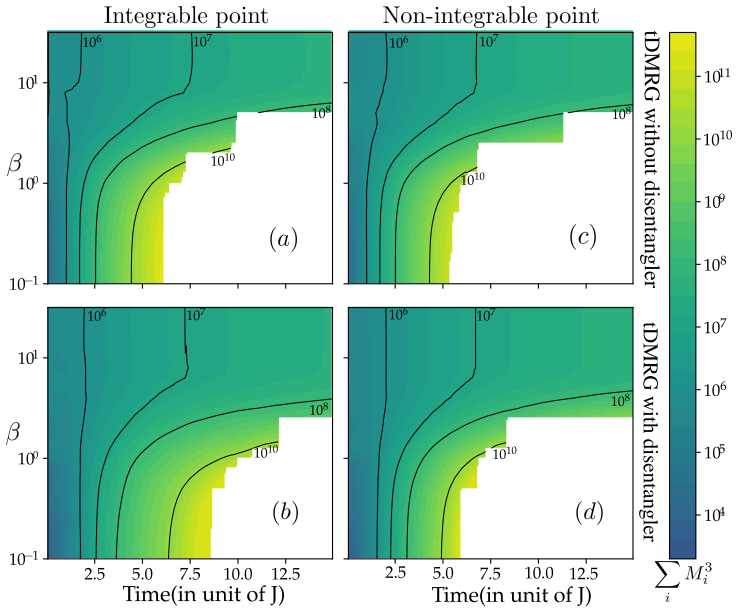

Figure 3.10: Computational complexity as a function of β and time. (a) and (b) are for integrable model ($J = 1$, $f = 2/5$, $\theta = \frac{1}{3}\cos^{-1}(2/5)$, $\phi = 0$) with and without disentangler unitary respectively. (c) and (d) are for non-integrable point $J = 1$, $f = 2/5$, $\theta = 0.3$, $\phi = 0$ with and without disentangler unitary respectively. Colors indicate a measure of the computational cost. Contour lines connect points of same computational cost. The truncation cutoff was maintained at $\epsilon = 10^{-9}$ throughout the calculations.

3.6 Summary and Outlook

The constraints imposed by the extensive number of local conservation laws in integrable systems manifest in many different ways - such as failure to thermalize to a Gibbs ensemble, long term memory of initial states which strongly influence equilibrium steady state properties, unusual features in energy spectral correlations, and anomalous signatures in measurable long term response functions such as conductivities. The precise relation between these features has been extensively investigated in the past several decades. This study uses extensive tDMRG calculations to characterize the anomalous zero frequency peak parametrized by the thermal Drude weight at integrable points of the $\mathbb{Z}_3$ chiral clock model.

The thermal Drude weight is nonzero at all finite temperatures and vanishes as a power law $\sim 1/T^2$ at large temperatures and appears to decay exponentially with $1/T$ at low temperatures. At the critical point (gaplesss) the low temperature Drude weight fits a linear behavior with T till the lowest temperature we studied ($T = 0.1$). These observations are consistant with what was observed in the gapped and gapless phases of the XXZ model.

The numerically obtained Drude weights (from current correlators) shows excellent agreement with the Mazur bound based on the simplest conserved charge $Q^{(2)}$ (Eq. 3.21) derived from the transfer matrix and suggests that the thermal current has finite overlap only with one conserved charge. Explicit calculations using the next conserved charge $Q^{(3)}$ is consistent with this.

The thermal current operator is however not identical to the conserved charge $Q^{(2)}$. This corresponds to a scenario where part of the energy current is conserved manifesting as the finite Drude weight. The difference between the current and the conserved charge results in a non-trivial finite frequency part to κ_{reg}. This is unlike the case of the XXZ model where the current is a conserved charge and $\kappa_{\text{reg}} = 0$.

The regular part of the dynamical conductivity shows a wide peak at frequencies which could be correlated with the energies of the simplest domain walls. We also find a small finite conductivity near zero frequency suggesting the possibility of a diffusive component to the energy transport in addition to the ballistic part.

We used ancilla disentangler to increase the maximum times upto which we could compute the correlators. For the integrable points, this allowed us to efficiently access the asymptotically long time behavior of the correlator. However, for the non integrable points we checked, the improvements afforded by the method were insufficient to access long time features of the corelators. More careful choice of the non-integrable parameter regime, use of other disentangler schemes [166], alternate computing schemes [172] or truncation methods [87, 173] may be helpful in accessing longer time scales.

In this chapter, we have characterized the anomalous transport properties at the chiral but time reversal invariant points in the integrable parameter space of the model. The similarities of our results with the XXZ model highlights the universality of the relation between integrability and anomalous transport, and suggests similar qualitative features for the time reversal broken ($\phi \neq 0$) regime as well. However it will be interesting to understand how broken time reversal invariance manifest in the anomalous transport features. The model also provides an interesting arena to study dynamics and transport at superintegrable[162, 163] points and effects of integrability breaking perturbations on them.

Appendix 3.A Transfer matrix and conserved charges

In this section, we give an outline for the derivation of the conserved charges of quantum $\mathbb{Z}_3$ chiral clock model from the transfer matrix for a classical 2D chiral clock model. Here we borrow the results for the transfer matrix from Ref [153].

The energy density of the classical 2D model is [147]

$$\mathcal{E} = -2\text{Re}\sum_{j,k} E^v Z_{j,k} Z^\dagger_{j+1,k} + E^h Z_{j,k} Z^\dagger_{j,k+1} \tag{3.23}$$

where E^v and E^h are complex coupling strengths along vertical and horizontal directions of the 2D square lattice, respectively and Z takes values from $\{1, \omega, \omega^2\}$. (j, k) label site coordinates on the 2D lattice.

The transfer matrix (with periodic boundary conditions) can be written as

$$T_D = \sum_{j=0}^{2} (\sigma_M^\dagger)^j l_j \left[\prod_{k=-M}^{M-1} (L_k L_{k+\frac{1}{2}}) \right] L_M (\sigma_M)^j \tag{3.24}$$

where the sites are indexed from $[-M, M]$.

$$L_k(u) = \sum_{n=0}^{2} \bar{l}_n(u) \tau_k^n$$
$$L_{k+\frac{1}{2}}(u) = \sum_{n=0}^{2} l_n(u) (\sigma_k \sigma_{k+1}^\dagger)^n$$

The weights in the transfer matrix, $\bar{l}_1, l_1, \bar{l}_2, l_2$ parametrize E^v, E^{v*}, E^h, E^{h*} of the statistical mechanics model and $l_0 = \bar{l}_0 = 1$.

For a certain parameters, $\mathbb{Z}_3$ chiral clock model becomes Bethe ansatz integrable. This implies choice of functions $l, \bar{l}$ such that the transfer matrices satisfy Lax pair conditions $[T(u), T(u')] = 0$ and $[T(u), H] = 0$ where H is a quantum Hamiltonian.

Ref [153] considered functions of the form $l_{1,2} = \alpha_{1,2} u + O(u^2)$ and $\bar{l}_{1,2} = \bar{\alpha}_{1,2} u + O(u^2)$ in which case H matches the quantum chiral clock Hamiltonian (Eq. 6.1). The Lax pair conditions can be shown to imply (see Ref [153] for details)

$$\alpha_m \sum_{k=0}^{2} \frac{\bar{S}_{m+k}}{\bar{S}_k} \omega^{-nk} = \bar{\alpha}_n \sum_{k=0}^{2} \frac{S_{n+k}}{S_k} \omega^{-mk} \tag{3.25}$$

for $m, n \in \{1, 2\}$ where

$$\bar{S}_m = \sum_{k=0}^{2} \omega^{mk} \bar{l}_k \quad , S_m = \sum_{k=0}^{2} \omega^{mk} l_k \tag{3.26}$$

which can be obtained from the star-triangle relation. These have solutions provided

$$\frac{\alpha_1^3 + \alpha_2^3}{\alpha_1 \alpha_2} = \frac{\bar{\alpha}_1^3 + \bar{\alpha}_2^3}{\bar{\alpha}_1 \bar{\alpha}_2} \tag{3.27}$$

These are equivalent to the integrability condition Eq. 3.4 using the definitions in Eq. 3.3 for the chiral clock model. In the rest of the calculations we restrict to the case where $\bar{\alpha}_1 = \bar{\alpha}_2 = \bar{\alpha}$ which corresponds to the case where $\phi = 0$ as was assumed throught this chapter.

Logarithm of the transfer matrix is the generator of an infinite set of local conserved charges *i.e.*

$$Q^{(k)} = \lim_{u \to 0} \frac{\mathrm{d}^k}{\mathrm{d}u^k} \ln T(u) \tag{3.28}$$

where $Q^{(k)}$ is the k^{th} conserved charge. In the rest of this section, we calculate Q^1, Q^2, Q^3.

At lowest order we get $Q^{(1)}$ to be the quantum Hamiltonian H in Eq. 6.1. To obtain the higher order terms, we extend the expansion for the functions $l, \bar{l}$ as follows

$$\begin{aligned} l_n(u) &= \alpha_n u + \beta_n u^2 + \gamma_n u^3 + O(u^4) \\ \bar{l}_n(u) &= \bar{\alpha}_n u + \bar{\beta}_n u^2 + \bar{\gamma}_n u^3 + O(u^4) \end{aligned} \tag{3.29}$$

for $n = 1, 2$. Note that β,γ are not complex conjugates of $\bar{\beta}$,$\bar{\gamma}$. We solve for these additional parameters by inserting Eq. 3.29 in Eq. 3.25 and equating coefficients of powers of u on both sides.

Equating coefficients of the lowest order in u in Eq. 3.25, we get the following solution parametrized by one free parameter:

$$\begin{aligned} \bar{\beta}_1 &= \omega(\frac{\bar{\alpha}}{\alpha_2}\alpha_1^2 - \bar{\alpha}^2) + (\frac{\bar{\alpha}}{\alpha_2})\beta_2 \\ \bar{\beta}_2 &= \omega^2(\frac{\bar{\alpha}}{\alpha_2}\alpha_1^2 - \bar{\alpha}^2) + (\frac{\bar{\alpha}}{\alpha_2})\beta_2 \\ 2(\alpha_1\beta_2 - \alpha_2\beta_1) &= \alpha_1^3 - \alpha_2^3. \end{aligned} \tag{3.30}$$

We can plug in solutions of Eq. 3.30 in the Eqs. 3.29, subsequently expand Eq. 3.24 and use Eq. 3.28 to get the the conserved charge $Q^{(2)}$ explicitly (this does not depend on the undetermined parameters γs). Demanding Hermiticity fixes the free parameter in Eq. 3.30 and we obtain,

$$\begin{aligned} Q^{(2)} = \sum_k [I_k + \imath \left(\frac{1}{2} + \omega\right)(\frac{\alpha_1^2\bar{\alpha}}{\alpha_2} - \bar{\alpha}^2)\tau_k + \\ \imath \left(\frac{1}{2} + \omega^2\right)(\frac{\alpha_1^2\bar{\alpha}}{\alpha_2} - \bar{\alpha}^2)\tau_k^\dagger] \end{aligned} \tag{3.31}$$

Similarly we can constrain γ by equating the subsequent order in u in Eq. 3.25 resulting in the following conditions involving γ and $\bar{\gamma}$

$$\begin{aligned} (\omega-1)(\bar{\alpha}\gamma_2 - \alpha_2\bar{\gamma_2}) &= 2(2+\omega)\alpha_2\bar{\alpha}\bar{\beta_1} + (\omega-4)\alpha_2\bar{\alpha}^3 \\ &-\alpha_1\bar{\alpha}(\alpha_2^2(\omega-4) + 2\beta_1(2+\omega)) \\ (\omega+2)(\bar{\alpha}\gamma_2 - \alpha_2\bar{\gamma_1}) &= 2(\omega-1)\alpha_2\bar{\alpha}\bar{\beta_2} + (\omega+5)\alpha_2\bar{\alpha}^3 \\ &-\alpha_1\bar{\alpha}(\alpha_2^2(\omega+5) + 2\beta_1(\omega-1)) \\ 3(\alpha_2\gamma_1 - \alpha_1\gamma_2) &= 2\alpha_2^2\beta_2(-3\omega) - 3(1+2\omega)\alpha_1\alpha_2(\bar{\alpha}^2 - 2\bar{\beta_1}) \\ &-\alpha_1^2(2\beta_1(-3\omega^2) - 3\alpha_2^2(1+2\omega)) \end{aligned} \tag{3.32}$$

These have a one parameter set of solutions (for γs; the other parameters were determined in the previous step) which we fix by demanding Hermiticity of $Q^{(3)}$(its explicit form does not depend

on higher order terms omitted in Eq. 3.29) which has the form:

$$\begin{aligned} Q^{(3)} = \sum_k [& A\sigma_k(\tau_k^\dagger + \tau_{k+1}^\dagger)\sigma_{k+1}^\dagger + B\sigma_k(\tau_k + \tau_{k+1})\sigma_{k+1}^\dagger - \\ & C(\tau_k\sigma_k\tau_{k+1} + \tau_k^\dagger\sigma_k\tau_{k+1}^\dagger)\sigma_{k+1}^\dagger + \\ & C\sigma_k(\tau_k^\dagger\tau_{k+1} + \tau_k\tau_{k+1}^\dagger)\sigma_{k+1}^\dagger + \\ & D\sigma_k(\tau_{k+1} + \tau_{k+1}^\dagger)\sigma_{k+2}^\dagger + \\ & E\sigma_k(\sigma_{k+1}\tau_{k+1} + \tau_{k+1}^\dagger\sigma_{k+1})\sigma_{k+2} + \\ & F\tau_k + G\sigma_k\sigma_{k+1}^\dagger \\ & + h.c] \end{aligned} \tag{3.33}$$

where

$$\begin{aligned} A &= \frac{\omega^2}{2}\bar{\alpha}\alpha_2^2 - \omega^2\bar{\alpha}^2\alpha_1, \\ B &= \frac{\omega}{2}\bar{\alpha}\alpha_2^2 - \omega\bar{\alpha}^2\alpha_1, \\ C &= \bar{\alpha}^2\alpha_1, \\ D &= -\bar{\alpha}\alpha_1^2, \\ E &= \omega\bar{\alpha}\alpha_1\alpha_2, \\ F &= 3\bar{\alpha}\alpha_1\alpha_2, \\ G &= \frac{3}{2}\bar{\alpha}\alpha_2^2 + \bar{\alpha}^2\alpha_1 + \frac{1}{2}\alpha_1^2\alpha_2. \end{aligned}$$

We find that both these charges $Q^{(2)}$ and $Q^{(3)}$ have terms with support on up to 3 sites. These are orthogonal under the norm $\langle , \rangle_\rho$ defined in the main text at all temperatures we tested.

Appendix 3.B Convergence of real-time data from tDMRG

Truncation cutoff (ϵ) affects the computational cost and accuracy of tDMRG calculation. We verified the convergence of our current-current correlator by comparing results at different ϵ. For $T = 1$, we observe in Fig. A.1 that the truncation cutoff 10^{-9} is sufficient. At larger cutoff (e.g $1e-7$), the $\mathrm{Re}\langle \mathrm{I(t)I}_{\frac{\mathrm{L}}{2}} \rangle$ decreases fast from around time 5 indicating reliability of the result only upto small timescales. On the other hand, for $\epsilon \leq 10^{-9}$ the asymptotic behaviour shows very small difference at long timescale indicating convergence of result.

In Fig. A.2, we observe that for the same truncation cutoff and bond dimensions, ancilla disentangler produces reliable results for significantly longer timescales.

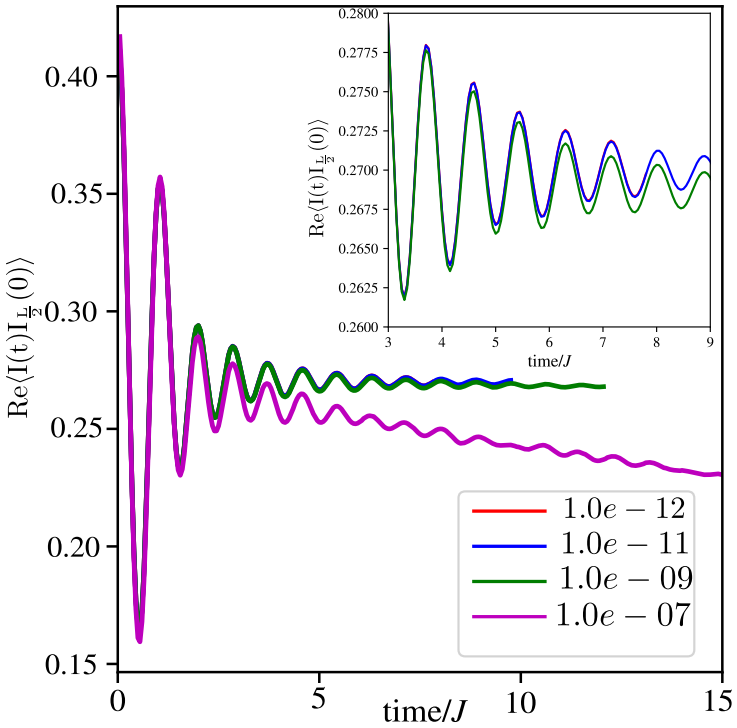

Figure A.1: Convergence of $\mathrm{Re}\langle I(t)I_{L/2}(0)\rangle$ with decreasing truncation cutoff. $J = 1$, $f = \frac{2}{5}$, $\theta = \cos^{-1}(\frac{2}{5})$, $T = 1$. Maximum bond dimension is 900 in all cases. (Inset) Magnified version of the $\mathrm{Re}\langle I(t)I_{L/2}(0)\rangle$ data. Notice the blue and red curves overlap.

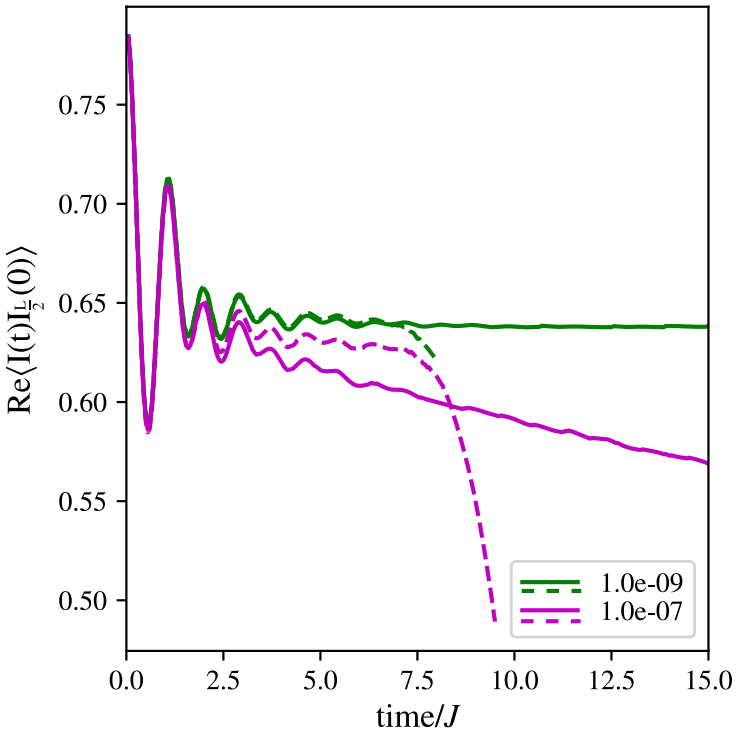

Figure A.2: Similar to Fig. A.1 but shows the effect of ancilla disentangler. Solid line is with tDMRG with disentangler unitary and dotted line is without application of ancilla disentangler. Maximum bond dimension is 900 in all cases. $J = 1$, $f = \frac{2}{5}$, $\theta = \cos^{-1}(\frac{2}{5})$, $T = 2$.

Appendix 3.C Choice of finite temperature disentangler unitary

As noted in the main text, invariance of the reduced density matrix under unitary transformations of the 3^L dimensional ancilla Hilbert space allow us to choose an optimal 'disentangler' unitary transformation of the ancilla that minimize entanglement growth. A search within the 3^{2L} dimensional parameter space of the unitary group $U(3^L)$ is computationally impossible, so we consider a one parameter set of anicilla unitaries of the form $e^{ih(\theta_{\text{anc}})}$ where $h(\theta_{\text{anc}})$ has the same form as the clock model Hamiltonian but with a parameter θ_{anc} replacing θ of the physical Hamiltonian.

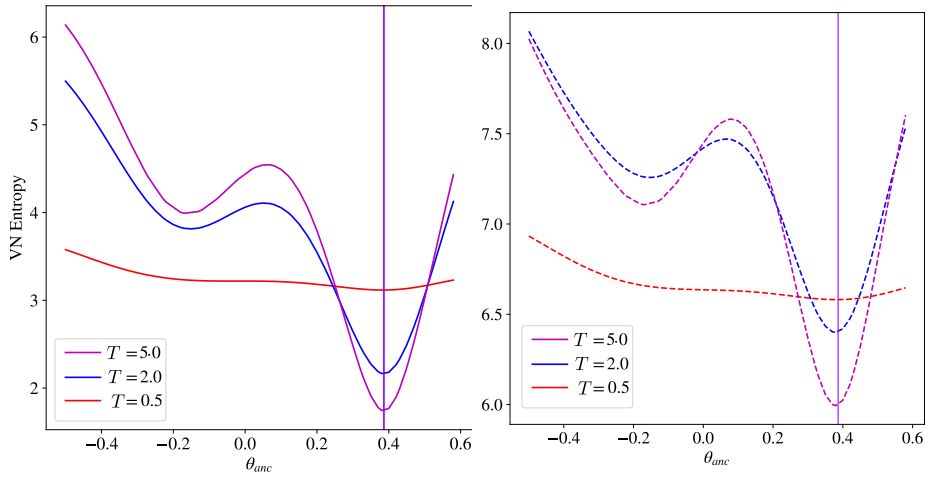

Figure A.3: Optimal value for θ_{anc} decided from the bipartite Von-Neumann entropy on bonds near the quench site. The violet vertical line corresponds to $\theta_{\text{anc}} = \theta$. The solid lines correspond to entanglement growth in thermal state and the dotted lines correspond to entanglement growth in thermal state evolved after quench. The entanglement is measured after time 2.5. Calculations are done at integrable point corresponding to $f = 2/5$ on a system of 30 physical sites.

We observe that for $\theta_{\text{anc}} = \theta$ (Fig. 3.C), the entanglement growth (as measured by the bipartite Von Neumann entropy) on the bonds near the quench site is minimum at any temperature. The disentangler is most effective at high temperature. Similar conclusion holds for non-integrable points too.

Appendix 3.D Consistency check of conductivity data

As discussed in section 3.3.3, we can evaluate the thermal conductivity using two equivalent expressions (*i.e.* Eq. 3.9 and Eq. 3.15). They should result in same values if we have data for correlator at all time. However, tDMRG calculation can provide reliable data only up to a finite timescale. Consequently, we incur a "finite-time error" in the discrete Fourier transform required for thermal conductivity calculation (Eq. 3.15). We can estimate this error from the difference in the values obtained from Eq. 3.9 and Eq. 3.15. In Figure A.4, we provide the data for 3 different temperature at a single point ($f = 2/5$) on integrable line. It can be readily observed that the estimates from Eq. 3.9 (solid line) and Eq. 3.15 (dotted line) match quite well for most finite frequency region with significant difference between them only at low frequency. This is

expected as low-frequency regime gets most affected by long time data. However, the estimated errror obtained here is order of magnitude smaller than Drude weight.

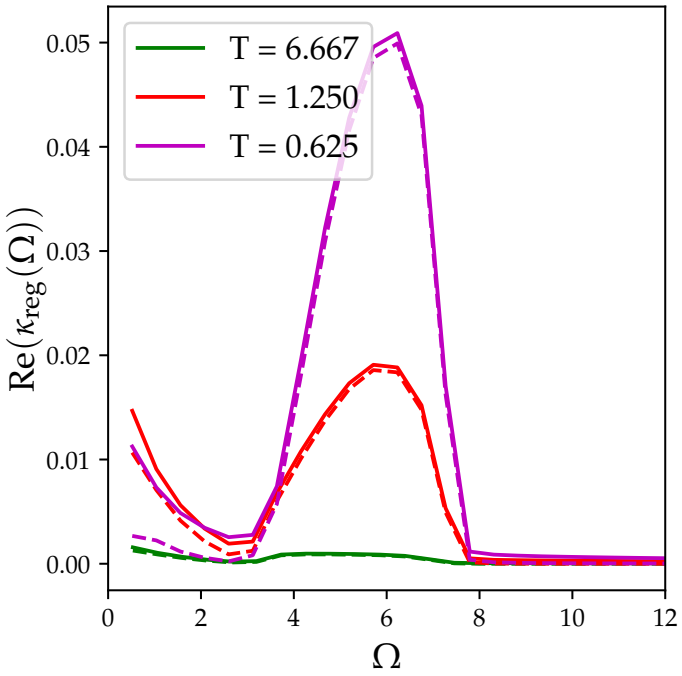

Figure A.4: Re κ_{reg} obtained from eq.3.9 is shown in solid line and the same from 3.15 is shown in dotted line. Notice both curves overlap for large Ω while deviation can be observed for small Ω.

4

Exact Full Counting Statistics in Non-Equilibrium Steady States

THE study of thermal-transport in Chapter 3 through Drude weights characterizes a quantum state through expectation values of local observables and their low-order time correlations. This utilizes the linear response regime, but it captures only the first few moments of the distributiion of local observable. The distinction of local observables has become accessible on modern programmable quantum simulators [174, 175, 176, 177], where the elementary output of an experiment is not an expectation value but a sample from the joint distribution of L single-site projective measurements, and repeated sampling reconstructs the full distribution $P(m)$ of a spatially averaged observable $\hat{m} = L^{-1}\sum_i \hat{o}_i$ directly. In Chapter 4 we exploit this shift of perspective: working with the exact solution of the boundary-driven XXZ chain's NESS (Sec. 1.5), we compute not only the mean of $\hat{m}$ but its distribution and *rate function*, which governs the exponentially suppressed probability of observing an atypical fluctuation in a system of size L. The mathematical framework for this shift from expectation values to full distributions is the theory of large deviations introduced in Chapter 1.

4.1 Introduction

Expectation values of local observables in the long-time limit of typical unitarily evolving, large quantum manybody systems are described by a Gibbs ensemble or a generalized Gibbs ensemble with chemical potentials determined by the expectation values of the conserved charges in the initial state. Less is known about description of local properties and correlations in steady states of nonequilibrium systems with nonzero charge current except when a hydrodynamic description is available. Local properties in general out-of-equilibrium states of interacting microscopic models are usually difficult to access due to the computational cost involved in

This chapter is adapted from the publication: **Sandipan Manna** and G. J. Sreejith, "Full distribution and large deviations of local observables in an exactly solvable current carrying steady state of a strongly driven XXZ chain," *Phys. Rev. E* **111**, 044139 (2025).

producing accurate microscopic representation of the nonequilibrium steady state (NESS).

Dynamics of quantum many-body systems in contact with external reservoirs has been a major focus of both theoretical and experimental investigations in recent years. In the weak coupling regime, Lindblad type master equation [10, 42] can approximate the effective nonunitary dynamics of the system after integrating out the reservoir degrees of freedom. We study a specific case of an XXZ spin chain coupled at the ends to spin baths represented by maximally polarizing Lindblad couplings. Despite strong interactions and strong bath coupling that are well outside the linear response regime, the NESS can be exactly represented in MPS form [11]. Several closely related models also admit exact NESS representations in various forms [178, 179, 180, 181, 182, 183, 184]. We bypass the numerical limitations in the usual studies of interacting nonequilibrium systems by using the exact, numerically convenient MPS representation of the NESS presented in Ref. [11] to describe its features.

In addition to correlations and expectation values of the magnetization, we also calculate the full distribution of the local spin observables in the NESS. The full distribution can be a useful characterizing tool in experimental cold atom systems due to access to the same through time-of-flight methods and snapshot images with single-atom resolution on such platforms [174, 175, 176, 177]. This has inspired studies of full distribution of local observables and current in diverse settings where demonstrative calculations can be performed on microscopic toy models of quantum many body systems such as in 1-D Bose gas under quantum quench [185, 186, 187, 177], ground states of XXZ chain [188], ground states of 2D Bose Hubbard model [189], XXZ chain after quench [190, 191, 15], 2D/3D Heisenberg model after quench [192], free fermion and XY model ground states [193, 194], ground state of Haldane Shastry model [195], long range interacting Ising model [196], quenched Ising models with dynamical confinement [197] and random circuits [198, 199]. The integrated current distribution that characterizes dynamical processes has also been calculated in random quantum circuits [14], in the driven XX model [179] and the XXZ chain with dephasing baths [200].

This chapter studies the distribution of local observables in the current carrying steady state of an interacting spin system where this calculation can be reliably performed. Calculations of local properties using the solution for NESS in the MPS form reduces to numerically convenient transfer matrix evaluations. We present explicit expressions of the spin correlations and entropy density as well as the scaled cumulant generating function (SCGF) for the z-magnetization density, z-domain wall density, and z-antiferromagnetic ordering density in the XX model (Ising anisotropy $\Delta = 0$). We find that the increasing current causes short range antiferromagnetic ordering reflected in the dependence of local spin densities on spin current in the bulk. In the finite Δ setting, numerically exact results in the limit of infinite system size can be obtained when Δ has the form $\cos\frac{p}{q}\pi$ for co-prime integers p, q. We also analyze the effect of finite system size on the SCGF of the z-magnetization density. For finite p and q, the asymptotic limit is approached exponentially. We show that the rate of approach to the asymptotic large system size limit is a strongly discontinuous function of Δ. The rate of convergence to aymptotic SCGF vanishes with increasing p and q. This, for instance, implies that $(p, q) = (1001, 4001)$ has a much smaller gap than $(p, q) = (1, 4)$ though they have similar values of Δ.

The chapter is organized as follows. We introduce the model in Sec. 4.2 and the exact

representation of the NESS in terms of MPS in Sec. 4.3. We provide a brief overview of the proof of the MPS representation of the NESS following Ref. [11]. This section establishes the notation that we use in the rest of the chapter. In Sec. 4.4, we present the results for the noninteracting (XY limit) limit of the model where analytical calculations are possible. We calculate the full distribution of the local observables, the two-point correlations, and the entropy density in the NESS. In Sec. 4.5, we present the results on full distribution of local magnetization and spin current for the general XXZ model at finite Ising anisotropy Δ. We also discuss the symmetries of the NESS and the implications of these symmetries on its properties. Section 4.5.5 discusses rate function (also referred to as large deviation function) for finite systems as well as asymptotic limit of the SCGF. We conclude in Sec. 4.6. Our primary contribution are the results beyond expectation value of local observables, i.e., results on full distribution and large deviation statistics of local observables in a strongly driven interacting spin chain.

4.2 Model

We study a spin-1/2 XXZ chain of length N coupled to spin-baths at both ends. The time evolution $\partial_t \rho = \mathcal{L}\rho(t)$ of the density matrix is determined by the Liouvillian $\mathcal{L}$,

$$\mathcal{L}\rho = -\imath[H_{XXZ}, \rho] + \epsilon \mathcal{D}_1 \rho + \epsilon \mathcal{D}_N \rho. \tag{4.1}$$

The evolution in the bulk is governed by the Hamiltonian with local density $h_{i,i+1}$

$$H_{XXZ} = \sum_{i}^{N-1} h_{i,i+1} = J \sum_{i} \sigma_i^x \sigma_{i+1}^x + \sigma_i^y \sigma_{i+1}^y + \Delta \sigma_i^z \sigma_{i+1}^z \tag{4.2}$$

where Δ is the Ising anisotropy, σ_i^α are Pauli matrices and ϵ is the strength of the coupling between the chain and the bath. We will set $|J| = 1$ in all calculations. The dissipator $\mathcal{D}_k \rho$ has the Lindblad form

$$\mathcal{D}_k \rho(t) = 2 L_k \rho(t) L_k^\dagger - \{L_k^\dagger L_k, \rho(t)\} \tag{4.3}$$

acting on spins at the two ends of the chain $k = 1, N$. $L_1 = \sigma^+$ and $L_N = \sigma^-$ are the jump operators and $\sigma^\pm = \frac{\sigma^x \pm \imath \sigma^y}{2}$. With these, the dissipative terms at the two ends simplify to

$$\begin{aligned} \mathcal{D}_1 \rho &= (\sigma_1^+ \rho \sigma_1^- - P_1^\downarrow \rho) + \text{H.c.}, \\ \mathcal{D}_N \rho &= (\sigma_N^- \rho \sigma_N^+ - P_N^\uparrow \rho) + \text{H.c.}, \end{aligned} \tag{4.4}$$

where P_k^ν represents the projector onto the state ν acting on site k.

We are interested in the NESS density matrix ρ_∞ which satisfies $\mathcal{L}\rho_\infty = 0$. The z-magnetization density profile and the energy density profile in the NESS are shown in Fig. 4.1. For $|\Delta| < 1$, the bulk shows a flat zero magnetization profile in the thermodynamic limit, with a finite magnetization at both ends. Such flat charge density profiles are ubiquitous in the NESS of integrable and ballistic quantum chains [99, 201]. The energy density profile shows a similar behavior with a jump at the ends and flat profile in the bulk. For $|\Delta| > 1$, the spins are close

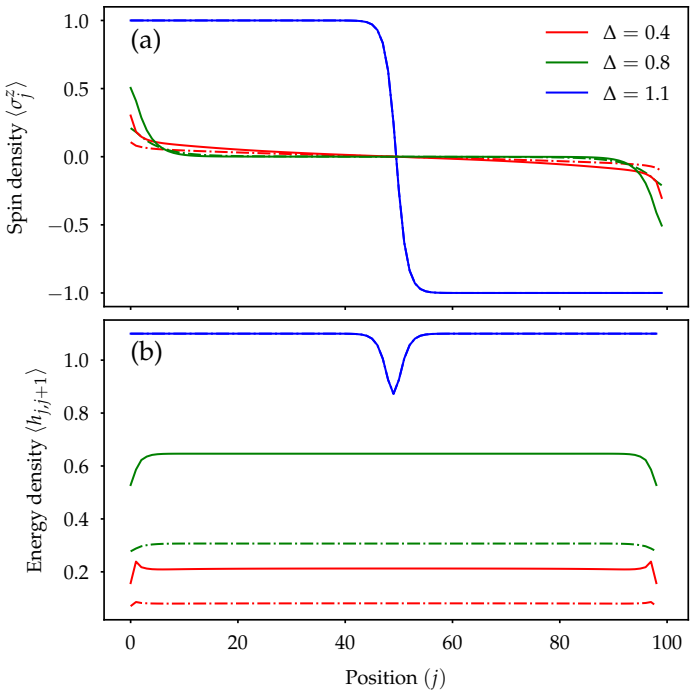

Figure 4.1: (a) Local z-direction magnetization and (b) local energy density as a function of position. The solid lines and dotted lines are for $\epsilon = 1$ and 0.5, respectively. Results for system size $N = 100$.

to maximally polarized but along opposite directions on the left and right halves of the chain, with a sharp jump in magnetization at the center. The energy density shows a similar flat profile except near the center. Figure 4.1 shows the profiles for $\Delta > 0$. For $\Delta < 0$, the spin profile remains the same but the energy profile is sign-reversed (Also see discussion of symmetries in Sec. 4.5.1).

Spin and energy expectation values in the Fig. 4.1 are obtained from the exact solutions from Ref. [11] summarized in Sec. 4.3. In this chapter, we use the exact solutions and go beyond the expectation values of local observables and study their correlations and the full distribution in large blocks as well as the entropy in the ρ_∞. Calculation of such quantities requires the ρ_∞ for large system sizes with high precision so that longer range and multisite correlations contributing to the full distribution are faithfully captured in the NESS. Direct calculation of ρ_∞ by exact

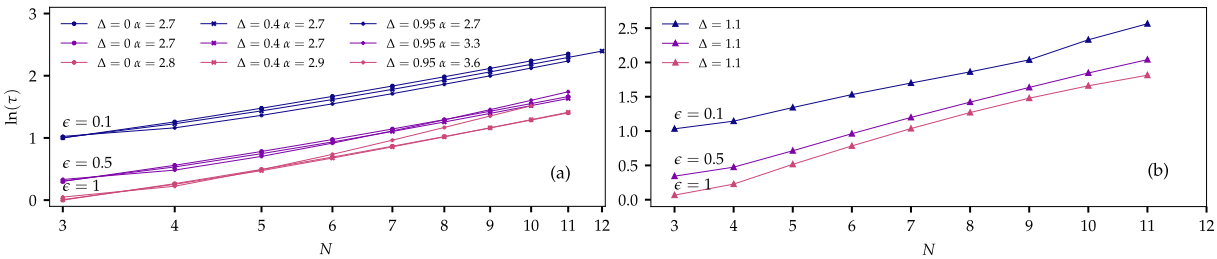

Figure 4.2: Relaxation time scale τ as a function of system size. (a) In the gapless regime the relaxation time appears to increase with system size as $\tau \sim N^3$. Exponent was obtained by fitting the largest three N values in each case to $\tau \sim N^\alpha$. The plot is in log-log scale.(b) In the gapped regime the relaxation time,$\tau \propto \exp(cN)$. The plot is in semilog scale.

diagonalization (ED) of $\mathcal{L}$ is unfeasible beyond $N \sim 12$ sites. Accurate TEBD estimation is also impractical for systems exceeding ~ 100 sites, as the time scale required for relaxation to the NESS extends past the regime where tensor network algorithm predictions remain reliable.

Figure 4.2 shows the rapid growth of relaxation time scale τ (estimated in small systems using ED of the Liouvillian as the reciprocal of the eigenvalue with the second largest real part) as a function of system size N. As was already demonstrated in Ref. [202], the relaxation time scales with system size as $\tau \propto N^3$ for $|\Delta| < 1$ and $\tau \propto \exp(cN)$ for $|\Delta| > 1$. The latter scaling is due to the maximally polarized regions in the chain that suppress the dynamics that leads to relaxation. The τ scales as $\sim N^3$ for all Δ if the baths are not maximally polarized [202]. While Δ within each phase has little effect on τ, relaxation time increases with decreasing bath coupling ϵ through the amplitude of the power-law and exponential scaling.

We take advantage of the access to the exact solution for ρ_∞ of the nontrivial interacting system to calculate the full distribution and rate functions for the fluctuations of the local observables in the bulk of the chain demonstrating the large deviation principle for these quantities. Additionally, we calculate the correlations and entropy density in ρ_∞.

4.3 MPS form of the nonequilibrium steady state

The NESS ρ_∞ can be exactly expressed in a matrix product form as was shown in Ref. [11, 44]. We first state the solution. We also provide a short summary of the proof after this for completeness. We will need only the solutions shown in Eq. [4.5, 4.6, 4.50] in the rest of the chapter. In the subsequent subsection, we also illustrate the construction of MPO for local observables and the corresponding transfer matrix representations.

4.3.1 MPS Solution

The NESS ρ_∞, being a positive semidefinite matrix, can be expressed as a product $S_N S_N^\dagger$. An ansatz for S_N can be written as a matrix product state (MPS) over Pauli strings of the following form:

$$\begin{aligned} S_N &= \sum \psi^{s_1 s_2 s_3 \cdots} \times \sigma^{s_1} \otimes \sigma^{s_2} \otimes \ldots \sigma^{s_N}, \\ \psi^{s_1 s_2 s_3 \cdots} &= \langle 0| \prod_{i=1}^{N} A_{s_i} |0\rangle. \end{aligned} \tag{4.5}$$

Here, s_i takes values from $\{+, -, 0\}$, σ^{s_i} acts on the i^{th} site and $\sigma^0 = \mathbb{I}/\sqrt{2}$. The local tensors A_s act on the bond Hilbert space H_B and have the following form

$$\begin{aligned} A_0 &= \sqrt{2}|0\rangle\langle 0| + \sum_{r=1}^{\infty} \sqrt{2} a_r^0 |r\rangle\langle r|, \\ A_+ &= \imath\epsilon |0\rangle\langle 1| + \sum_{r=1}^{\infty} a_r^+ |r\rangle\langle r+1|, \\ A_- &= |1\rangle\langle 0| + \sum_{r=1}^{\infty} a_r^- |r+1\rangle\langle r|. \end{aligned} \tag{4.6}$$

H_B is spanned by the orthonormal states $|r\rangle$, $r = 0, 1, \ldots$. The explicit form of the matrix elements are given in the appendix Eq. 4.50.

We briefly comment on the specific structure of the ansatz. Firstly, while the most general

ansatz for S_N would contain $\sigma_z/\sqrt{2}$ in addition to $\{\sigma^{\pm}, \sigma^0\}$, S_N does not contain σ_z. Secondly, symmetries of $\mathcal{L}$ implies that the density matrix commutes with the spin operator $S_z = \sum_i \sigma_i^z$, i.e $[S_z, S_N S_N^\dagger] = [S_z, S_N] S_N^\dagger - \text{H.c.} = 0$. The above ansatz assumes specifically that $[S_z, S_N] = 0$. This local symmetry of S_N suggests that it can be written in terms of quantum number conserving tensors A (see for instance, Ref. [69]) where each bond index is associated with a charge. The tri-diagonal structure in the above ansatz assumes that the dimension of each charge sector is 1 implying the states can be labeled by the charge. The symmetry $[S_z, S_N] = 0$ implies that the symmetry charge of the bond state appearing on the left and right ends are the same and can be chosen to be 0. Last, boundary conditions imply that $A_-|0\rangle = 0$ which suggests that negative bond charges are not needed.

4.3.2 Summary of the proof

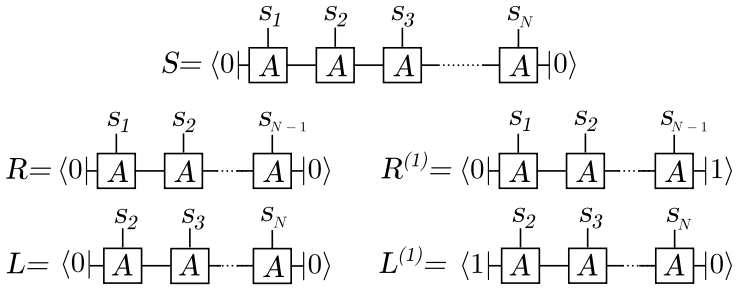

Figure 4.3: MPS representation of $L, L^{(1)}$ and $R, R^{(1)}$ acting on sites $1 < i \leq N$ and $1 \leq i < N$ respectively. The operators $L^{(1)}$ and L differ in the bond charge on the left end. Similarly $R^{(1)}$ and R differ in the bond charge at the right end. The leg indices are Pauli indices s_i.

Before sketching the proof, it is useful to define the operators shown in Fig. 4.3 in their MPS form. Operators L and R are equivalent to S_{N-1} but act on the $N-1$ sites $2, 3 \ldots N$ and $1, 2, \ldots N-1$ respectively. Operators $R^{(1)}$ and $L^{(1)}$ are similar to R and L respectively but unlike them these are terminated on the left and right ends respectively by $|1\rangle$ instead of $|0\rangle$.

We first state a sufficient condition on S_N such that $S_N S_N^\dagger$ is the steady state. If S_N can be written as

$$\begin{aligned} S_N &= \mathbb{I}_1 \otimes L + \imath\epsilon\sigma_1^+ \otimes L^{(1)} \\ S_N &= R \otimes \mathbb{I}_N + R^{(1)} \otimes \sigma_N^- \end{aligned} \tag{4.7}$$

and it satisfies the following divergence condition

$$[H, S_N] = -\imath\epsilon(\sigma_1^z \otimes L - R \otimes \sigma_N^z) \tag{4.8}$$

then $\rho_\infty = S_N S_N^\dagger$ is annihilated by the $\mathcal{L}$.

To see this, we consider the action of the dissipator, on the density matrix. Using Eq. 4.4 in Eq. 4.7, we get

$$\begin{aligned} \epsilon\mathcal{D}_1 S_N S_N^\dagger &= \epsilon(\sigma_1^z \otimes LL^\dagger + \imath\epsilon\sigma_1^- \otimes LL^{(1)^\dagger}) + \text{H.c.}. \\ \epsilon\mathcal{D}_N S_N S_N^\dagger &= -\epsilon(\sigma_N^z \otimes RR^\dagger + \sigma_N^+ \otimes RR^{(1)^\dagger}) + \text{H.c.}.. \end{aligned} \tag{4.9}$$

By identifying terms similar to Eq. 4.7 in the ight-hand side (RHS) we see that the first and second lines are $\epsilon\sigma_1^z L S_N^\dagger + \text{H.c.}.$ and $-\epsilon S_N R^\dagger \sigma_N^z + \text{H.c..}$, respectively and therefore

$$\epsilon(\mathcal{D}_1 + \mathcal{D}_N) S_N S_N^\dagger = \epsilon(\sigma_1^z \otimes L - R \otimes \sigma_N^z) S_N^\dagger + \text{H.c..}$$

This has to be canceled by $-\imath[H, S_N S_N^\dagger]$ so that $\mathcal{L} S_N S_N^\dagger = 0$. Using the Leibnitz rule for the commutator,

$$\imath[H, S_N S_N^\dagger] = \imath[H, S_N] S_N^\dagger + \text{H.c..}$$

Comparing the RHS of the above equations we see that Eq. 4.8 (in addition to Eq. 4.7) is a sufficient condition $S_N S_N^\dagger$ to be the steady state. Solutions to these are presented in Appendix 4.A.

4.3.3 Expectation value as transfer matrix

The expectation value of an operator O is given by

$$\langle O \rangle = \text{Tr}(S_N^\dagger O S_N)/Z$$

where $Z = \text{Tr}(S_N^\dagger S_N)$,. Expectation value of a single site operator O on site k can be written as $\langle 0|T^{k-1} V_O T^{n-k}|0\rangle/Z$ where $|0\rangle \equiv |0,0\rangle \equiv |0\rangle \otimes |0\rangle \in H_B \times H_B$, the transfer matrix V_O, which maps state $jj' \in H_B \times H_B$ to the state $ii' \in H_B \times H_B$, is given by,

$$[V_O]_{ii'}^{jj'} = \quad = \sum_{\mu,\nu=\pm,0} A_\mu^{i,j} A_\nu^{i',j'} \tilde{O}_{\mu\nu}$$

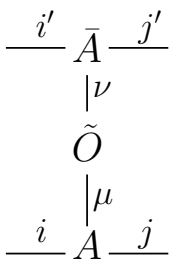

and $T = V_{\mathbb{I}}$. The normalization is $Z = \langle 0|T^N|0\rangle$. The 4×4 matrix $\tilde{O}$ is given by

$$\tilde{O}_{\mu\nu} = \text{Tr}[\sigma_\mu^\dagger O \sigma_\nu]$$

where $\sigma_\mu, \sigma_\nu \in \{\mathbb{I}/\sqrt{2}, \sigma^-, \sigma^+, \sigma^z/\sqrt{2}\}$. Expectation values of direct product of single site operator $O_j O'_{j+1}$ can be calculated as $\langle 0|T^{j-1} V_{O_j} V_{O'_{j+1}} T^{N-j-1}|0\rangle/Z$.

Now we consider the case of more general operator O, which cannot be written as a direct product of single site operators. Such an observable has an MPO representation

$$O \equiv$$

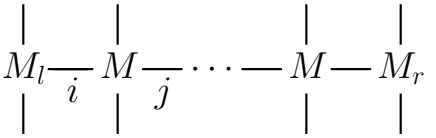

where the elements M_{ij} of the tensors (for each bond index pair i, j) are single-site operators. The expectation value of O acting on sites a to $a + l$ can be written as

$$\text{Tr}[\rho O] = \langle 0|T^{a-1} V_{M_a} V_M^{l-1} V_{M_{a+l}} T^{N-a-l}|0\rangle/Z, \tag{4.10}$$

where V_M is obtained by $[V_M]_{ij} = V_{M_{ij}}$ for the single site operator M_{ij}, $V_{M_{ij}}$ was defined earlier in this section.

We now illustrate this with a specific example of the operator corresponding to the imaginary field generating function of the z-domain wall count in a block from a to $a+l$. This can be written as $\mathcal{G}(\lambda) = \mathrm{Tr}[\rho O]$ where $O = \exp(\imath\frac{\lambda}{2}\sum_{i=a}^{a+l-1}\sigma_i^z\sigma_{i+1}^z)$ up to a phase factor which we ignore for this discussion. O can be expressed as an MPO with with local tensors of bond dimension 2 as $O = M_a M^{l-1} M_{a+l}$ where

$$M_a = \begin{bmatrix} \mathbb{I} & \sigma^z \end{bmatrix} \quad M_{a+l} = \begin{bmatrix} \mathbb{I}\cos\frac{\lambda}{2} \\ \imath\sigma^z \sin\frac{\lambda}{2} \end{bmatrix},$$
$$M = \begin{bmatrix} \mathbb{I}\cos\frac{\lambda}{2} & \sigma^z\cos\frac{\lambda}{2} \\ \imath\sigma^z\sin\frac{\lambda}{2} & \imath\mathbb{I}\sin\frac{\lambda}{2} \end{bmatrix}. \tag{4.11}$$

Operators here are multiplied as tensor product. We obtain the corresponding transfer matrices as the following block matrices

$$V_{M_a} = \begin{bmatrix} T & V_{\sigma^z} \end{bmatrix} \quad V_{M_{a+l}} = \begin{bmatrix} T\cos\frac{\lambda}{2} \\ \imath V_{\sigma^z}\sin\frac{\lambda}{2} \end{bmatrix}$$
$$V_M = \begin{bmatrix} T\cos\frac{\lambda}{2} & V_{\sigma^z}\cos\frac{\lambda}{2} \\ \imath V_{\sigma^z}\sin\frac{\lambda}{2} & \imath T\sin\frac{\lambda}{2} \end{bmatrix}.$$

With these, the generating function is given by

$$\mathcal{G}(\lambda) = \langle 0|T^{a-1}V_{M_a}V_M^{l-1}V_{M_{a+l}}T^{N-a-l}|0\rangle/Z. \tag{4.12}$$

The state S_N has a maximum bond dimension of $N/2$. For a generic operator O of MPO bond dimension χ, transfer matrices T, V_{M_l}, V_M and V_{M_r} in general have sizes $N^2/4\times N^2/4$, $N^2/4\times N^2\chi/4$, $N^2\chi/4\times N^2\chi/4$ and $N^2\chi/4\times N^2/4$ respectively. For large systems multiplication of these matrices can be prohibitively expensive without suitable truncation of their dimensions.

However, in the case of operators O that can be written as a polynomial in $\{\sigma_z, \mathbb{I}\}$ such as $\mathcal{G}$ introduced before, the evaluation is made efficient by the fact that $\tilde{O}_{\mu\nu} \propto \delta_{\mu\nu}$, and the transfer matrices V_{σ_z} and T conserve the quantity $Q(i, i' \in H_B \times H_B) = i - i'$ in the bond indices:

$$[V_{\sigma_z}]_{ii'}^{jj'} = T_{ii'}^{jj'} = 0 \text{ if } Q(i,i') \neq Q(j,j') \tag{4.13}$$

Since $Q(0,0) = 0$ at the two ends and Q is conserved by T and V, only the $Q = 0$ sector is relevant in every bond and T, V can be restricted to the $Q = 0$ sector. This restriction reduces the dimension of the transfer matrices in the relevant sector ($Q = 0$) to $N/2$ for T and $N\chi/2$ for V_M. Calculations using such small transfer matrices can be efficiently performed to high precision due to the $O(N)$ scaling of the matrix sizes.

For the case of $O = \sigma_z$ and $O = \mathbb{I}$, $\tilde{O} \equiv \mathrm{diag}(0,-1,1,0)$ and $\mathrm{diag}(1,1,1,1)$ respectively. The

transfer matrices V_{σ_z} and $T = V_{\mathbb{I}}$, restricted to the $Q = 0$ sector are given by

$$V_{\sigma_z} = \sum_{r=0}^{\infty} |a_r^+|^2 |r\rangle\langle r+1| - |a_r^-|^2 |r+1\rangle\langle r| \tag{4.14}$$

$$T = \sum_{r=0}^{\infty} |a_r^+|^2 |r\rangle\langle r+1| + |a_r^-|^2 |r+1\rangle\langle r| + 2|a_r^0|^2 |r\rangle\langle r| \tag{4.15}$$

where $|r\rangle$ here denotes the $|r, r\rangle \in H_B \times H_B$.

4.4 Results for $\Delta = 0$

In the XX limit ($\Delta = 0$), the tensors A can be truncated to 2×2 matrices,

$$A^0 = \sqrt{2} \begin{bmatrix} 1 & 0 \\ 0 & \frac{\imath\epsilon}{2} \end{bmatrix}, \; A^+ = \begin{bmatrix} 0 & \imath\epsilon \\ 0 & 0 \end{bmatrix}, \; A^- = \begin{bmatrix} 0 & 0 \\ 1 & 0 \end{bmatrix}.$$

The truncation is due to the fact that the matrix elements in A that take the state out of the space spanned by $\{|0\rangle, |1\rangle\}$ are 0 (See Appendix 4.A.1). The transfer matrix in the bond charge sector $Q = 0$ (Eq. 4.15) becomes,

$$T = \begin{bmatrix} 2 & \epsilon^2 \\ 1 & \frac{\epsilon^2}{2} \end{bmatrix}$$

which acts on the space spanned by $|0, 0\rangle, |1, 1\rangle$ in the $Q = 0$ subspace of $H_B \otimes H_B$. The truncation of the dimensions of the T and V_{σ_z} allows us to obtain exact closed form expressions for various quantities. In this section, we calculate the properties of local spin operators in the XX limit.

Mean and two-point correlations of spins: The transfer matrix V_{σ_z} in the $Q = 0$ sector (Eq. 4.14) is given by,

$$V_{\sigma_z} = \begin{bmatrix} 0 & \epsilon^2 \\ -1 & 0 \end{bmatrix}.$$

The magnetization $\langle\sigma_z\rangle$ on the ith site can be calculated as $\langle T^{i-1} V_{\sigma_z} T^{N-i}\rangle / Z$. This is exactly 0 except at the two ends where the magnetization increases monotonically with ϵ as $\pm\epsilon^2/(\epsilon^2+4)$.

The two-point σ_z correlator can be calculated as

$$\langle\sigma_z^i \sigma_z^j\rangle = \langle 0|T^{i-1} V_{\sigma_z} T^{j-i-1} V_{\sigma_z} T^{N-j}|0\rangle / Z$$

The connected two point correlator is zero except on adjacent sites when it is $-4\epsilon^2/(\epsilon^2+4)^2$[184].

Now we consider the magnetization in the x direction. The density matrix commutes with S_z and therefore magnetization $\langle\sigma^x\rangle$ is 0 everywhere. The two point correlator $\langle\sigma_i^x \sigma_j^x\rangle$ can be calculated as $2\mathrm{Re}\langle\sigma_i^+ \sigma_j^-\rangle$. We can calculate $\langle\sigma_i^+ \sigma_j^-\rangle$ using

$$\langle\sigma_i^+ \sigma_j^-\rangle = \langle 0|T^{i-1} V_{\sigma^+} T_{+-}^{j-i-1} V_{\sigma^-} T^{N-j}|0\rangle / Z.$$

Note that $V_{\sigma^\pm}$ alters the Q by ± 1. T_{+-} is the transfer matrix in the $Q = 1$ subspace of $H_B \times H_B$.

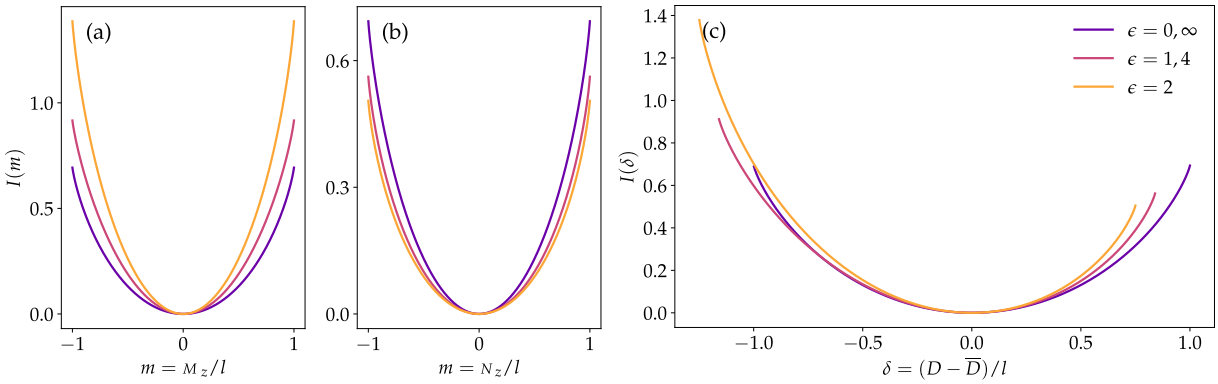

Figure 4.4: Rate functions for the (a) magnetization, (b) staggered magnetization and (c) domain wall density in the NESS of the XX model obtained from Legendre transform of Eq. 4.20, Eq. 4.22 and Eq. 4.25 for different representative values of ϵ. Rate functions are the same at ϵ and $4/\epsilon$.

The $\mathrm{Q} = 1$ subspace implies that the bonds can be in a one-dimensional space spanned by the state $|0, 1\rangle$. This is because the matrix elements of A that take the bond state out of this space vanish. These are given by

$$T_{+-} = -\imath\epsilon/2, \quad V_{\sigma^+} = -\imath\epsilon \begin{bmatrix} 1 \\ 1/2 \end{bmatrix}, \quad V_{\sigma^-} = \begin{bmatrix} 1 & \frac{\epsilon^2}{2} \end{bmatrix}.$$

The two point correlation in the bulk can be calculated to be

$$\langle \sigma^x_p \sigma^x_{p\pm k} \rangle = 4 \left(\frac{2\epsilon}{\epsilon^2 + 4} \right)^k \cos \frac{\pi k}{2}, \tag{4.16}$$

assuming $p, p \pm k$ are not the ends 1 or N.

The correlations are 0 for all odd values of the distance k and otherwise is oscillatory with an exponentially decaying amplitude $\sim [2\epsilon/(4 + \epsilon^2)]^k$. Local spin current expectation value can be calculated as $2J\mathrm{Im}\langle \sigma^+_i \sigma^-_{i+1} \rangle$ and gives

$$\langle J^s \rangle = \frac{2\epsilon}{4 + \epsilon^2} J. \tag{4.17}$$

4.4.1 Distribution of local observables in a block

z-magnetization We now study the distribution of the local observables in the system. The total magnetization in a block of size l between a and $a + l$ is given by ($N = 2n + l$),

$$M^z_l = \sum_{j=a+1}^{a+l} \sigma^z_j$$

M_l^z has eigenvalues $M \in [-l, l]$. The imaginary field generating function $\mathcal{G}_{M_l^z} = \langle e^{\imath\lambda M_l^z}\rangle$ for the magnetization distribution can be written as $\langle 0|T^n V_{ez}^l T^n|0\rangle/Z$ where (in the $Q = 0$ sector)

$$V_{ez}(\lambda) = T\cos\lambda + \imath V_{\sigma_z}\sin\lambda = \begin{bmatrix} 2\cos\lambda & e^{i\lambda}\epsilon^2 \\ e^{-i\lambda} & \frac{1}{2}\epsilon^2\cos\lambda \end{bmatrix}$$

The generating function $\mathcal{G}_{M_l^z}$ in the *bulk* is independent of number of sites on the left and right of the block and can be calculated to be

$$\mathcal{G}_{M_l^z}(\lambda) = \frac{\alpha_+^{l+1} - \alpha_-^{l+1}}{\alpha_+ - \alpha_-} \tag{4.18}$$
$$\alpha_\pm = \frac{1}{2}\left(\cos\lambda \pm \sqrt{\cos^2\lambda + \left(\frac{4\epsilon}{4+\epsilon^2}\right)^2 \sin^2\lambda}\right)$$

The distribution of magnetization can be obtained as the Fourier transform of $\mathcal{G}_{M_l^z}$. M_l^z at $\epsilon = 0$ and $\epsilon \to \infty$ has the binomial distribution $P(M) = C^l_{(l+M)/2}$ (where $C^a_b = \frac{a!}{b!(a-b)!}$ are binomial coefficients) as expected for uncorrelated spins in the infinite-temperature ensemble. At $\epsilon = 2$, the distribution is given as $P(M) = C^{2l+2}_{l+1-M}$ where $\{M\}$ is the set of eigenvalues of M_l^z. For general ϵ, the distribution has zero mean and the variance is

$$\mathrm{var}(M_l^z) = (l+1)\frac{8\epsilon^2}{(4+\epsilon^2)^2} - l. \tag{4.19}$$

The generating function along the real counting field λ can be calculated in a similar way. This lets us obtain the SCGF as follows,

$$\Phi_{M_l^z}(\lambda) = \lim_{l\to\infty}\frac{\ln\langle e^{\lambda M_l^z}\rangle}{l} = \ln\frac{1}{2}\left(\cosh\lambda + \sqrt{\cosh^2\lambda - \left(\frac{4\epsilon}{4+\epsilon^2}\right)^2\sinh^2\lambda}\right) \tag{4.20}$$

suggesting that the distribution satisfies the large deviation principle i.e. $P(m) \approx e^{-lI(m)}$ where $I(m)$ is the large deviation rate function and $m = M_l^z/l$ is the magnetization density. The rate function $I_\epsilon(m)$ of the magnetization density can be obtained through a Legendre transformation of Φ (assuming Gärtner-Ellis theorem[12, 13]). The rate function can be explicitly computed at $\epsilon = 0, \infty, 2$:

$$I_{\epsilon=0,\infty}(m) = H((1+m)/2)$$
$$I_{\epsilon=2}(m) = 2H((1+m)/2) - 2H(1/2)$$

where H is the binary entropy function. For general ϵ, the rate function can be obtained by numerical Legendre transformation. The rate function (shown for representative values of ϵ in Fig. 4.4(a)) interpolates between the above two functions for other ϵ. The distribution is qualitatively the same at all ϵ, it is narrowest at $\epsilon = 2$ and broadens on either side of 2.

Staggered magnetization Generating function for the staggered magnetization distribution in a block of $2l$ spins $N_{2l}^z = \sum_{j=x+1}^{x+2l}(-1)^j\sigma_j^z$ can be computed as $\langle T^n V_{en}^l T^n\rangle/Z$ where $V_{en}(\lambda) =$

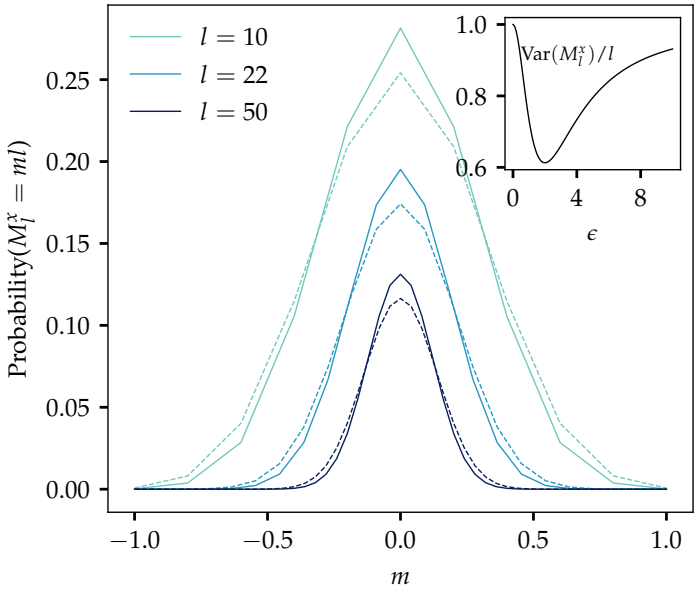

Figure 4.5: Distribution of M_l^x at $\Delta = 0$ for $\epsilon = 1$ (solid line) and 10 (dashed line) The three different colors show different block sizes l. (Inset) Dependence of $\mathrm{Var}(M_l^x)$ on ϵ. $N = 100$.

$V_{ez}(\lambda)V_{ez}(-\lambda)$. This can be explicitly computed to see that the mean is 0 and the variance of the distribution is given by

$$\mathrm{var}(N_l^z) = \left(\frac{4\epsilon}{4+\epsilon^2}\right)^2 (l - 1/2) + 2l \tag{4.21}$$

The SCGF for staggered magnetization can be calculated as the following.

$$\Phi_{N_l^z}(\lambda) = \frac{1}{2}\log\frac{1}{2}\left(\cosh^2(\lambda) + \frac{8\epsilon^2\sinh^2(\lambda)}{(\epsilon^2+4)^2} + \cosh(\lambda)\sqrt{\cosh^2(\lambda) + \frac{16\epsilon^2\sinh^2(\lambda)}{(\epsilon^2+4)^2}}\right) \tag{4.22}$$

The rate function for the staggered magnetization density can be found from numerical Legendre transformation. This is shown in Fig. 4.4(b). The distribution is broadest at $\epsilon = 2$ but narrows for values of ϵ away from this.

Domain wall count: Here, we calculate the distribution of domain wall count as

$$D_l^z = \frac{1}{2}\sum_{j=x+1}^{x+l-1} 1 - \sigma_j^z\sigma_{j+1}^z.$$

in a block of size l. The generating function can be obtained using the MPO form described in Eq. 4.11.

$$\langle e^{\lambda D_l^z}\rangle = e^{\frac{\lambda}{2}l}\frac{\zeta_+ + \zeta_-}{\zeta_+ - \zeta_-}\left(\frac{\zeta_+^{l+1} - \zeta_-^{l+1}}{\zeta_+ + \zeta_-} + \zeta_+^l - \zeta_-^l\right) \tag{4.23}$$

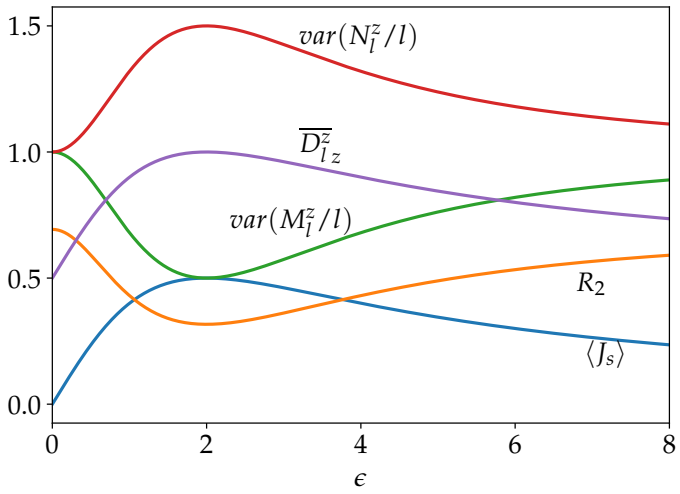

Figure 4.6: Current as a function of the coupling ϵ shown along with bipartite entropy, variance of the distribution of block magnetization, staggered magnetization and mean domain wall count in the XX model.

where l is the number of bonds in the block and

$$\zeta_\pm = \frac{1}{2}\cosh\frac{\lambda}{2} \pm \frac{1}{2}\sqrt{\cosh^2\frac{\lambda}{2} + \left(\frac{4\epsilon}{4+\epsilon^2}\right)^2 \cosh\frac{\lambda}{2}\sinh\frac{\lambda}{2}}$$

The distribution has a mean and variance

$$\begin{aligned} \overline{D_l^z} &= l(1 - \tfrac{4\epsilon}{4+\epsilon^2}) \\ \mathrm{var}(D_l^z) &= \tfrac{1}{8}\left(\tfrac{4\epsilon}{4+\epsilon^2}\right)^4 \left(1 - \tfrac{3l}{2}\right) + l \end{aligned} \tag{4.24}$$

At large-l limit, the SCGF for domain wall count is given by,

$$\Phi_{D_l^z} = \lim_{l\to\infty} \frac{\ln\langle e^{\lambda D_l^z}\rangle}{l} = \ln\zeta_+ \tag{4.25}$$

The rate function for the deviation $D_l^z - \overline{D_l^z}$ is shown in Fig. 4.4(c).

x-Magnetization: The generating function for x-magnetization can also be calculated using transfer matrices but of a larger dimension 4×4. We could not analytically construct powers of these larger transfer matrices and therefore the SCGF could not be obtained in a closed form. However these can be numerically multiplied to obtain the distribution. Figure 4.5 shows the numerically obtained distribution at different values of ϵ. The variance of the distribution is qualitatively similar to that of the z-magnetization. Figure 4.6 summarizes the variance of different local observables discussed in this section.

4.4.2 Bipartite entropy at $\Delta = 0$

Last, we calculate the second Renyi entropy in a system bi-partitioned into N_A and $N_B = N - N_A$ sites, $R_2 = -\frac{1}{N_A}\ln[(\mathrm{Tr}_B[\rho])^2]$ which can also be computed with a generalization of the transfer

matrix method. The entropy per site is given by,

$$R_2 = -\frac{1}{N_A} \ln \frac{\langle 0|\mathbb{X}^{N_A}\mathbb{T}^{N_B}|0\rangle}{\langle 0|\mathbb{T}^{N}|0\rangle}. \tag{4.26}$$

Here, $|0\rangle \equiv |0,0\rangle$. We represent the tensor diagrams necessary to evaluate the expression for R_2 below in Fig.4.7. The figure illustrates calculation of R_2 for the reduced density matrix of first two sites in a system consisting of four sites.

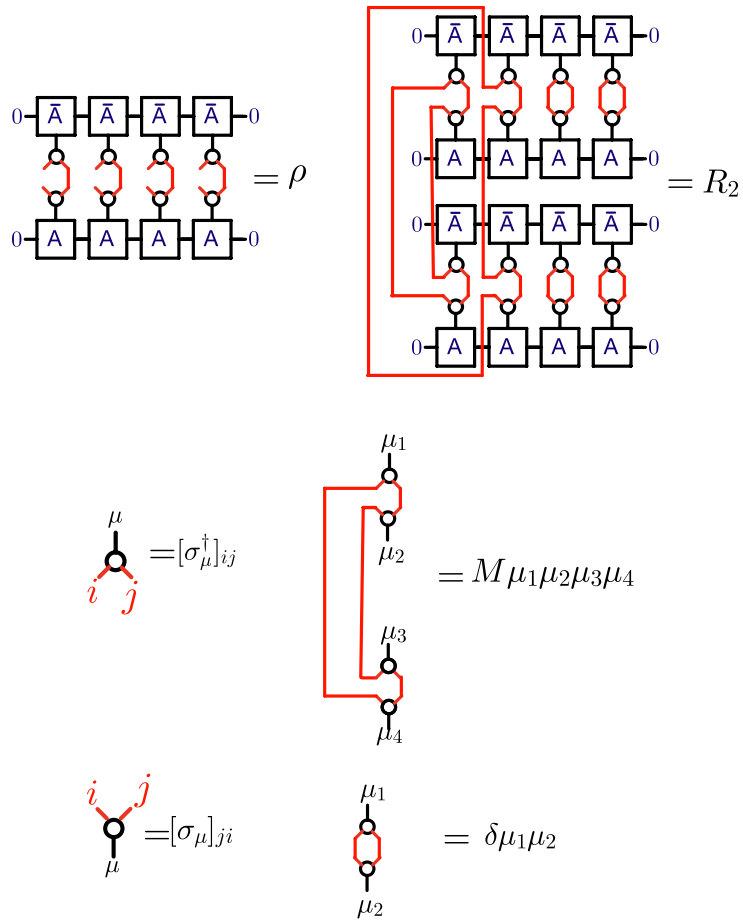

Figure 4.7: The tensor diagrams that are evaluated to obtain Bipartite Renyi entropy. Density matrix ρ in terms of S_N, expression of R_2 and M (see the expression for $\mathbb{X}$) is shown.

The transfer matrices $\mathbb{T}$ and $\mathbb{X}$ act on H_B^4 and can be written as

$$\mathbb{T}^{j_1 j_2 j_3 j_4}_{i_1 i_2 i_3 i_4} = \sum_{\mu_1,\mu_2\in\{\pm 1,0\}} \bar{A}^{i_1 j_1}_{\mu_1} A^{i_2 j_2}_{\mu_1} \bar{A}^{i_3 j_3}_{\mu_2} A^{i_4 j_4}_{\mu_2}$$

and

$$\mathbb{X}^{j_1 j_2 j_3 j_4}_{i_1 i_2 i_3 i_4} = \sum_{\mu_i\in\{\pm 1,0\}} \bar{A}^{i_1 j_1}_{\mu_1} A^{i_2 j_2}_{\mu_2} \bar{A}^{i_3 j_3}_{\mu_3} A^{i_4 j_4}_{\mu_4} M_{\mu_1\mu_2\mu_3\mu_4}$$

where $M \equiv \mathrm{Tr}[\sigma^\dagger_{\mu_1}\sigma_{\mu_2}\sigma^\dagger_{\mu_3}\sigma_{\mu_4}]$. For the case of the XX model this can be evaluated explicitly by substituting exact form of 2×2 A matrices (presented in Sec.4.4) in the expressions of $\mathbb{T}, \mathbb{X}$,

$$\lim_{n_A\to\infty} R_2(\Delta = 0) = -\ln \frac{1+\theta^2/2+\sqrt{1+\theta^2}}{4}, \text{ where } \theta = \frac{4\epsilon}{4+\epsilon^2}. \tag{4.27}$$

Discussion

Spin current as a function of ϵ shows a peak value at $\epsilon = 2$ (Fig. 4.6). The variance of block magnetization as well as entropy per site also shows a minimum at the same point. The domain wall count and staggered magnetization shows a maximum at this point. The ϵ dependencies of the means, variances, distributions, rate functions, correlations, and the entropy found in the previous sections occur through combination $2\epsilon/(4+\epsilon^2)$ which is also the expectation value of spin current. The current is same at two different bath couplings ϵ and $4/\epsilon$. The physical quantities mentioned in the previous sections are the same at these two values of the couplings. This suggests that the state of the system deep in the bulk is determined by the current.

The eigenstates of the current operator on a bond are given by $|\uparrow\uparrow\rangle$, $|\downarrow\downarrow\rangle$, $|\downarrow\uparrow\rangle \pm \imath|\uparrow\downarrow\rangle$ wherein the first two has eigenvalue 0 while the last two have eigenvalues $\pm J$ i.e they carry spin current in opposite directions. The maximum value of the NESS current injected through the chain using the boundary coupling is however only $\langle J^s\rangle = J/2$ which is less than the largest eigenvalue of the current.

The two site density matrix of the state can be explicitly computed using the two site correlators. We find that the two site density matrix is diagonal in the eigenbasis of the current. Population of the space of fixed current eigenvalues are ($J_s = 0$ subspace is 2 dimensional)

$$\begin{aligned} p(J^s = 0) &= \tfrac{1-\langle J^s\rangle^2}{2}, \\ p(J^s = \pm J) &= \tfrac{1+\langle J^s\rangle^2}{4} \pm \tfrac{\langle J^s\rangle}{2}. \end{aligned}$$

It can be checked that this is the maximum entropy two-site state with fixed $\langle J^s\rangle$.

The states with higher current have higher populations of the two current carrying eigenstates. These two-sites states have antiferromagnetic correlations. This current induced short range antiferromagnetic correlation provides a qualitative picture for the higher domain wall count, broader staggered magnetization distribution and narrow magnetization distribution when the current is higher.

4.5 Results for $\Delta \neq 0$

4.5.1 Symmetry transformations

We can infer several features of the NESS from the transformation properties of $\mathcal{L}$ and the uniqueness of the NESS. We begin by considering some simple transformations of the Liouvillian.

The unitary transformation u that rotates the spins on alternate sites $1, 3, \ldots$ by π around the z axis maps the Hamiltonian $H(J, \Delta)$ to $H(-J, -\Delta)$. The jump operators ($\sim \sigma^{\pm}$) may pick up a sign but the dissipators $\mathcal{D}_{1,n}$, being quadratic in the jump operators, are invariant. So $\mathcal{L}(J, \Delta)$ transforms to $\mathcal{L}(-J, -\Delta)$ under u. From uniqueness of the NESS we conclude that steady state at parameters $-J, -\Delta$ can be obtained from those at J, Δ by

$$\rho_\infty(-J, -\Delta) = u\rho_\infty(J, \Delta)u^\dagger.$$

From the definition of $\mathcal{L}$ in Eq. 4.1 it is easy to check that $(\mathcal{L}_{J,\Delta}[\rho])^* = \mathcal{L}_{-J,\Delta}[\rho^*]$ in the z

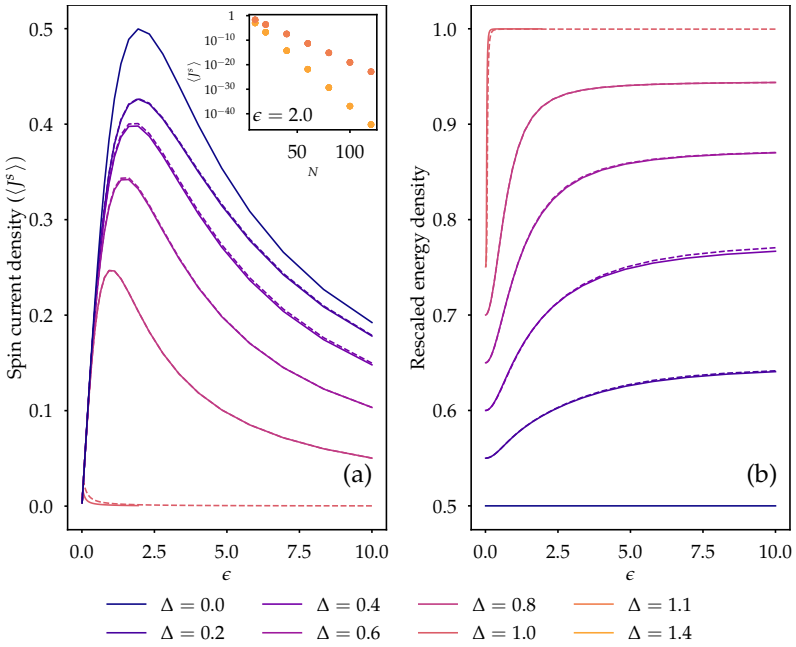

Figure 4.8: (a) Expectation value of spin current as a function of ϵ at different Δ. The solid lines and dotted lines are for system sizes $N = 100, 60$ respectively. (inset) Variation of current in the insulating regime ($\Delta > 1$) with system size N for two systems at $\Delta = 1.1, 1.4$ at $\epsilon = 2$. The scale is semi-log i.e. demonstrates $\langle J^s \rangle \propto e^{-cN}$ where c depends on Δ. (b) Rescaled energy density at the center as a function of ϵ. y-axis shows $(h^{NESS}_{j,j+1} - h^{gs}_{j,j+1})/B$ where h^{gs} is the ground state of the bond Hamiltonian and B is the bandwidth of the energy spectrum. j is taken to be the center of the chain for $\Delta < 1$ and $j \sim N/4$ for $\Delta > 1$.

basis. This implies that

$$\rho_\infty(-J, \Delta) = \rho^*_\infty(J, \Delta).$$

Last, we consider unitary transformation $U = \mathcal{I}u_x$ where $\mathcal{I}$ is spatial inversion and u_x is a π rotation of all spins about the x axis (which changes the sign of σ_z and σ_y) . The Liouvillian is invariant under this transformation as u_x keeps H invariant but interchanges the σ^+ and σ^- thereby interchanging the left and right jump operators; the latter is undone by $\mathcal{I}$. Assuming uniqueness of ρ_∞, it is also invariant under U.

The first two results imply that spin profile $\langle S_z \rangle$ is invariant under changes in signs of J and/or Δ. For a block of spins in the center of the chain, the last result implies that the generating function $\mathcal{G}^z(\lambda)$ in a block at the center of the chain is an even function of λ. This implies that the distribution of magnetization and the rate function $W(m = M_z/l)$ are even functions.

The spin current is given by $J^S = \imath J(\sigma^+_j \sigma^-_{j+1} - \sigma^-_j \sigma^+_{j+1})$. The first two transformation properties of the NESS imply that J^S is even under change of sign of J and/or Δ. Similarly, the first two properties imply that expectation value of the energy density h (Eq. 4.2) changes sign when sign of J or Δ is changed. They also imply that x-magnetization and staggered magnetization interchange roles under change of sign of Δ.

It can also be shown that the energy current J_E at the center of the chain changes sign under the symmetry U of the density matrix, so it has zero expectation value throughout the chain.

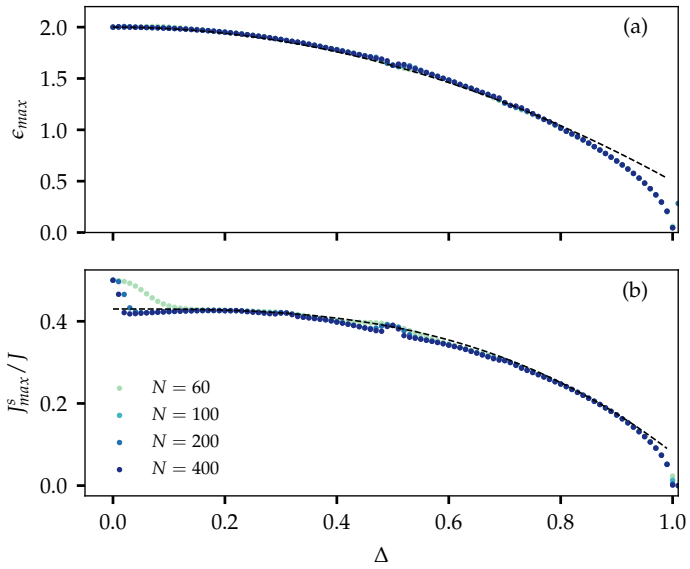

Figure 4.9: (a) ϵ corresponding to the maximum of the spin current as a function of Δ. (b) Peak current as a function of Δ. Dotted black lines show the quadratic (panel (a)) and cubic (panel (b)) fits. Different colors denote different system sizes. Black dotted lines are quadratic(cubic) fit to data in panel a(b). (as discussed in main text)

4.5.2 Expectation value of spin current and energy

Like the case of $\Delta = 0$, spin current as a function of ϵ has a maximum at some $\epsilon_{\max}$ (Fig. 4.8 (a)). For fixed ϵ current decreases with Δ. At small ϵ, the current is $\epsilon/2$, independent of Δ. Current is system size N independent for $\Delta < 1$, decays exponentially with N for $\Delta > 1$ (Fig. 4.8 (a) inset). At $\Delta = 1$, the current decays as $1/N^2$ [11]. At large ϵ, the current decays as $1/\epsilon$ at $\Delta = 0$ (Eq. 4.17) and $\Delta = 1$.

The coupling at peak current is $\epsilon_{\max} = 2$ at $\Delta = 0$ and decreases to $\epsilon_{\max} = 0$ as Δ increases to 1 (Fig. 4.9(a)). We empirically find this to be closely approximated by $\epsilon_{\max} \approx 2 - 3\Delta^2/2$. The peak current shows a discontinuous jump from $\max[J^s] = J/2$ to a smaller value as Δ changes from 0. The discontinuity appears to be smoothened by the finite size effect. For $\Delta > 0$, we empirically find that the peak current is well approximated by $\max[J^s] = 0.43 - 0.35\Delta^3$ till Δ close to 1.

Energy current is exactly 0 due to the symmetries discussed in the previous section. Energy density is a constant deep in the bulk for $0 < \Delta < 1$. This bulk value increases monotonically with ϵ and Δ as shown in Fig. 4.8(b).

4.5.3 Entropy

Numerically obtained values of entropy per site in a bipartitite system with equal halves is shown in Fig. 4.10. The entropy is $\ln 2$ for $\epsilon = 0$ and $\epsilon = \infty$ representing an infinite temperature state at $\Delta = 0$. This appears to hold for small Δ as well in finite size calculations. The bipartite Renyi entropy (R_2) decreases with ϵ initially till some $\epsilon_{\min}^{\text{entropy}}(\Delta)$ and then increases at larger ϵ. Entropy decrease with Δ until $\Delta = 1$, after which the spins are nearly maximally polarized and

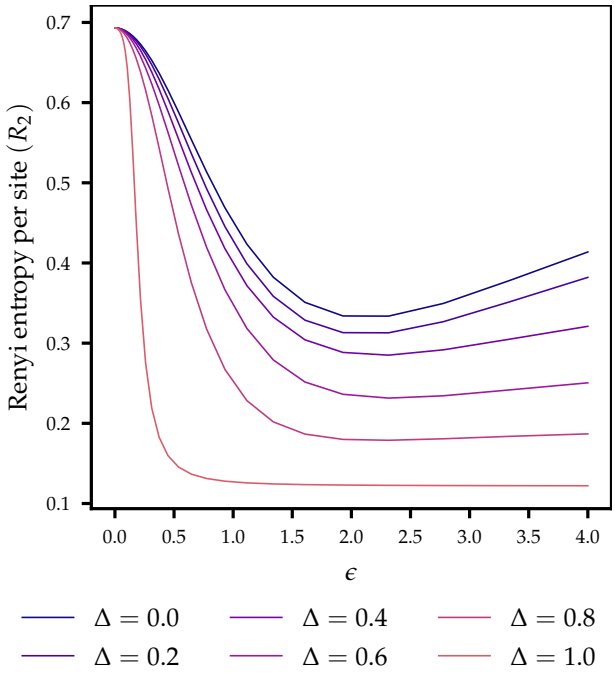

Figure 4.10: Bipartite Renyi Entropy per site (R_2) as a function of ϵ for different values of Δ. $N = 20$ and $N_A = 10$.

have $R_2 \approx 0$.

Qualitative features for the von Neumann entropy of small subsystems of size 4 showed similar features. Entropy is lower at the ends and higher in the bulk. Unlike the case of $\Delta = 0$, the minimum of the entropy as a function of ϵ does not coincide with current maximum.

4.5.4 Spin correlations

Figure 4.11(a) shows the connected correlator between the z components of the spins at the center and other sites. Qualitative properties of the z-correlations remain the same as that in $\Delta = 0$, adjacent sites are anti-correlated but correlations at larger distance remain weak even at larger Δ and ϵ.

Figure 4.11(b) shows the representative examples of correlations between the x-components of the spins. $\langle \sigma_i^x \sigma_{\frac{N}{2}}^x \rangle$ is short ranged but stronger than $\langle \sigma_i^z \sigma_{\frac{N}{2}}^z \rangle$. It is oscillatory with an envelop rapidly decaying with distance. x-correlations appear stronger at larger Δ and ϵ. In the limit of large N, correlation lengths show strong discontinuous Δ dependence, and are consistent with the eigenvalues of the transfer matrix. The correlations are primarily short ranged. However, asymptotic tails containing small amplitude correlations that decay slowly with distance are present.

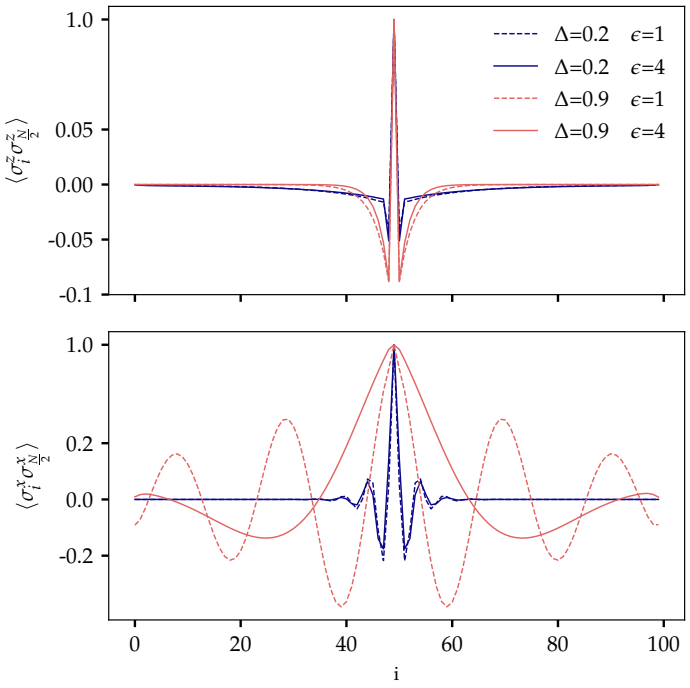

Figure 4.11: Representative examples of the equal time correlation of the spin at the center of the chain with other spins as a function of position(i) . $\langle \sigma_i^z \sigma_{\frac{N}{2}}^z \rangle$ (panel (a)) and $\langle \sigma_i^x \sigma_{\frac{N}{2}}^x \rangle$ (panel (b)) for different values of Δ and ϵ. Solid and dashed lines denote $\epsilon = 4$ and 1 respectively.

4.5.5 Scaled cumulant generating function and rate function for magnetization

In this section, we present the SCGF and rate function (also referred to as large deviation function(LDF)) for the magnetization density $m = M_l^z/l$. This characterizes the magnetization distribution in a block of l sites in the middle of a chain of length $N = 2n + l$ where n denotes the chain length outside the block of interest on both sides. The SCGF $\phi_{M_l^z}(\lambda)$ is calculated as $\frac{1}{l} \ln\langle e^{\lambda M_l^z} \rangle$ for real valued λ. Unlike the $\Delta = 0$ case, the SCGF cannot be analytically calculated. However, we can compute the SCGF in a numerically exact way using the transfer matrix approach (Sec. 4.4). The large deviation function can be calculated in principle by Legendre transformation after taking $N \to \infty$ (this is equivalent to $n \to \infty$) followed by $l \to \infty$ limit on SCGF. We choose Δ values such that $\omega = \arccos \Delta$ is a rational multiple of π i.e $\omega = \frac{p}{q}\pi$ where p, q are co-prime integers. For these cases, we can access the asymptotic-N, l behavior of the SCGF. Accessing asymptotic-N limit is not possible for generic Δ as the transfer matrices have infinite dimesion in those cases when $N \to \infty$. We focus on the $\omega = \frac{p}{q}\pi$ cases in the rest of this section.

The probability distribution $P(m)$ of local observables like M_l^z can also be obtained directly as the inverse Fourier transform of the imaginary field SCGF $\phi_{M_l^z}(\imath\lambda) = \frac{1}{l} \ln\langle e^{\imath\lambda M_l^z} \rangle$ for finite systems. The rate function can then be computed as $-\frac{1}{l} \ln \frac{P(m)}{P(0)}$. The probability of large deviations from mean value of magnetization becomes exponentially suppressed for large l, requiring numerically expensive high-precision calculations. We present a comparison between this approach and the rate function estimated from Legendre transform in Appendix 4.B demonstrating the equivalence

of both approaches in systems as large as $l = 280$ and $N = 400$.

In the remainder of this section, we exclusively present the results for the rate function estimates obtained from the numerical Legendre transform of SCGF. We present the data for $\epsilon = 0.1, 1.0$ and 10.0 as demonstrative cases.

The finite-size SCGF is calculated for the steady state as follows,

$$\phi_{M_l^z}(\lambda, l, N) = \frac{1}{l} \ln \mathrm{Tr}(\rho_\infty e^{\lambda \sum_{k=1}^{l} \sigma_z^k}) \tag{4.28}$$

which can be evaluated using the transfer matrix approaches in Sec. 4.3.3. It can be inferred by looking at the elements of transfer matrix (See Appendix 4.A.1) and MPO representation of the generating function that the corresponding matrices get truncated to the dimension q for $\Delta = \cos(p\pi/q)$. This allows us to get asymptotic behavior of SCGF and rate function in a numerically exact way. The transfer matrix, T has a spectral decomposition $T = \sum_{i=1}^{q} t_i \mathcal{T}_{i,R} \mathcal{T}_{i,L}^T$ where $t_i, \mathcal{T}_{i,R}, \mathcal{T}_{i,L}$ are i-th eigenvalue, corresponding right and left eigenvectors of T respectively.

To compute SCGF, we need the transfer matrix corresponding to $e^{\lambda M_l^z}$ as well. We represent it as U which has the following expression.

$$U(\lambda) = \sum_{r=0}^{\infty} e^{-\lambda} |a_r^+|^2 |r\rangle\langle r+1| + e^{\lambda} |a_r^-|^2 |r+1\rangle\langle r| + 2\cosh(\lambda) |a_r^0|^2 |r\rangle\langle r| \tag{4.29}$$

Equation 4.28 can be expanded as,

$$\phi_{M_l^z}(\lambda, l, N) = \frac{1}{l} \ln \frac{\langle 0|T^n U^l T^n|0\rangle}{\langle 0|T^{2n+l}|0\rangle} \tag{4.30}$$

where we have assumed the system has $N = 2n + l$ sites in total and observables are calculated in a block of length l in the middle of the chain. In the $n \to \infty$ limit with finite l, this further simplifies to

$$\phi_{M_l^z}(\lambda, l, \infty) = \lim_{N\to\infty} \phi_{M_l^z}(\lambda, l, N) = \frac{1}{l} \ln \frac{\mathcal{T}_{1,L}^T U^l \mathcal{T}_{1,R}}{\mathcal{T}_{1,L}^T \mathcal{T}_{1,R}} \left(\frac{1}{t_1}\right)^l. \tag{4.31}$$

$\mathcal{T}_{1,R}, \mathcal{T}_{1,L}^T$ and t_1 are dominant right and left eigenvectors and corresponding eigenvalue of T respectively. By considering a similar spectral decomposition of $U = \sum_{i=1}^{q} u_i \mathcal{U}_{i,R} \mathcal{U}_{i,L}^T$, we can obtain the asymptotic N, l limit of SCGF,$\Phi_{M_l^z}(\lambda)$. We have numerically verified that for all the cases studied here, the spectral gap between two dominant eigenvalues of T and U is finite which justifies the following expressions. The spectral gap goes down as $\Delta \to 1$. (see Appendix 4.C),

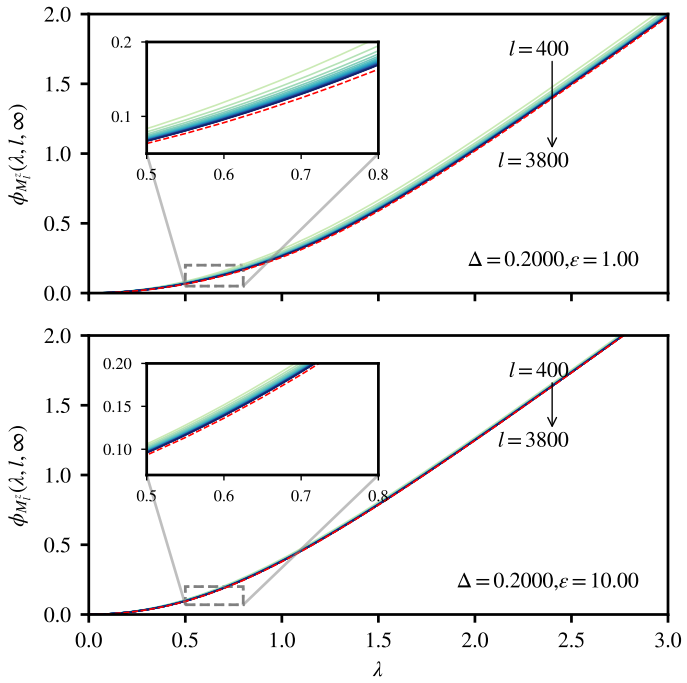

Figure 4.12: The SCGF numerically estimated for finite l and $N \to \infty$ for $\Delta = \cos(17\pi/39) \approx 0.2$ and $\epsilon \in [1.0, 10.0]$. Insets show the zoomed in regions. The color grading goes from light green ($l = 400$)) to blue ($l = 3800$) in step of 400. The red dotted line indicates SCGF at $l \to \infty$ obtained using Eq. 4.31.

$$\Phi_{M_l^z}(\lambda) = \phi_{M_l^z}(\lambda, \infty, \infty) = \lim_{l\to\infty} \phi_{M_l^z}(\lambda, l, \infty) = \lim_{l\to\infty} \frac{1}{l} \ln \frac{(\mathcal{T}_{1,L}^T \mathcal{U}_{1,R})(\mathcal{U}_{1,L}^T \mathcal{T}_{1,R})}{(\mathcal{T}_{1,L}^T \mathcal{T}_{1,R})(\mathcal{U}_{1,L}^T \mathcal{U}_{1,R})} \left(\frac{u_1}{t_1}\right)^l = \ln \frac{u_1}{t_1}$$

Expanding $\Phi_{M_l^z}(\lambda)$ up to second order in λ we can obtain the asymptotic-N, l variance. This will be discussed in the next subsection. Subsequently, leading order finite-l correction to $\phi_{M_l^z}(\lambda, \infty, \infty)$ can be estimated by expanding Eq. 4.31,

$$\phi_{M_l^z}(\lambda, l, \infty) - \Phi_{M_l^z}(\lambda) = \frac{1}{l} \ln \left(1 + \alpha \left(\frac{u_2}{u_1}\right)^l\right) + \text{subleading terms}, \tag{4.32}$$

where $\alpha = \frac{(\mathcal{T}_{1,L}^T \mathcal{U}_{2,R})(\mathcal{U}_{2,L}^T \mathcal{T}_{1,R})}{(\mathcal{T}_{1,L}^T \mathcal{U}_{1,R})(\mathcal{U}_{1,L}^T \mathcal{T}_{1,R})}$. This suggests that SCGF approaches the asymptotic-l value $\Phi_{M_l^z}(\lambda)$ as $\frac{C_1}{l} e^{-C_2 l}$ where C_1 and C_2 depends on Δ, ϵ and counting field λ i.e l dependence of SCGF is asymptotically exponential.

We present the SCGF obtained for finite-l and its asymptotic-l behavior in Fig. 4.12 for $\Delta = \cos(17\pi/39) \approx 0.2$ and $N \to \infty$. The finite-l SCGF is obtained using Eq. 4.31. The finite-size effect is largest at intermediate ϵ.

We show the convergence of SCGF to its asymptotic-l value in Fig. 4.13 for two values of counting field λ at multiple ϵ, Δ. The deviation from asymptotic limit of SCGF due to finite l is almost entirely captured by the first order terms in Eq. 4.32 (shown using solid lines in Fig. 4.13).

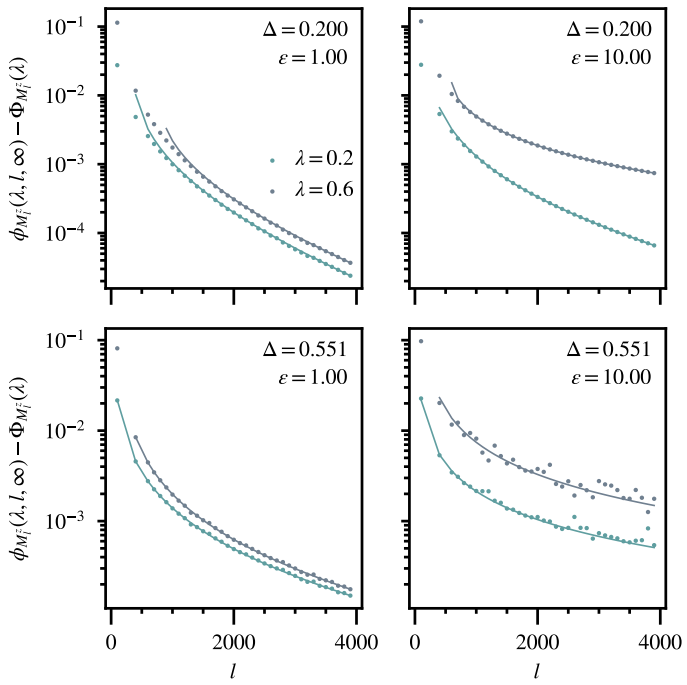

Figure 4.13: The first order correction to asymptotic SCGF as a function of blocksize l at $N \to \infty$. We represent the data for $\Delta = \cos(17\pi/39) \approx 0.2$ (top panel) and $\Delta = \cos(11\pi/35) \approx 0.551$ (bottom panel) . The dots denote the difference of finite-l SCGF from its asymptotic limit. The solid lines indicate the leading order correction obtained from Eq. 4.32. The data shows two values of counting field ,$\lambda = 0.2$ and 0.6.

The decay constant C_2 depends on the gap between the lowest two eigenvalues u_2, u_1. For Δ of the form $\cos\frac{p}{q}\pi$, the gap is shown as a function of Δ in Fig. 4.18 in Appendix 4.C. The gap decreases with p and q. This implies that even if p/q and p'/q' are arbitrarily close to each other, if p', q' are larger than p, q, then their gaps will differ. Thus the gap is a highly discontinuous function of Δ.

From the SCGF, we can then obtain a finite-size estimate of the rate function $I(m, l, N)$ using a Legendre transform of the SCGF (assuming Gärtner-Ellis theorem[12, 13]),

$$I(m, l, N) = \sup_{\lambda \in \mathcal{R}} \{\lambda m - \phi_{M_l^z}(\lambda, l, N)\} \tag{4.33}$$

Figure 4.14 shows the convergence of finite-l estimate of the rate function for average magnetization $m = M_l^z/l$ in a block of size $l(400 \leq l \leq 3800)$ for multiple ϵ values in the $n \to \infty$ limit. The finite-size effect in the estimate of SCGF is expected to show up in rate function estimate as well. This can be clearly seen in the inset. Note that the finite-l effect is minimal at small ϵ regime, grows in intermediate ϵ and is suppressed in large ϵ.

Finally, to complete the discussion, we study the finite-N effect in rate function and its scaling properties in Appendix 4.D.

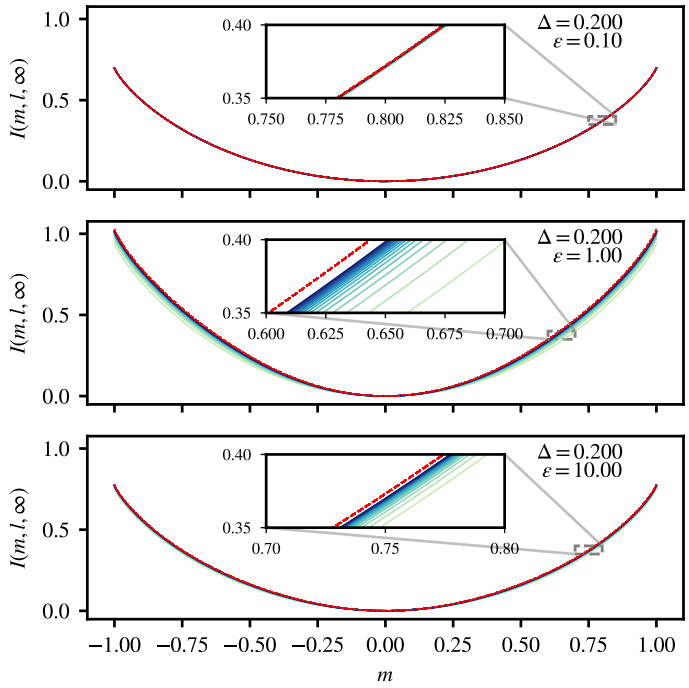

Figure 4.14: The rate function corresponding to the distribution of the average magnetization $m = M_z/l = \sum \sigma_z/l$ in a block of size l for NESS at $\Delta = \cos(17\pi/39) \approx 0.2$ and $\epsilon = 0.1, 1.0$ and 10.0 at $N \to \infty$. Different lines represent different l. The color grading goes from light green ($l = 400$)) to blue ($l = 3800$) in step of 400. The red dotted line is the asymptotic large-l rate function obtained from Legendre transformation of Eq. 4.31. (Inset) The zoomed in view of the main figure at extreme m.

4.5.6 Properties of magnetization distribution

In this section, we look at the distribution of transverse magnetization in the block. This calculation cannot be performed in large systems as the transfer matrices cannot be restricted to the charge $Q = 0$ block of the bond Hilbert space. Nevertheless explicit calculation can be performed in smaller systems.

Figure 4.15 shows the distribution of $M_l^x = \sum_{i=1}^{l} \sigma_i^x$ in a block of size l in the middle of a chain of $N = 100$ sites for different values of ϵ and Δ. At large values of $\Delta > 0.9$ the distribution shows a double peak structure in small block sizes, which merges into a single peak in larger blocks. This suggests a short range ferromagnetic ordering at large Δ for σ^x. The ordering is stronger - they persist to larger blocks - as ϵ increases. Similar short range ordering was observed in the ground state of XXZ chain at large Δ [188]. At $\Delta < 0.9$ no double peak structure was observed.

When Δ is negative, from symmetry considerations (See Sec:4.5.1), we see that this short range x order is antiferromagnetic in nature.

Finally, we discuss the trend of variance of M_l^z with $\langle J^s \rangle$. It can be expressed as follows,

$$\mathrm{var}(M_\mathrm{l}^\mathrm{z}) = \mathrm{Tr}(\rho_\infty (M_\mathrm{l}^\mathrm{z})^2) - (\mathrm{Tr}(\rho_\infty M_\mathrm{l}^\mathrm{z}))^2 \tag{4.34}$$

The second term (i,e. mean z-magnetization) in the expression for variance is 0 for $\Delta < 1$. In this case as well, we can study the asymptotic-N, l behavior at $\omega = p\pi/q$ points i.e rational

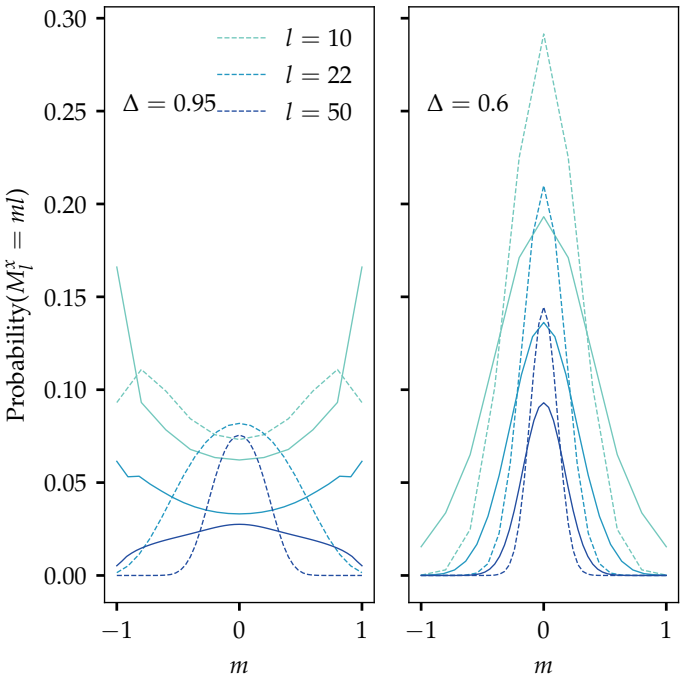

Figure 4.15: Distribution of M_l^x. (a) $\Delta = 0.95$ for $\epsilon = 1$(dashed lines) and 4 (solid lines). (b) $\Delta = 0.6$ for $\epsilon = 1$(dashed lines) and 4 (solid lines). Legend shows the blocksizes (l) studied.

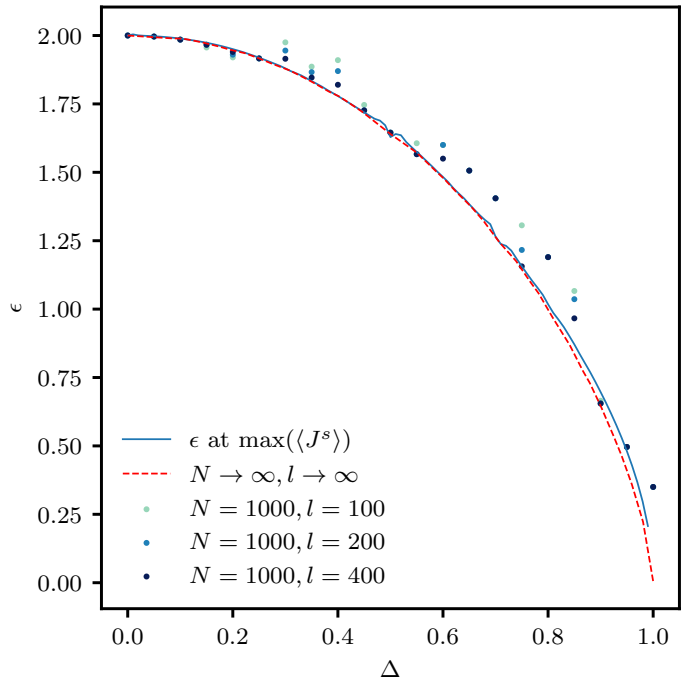

Figure 4.16: Comparison of ϵ values where $\langle J^s \rangle$ attains maximum (solid blue line) and var(M_l^z) attains minimum. The solid blue line represents the ϵ where $\langle J^s \rangle$ is maximum. The dashed red line shows the ϵ where var(M_l^z) is minimum at asymptotic-l, N limit. The dots are from the variance obtained in finite size calculation.

multiple of π. Equation 4.34 evaluates to the following in asymptotic-N, l limit,

$$\lim_{l\to\infty}\lim_{N\to\infty} \mathrm{var}(\mathrm{M}_\mathrm{l}^\mathrm{z}) = \frac{(\mathcal{T}_{1,\mathrm{L}}^{\mathrm{T}}\, T_{\mathrm{diag}}\mathcal{T}_{1,\mathrm{R}})}{(\mathcal{T}_{1,\mathrm{L}}^{\mathrm{T}}\mathcal{T}_{1,\mathrm{R}})t_l} \tag{4.35}$$

where T_{diag} denotes the diagonal part of of transfer matrix, T. This can be obtained from expansion of Eq. 4.31 and keeping the $O(\lambda^2)$ term. We present data for finite-N, l by taking numerical second derivative of Eq. 4.30 with λ. The data is presented in Fig. 4.16. We also present the asymptotic-N, l behavior of variance with the dashed red line (Eq. 4.35).

We observe that the ϵ at minimum of var(M_l^z) overlaps with ϵ where maximum of $\langle J^s\rangle$ is attained at asymptotic limit. The ϵ at minimum of var(M_l^z) deviates from the ϵ at max$(\langle J^s\rangle)$ for finite size calculations. This observation further supports the effect of correlation induced by spin current in the bulk for finite Δ.

4.6 Conclusion

In this chapter, we have characterized the current carrying NESS of an XXZ model with maximally polarizing Lindblad couplings at the boundary by calculating the spin correlations and full distribution of the spin densities. The calculation of the full distribution function which in general requires accurate information about the steady state is made possible by the exact solution of the NESS in a MPS form [11]. The state carries a current that can be tuned via the strength of the coupling to the bath ϵ. The current initially increases and then decreases as ϵ is increased from 0. Bulk properties such as the correlations, distribution of observables and the entropy in the steady state are determined by both the Hamiltonian parameters and the current in the system. Though the MPS form does not yield closed form expressions in general, calculations of correlations and distribution functions are reduced to multiplications of transfer matrices of dimensions at most linear in the system size enabling numerically exact calculations.

The NESS in the $\Delta = 0$ case corresponding to the XX model has an especially simple 2×2 transfer matrix; and we can get exact closed form expressions for various quantities such as spin-spin correlations in the XY plane and along z directions, entropy per site etc. The scaled cumulant generating functions of magnetization, staggered magnetization and domain wall densities in the z-direction can also be calculated exactly allowing explicit demonstration of the large deviation principle. These also allow numerically exact calculation of rate functions using numerical Legendre transforms. The rate functions do not show any indication of a singularity as a function of the current or ϵ. At least at the level of the two site density matrix, the state is described by a maximal entropy ensemble with a constraint on its spin current expectation value. The various physical quantities that we studied, namely the entropy density, spin correlators and distributions (of z-magnetizations, staggered magnetizations, domain wall count) depends on the ϵ only through the current expectation value $J \propto= \frac{2\epsilon}{4+\epsilon^2}$. The variances of the distributions show an extremum when the current is maximized as a function of the boundary coupling constant. In particular, the z-magnetization shows a minimum variance when the current is maximized. This can be qualitatively understood from the increased population of the antiferromagnetic two site states as the current is increased. This results in a reduction of the probability of occurrence

of large-magnetization states, and therefore, in a narrower z-magnetization distribution.

All magnetization distribution functions in the XX model are qualitatively similar to that of the infinite temperature ensemble as a result of the short range spin correlations in the NESS. This chapter explored only the case where spin-chemical-potential μ at the ends are maximal (± 1) and when the dynamics has an exact $U(1)$ rotation symmetry about the z-axis. Using a fermionic representation of the spins, different from what has been used here, the NESS in the XY model can be studied at $|\mu| \neq 1$. These are known to exhibit unusual nonequilibrium phase transitions [184, 203]. It will be interesting to see if and how these phase transitions impact the full distributions. We leave this for future investigations.

Using the MPS solution, we could obtain numerically exact calculations for systems at finite Δ as well. We obtain the rate function at asymptotic limit for cases where $\Delta = \cos(\omega)$ with $\omega = p\pi/q$ and present a detailed analysis on convergence with blocksize. The results for these satisfy the large deviation principle for local observables in an interacting strongly driven quantum system. We find that finite block-size corrections in the rate function estimation are higher at the intermediate ϵ when the current is maximal. We find that narrowing of the z-magnetization distribution when the current is maximized happens in the case of $\Delta > 0$ as well. Surprisingly, the exponential decay rate of approach to the asymptotic form of the SCGF is a strongly discontinuous function Δ, with the decay rate vanishing as p, q increase. This suggests that for irrational values of ω, the finite block-size effect will be much stronger, it is unclear from our calculations if these satisfy large deviation principle.

The x-magnetization distribution in large systems show qualitatively similar behavior to the z-magnetization possibly due, again, to weak long range correlations. However at large $\Delta \gtrapprox 0.9$ and large ϵ, the x-distributions show a prominent double peak structure in small blocks indicating short range ordering in the x-direction, similar to what was described in existing literature on the ground state of the XXZ model [188].

Appendix 4.A Solution to divergence condition

In this Appendix, we find solutions for S_N that satisfy Eq. 4.8 and Eq. 4.7. We first find the algebra of A tensors that solve the conditions and in the subsequent section construct an explicit form of A that solves the algebra.

First we argue that the commutator $[H, S_N]$ is a combination of Pauli strings that each have σ^z on exactly one site. It is sufficient to show this for individual terms of the commutator:

$$[h_{j,j+1}, S_N] = \sum_{\{r_i\}} \langle 0|A_{r_1} \dots A_{r_n}|0\rangle \sigma^{r_1}\sigma^{r_2}\dots\sigma^{r_{j-1}} \left[h_{j,j+1}, \sigma^{r_j}\sigma^{r_{j+1}}\right] \sigma^{r_{j+2}}\dots\sigma^{r_n}$$

We have omitted the tensor product symbols for compactness. The commutator affects only the sites $j, j+1$. From explicit evaluation, it can be seen that the commutator of any of the terms inside $h_{j,j+1}$ namely $\sigma_+^j\sigma_-^{j+1}$, $\sigma_j^-\sigma_{j+1}^+$ or $\sigma_j^z\sigma_{j+1}^z$ with $\sigma^{r_j}\sigma^{r_{j+1}}$ for any $r_j, r_{j+1} \in \{\pm, 0\}$ either vanishes or produces terms that contain exactly one σ^z. Thus $[H, S_N]$ is a linear combination of Pauli strings with σ^z occurring exactly once in each string.

Equation 4.8 demands that among these, only the strings in which σ^z occur at the ends have finite amplitude, which implies that for all sites other than the two ends i.e. for sites $2 \le j \le N-1$ the following is true

$$\mathrm{Tr}\left[\sigma_{j-1}^{a\dagger}\sigma_j^{z\dagger}\sigma_{j+1}^{b\dagger}\left[h_{j-1,j} + h_{j,j+1}, S_N\right]\right] = 0 \text{ for all } a, b \in \{\pm 1, 0\}\,.$$

This is satisfied if

$$\sum_{r_1,r_2,r_3\in\{\pm,0\}} \mathrm{Tr}\left[\sigma^{a\dagger}\sigma^{z\dagger}\sigma^{b\dagger}\left[h_{12}+h_{23}, \sigma^{r_1}\sigma^{r_2}\sigma^{r_3}\right] A_{r_1}A_{r_2}A_{r_3}\right] = 0 \text{ for all } a, b \in \{\pm 1, 0\} \tag{4.36}$$

These nine equations result in eight constraints of the form

$$[A_0, A_\pm A_\mp] = 0 \tag{4.37}$$

$$\{A_0, A_\pm^2\} = 2\Delta A_\pm A_0 A_\pm \tag{4.38}$$

$$\Delta A_0^2 A_\pm - A_0 A_\pm A_0 = A_\mp A_\pm^2 - A_\pm A_\mp A_\pm \tag{4.39}$$

$$\Delta A_\pm A_0^2 - A_0 A_\pm A_0 = A_\pm^2 A_\mp - A_\pm A_\mp A_\pm \tag{4.40}$$

which are equivalent to the constraints given in Eq. 9 of Ref. [11]. The first line is obtained from considering $(a, b) = (2, 3)$ and $(3, 2)$ in Eq. 4.36, second line from $(2, 2)$ and $(3, 3)$, the third line from $(1, 3)$ and $(1, 2)$, and last line from $(3, 1)$ and $(2, 1)$. These constraints eliminate occurrence of σ^z on any site $2 \le i < N$.

Now we consider the terms in $[h_{12}, S_N]$ that contain a σ_z^1. These should be nonvanishing such that the RHS of Eq. 4.8 is reproduced. $[h_{12}, S_N]$ can be explicitly calculated to be

$$\sqrt{2}\sigma_1^z\left[\sigma_2^- M + \sigma_2^+ P + \sigma_2^0 E\right] \times \sum_{r_3,r_4,\dots,r_N} A_{r_3}A_{r_4}\dots A_{r_N}|0\rangle \prod_{i=3}^{N}\sigma^{r_i}$$

where

$$M = \langle 0|A_- A_0 - \Delta\langle 0|A_0 A_-$$
$$P = -\langle 0|A_+ A_0 + \Delta\langle 0|A_0 A_+$$
$$E = \langle 0|A_- A_+ - \langle 0|A_+ A_-$$

To satisfy Eq. 4.8, the above terms should reproduce $\sigma_z L$. Comparing coefficients of $\sigma_\pm, \sigma_0$ on the second site, we see that the commutator correctly produces the $\sigma_z L$, if $P = -\imath\epsilon\langle 0|A_+/\sqrt{2}$, $M = -\imath\epsilon\langle 0|A_-/\sqrt{2}$, and $E = -\imath\epsilon\langle 0|A_0/\sqrt{2}$ are satisfied. These are satisfied if the following conditions are imposed on the A operators:

$$\langle 0|A_0 = \langle 0|\sqrt{2}, \quad \langle 0|A_- = 0, \quad \langle 0|A_+ A_- = \imath\epsilon\langle 0| \tag{4.41}$$

To see that these solve the constraint $P = -\imath\epsilon\langle 0|A_+$, we multiply both sides of Eq. 4.39 by $\langle 0|$ to get

$$\Delta\langle 0|A_0^2 A_+ - \langle 0|A_0 A_+ A_0 = \langle 0|A_- A_+^2 - \langle 0|A_+ A_- A_+$$

This reduces to the desired equation $\sqrt{2}P = -\imath\epsilon\langle 0|A_+$ if Eq. 4.41 are satisfied.

Similar analysis on the right edge gives the following boundary conditions

$$A_0 = \sqrt{2}|0\rangle, \quad A_+|0\rangle = 0, \quad A_+ A_-|0\rangle = \imath\epsilon|0\rangle \tag{4.42}$$

Eq. 4.41, Eq. 4.42 also imply Eq. 4.7.

4.A.1 Finding the matrix elements of A

Now we construct explicit matrix form of the algebra given in Eq. 4.37-4.40 and the boundary conditions Eq. 4.41,4.42 assuming the tridiagonal structure of the solutions shown in Eq. 4.6 of the main text. We do this by writing Eq. 4.37-4.40 and Eq. 4.41,4.42 in terms of $a_\pm$ and a_0. This gives the following conditions on a's

$$a_r^0 + a_{r+2}^0 = 2\Delta a_{r+1}^0 \text{ for } r \geq 0 \tag{4.43}$$
$$2(\Delta a_0^0 - a_1^0)a_0^0 = -a_0^+ a_0^- \tag{4.44}$$
$$2(\Delta a_r^0 - a_{r+1}^0)a_r^0 = a_{r-1}^+ a_{r-1}^- - a_r^+ a_r^- \text{ for } r > 0 \tag{4.45}$$

with the boundary conditions

$$a_0^0 = 1, \quad a_0^- = 1 \quad a_0^+ = \imath\epsilon \tag{4.46}$$

Equations 4.43 and 4.44 along with the boundary conditions have the solution (for $r \geq 0$)

$$a_r^0 = \cos(r\omega) + \imath\epsilon\frac{\sin(r\omega)}{2\sin\omega} \tag{4.47}$$

where we defined ω by $\cos\omega = \Delta$. The recursion relation in Eq. 4.45 allows us to obtain

$$a_r^+ a_r^- = \imath\epsilon - \sum_{s=0}^{r} 2(\Delta a_s^0 - a_{s+1}^0)a_s^0 \tag{4.48}$$

The summation can be performed exactly after plugging in the solution for a_s^0 to get

$$a_r^+ a_r^- = -\left[1 + \frac{\epsilon^2}{4\sin^2\omega}\right]\sin(r\omega)\sin(r\omega+\omega) + \frac{\imath\epsilon}{\sin\omega}\cos(r\omega)\,\sin(r\omega+\omega) \tag{4.49}$$

Solution to these can be chosen to be (for $r \geq 1$)

$$a_r^+ = \frac{\sin(r\omega+\omega)}{\sin\omega}; \quad a_r^- = -\left[1 + \frac{\epsilon^2}{4\sin^2\omega}\right]\sin(r\omega)\sin\omega + \imath\epsilon\cos(r\omega) \tag{4.50}$$

From the expressions for a_r^+ and a_r^-, we can readily observe that $a_r^+ = 0$ or $a_r^+ = 0$ at $r = q$ when $\omega = p/q$ i.e a rational fraction (depending on q being even or odd). This makes it possible to truncate the corresponding transfer matrix to a $q \times q$ block as the the vanishing of a_q^+ prohibits transition from state q to $q+1 \in H_B \times H_B$. We utilize this property in Sec. 4.5.5 in main text.

An alternative solution for coefficients in $A_\pm$ is given in Ref. [11], we have checked extensively that the two produce identical results.

Appendix 4.B Rate function from full distribution

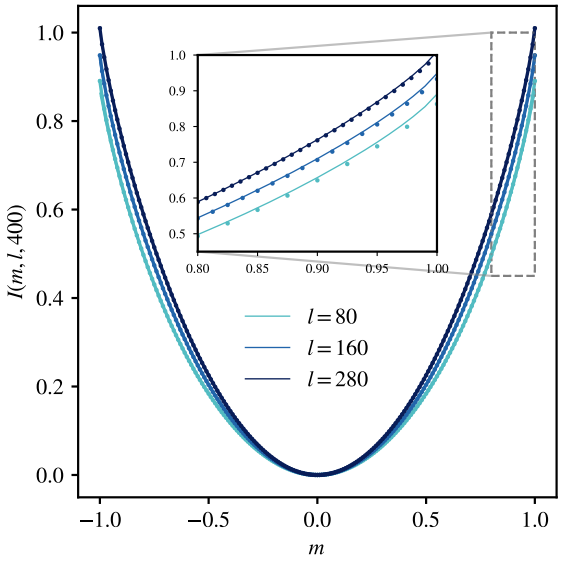

Figure 4.17: Comparison of rate function obtained through Legendre transformation of SCGF (solid lines) and full probability distribution (dots) for a system with $N = 400$ and multiple blocksizes l. The inset shows zoomed in region at the edge. $\Delta = 0.4, \epsilon = 1.0$

In this Appendix, we compare the rate function obtained from Legendre transformation of SCGF to direct estimation of the rate function from the full probability distribution.

$$I(m, l, N) = -\frac{1}{l}\ln\frac{P(m)}{P(0)} \tag{4.51}$$

To obtain the full probability distribution for large blocksize l, we need to utilize high-precision calculation as the probability of extreme magnetization is exponentially suppressed. We compared the rate function estimated through both the Legendre transformation approach and full distribution for $\Delta = 0.4, \epsilon = 1.0$ and a system consisting of $N = 400$ sites in Fig. 4.17. For the full distribution data reported here, we carried out the calculation with a floating point precision of 600 bits (implemented using ArbNumerics library in Julia). The deviation between these two approaches is minimal. The deviation is maximum at the extreme m values (shown in Inset of Fig. 4.17).

Appendix 4.C Ratio of dominant eigenvalues of transfer matrices

In main text, we have shown the leading order correction to asymptotic-N, l SCGF due to finite l in eq. 4.32. For $\Delta = \cos\frac{p}{q}\pi$, for rational values of p/q, convergence to large-l SCGF is exponential in l with the rate of convergence decided by the ratio of first two dominant eigenvalues of U (See Sec. 4.5.5). Figure 4.18 shows the behavior of $\frac{u_2}{u_1}$ for a set of Δ values $\Delta = \cos(p\pi/q)$ where p, q are co-prime integers less than 40. The relative gap $1 - u_2/u_1$ decreases with p as shown in Fig. 4.18(right) and for each value of p, the relative gap decreases with q as shown in Fig. 4.18(left). The ratio goes down as Δ approaches 1, thus a very slow convergence to asymptotic SCGF is expected in the Heisenberg limit suggesting large finite-size effects.

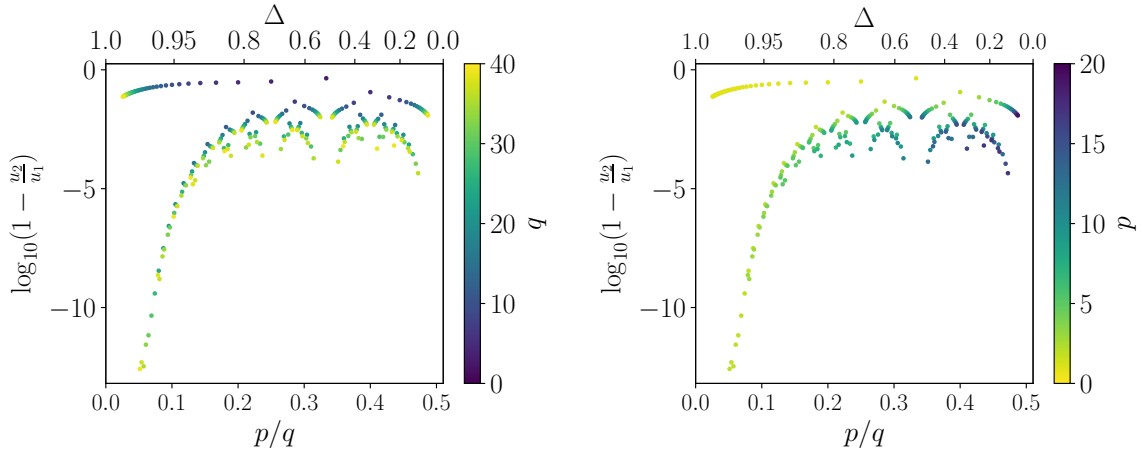

Figure 4.18: Log of deviation of ratio of dominant eigenvalues of transfer matrix from 1 corresponding to $U(\lambda)$ where $\lambda = 0.6$ (See Sec. 4.5.5) and $\epsilon = 1.0$. We look at a set of Δ which can be expressed as $\Delta = \cos(p\pi/q)$ with $q \leq 40$. The left panel has the points colored according to q and the right panel has the points colored according to p. Similar results hold for general values of λ.

Appendix 4.D Finite-N rate function

To investigate the behavior of $I(m, l, N)$ with N, we take an ansatz for the rate function as follows:

$$I(m, l, N) \propto Ae^{-bN} + I(m, l, \infty) \tag{4.52}$$

where $I(m, l, \infty)$ denotes the rate function at fixed l and m with $N \to \infty$. We test the validity of our scaling ansatz by investigating the convergence of $I(m, l, N)$ to large-N asymptotic value, $I(m, l, \infty)$.In Fig. 4.19, we verify our exponential scaling ansatz in Eq. 4.52. The data for $\Delta = 0.2$ and multiple l, ϵ and m is presented in Fig. 4.20. The fitting parameters depend on δ, ϵ and m. The fits clearly support the exponential ansatz for scaling of rate function with N at fixed l.

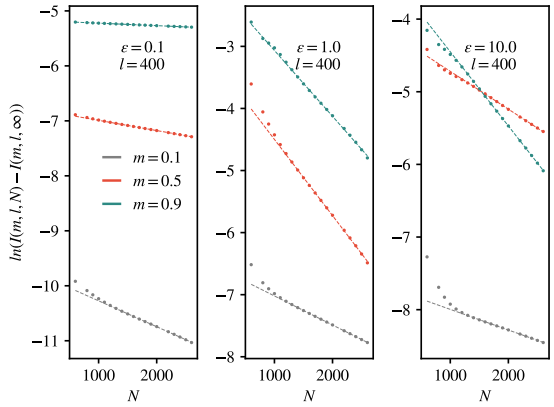

Figure 4.19: Scaling of rate function with N at $l = 400$ for $\Delta = 0.2$ and multiple value of ϵ and m. The dots ar actual value obtained from simulation. The solid lines are fits obtained from Eq. 4.52.

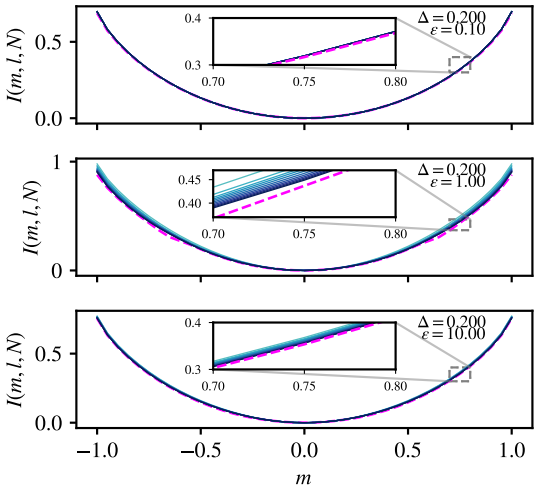

Figure 4.20: The rate function corresponding to the distribution of the average magnetization $m = M_z/l = 1/l \sum \sigma_z$ in a block of size $l = 400$ for NESS at $\Delta = 0.2$ and $\epsilon = 0.1, 1.0$ and 10.0. Different lines represent different N. The color grading goes from light green ($N = 600$)) to blue ($l = 2600$) in step of 200. The magenta dashed line is the asymptotic large-N rate function obtained from Eq. 4.52 at each m. (Inset) The zoomed in view of the main figure at extreme m.

For all cases, exponential convergence to large-N asymptotic value is evident. The exponential convergence holds for all parameter regimes studied at large N (only representative examples are presented here).

5

Projected Ensemble in a system with local conserved charges

THE move from expectation values to full counting statistics made in Sec. 1.6 replaced $\langle \hat{m} \rangle$ with the full distribution $P(m)$ of a single spatially averaged observable, encoded through the rate function $I(m)$. A natural next step is to ask for the joint distribution not of a single observable but of *the full quantum state itself*: given a generic many-body pure state $|\psi_{AB}\rangle$, projective measurement of the bath B in a chosen basis yields a collection of post-measurement pure states on A, each occurring with its Born-rule probability. This *projected ensemble* contains the FCS of every local observable on A as a marginal: once the ensemble is known, the distribution of any $\hat{m}_A$ is obtained by evaluating $\hat{m}_A$ in each conditional state and reweighting. Asking how the projected ensemble itself becomes universal is therefore a strictly stronger demand than asking how any one $P(m)$ becomes thermal. In this chapter we will study this projected ensemble in a system that has an extensive number of locally supported conserved charges and explore how these charges affect the late time projected ensemble.

5.1 Introduction

The study of dynamics of local observables in generic isolated quantum many-body systems show that their expectation values equilibrate to a thermal value due to entanglement between subsystems and their complements. The Eigenstate Thermalization Hypothesis (ETH) [8, 9, 204, 46] formalizes this and relates this to the nature of eigenstates of generic Hamiltonians - reduced density matrices of local subsystems in the eigenstates match thermal ensembles determined by the eigenstate's energy density.

While conventional experiments are able to measure expectation values of local observables, modern quantum devices can make projective measurements of multiple degrees of freedom simultaneously through techniques like single-atom resolved fluorescence [205] blurring the system-

This chapter is adapted from the publication: **Sandipan Manna**, Sthitadhi Roy and G. J. Sreejith, "Projected ensemble in a system with conserved charges with local support," *Phys. Rev. B* **111**, 144302 (2025).

bath distinction [17, 206]. In such settings, the configuration of the entire system (e.g. an array of Rydberg atoms [207]/superconducting qubits [208]) is read out as a classical bitstring, thus capturing information at the level of individual degrees of freedom of the many body system [209, 210, 107, 211]. Statistical information of such repeated measurements enable investigation beyond simple expectation values of local observables described by subsystem density matrices.

These modern experimental capabilities have motivated the notion of a *projected ensemble* [16, 17] – ensemble of pure states on a local subsystem obtained from the outcome of projective measurements on its complement with the latter associating Born rule probabilities to the members of the ensemble. This defines a natural one among all purifications [212] of the subsystem's reduced density matrix. More explicitly, given multiple copies of a pure state $|\psi_{AB}\rangle$ of a system partitioned into A and B, the projected ensemble (PE) denoted as

$$\mathcal{E}_{\text{PE}}(\psi_{AB}) \equiv \{p(b_i),\ \ |\psi_A(b_i)\rangle\}_{b_i\in\mathcal{S}_B}\,, \tag{5.1}$$

is generated by complete set of projective measurements in B on the copies, each yielding a pure state $|\psi_A(b_i)\rangle$ on subsystem A with a probability given as $p(b_i) \equiv \langle\psi^{AB}|(\mathbb{I}_A \otimes |b_i\rangle\langle b_i|)|\psi^{AB}\rangle$ where $\mathcal{S}_B$ is the set of all possible measurement outcomes in B (for example, b_i can be a bitstring for a system of qubits) and $\mathbb{I}_A$ is the identity operator acting on subsystem A.

Conventionally, the ensemble can be characterized by its density matrix

$$\rho_A = \sum_i p_i\, |\psi_A(b_i)\rangle\, \langle\psi_A(b_i)| \equiv \sum_i p_i \rho_A(b_i)\,. \tag{5.2}$$

and contains all information about $\mathcal{E}_{\text{PE}}(\psi_{AB})$ that an external agent can possibly infer by measuring the pure states in the ensemble. The expectation value in the ensemble of a local observable O_A is the first moment of the expectation values of O_A in the states in the ensemble (5.1), or equivalently $\langle O_A\rangle = \sum_i p_i \langle O_A\rangle_{\psi_A(b_i)}$ and is fully determined by the density matrix.

Ensembles on the other hand contain more information in terms of the distributions of the states $|\psi_A(b_i)\rangle$ in the Hilbert space and can be characterized by higher moments of the distribution of states beyond the first moment. In PEs, the external agent can estimate the higher moments if the states $\psi_A(b_i)$ are supplemented with the measurement outcome data b_i.

This has given rise to the concept of *deep thermalization* [16, 213] which is a statement not just about ρ_A but regarding the entire ensemble (5.1) (and therefore arbitrary moments of it) approaching universal ensembles under generic quantum dynamics at late times. For example, in systems without any conservation laws, the PE approaches the Haar ensemble [214, 56] as has been demonstrated in experiments [17]. In systems with global charge conserving dynamics, starting from an atypical state such as a direct product state, the PE relaxes to various limiting ensembles at late time [215]. These limiting ensembles maximize the entropy in the state distribution over the accessible Hilbert space while respecting the conserved charges and constraints of the dynamics, suggesting a generalization of the second law of thermodynamics.

For example, under Hamiltonian dynamics (with energy conservation manifest) the PE approaches the Haar ensemble only when the initial state is at efffective infinite temperature whereas for finite temperatures it approaches the so-called Scrooge ensemble [63, 216] if the measurements in B are uncorrelated with the conserved charges. Correlation of measurement

basis with the conserved charges changes the limiting ensemble from Scrooge [63, 216] to a generalized Scrooge ensemble (GSE) [217] which is a convex combination of multiple Scrooge ensembles.

PE and related ideas have been studied in a variety of systems. The non-interacting free-fermion system was found to approach an ensemble determined by just the conserved charges of initial state [218]. A $U(1)$ charge conserving random unitary circuit was also investigated with focus on the effect of measurement basis [217]. Studies have been carried out in constrained systems [219] as well. In these cases too, it is expected that the general ensemble should be described by a maximum-entropy ensemble on the accessible Hilbert space satisfying the conditions imposed by the conserved charges in the initial state and the effective constraints on dynamics, thus describing a quantum Hilbert space ergodicity. Deterministic driving was also found to lead to the Haar ensemble [220]. In few specific cases such as the random unitary and dual-unitary circuits, PEs are analytically tractable with replica method [221, 222].

While much of the existing studies in this context so far has been on systems with no conservation laws or with global conserved charges, in this chapter, we focus on a system where the conserved charges have local support. And yet, for the late time ensemble of states to be described by universal ensembles, a necessary ingredient is that the systems should equilibrate, albeit to non-thermal ensembles. Many-body localized (MBL) systems [50, 223, 51, 224] represent a class of models which satisfy both the above requirements as they posses an extensive number of locally conserved charges [54, 53, 225, 226] and yet the dynamics shows dephasing resulting in approach to equilibrium [55, 227, 228].

We study the limiting ensembles and their dependence on measurement basis for initial states with finite values of local conserved charges. We observe that in this case, based on the first three moments of the distributions, PEs approach a Scrooge ensemble for any measurement basis in thermodynamic limit except when the measurement basis has a large overlap with the conserved charges.

In chaotic systems, the emergence of the universal ensembles (such as Haar or Scrooge) as the limiting cases for the projected ensembles are intimately connected to universal probability distributions of measurement-outcome probabilities, such as the Porter-Thomas distribution for the Haar ensemble. In our case also, we relate the measurement-basis dependence of the projected ensemble to the probability distribution of measurement-outcome probabilities and their deviations from the Porter-Thomas distribution.

This article is organized as follows. In Sec. 5.2, we give a brief review of projected ensemble and its construction. We also introduce Scrooge ensemble in this section. We numerically demonstrate the convergence of projected ensemble to Scrooge ensemble for a Floquet MBL model in Sec. 5.3. The phenomenological ℓ-bit model and PE constructed under time-evolved states generated with it is described in Sec. 5.4 where numerical results for the convergence of the PE to the Scrooge ensemble is also presented. The emergence of Porter-Thomas distribution in temporal ensemble is investigated in Sec. 5.5. Subsequently, we derive an expression for moments of the PE constructed with time-evolved states under ℓ-bit Hamiltonian in Sec. 5.6. We conclude our discussion in Sec. 5.7 commenting on possible extensions of our result.

5.2 Projected ensemble and Deep thermalization

Let $|\psi_{AB}\rangle \in \mathcal{H}_A \otimes \mathcal{H}_B$ be a pure state of a composite system of $L = L_A + L_B$ qubits (local Hilbert space dimension of 2). Given many copies of $|\psi_{AB}\rangle$, one can perform projective measurements on partition B in a complete orthogonal basis $\{b_h\}_{h\in[1,2^{L_B}]}$ which can be implemented using projectors of the form $\Pi_{b_h} = \mathbb{I}_A \otimes |b_h\rangle\langle b_h|$. Each measurement will produce a post-measurement pure state labeled by the measurement outcome b_h in B:

$$|\psi^{b_h}\rangle = \frac{1}{\sqrt{p(b_h)}}\Pi_{b_h}\psi_{AB} = \frac{1}{\sqrt{p(b_h)}}|\psi_A(b_h)\rangle \otimes |b_h\rangle \tag{5.3}$$

where $p(b_h) = \langle\psi_{AB}|\Pi_{b_h}|\psi_{AB}\rangle$ is the probability of obtaining measurement outcome b_h in B and $|\psi_A(b_h)\rangle$ is the conditional state in A given the outcome b_h. In this chapter, we will consider the set of states $\{b_h\}$ to be the joint eigenbasis of local spin operators $\vec{\sigma}.\hat{n}$ on each site along some arbitrary direction $\hat{n}$.

The projected ensemble is constructed with the pure states obtained from measurements and their corresponding probabilities, $\mathcal{E}_{\text{PE}} = \{p(b_h), |\psi_A(b_h)\rangle\}$, as in Eq. 5.1. An external agent, if provided with the closely related ensemble $\tilde{\mathcal{E}} = \{p(b_h), |\psi^{b_h}\rangle\}$, can estimate the distribution of states in $\mathcal{E}_{\text{PE}}$ from expectation values of non-local observables in $\tilde{\mathcal{E}}$. The protocol for the construction of the ensemble ensures that in the ensemble, two different states in A are not associated with the same b_h i.e. $\psi_A(b_h) \neq \psi_A(b'_h)$ implies $b_h \neq b'_h$. The label b_h then allows locating repeated occurrances of the same state $|\psi_A(b_h)\rangle$ and makes it possible to estimate conditional expectation values $\langle\hat{O}\rangle_{\psi_A(b_i)}$ of observables for each state in the ensemble. The k-th moment of the distribution of expectation values of $\hat{O}$ is $\sum_i p(b_i)\langle\hat{O}\rangle^k_{\psi^{b_i}_A}$. Moments of all observables are directly related to k-th moment of the ensemble defined as follows.

$$\rho_A^{(k)} = \sum_{b_i\in\mathcal{S}_B} p(b_i)(|\psi_A(b_i)\rangle\langle\psi_A(b_i)|)^{\otimes k} \tag{5.4}$$

These moments can be used to characterize and compare distribution of states in different ensembles.

For a random state in the Hilbert space, the PE will converge to a Haar ensemble in the A subsystem. This holds true even when ψ_{AB} is obtained by time evolution of an effectively infinite temperature state of a chaotic Hamiltonian[16]. The proximity of two ensembles can be gauged by the trace distance between their k-th moments,

$$\Delta^{(k)}(\mathcal{E},\mathcal{E}') = \frac{1}{2}\text{Tr}\left[\sqrt{\left(\rho_{\mathcal{E}}^{(k)} - \rho_{\mathcal{E}'}^{(k)}\right)^\dagger\left(\rho_{\mathcal{E}}^{(k)} - \rho_{\mathcal{E}'}^{(k)}\right)}\right]. \tag{5.5}$$

The Haar distribution for A can be written as a measure over normalized quantum states $|\psi\rangle$ as below,

$$P_{\text{Haar}}(\psi) = \int_{-\infty}^{\infty}\delta\left(\psi - \frac{\tilde{\Psi}}{\|\tilde{\Psi}\|}\right)\prod_{i=1}^{D}\frac{D}{\pi}\exp[-D|\tilde{\Psi}_i|^2]d^2\tilde{\Psi}_i \tag{5.6}$$

where D is the Hilbert space dimension of A. Here $\tilde{\Psi} = (\tilde{\Psi}_1,\ldots,\tilde{\Psi}_D)$ is an unnormalized random vector whose components are drawn independently from the complex Gaussian measure

$\frac{D}{\pi}\exp[-D|\tilde{\Psi}_i|^2]d^2\tilde{\Psi}_i$ in Eq. (5.6). This Gaussian measure is invariant under unitary rotations $\tilde{\Psi} \to U\tilde{\Psi}$, so the *direction* of $\tilde{\Psi}$ is uniformly distributed on the unit sphere, independent of its norm $\|\tilde{\Psi}\|$. The delta function in Eq. (5.6) projects out this norm, defining the normalized state $\psi = \tilde{\Psi}/\|\tilde{\Psi}\|$, which therefore inherits a uniform (Haar) distribution over pure states. Thus, sampling $\tilde{\Psi}$ from independent complex Gaussians and normalizing is a standard method for generating Haar-random states.

For systems with global conserved charges $\{Q\}$, the reduced density matrix ρ_A equilibrates to $\exp[-\sum_Q \lambda_Q Q_A]$ and the the limiting ensemble for the PE is found to approach the Scrooge ensemble[217, 16] if the measurement basis $\{b_h\}$ does not reveal any information about the density of conserved charges (e.g. energy) in B i.e have 0 overlap with the the eigenstates of conserved charges (energy). The measurement in the joint eigenbasis of $\{\sigma_i^x\}_{i\in B}$ for a system with a globally conserved $U(1)$ charge $Q = \sum_{i=1}^{L}\sigma_i^z$, would be such an example.

Scrooge ensemble ($\mathcal{E}_{\text{Scrooge}}$) can be constructed as a distortion of the Haar ensemble such that it reproduces a given density matrix ρ as its first moment. Formally, we can represent it as the following,

$$\mathcal{E}_{\text{Scrooge}}(\rho) = \left\{ D\langle\psi|\rho|\psi\rangle, \frac{\sqrt{\rho}|\psi\rangle}{\sqrt{\langle\psi|\rho|\psi\rangle}} \right\}_{\psi\in\mathcal{E}_{\text{Haar}}} \tag{5.7}$$

Given a ρ, the Scrooge ensemble [63, 216] is the unique ensemble such that it has the minimum accessible information as shown in Ref. [63], thus manifesting a maximal entropy principle[215] in the full Hilbert space. The moments of the Scrooge ensemble are given by

$$\rho_{\text{Scr}}^{(k)} = \int d\psi \left(\frac{\sqrt{\rho}|\psi\rangle\langle\psi|\sqrt{\rho}}{|\sqrt{\rho}|\psi\rangle|^2} \right)^{\otimes k} \langle\psi|\rho|\psi\rangle P_{\text{Haar}}(\psi) \tag{5.8}$$

If the measurement basis reveals partial information about the conserved charges in B, it is conjectured that the PE at late times, converges to a weighted sum of Scrooge ensembles, referred to as the generalized Scrooge ensemble (GSE) [215, 217]. Consider a global conserved charge and a measurement operator on each site that has a finite overlap with conserved charge. There is a probability of obtaining any given outcome b_h which we denote as $p_d(b_h)$ and an associated reduced density matrix $\overline{\rho}_A(b_h)$. The charge in A and therefore its density matrix is constrained by the charge in B which is in turn constrained by the measurement outcome b_h. The k-th moment of the GSE is then given,

$$\rho_{\text{GSE}}^{(k)} = \sum_{b_h} p_d(b_h)\rho_{\text{Scr}}^{(k),b_h}, \tag{5.9}$$

where $\rho_{\text{Scr}}^{(k),b_h}$ is the k-th moment of the Scrooge ensemble corresponding to the density matrix $\overline{\rho}_A(b_h)$. For the special case where the outcome b_h reveals no information about the conserved charge in B(and therefore no information about the conserved charge in A), the steady state density matrix $\overline{\rho}_A(b_h)$ is independent of b_h, resulting in Eq. 5.9 reducing to a single Scrooge ensemble.

If the independent set of conserved charges, instead, are locally supported, information about those in subsystem B reveal no information about the charges in A. As a result, the

steady state density matrix in A conditional on the measured outcome in B is independent of measured outcome. One expects that the projected ensemble of states in A approaches, at late times, the same maximum entropy ensemble irrespective of the outcome in B, and therefore by the same arguments as above the unconditioned distribution approaches the Scrooge ensemble $\mathcal{E}_{\text{Scrooge}}(\rho_{A,\infty})$ (see Eq. 5.7) with $\rho_{A,\infty}$ being the steady state reduced density of matrix of A as $t \to \infty$. In the following we numerically demonstrate and semi-analytically prove for a specific model, that this is indeed the case – this constitutes the central result of this chapter.

5.3 Numerical results for a disordered Floquet spin chain

In this section, we establish numerically the phenomenology using a disordered Floquet spin-1/2 chain described by the Floquet unitary U_F given by

$$\begin{aligned} U_F &= \exp[-i\tau H_X]\, \exp[-i\tau H_Z] \quad \text{with}\,, \\ H_X &= g\Gamma \sum_{i=1}^{L} \sigma_i^x\,, \\ H_Z &= \sum_{i=1}^{L-1} \sigma_i^z \sigma_{i+1}^z + \sum_{i=1}^{L} (h + g\sqrt{1-\Gamma^2}\epsilon_i)\sigma_i^z]\,, \end{aligned} \tag{5.10}$$

where $\{\sigma_i^\mu\}$ is the set of Pauli matrices representing the spins-1/2 and $\epsilon_i \sim \mathcal{N}(0,1)$ are independent random numbers drawn from a standard Normal distribution. The rationale behind choosing this model is twofold. First, the model has been shown [229] to exhibit MBL-like dynamics for numerically accessible system sizes over very long timescales, robustly, in the sense that the MBL regime has a finite extent in the parameter space. In particular for the choice of parameters, $g = 0.9045$, $h = 0.809$, and $\tau = 0.8$, there is a putative many-body localization transition at $\Gamma_c \approx 0.3$ with the model in an ergodic phase for $\Gamma > \Gamma_c$ and in a MBL regime for $\Gamma < \Gamma_c$. Second, the model has no global symmetries and in the MBL regime, the only conserved charges are the emergent local integrals of motion [54, 53, 226, 225]. The model therefore allows us to understand cleanly the fate of the PE in the presence of locally supported conserved charges without any global conservation laws contaminating the results.

We consider initial states of a direct product form

$$|\psi_0\rangle = \bigotimes_{i=1}^{L} \left(\cos\frac{\theta_i}{2} |\uparrow\rangle_i + e^{\imath\phi_i} \sin\frac{\theta_i}{2} |\downarrow\rangle_i \right)\,, \tag{5.11}$$

where $|\uparrow\rangle_i (|\downarrow\rangle_i)$ denote the state of the spin at site i polarized along the positive(negative) z-axis. The form in Eq. 5.11 implies that initially the states of the individual spins are picked uniformly from the Bloch sphere with θ and ϕ (denoting the polar and azimuthal angles) are sampled accordingly. Each initial state is therefore parameterized by a vector $\boldsymbol{\theta} \equiv \{\theta_1, \theta_2, ..., \theta_L\}$ and $\boldsymbol{\phi} \equiv \{\phi_1, \phi_2, ..., \phi_L\}$. We consider the subsystem A to be the first L_A sites of the chain.

As the explicit form of the locally conserved charge operators are unavailable, we directly construct the moments of the Scrooge ensemble as follows. For a given initial state the reduced

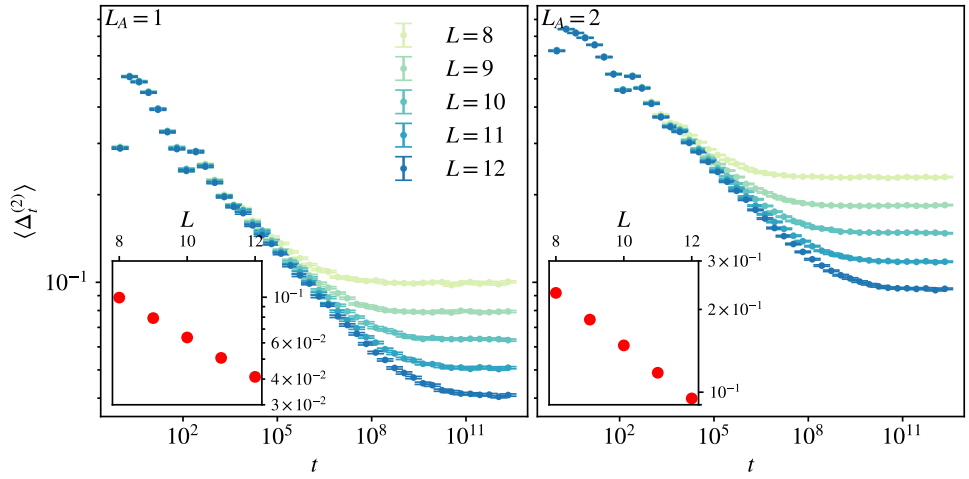

Figure 5.1: Distance between the second moments of the Scrooge ensemble and the PE (see Eq. 5.17 for definition) for the disordered Floquet spin chain (described by Eq. 5.10) in the MBL regime with $\Gamma = 0.15$. The left and right panels correspond to $L_A = 1$ and 2 respectively. The insets show the exponential decay of $\Delta_t^{(k)}$ with L in the limit of $t \to \infty$. The trace distances are averaged over 500 disorder realizations and over 10 random initial states for each realization.

density matrix of subsystem A in the limit of infinite time is given by

$$\rho_{A,\infty} = \sum_{\omega} \left[\mathrm{Tr}_B \left| \omega \right\rangle \left\langle \omega \right| \right] \left| \left\langle \psi_0 | \omega \right\rangle \right|^2 , \tag{5.12}$$

where $\{|\omega\rangle\}$ denotes the set of eigenstates of the Floquet unitary U_F in Eq. 5.10. With the $\rho_{A,\infty}$ at hand, and its eigenvectors and eigenvalues denoted as $\{\lambda_m, |m\rangle\}$, one can obtain the k-th moment of the corresponding Scrooge ensemble as [215]

$$\rho_{\mathrm{Scr}}^{(k)} = \sum_{\boldsymbol{m}} \sum_{\sigma \in S_k} \rho_{\mathrm{Scr},\boldsymbol{m}}^{(k)} \left| \boldsymbol{m} \right\rangle \left\langle \sigma(\boldsymbol{m}) \right| , \tag{5.13}$$

where $|\boldsymbol{m}\rangle = |m_1, m_2, \cdots, m_k\rangle$ is a state in the k-replicated Hilbert space, $|\sigma(\boldsymbol{m})\rangle$ is permutation of $|\boldsymbol{m}\rangle$, and the matrix element

$$\rho_{\mathrm{Scr},\boldsymbol{m}}^{(k)} = \left(\prod_m \frac{1}{\lambda_m} \right) \frac{\partial^k \Lambda_k}{\partial \mu_{m_1} \cdots \partial \mu_{m_k}} \bigg|_{\mu_i = \lambda_i^{-1}} , \tag{5.14}$$

where

$$\Lambda_k(\mu_1, \cdots) = \sum_j \frac{\mu_j^{k-2} \ln \mu_j}{\prod_{i \neq j} (\mu_j - \mu_i)} . \tag{5.15}$$

A brief outline for Eq. 5.13

A brief derivation of Eq. 5.13 proceeds in two steps.

Step 1: permutation structure. It is convenient to first work with the *unnormalized* Scrooge ensemble, in which $|\tilde{\Psi}\rangle = \sum_m \tilde{\Psi}_m |m\rangle$ has independent complex Gaussian components in the eigenbasis of ρ, with variance set by the eigenvalues λ_m,

$$P(\tilde{\Psi}) = \prod_{m=1}^{D} \frac{1}{\pi\lambda_m} \exp\left[-\frac{|\tilde{\Psi}_m|^2}{\lambda_m}\right]. \tag{5.16}$$

The normalized state is $|\psi\rangle = |\tilde{\Psi}\rangle/\|\tilde{\Psi}\|$. Each component $\tilde{\Psi}_m$ has an independent, uniformly random phase, and this phase invariance survives normalization. A matrix element of the k-th moment, $\langle \boldsymbol{m}|\rho^{(k)}_{\text{Scr.}}|\boldsymbol{m}'\rangle = \mathbb{E}\left[\prod_{i=1}^{k} \psi_{m_i}\psi^*_{m'_i}\right]$, therefore vanishes under the average unless every phase cancels — that is, unless $\{m'_1, \ldots, m'_k\}$ reproduces $\{m_1, \ldots, m_k\}$ exactly, i.e. $\boldsymbol{m}' = \sigma(\boldsymbol{m})$ for some $\sigma \in S_k$. This gives the permutation-restricted structure of Eq. (5.13).

Step 2: the coefficients. To evaluate the surviving elements $\rho^{(k)}_{\text{Scr.},\boldsymbol{m}} = \mathbb{E}\left[\|\tilde{\Psi}\|^{-2k} \prod_{i=1}^{k} |\tilde{\Psi}_{m_i}|^2\right]$, use the Schwinger identity $\|\tilde{\Psi}\|^{-2k} = \frac{1}{\Gamma(k)} \int_0^\infty dt\, t^{k-1}\, e^{-t\|\tilde{\Psi}\|^2}$ to decouple the normalization from the Gaussian average. The extra factor $e^{-t\|\tilde{\Psi}\|^2}$ simply reweights each component's variance, $\lambda_m \to \lambda_m/(1+t\lambda_m)$, so the remaining Gaussian moments are elementary, leaving a single integral over t with an overall Jacobian $\prod_j (1+t\lambda_j)^{-1}$. Performing this integral (by partial fractions, or equivalently residues at $t = -\lambda_j^{-1}$) produces exactly the closed form of $\rho^{(k)}_{\text{Scr.},\boldsymbol{m}}$ quoted below Eq. (5.13), expressed as derivatives of the symmetric function $\Lambda_k(\mu_1, \ldots, \mu_D)$ with respect to $\mu_m \equiv \lambda_m^{-1}$. We refer the reader to Appendix H of Ref. [215] for the complete residue calculation.

We compare the so-obtained k^{th} moments of the Scrooge ensemble with the k^{th} moments of the projected ensemble, $\mathcal{E}_{\text{PE}}(\psi_t)$ obtained from the time-evolved state $|\psi_t\rangle = U_F^t |\psi_0\rangle$. In particular, we compute the trace distance defined in Eq. 5.5,

$$\Delta_t^{(k)} \equiv \Delta^{(k)}\left(\mathcal{E}_{\text{Scrooge}}(\rho_{A,\infty}), \mathcal{E}_{\text{PE}}(\psi_t)\right), \tag{5.17}$$

and study its behavior with t and L for fixed L_A. The results for $k = 2$ are shown in Fig. 5.1 where the measurement operators on B are the σ_i^x operators. Note however, that the qualitative features of the results in this case are expected to remain the same for any generic set of single-site projective measurements on B as the local conserved charges on B can point along arbitrary directions and can have a support with size greater than 1 depending on the specific disorder realization of U_F. The results in Fig. 5.1 show that $\Delta_t^{(2)}$ decays with t and saturates to a values which decays exponentially in L. This provides strong hints towards the fact in the limit of $L \to \infty$ and $t \to \infty$, the PE is the same as the Scrooge ensemble corresponding to $\rho_{A,\infty}$. In the following sections, we show analytically that this is indeed the case using a phenomenological model of MBL.

5.4 Phenomenological MBL model

As an effective, phenomenological model of MBL at strong disorder we consider the ℓ-bit model [54, 53, 226, 225]. The Hamiltonian for the model is given by

$$H_{\ell\text{-bit}} = \sum_i J_i \sigma_i^z + \sum_{i<j} J_{ij} \sigma_i^z \sigma_j^z + \sum_{i<j<k} J_{ijk} \sigma_i^z \sigma_j^z \sigma_k^z \,, \tag{5.18}$$

with the couplings taken as random and decaying exponentially between the spins in their support as

$$J_i{=}u_i, \;\; J_{ij}{=}u_{ij} e^{-(j-i)/\xi}, \;\; J_{ijk}{=}u_{ijk} e^{-(k-i)/\xi} \,, \tag{5.19}$$

where u's are picked from uniform distribution over $[-W, W]$, and ξ is an effective localization length scale. Throughout this chapter we take $W = 1$ and time is always in units of W^{-1}, and ξ is taken to be 2. The model has strictly 1-local conserved charges $\{\sigma_i^z | 1 \leq i \leq L\}$. In this case also we consider initial states of the form in Eq. 5.11.

5.4.1 Approach of the projected ensemble to the Scrooge ensemble in time

At long times, dephasing due to the interaction terms takes the reduced density matrix ρ_A to a diagonal form in the energy eigenbasis which for the ℓ-bit model (Eq. 5.18) is just the σ^z-product state basis,

$$\rho_{A,\infty} \to \bigotimes_{i=1}^{L_A} \rho_i^\infty \;\; \text{with } \rho_i^\infty = \text{diag}[\cos^2 \frac{\theta_i}{2}, \sin^2 \frac{\theta_i}{2}] \,. \tag{5.20}$$

To construct the PE, as in the previous section, we time-evolve the initial state with the ℓ-bit Hamiltonian (Eq. 5.18), $|\psi_t\rangle = e^{-\imath H_{\ell\text{-bit}} t} |\psi_0\rangle$ and perform measurements in B subsystem of observable $\otimes_{i=L_A+1}^{L} \sigma_i^n$ where $\sigma_i^n \equiv \boldsymbol{\sigma}_i \cdot \hat{n}$ is the Pauli spin operator on site i in the direction $\hat{n}$. The latter is parametrized by the polar angle $\alpha \in [0, \pi]$ that $\hat{n}$ makes with the z-axis. The results are independent of the azimuthal angle defining $\hat{n}$ and therefore we choose it to be 0 throughout. The bitstrings $b_h \in (0,1)^{\otimes L_B}$ obtained from the measurement at an angle α correspond to states (in terms of the computational basis states $|\uparrow\rangle$ and $|\downarrow\rangle$ on each site),

$$\begin{aligned} |0\rangle &\equiv \cos \frac{\alpha}{2} |\uparrow\rangle + \sin \frac{\alpha}{2} |\downarrow\rangle \;, \\ |1\rangle &\equiv \sin \frac{\alpha}{2} |\uparrow\rangle - \cos \frac{\alpha}{2} |\downarrow\rangle \;. \end{aligned} \tag{5.21}$$

Note that the limit of $\alpha = 0$ is pathological as in that case the measurements coincide completely with the conserved charges. For much of what we discuss below we consider $\alpha \neq 0$.

From the infinite-time reduced density matrix of A in Eq. 5.20, the moments of the Scrooge ensemble can also be constructed directly as in the previous section and the distance of the PE from the Scrooge ensemble as a function of time can be studied using $\Delta_t^{(k)}$ defined in Eq. 5.17, as shown in Fig. 5.2 for $k = 2$ and $k = 3$. The results are qualitatively similar to those of the disordered Floquet Ising spin chain (see Fig. 5.1) – the trace distance of the moments of the PE and the Scrooge ensemble decay as a power-law in t, and for a finite L saturate to a value

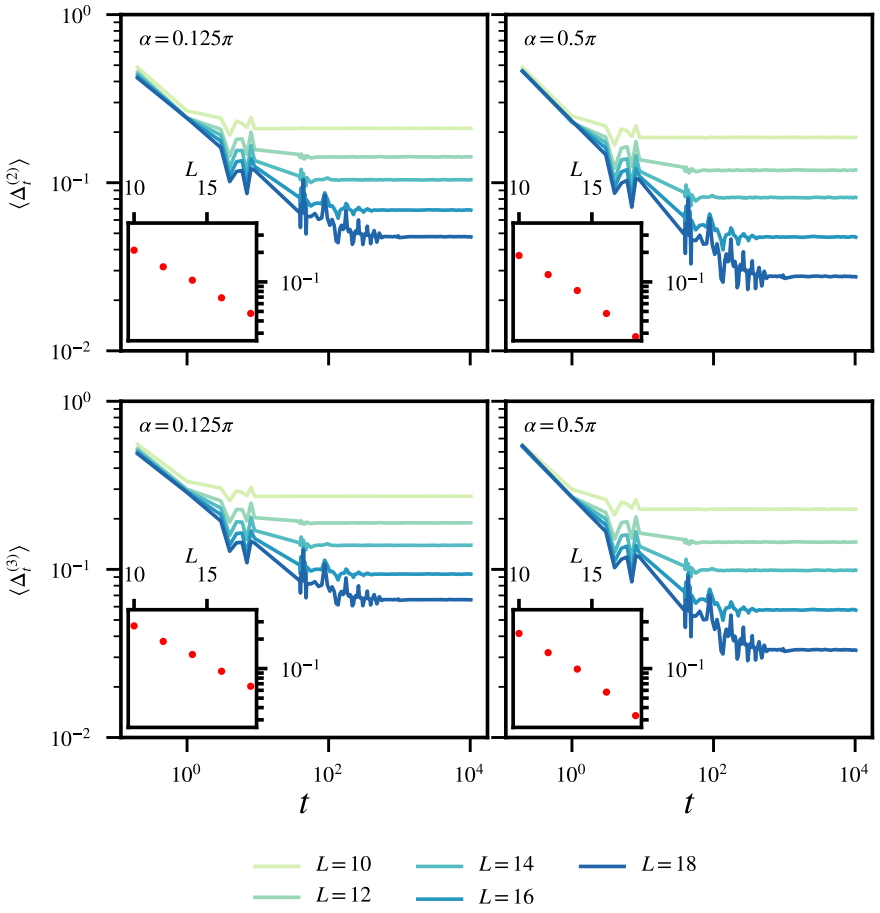

Figure 5.2: Distance between the second and third moments of the PE, $\langle \Delta_t^{(2)} \rangle$ (top) and $\langle \Delta_t^{(3)} \rangle$ (bottom), from those of the Scrooge ensemble for two measurement angles, $\alpha = \pi/8$ (left) and $\alpha = \pi/2$ (right) for the ℓ-bit Hamiltonian (Eq. 5.18). For both cases, at long time, $\langle \Delta_t^{(k)} \rangle$ saturates to an asymptotic value which goes down exponentially with increasing L (see insets). For these plots, $L_A = 2$ and the trace distances are averaged over 500 disorder realizations and over 10 random initial states for each realization.

which itself decays exponentially with L. The power law exponent for decay of $\langle \Delta_t^{(3)} \rangle$ with time remains same as that of $\langle \Delta_t^{(2)} \rangle$ (within errorbar) and depends on α. For the coupling strength we studied here,$\langle \Delta_t^{(2)} \rangle \propto t^{-0.33 \pm 0.06}$ for $\alpha = \pi/2$ and $\langle \Delta_t^{(2)} \rangle \propto t^{-0.24 \pm 0.05}$ for $\alpha = \pi/8$.

5.4.2 Dependence of the projected ensemble on the measurement angle

In Fig. 5.2, the results were shown only for two measurement angles α. We next show results for how the moments of the PE depend on α.

α dependence of the matrix elements: First, we look at the asymptotic values of matrix elements in the moments of PE as a function of measurement angle α. Representative results for matrix elements are shown in Fig. 5.3, for both $L_A = 1$ and 2. The results show that individual matrix elements approach the Scrooge distribution's moments (red dotted lines) with increasing L if the measurement is not aligned with the conserved charges. This qualitative trend appears

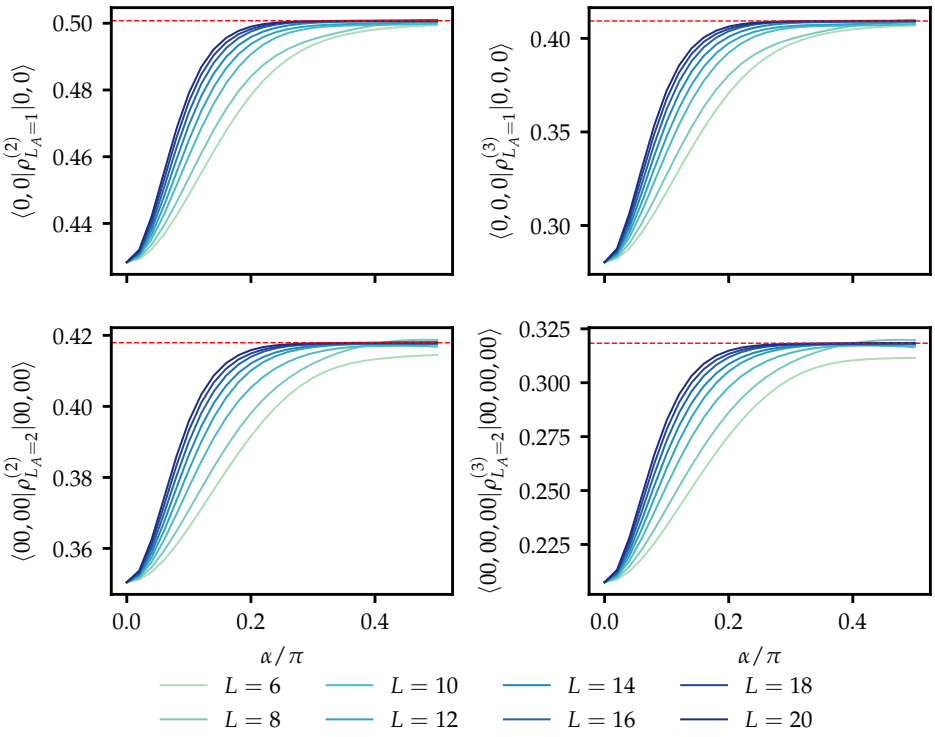

Figure 5.3: Time averaged matrix elements of higher moments for different system sizes. (Top) Left panel shows $\langle 0,0|\rho^{(2)}_{L_A=1}|0,0\rangle$ and right panels shows $\langle 0,0,0|\rho^{(3)}_{L_A=1}|0,0,0\rangle$ where $\rho^{(2)}_{L_A=1}, \rho^{(3)}_{L_A=1}$ are moments for L_A=1. (Bottom) Left panel shows $\langle 00,00|\rho^{(2)}_{L_A=2}|00,00\rangle$ and right panel shows $\langle 00,00,00|\rho^{(3)}_{L_A=2}|00,00,00\rangle$ where $\rho^{(2)}_{L_A=2}, \rho^{(3)}_{L_A=2}$ are moments for L_A=2. The red dotted lines are the corresponding Scrooge values. The initial state is a direct product state (Eq. 5.11) with $\theta_1 = 2\pi/5$ and $\theta_2 = \pi/5$ (for $L_A = 2$). To reduce fluctuation about mean value, we average the moments calculated at 90 different times at regular intervals in the time window $Wt = 8000$ to 10000. Legend shows the L value corresponding to different colors.

to hold for all such matrix elements, which suggests that the PE approaches asymptotically the Scrooge ensemble in the limit of $L_B \to \infty$ for $\alpha \gtrsim 0.1\pi$. These results on finite size effects and α dependence are in consonance with further independent numerical results in Sec. 5.5. For $\alpha = 0$, that is when the measurement is perfectly aligned with the conserved charges, the PE does not converge to Scrooge ensemble and shows no system size dependence.

α dependence of the trace distance: Finally, in Fig. 5.4, we present the asymptotic trace distance as a function of L. For $\alpha \gtrsim \pi/8$, the trace distance (for both $\Delta^{(2)}$ and $\Delta^{(3)}$) between PE and Scrooge ensemble decays exponentially with L as $\sim \exp(-\lambda L)$ with $\lambda \approx 0.23$. Interestingly, the same exponential decay rate was also found in the Floquet MBL model (Fig. 5.1). For α close to 0, the decay is slower and deviates from exponential form for the range of L studied. This is consistent with the deviation of the matrix elements of the PE from those of the Scrooge ensemble for the available system sizes.

To summarize, the numerical results presented in this section point towards the fact that for the ℓ-bit model also, the PE at long times and large system sizes approaches the Scrooge ensemble unless the measurement basis closely aligns with the conserved charges. For $\alpha \gtrsim 0.1\pi$, scaling of

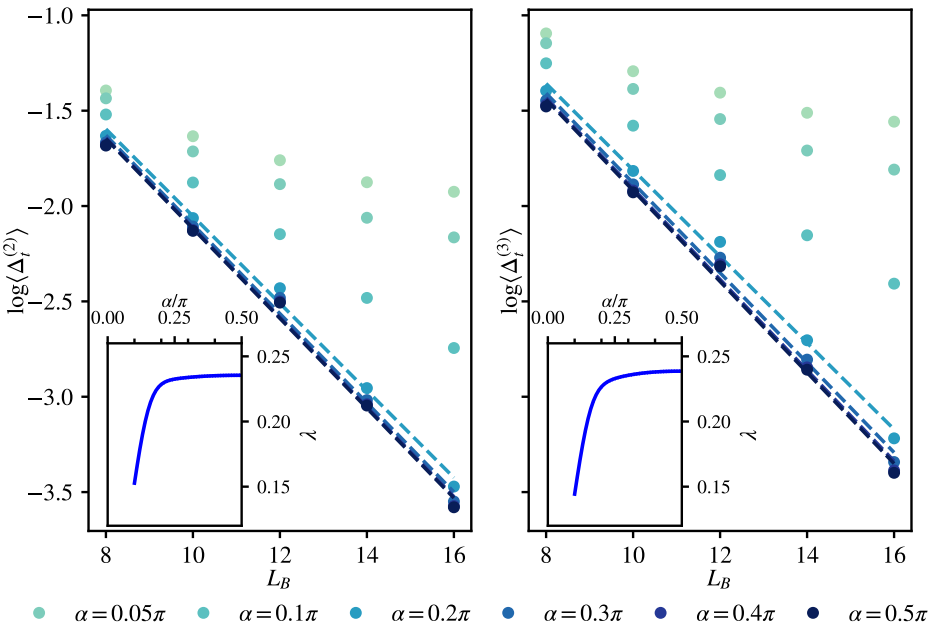

Figure 5.4: Asymptotic trace distance between Scrooge ensemble and PE as a function of L for $L_A = 2$. Different colors denote different measurement angles α between 0.05π and $\pi/2$ (legend). The two panels show the trace distances for second (left) and third (right) moments. Insets shows the decay rate λ (estimated by fitting the trace distance to $e^{-\lambda L}$) as a function of measurement angles. The slope (λ) obtained from exponential fit for $\alpha > 0.1\pi$. For other values of α, the trend deviates substantially from an exponential within the range of L studied. The trace distances are averaged over 500 disorder realizations and over 10 random initial states at time $Wt = 10000$.

the numerically obtained moments in the finite systems suggest that the trace distance vanish in the thermodynamic limit. In the following we will demonstrate this by showing semi-analytically, using empirical results from the probabilities of measuring bitstrings, that the matrix elements of the k^{th} moment of the PE at $L, t \to \infty$ are identical to those of the Scrooge ensemble.

5.5 Temporal ensemble and probability distribution of the probabilities (PoP) of bitstrings

A key observation that helps in computing the matrix elements of the higher-moments of the PE at late times is that they approach steady values with small temporal fluctuations that, crucially, decrease with increasing L_B. Representative numerical evidence for this is shown in Fig. 5.5 where it is seen that the matrix element of $\rho_A^{(2)}(t)$ fluctuate less around their steady-state values for larger systems sizes. Other matrix elements of $\rho_A^{(2)}(t)$ and also matrix elements for other values of k and α that we studied show similar qualitative behavior. This key empirical observation suggests that we can understand the steady-state values by performing an average of the matrix elements over time. This motivates the definition of a *temporal ensemble* of states consisting of the states sampled from the time-evolution trajectory of an initial state under a given Hamiltonian. Of particular significance will be understanding the probability distribution of the probabilities (PoP) of measuring individual bitstrings $b \in \{b_h\}$ of the entire system in the

temporal ensemble of late-time states.

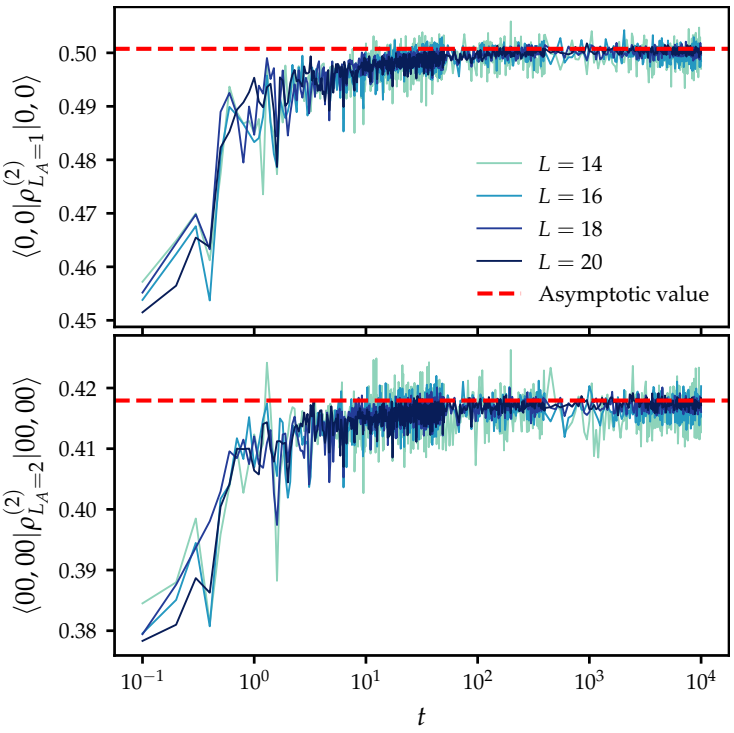

Figure 5.5: The matrix elements in second moments of PE saturate at long timescale to their asymptotic value at measurement along an axis with $(\alpha) = \pi/4$ for both $L_A = 1$ (Top) and 2 (Bottom). The fluctuation about the asymptotic value (red dotted line) gets suppressed with increasing L. The initial state is a direct product state (eq. 5.11) with $\theta_1 = 2\pi/5$ and $\theta_2 = \pi/5$ (for $L_A = 2$).

The temporal ensemble is defined as the collection of states $\{|\psi_t\rangle\}$ occurring in the quantum trajectory of the initial direct product state $|\psi_0\rangle$ (taken as in Eq. 5.11) over a suitably large temporal window at late times. Functionally, this can be taken to be the ensemble formed by sampling the states at times $t \in [\tau_1, \tau_2]$ at regular intervals of length δt:

$$\mathcal{E}_{\text{temp}} = \left\{ \frac{\delta t}{\tau_2 - \tau_1}, e^{-\imath H t} |\psi_0\rangle \right\}_{t\in[\tau_1,\tau_2]} . \tag{5.22}$$

Upon measuring $\{\sigma^n_i\}_{i=1\ldots L}$ at every site of the system, (recall $\sigma^n_i = \boldsymbol{\sigma}_i \cdot \hat{n}$ and $\hat{n}$ is parametrized by the polar angle α) on the state $|\psi_t\rangle$, the probability of getting a bitstring b is $p(b) = |\langle \psi_t | b\rangle|^2$. Over the ensemble of states in the temporal ensemble (Eq. 5.22) there is a probability distribution of the probability $p(b)$, and hence the name probability of probability (PoP). We denote the PoP of bitstring b as PoP_b. This is also the distribution of expectation values of the projector into a bitstring b for states in the temporal ensemble.

Figure 5.6 shows PoP_b over the temporal ensemble for two specific bitstrings (which are taken as representative examples) for three different values of α, for a fixed initial state and disorder realization.

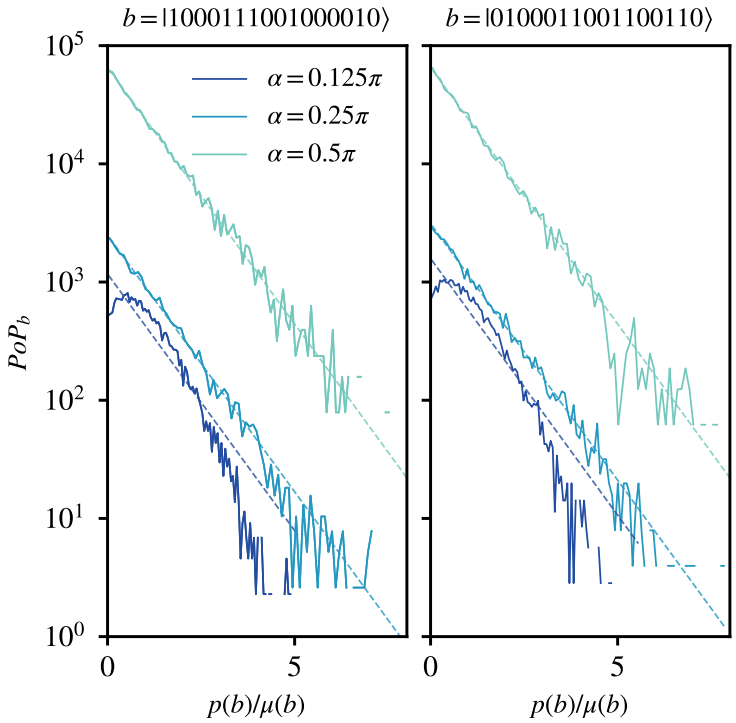

Figure 5.6: Distribution of probabilities of measurement bitstrings in the temporal ensemble, $\mathcal{E}_{\text{temp}}$, defined in Eq. 5.22. $\mathcal{E}_{\text{temp}}$ is constructed with 10000 states sampled in the time interval, $8000 - 10000$ (in unit of W^{-1}) with uniform spacing. Results are shown for three different measurement angles, α, and the dotted lines show the Porter-Thomas distributions (defined in Eq. 5.23) with the means obtained using Eq. 5.24. The two panels show two representative bitstrings (written above the figure) for a system with $L = 16$.

We find that the PoP_b is well-described by the Porter-Thomas distribution[1]

$$PT_b(p) = \frac{1}{\mu_b} e^{-\frac{p}{\mu_b}}, \tag{5.23}$$

where μ_b is the average of $p(b)$ over the temporal ensemble. In Fig. 5.6, the PoPs are shown by the solid lines whereas the Porter Thomas distributions with the corresponding means are depicted by the dashed lines, with the two showing good agreement between each other. The agreement is worse for α close to zero, which we will argue shortly is due to finite-size effects.

The mean μ_b depends on the bitstring b, the initial state, the angle α parameterizing the measurement basis as

$$\mu_b(\alpha, \psi_0) = \sum_{z_\nu} |\langle \psi_0 | z_\nu \rangle|^2 |\langle b | z_\nu \rangle|^2, \tag{5.24}$$

where $\{|z_\nu\rangle\}$ are the eigenstates of the Hamiltonian, which for the ℓ-bit Hamiltonian (Eq. 5.18) are also σ^z-product states. For $\alpha = \pi/2$, the bitstrings $|b\rangle$ are σ^x-product states such that $|\langle b|z_\nu\rangle|^2 = D^{-1}$, with $D = 2^L$ the Hilbert-space dimension, for all b and z_ν. In this limit,

[1] Comparison of PoP with Porter-Thomas distribution is meaningful only for $\alpha \neq 0$. For the pathological case of $\alpha = 0$, $|b\rangle$ are σ^z-product states and therefore coincide with the eigenstates of the ℓ-bit Hamiltonian. As a result $p(b)$ for a given b is a constant over the temporal ensemble, given by $|\langle \psi_0 | b \rangle|^2$, and the PoP is δ-function ditributed, $PoP_b(p) = \delta(p - |\langle \psi_0 | b \rangle|^2)$.

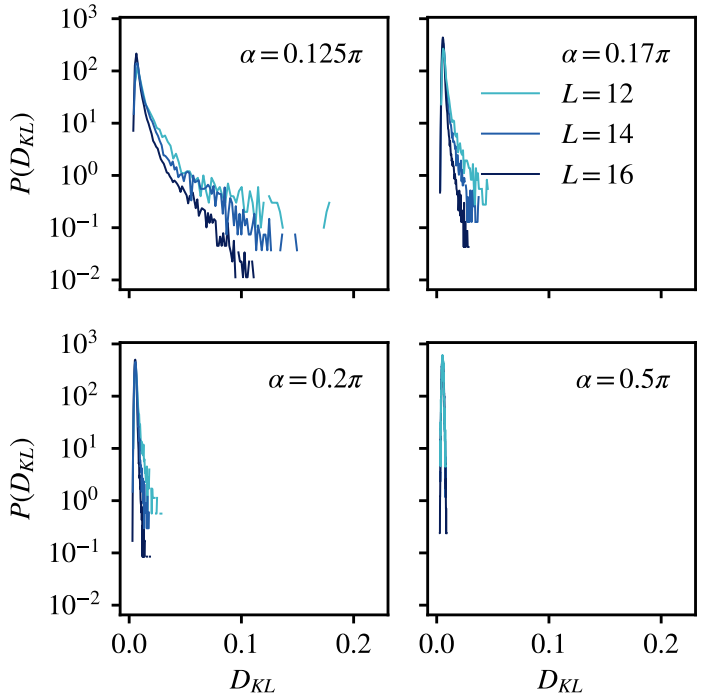

Figure 5.7: The distribution of KL divergence between the Porter-Thomas distribution and PoP ($D_{KL}(\mathrm{PoP}_b||PT_b)$) across all b (see Eq. 5.25 for definition). Different panels correspond to different α and in all cases the distributions get more concentrated around 0 with increasing L. Number of bins to obtain the histogram is kept same across all system sizes. The PoP_b is obtained in a temporal ensemble with 10000 states sampled with equal spacing in time interval $8000 - 10000$ in unit of W^{-1}.

$\mu_b = 1/D$ is independent of the bitstring b as well as of initial state and the measurement angle α. For generic $\alpha \neq \pi/2$, the PoP continues to be Porter-Thomas distributed but with the appropriate mean given in Eq. 5.24.

While the results in Fig. 5.6 show the Porter-Thomas distribution for the PoP for two representative bitstrings, to ascertain the agreement between PT_b and PoP_b for arbitrary b, we look at their difference quantified by the Kullback–Leibler (KL) divergence. For a particular bitstring b, the KL divergence between PT_b and PoP_b, is defined as

$$D_{KL}(\mathrm{PoP}_b||PT_b) = \int dp\ \mathrm{PoP}_b(p) \ln\left(\frac{\mathrm{PoP}_b(p)}{PT_b(p)}\right) . \tag{5.25}$$

In the results presented, the integral in Eq. 5.25 is calculated by discretization and using the estimated PoP_b obtained by binning.

In Fig. 5.7, we present the distribution over b of $D_{KL}(\mathrm{PoP}_b||PT_b)$ for different measurement angles α. The distributions are strongly concentrated near 0. This indicates that for most measurement bitstrings, the $\mathrm{PoP}_b(p)$ closely matches with $PT_b(p)$. For the smaller values of α, close to zero, the distributions of $D_{KL}(\mathrm{PoP}_b||PT_b)$ develop a tail indicating deviations of the PoP_b from the PT_b for some b – this can also be seen in Fig. 5.6 for the smallest values of α presented. The finite-time effect behind the appearance of the tail at small α can be ruled out as the temporal ensemble is constructed with states sampled at sufficiently late-time

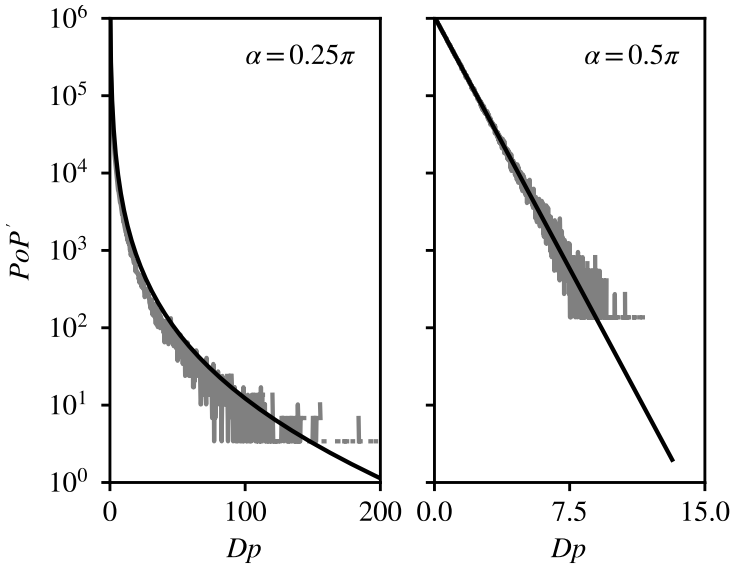

Figure 5.8: The PoP′ distribution of measurement bitstrings for a single state at $Wt = 10000$ following time evolution of an initial random direct product state under the ℓ-bit Hamiltonian in Eq. 5.18. The orange line denotes the sum of Porter-Thomas distributions shown in Eq. 5.26. Data for $L = 20$. For $\alpha = \pi/2$ (right panel), all the Porter-Thomas distributions are with the same mean $1/D$ such that the PoP′ is also a Porter-Thomas distribution.

(see Appendix 5.B). However, these tails are suppressed with system size suggesting in the thermodynamic limit, PoP_b is indistinguishable from PT_b for all b except when α close to 0.

As another evidence for the PoP_b being indistinguishable from PT_b, we also look at the distribution PoP' of probabilities of bitstring outcomes across all bitstrings but calculated for a single state in the temporal ensemble. In other words, this is the distribution of $p(b) = |\langle\psi_t|b\rangle|^2$ computed for a fixed $|\psi_t\rangle$ across all b. Figure 5.8 shows this distribution (gray lines) for two different values of α, $\pi/4$ and $\pi/2$. For both these cases, the distribution fits to a sum of Porter-Thomas distributions corresponding to individual bitstrings (with means $\mu(b)$ given by Eq. 5.24),

$$\text{PoP}'(p) = \frac{1}{2^L}\sum_b PT_b(p)\,. \tag{5.26}$$

The black lines in Fig. 5.8 show these fits. Note that for $\alpha = \pi/2$, $\mu_b = 1/D\ \forall\ b$ such that PoP′ is also a Porter-Thomas distribution with mean $1/D$ [230]; this is evident in the right panel of Fig. 5.8.

It is known that for general bitstring measurements, the PoPs are expected to be Porter-Thomas distributed with a mean of $1/D$ for random states [209]. Such random states are characterized by a Page value for the von Neumann entropy of bipartite entanglement [57]. On the other hand, for $\alpha = \pi/2$, (σ^x-measurements) we find the PoPs to be a Porter-Thomas distribution with mean $1/D$ even though the states have much lower bipartite entanglement entropy than the Page value [227, 228] indicating that they are far from a random state.

5.6 Matrix elements of Projected Ensemble and Scrooge Ensemble for ℓ-bit Hamiltonian

In this section, we use the results for the PoP obtained in Sec. 5.5 to show that the projected ensemble approaches the Scrooge ensemble in the limit of $L_B, t \to \infty$. In Sec. 5.6.1 we derive the expressions for the matrix elements of the k^{th} moments of the PE and in Sec. 5.6.2 we derive the same for the Scrooge ensemble, and show that they are identical.

Before proceeding, it will be useful to define some notation. The set of bitstrings corresponding to the σ^z-product states in subsystem A, B, and the entire system are denoted by $\mathcal{Z}_A$, $\mathcal{Z}_B$, and $\mathcal{Z}_{AB}$ respectively. The bitstrings in A are denoted as $z_A \equiv (z_{A,1}, z_{A,2}, \ldots, z_{A,L_A}) \in \mathcal{Z}_A$ where $z_{A,i} = 0, 1$ denotes the bit at site i. Similarly, the bitstrings in B are denoted as $z_B \equiv (z_{B,L_A+1}, z_{B,L_A+2}, \ldots, z_{B,L}) \in \mathcal{Z}_B$. The bitstrings in the entire system are the concatenation of the bitstrings z_A and z_B such that $z_{AB} \equiv (z_A, z_B) \in \mathcal{Z}_{AB}$. Since we will be interested in arbitrary moments of the PE and the Scrooge ensemble, we denote the basis states in the k-replicated Hilbert space of A as

$$|Z_A\rangle \equiv |z_A^{(1)}, z_A^{(2)}, \cdots, z_A^{(k)}\rangle = \otimes_{i=1}^{k} |z_A^{(i)}\rangle \ . \tag{5.27}$$

Finally, for a given initial state of the form Eq. 5.11, parametrized by $(\boldsymbol{\theta}, \boldsymbol{\phi})$ we define tensors $[M]_{i,s}$ on each site i with

$$M_{i,0} = \cos(\theta_i/2) \,, \quad M_{i,1} = e^{\imath\phi_i} \sin(\theta_i/2) \,, \tag{5.28}$$

and we also define

$$M_{z_{AB}} = M_{z_A} M_{z_B} = \left(\prod_{i=1}^{L_A} M_{i,z_{A,i}} \right) \left(\prod_{j=L_A+1}^{L} M_{j,z_{B,j}} \right) \ . \tag{5.29}$$

With this notation, the initial state (Eq. 5.11) can be rewritten as

$$|\psi_0\rangle = \sum_{z_{AB} \in \mathcal{Z}_{AB}} M_{z_{AB}} |z_{AB}\rangle \ , \tag{5.30}$$

and the reduced density matrix of A at infinite-time (Eq. 5.20) can be rewritten as

$$\rho_{A,\infty} = \sum_{z_A \in \mathcal{Z}_A} p(z_A) |z_A\rangle \langle z_A| \ ; \quad p(z_A) = |M_{z_A}|^2 \,. \tag{5.31}$$

5.6.1 Matrix elements of the projected ensemble

We will first express the matrix elements of the k^{th} moment of the PE at an arbitrary time t and an arbitrary measurement basis (α) on B and then take the limit of $t \to \infty$ for which we will average the matrix elements over the temporal ensemble defined in Sec. 5.5. Since the states $\{|z_{AB}\rangle\}$ are also the eigenstates of the ℓ-bit Hamiltonian (Eq. 5.18), with eigenvalues $\{E_{z_{AB}}\}$,

the state at time t can be written as

$$|\psi_t\rangle = \sum_{z_{AB}\in\mathcal{Z}_{AB}} e^{-\imath t E_{z_{AB}}} M_{z_{AB}} |z_{AB}\rangle \ . \tag{5.32}$$

If the measurement on B produces a bitstring b, then the *unnormalized* conditional state on A is given by

$$|\tilde{\psi}_{t,A}(b)\rangle = \sum_{z_A\in\mathcal{Z}_A} M_{z_A}\varphi_t(b|z_A)\,|z_A\rangle \ , \tag{5.33}$$

where

$$\varphi_t(b|z_A) = \sum_{z_B\in\mathcal{Z}_B} M_{z_B} e^{-\imath t E_{z_{AB}}} \langle b|z_B\rangle \ , \tag{5.34}$$

and the normalized version of the state in Eq. 5.33 is given by

$$|\psi_{t,A}(b)\rangle = \frac{|\tilde{\psi}_{t,A}(b)\rangle}{\sqrt{p_t(b)}} \ ; \ p_t(b) = \langle\tilde{\psi}_{t,A}(b)|\tilde{\psi}_{t,A}(b)\rangle \ . \tag{5.35}$$

The quantity $p_t(b|z_A) \equiv |\varphi_t(b|z_A)|^2$ defined via Eq. 5.34 has the physical meaning that it is the probability of obtaining the bitstring b upon measurements (at angle α) on B at time t given the σ^z-bitstring in A is z_A. The probability of obtaining the bitstring b in B due to the measurement on the state $|\psi_t\rangle$ in Eq. 5.32 is therefore

$$p_t(b) = \sum_{z_A\in\mathcal{Z}_A} p_t(b|z_A)p(z_A) = \sum_{z_A\in\mathcal{Z}_A} |\varphi_t(b|z_A)|^2 p(z_A)\,, \tag{5.36}$$

with $p(z_A)$, given in Eq. 5.31, the probability of measuring the bitstring z_A in A which remains constant with t. Using Eq. 5.35 and Eq. 5.36, an arbitrary matrix element of the k^{th} moment of the PE (defined in Eq. 5.4) can be written as

$$\langle Z'_A|\rho^{(k)}_{A,t}|Z_A\rangle = \prod_{i=1}^{k} M^*_{z'^{(i)}_A} M_{z^{(i)}_A} \times \sum_b \frac{\prod_{i=1}^k \varphi^*_t(b|z'^{(i)}_A)\varphi_t(b|z^{(i)}_A)}{[p_t(b)]^{k-1}} \ . \tag{5.37}$$

To estimate the matrix elements at late times, it is useful to introduce the k^{th} *no-resonance condition* [215]. The spectrum of a Hamiltonian satisfies satisfies this condition if for any two different size-k sets of energy eigenvalues, their sums are different. We expect the ℓ-bit Hamiltonian to satisfy this condition due to the random interactions between the spins. Under this assumption and noting the time-dependence of φ_t in Eq. 5.34, we expect any matrix element in Eq. 5.37 to have an oscillatory component and therefore evaluate to zero, unless $|Z_A\rangle$ and $|Z'_A\rangle$ are equal up to a permutation, $(z^{(1)}_A, \cdots, z^{(k)}_A) = \sigma(z'^{(1)}_A, \cdots, z'^{(k)}_A)$ for some permutation operator $\sigma \in S_k$ with S_k the permutation group of k elements. More over note that the matrix elements are invariant under the permutations of the replicas. The k^{th} moment of the PE can

therefore be expressed as

$$\rho_A^{(k)} = \sum_{Z_A} \sum_{\sigma \in S_k} |Z_A\rangle \langle \sigma(Z_A)| \, \varrho_{Z_A}^{(k)} , \tag{5.38}$$

where $|Z_A|$ is the number of unique z_A bitstrings among the k-replicas, and the matrix element is given by

$$\varrho_{Z_A}^{(k)} = \sum_b \frac{\prod_{i=1}^k p(z_A^{(i)}) p_t(b|z_A^{(i)})}{[\sum_{z^A \in \mathcal{Z}^A} p(z_A) p_t(b|z_A)]^{k-1}} . \tag{5.39}$$

We will now use the observation made in Sec. 5.5 that the matrix elements of $\rho_{A,t}^{(k)}$ saturate to steady-state values at long times with temporal fluctuations that decay to zero with system size (see Fig. 5.5). This allows us to approximate the matrix elements in Eq. 5.37 at late-times as their temporal average which can be implemented by averaging the matrix elements over the temporal ensemble, $\mathcal{E}_{\text{temp}}$, defined in Eq. 5.22.

Before averaging the matrix element over the temporal ensemble, we note two points about the distribution of $p_t(b|z_A)$ in $\mathcal{E}_{\text{temp}}$. Firstly, $\varphi_t(b|z_A)$ in Eq. 5.34 is a sum over z_B of phases $e^{\imath E_{z_{AB}} t}$ that depend on z_A, resulting in $p_t(b|z_A) = |\varphi_t(b|z_A)|^2$ for different z_A being uncorrelated in the temporal ensemble at late times except when $\alpha \to 0$. In the latter case, $p_t(b|z_A)$ is independent of z_A and causes, large deviation of the point at $\alpha = 0$ in Fig. 5.3 from the Scrooge ensemble arises from this correlation. Secondly, $\varphi_t(b|z_A)$ can be interpreted as the amplitude of a bitstring b in a time-evolved state with a modified ℓ-bit Hamiltonian H_B which is obtained from H (Eq. 5.18) by setting the degrees of freedom in A to classical values determined by z_A. We therefore expect the probability distribution of $p_t(b|z_A)$ to be described by a Porter-Thomas distribution (5.23) (as discussed in Sec. 5.5) with a mean given by

$$\mu(b) = \sum_{z^B \in \mathcal{Z}^B} |M_{z_B}|^2 |\langle b|z_B\rangle|^2 . \tag{5.40}$$

The matrix element in Eq. 5.39 upon averaging over the temporal ensemble can thus be expressed as

$$\varrho_{Z_A}^{(k)} = \sum_b \int \left(\prod_{z_A} \frac{dp(b|z_A)}{\mu(b)} e^{-\frac{p(b|z_A)}{\mu(b)}} \right) \times \frac{\prod_{i=1}^k p(z_A^{(i)}) p_t(b|z_A^{(i)})}{[\sum_{z^A \in \mathcal{Z}^A} p(z_A) p_t(b|z_A)]^{k-1}} . \tag{5.41}$$

Though $p(b|z_A A) \in [0,1]$, since $\mu(b)$ is typically much smaller than 1 and the integrand decays exponentially with $p(b|z_A)/\mu(b)$, we can extend the upper limit of integration over $p(b|z^A)$ from 1 to ∞. Performing a variable transformation $\frac{p(b|z_A)}{\mu(b)} p(z_A) \to Y_{z_A}$ and noting that $\sum_b \mu(b) = 1$, we obtain for the matrix element

$$\varrho_{Z_A}^{(k)} = \int \left(\prod_{z_A} \frac{dY_{z_A}}{p(z_A)} e^{-\frac{Y_{z_A}}{p(z_A)}} \right) \frac{\prod_{i=1}^k Y_{z_A^{(i)}}}{\left(\sum_{z_A} Y_{z_A} \right)^{k-1}} . \tag{5.42}$$

We will next compute the corresponding matrix elements of the Scrooge ensemble and show that

they are identical to the result obtained above in Eq. 5.42.

5.6.2 Matrix elements of the Scrooge ensemble

In order to derive the matrix elements of the Scrooge ensemble, corresponding to $\rho_{A,\infty}$, we will use the fact that it can be viewed as a distortion of the Haar ensemble as in Eq. 5.7 and its k^{th} moment, following Eq. 5.8 is given by

$$\rho^{(k)}_{A,\text{Scr}} = D_A \int d\psi \; P_{\text{Haar}}(\psi) \frac{(\sqrt{\rho_{A,\infty}}|\psi\rangle\langle\psi|\sqrt{\rho_{A,\infty}})^{\otimes k}}{\langle\psi|\rho_{A,\infty}|\psi\rangle^{k-1}}\,, \tag{5.43}$$

where $D_A = 2^{L_A}$ is the Hilbert-space dimension of A and the integral is over Haar-random states in A. Note from Eq. 5.31 that $\rho_{A,\infty}$ is diagonal in the σ^z-product state basis with eigenvalues $p(z_A)$, such that the matrix element can be written as

$$\langle Z'_A|\rho^{(k)}_{A,\text{Scr}}|Z_A\rangle = D_A \int d\psi \; P_{\text{Haar}}(\psi) \times \frac{\prod_{i=1}^k \sqrt{p(z_A^{(i)})p(z_A^{\prime(i)})}\psi_{z_A^{(i)}}\psi^*_{z_A^{\prime(i)}}}{[\sum_{z_A} p(z_A)|\psi_{z_A}|^2]^{k-1}}\,. \tag{5.44}$$

where $\psi_{z_A} = \langle z_A|\psi\rangle$. Due to the Haar averaging the product of the amplitudes $\psi_{z_A^{(i)}}\psi_{z_A^{\prime(i)}}$ in the numerator of the above equation, the matrix elements vanishes unless $|Z_A\rangle$ and $|Z'_A\rangle$ are equal upto a permutation, exactly analogous to the PE at late times. The k^{th} moment of the Scrooge ensemble therefore has the form identical to that in Eq. 5.38 but with the corresponding matrix element given by

$$\varrho^{(k)}_{\text{Scr},Z_A} = D_A \int d\psi \; P_{\text{Haar}}(\psi) \qquad \frac{\prod_{i=1}^k p(z_A^{(i)})|\psi_{z_A^{(i)}}|^2}{[\sum_{z_A} p(z_A)|\psi_{z_A}|^2]^{k-1}}\,. \tag{5.45}$$

The integral over the Haar random states can be performed using standard techniques (see Appendix 5.A for details) which yields

$$\varrho^{(k)}_{\text{Scr},Z_A} = \int \left(\prod_{z_A} \frac{dX_{z_A}}{p(z_A)} e^{-\frac{X_{z_A}}{p(z_A)}}\right) \frac{\prod_{i=1}^k X_{z_A^{(i)}}}{\left(\sum_{z_A} X_{z_A}\right)^{k-1}}\,, \tag{5.46}$$

for the matrix element $\varrho^{(k)}_{\text{Scr},Z_A}$. Comparing the expression for the Scrooge ensemble in Eq. 5.46 with that obtained for the PE in Eq. 5.42, it is straightforward to see that they are identical with the identification of the integration variables $X_{z_A} \leftrightarrow Y_{z_A}$. This concludes our proof of the statement that if PoP of bitstrings approach uncorrelated PT distributions, the PE at late times approaches the Scrooge ensemble corresponding to $\rho_{A,\infty}$.

5.7 Conclusion

In this chapter, we investigated the projected ensemble obtained by single site measurements of all qubits outside a small subsystem of a unitarily evolving system with has (quasi)locally conserved

charges. In particular, we numerically studied a strongly disordered Floquet spin-chain known to exhibit MBL dynamics for very long timescales as well as an ℓ-bit model, a phenomenological model which is manifestly MBL and has an extensive number of 1-local conserved charges, $\{\sigma_i^z\}$. Our analysis suggests that for generic measurement bases not very close to the conserved charges, the PE converges to the Scrooge ensemble (in the limit of large number of measured qubits). Specifically for the ℓ-bit model, the projected ensemble converges to a Scrooge ensemble if the qubits are measured along angles (α that parametrize the polar angle of the direction $\hat{n}$ for the Pauli observables $\boldsymbol{\sigma} \cdot \hat{n}$ that are measured on each site) that are not close to the direction of the conserved charges (α=0 for σ_i^z). Numerical tests on first three moments confirm that the the PE indeed approaches a k=3-design of the Scrooge ensemble. For α near 0, the bitstring measurement probabilities develop correlations that cause a deviation from Scrooge ensemble moments. It is unclear how these correlations scale with system size. Numerical results within available system sizes show exponential decay of trace distances of the moments from the Scrooge values for all $\alpha \gtrsim 0.1\pi$.

This behavior is in contrast to cases with global conserved charges where the PE converges to a angle dependent convex mixture of Scrooge ensembles, called the generalized Scrooge ensemble [215, 217]. In this case, revelation of partial information about the charges in subsystem B due to measurements also reveals partial information about the charges in subsystem A as the two are related via the global constraint.

On the other hand, in the case with locally conserved charges, even though measurements reveal information (even if partial) about the charges local to B, they do not reveal anything about the charges in the subsystem A. The PE should then approach the ensemble that maximizes the entropy subject to the constraints of the charges in A; this is nothing but the Scrooge ensemble constructed out of $\rho_{A,\infty}$. In the pathological case of $\alpha = 0$, when the measurements basis perfectly coincides with the conserved charges and the asymptotic PE is different from the Scrooge ensemble. The asymptotic PE of states in A obtained by σ^z-measurements on B has a trivial form (see Appendix 5.C).

The convergence to the Scrooge ensemble can be related to the fact that the probability distribution PoP of the expectation values of Π_b (projectors into specific bitstring states for the measured observables) in the temporal ensemble (made of states sampled from the time evolution trajectory) approach the Porter-Thomas distribution in the long time limit. We find, numerically, that the distribution indeed approaches the Porter-Thomas distribution. This empirical result, which is expected in the PoP of chaotically evolving systems, is surprising here given that the ℓ-bit Hamiltonian has a large number of local conserved charges. Though, we have not been able to prove these empirical results, we believe that this may be related to ergodicity in the unitary group $U(2^L)$ of the trajectories of all unitaries of the form $U_x U_t$ where U_t is the unitary time evolution operator and U_x are all elements of the stabilizer group of the bitstring states.

Though the results presented are for the ℓ-bit Hamiltonian with finite interaction range (taken to be $\xi = 2$ here), the results regarding the limiting distributions are valid even for longer range interacting systems with the same 1-local-conserved charges. The latter will approach the same limiting ensembles faster. A question for the immediate future is to understand the the mechanism that produces the power-law in time behavior in the approach to the Scrooge ensemble. In

particular, it will be interesting to understand if this power-law decay is related to the power-law decay of temporal fluctuations of local observables in the MBL phase [55] or the power-law decay of bipartite purity (equivalent to logarithmic growth of bipartite entanglement) [227, 228] in MBL systems.

Finally, note that while the local conserved charges in the ℓ-bit Hamiltonian were manifestly built-in, in a genuine MBL systems, they are expected to be emergent at strong disorder. It remains a question as to whether the PE and its higher moments can shed deeper insights and lead to better understanding of the MBL regime that goes beyond the breakdown of conventional ETH.

Appendix 5.A Calculation of matrix elements for kth moments of the Scrooge ensemble

In this appendix, we provide some details of the derivation of the matrix elements of the moments of the Scrooge ensemble, in particular, the steps involved in obtaining the result in Eq. 5.46 from Eq. 5.45. The steps follow closely the derivation of the Scrooge ensemble in Ref. [215].

The integration over the Haar measure can be explicitly performed using

$$P_{\text{Haar}}(\psi)d\psi = \frac{(D_A-1)!}{\pi^{D_A}}\delta(1-\sum_{z_A}|\psi_{z_A}|^2)\prod_{z_A}d^2\psi_{z_A}\,. \tag{5.47}$$

However, since the integrand in Eq. 5.45 depends only on $\{|\psi_{z_A}|^2\}$ the integral over the phases in ψ_{z_A} can be done trivially. Defining a new variable $X_{z_A} = p(z_A)|\psi_{z_A}|^2$, Eq. 5.45 on using Eq. 5.47 takes the form

$$\varrho^{(k)}_{\text{Scr},Z_A} = (D_A!)\int\left(\prod_{z_A}\frac{dX_{z_A}}{p(z_A)}\right)\delta\left(1-\sum_{z_A}\frac{X_{z_A}}{p(z_A)}\right)\frac{\prod_{i=1}^k X_{z_A^{(i)}}}{[\sum_{z_A}X_{z_A}]^{k-1}}\,. \tag{5.48}$$

The δ-function can be removed using a Laplace transform trick. We define

$$f^{(k)}_{Z_A}(t) = (D_A!)\int\left(\prod_{z_A}\frac{dX_{z_A}}{p(z_A)}\right)\delta\left(t-\sum_{z_A}\frac{X_{z_A}}{p(z_A)}\right)\frac{\prod_{i=1}^k X_{z_A^{(i)}}}{[\sum_{z_A}X_{z_A}]^{k-1}}\,, \tag{5.49}$$

with the identification that $\varrho^{(k)}_{\text{Scr},Z_A} = f^{(k)}_{Z_A}(t=1)$. The Laplace transform of Eq. 5.49 gives

$$\tilde{f}^{(k)}_{Z_A}(s) = \int_0^\infty dt\; e^{-st}f^{(k)}_{Z_A}(t) = (D_A!)\int\left(\prod_{z_A}\frac{dX_{z_A}}{p(z_A)}\right)\frac{\prod_{i=1}^k X_{z_A^{(i)}}}{[\sum_{z_A}X_{z_A}]^{k-1}}\exp\left(-s\sum_{z_A}\frac{X_{z_A}}{p(z_A)}\right) \tag{5.50}$$

$$= \frac{(D_A!)}{s^{D_A+1}}\int\left(\prod_{z_A}\frac{dX_{z_A}}{p(z_A)}e^{-\frac{X_{z_A}}{p(z_A)}}\right)\frac{\prod_{i=1}^k X_{z_A^{(i)}}}{[\sum_{z_A}X_{z_A}]^{k-1}}\,, \tag{5.51}$$

where in the second line we performed a change of variables $X_{z_A}\to X_{z_A}/s$. Since the inverse

Laplace transform of $D_A!/s^{D_A+1}$ is simply t^{D_A}, we have

$$\varrho^{(k)}_{\text{Scr},Z_A} = f^{(k)}_{Z_A}(t=1) = \int \left(\prod_{z_A} \frac{dX_{z_A}}{p(z_A))} e^{-\frac{X_{z_A}}{p(z_A)}} \right) \frac{\prod_{i=1}^{k} X_{z_A^{(i)}}}{[\sum_{z_A} X_{z_A}]^{k-1}} \,, \tag{5.52}$$

which is exactly the result in Eq. 5.46.

Appendix 5.B Comparison of $\mathcal{E}_{\text{temp}}$ with random phase ensemble

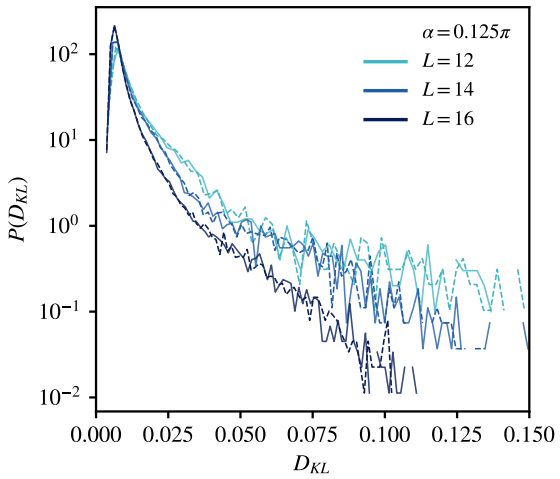

Figure 5.9: The random phase ensemble (dotted lines) is compared with the $\mathcal{E}_{\text{temp}}$ (solid lines) for $\alpha = \pi/8$. For all L values, the distribution of D_{KL} with PT for both ensembles match closely.

Here, we further investigate the appearance of long tail in distribution of D_{KL} for states in $\mathcal{E}_{\text{temp}}$. We construct the random phase ensemble ($\mathcal{E}_{\text{random-phase}}$)which is proposed to be the limiting ensemble of $\mathcal{E}_{\text{temp}}$ if the hamiltonian H satisfies the k-th no-resonance condition and the initial state has finite overlap with all energy eigenstates[215].

$$\mathcal{E}_{\text{random-phase}} = \left\{ \sum_{j=1}^{D} c_j e^{-\imath\phi_j} \, |z_j\rangle \right\}. \tag{5.53}$$

where $c_j = \langle\psi_0|E_j\rangle$ where E_j are energy eigenstates ($|z_j\rangle$ for ℓ-bit Hamiltonian) and ϕ_js are uniformly sampled from $[0, 2\pi]$. We keep equal number of states in $\mathcal{E}_{\text{random-phase}}$ and $\mathcal{E}_{\text{temp}}$. In Fig. 5.9, the distribution of D_{KL} is almost identical for both the ensembles. This rules out any finite-time effect for the appearance of the log-tail. It can be attributed purely to the effect of measurement basis.

Appendix 5.C Projected ensemble with σ^z-measurements

In this section, we derive the kth moment of the PE for the case of σ^z-measurements ($\alpha = 0$) and show that they are different from the Scrooge ensemble. Using the notation in Sec. 5.6, the

state at time t is given by

$$|\psi_t\rangle = \sum_{z_A \in \mathcal{Z}_A} \sum_{z_B \in \mathcal{Z}_B} M_{z_A} M_{z_B} e^{-\imath t E_{z_A z_B}} |z_A z_B\rangle \ , \tag{5.54}$$

such that a σ^z-measurement on B yields the bitstring z_B with probability $p(z_B) = |M_{z_B}|^2$ and the corresponding state on A is

$$|\psi_{A,t}(z_B)\rangle = \sum_{z_A \in \mathcal{Z}_A} M_{z_A} e^{-\imath t E_{z_A z_B}} |z_A\rangle \ . \tag{5.55}$$

Denoting $|M_{z_{A/B}}|^2 = p(z_{A/B})$, the k^{th} moment of the PE therefore has matrix elements

$$\langle Z'_A | \rho^{(k)}_{A,t} | Z_A \rangle = \sum_{z_B \in \mathcal{Z}_B} p(z_B) \prod_{i=1}^{k} M^*_{z'^{(i)}_A} M_{z^{(i)}_A} \exp\left[-\imath t \left(E_{z^{(i)}_A z_B} - E_{z'^{(i)}_A z_B} \right) \right] . \tag{5.56}$$

In the limit of $t \to \infty$, the k^{th} no-resonance condition again implies that the matrix element above is non-zero only if $|Z'_A\rangle$ is a permutation of $|Z_A\rangle$ such that

$$\rho^{(k)}_A = \sum_{Z_A} \sum_{\sigma \in S_k} |Z_A\rangle \langle \sigma(Z_A)| \, \varrho^{(k)}_{Z_A} \, , \tag{5.57}$$

and the matrix element is given by

$$\varrho^{(k)}_{Z_A} = \prod_{i=1}^{k} p(z^{(i)}_A) \, . \tag{5.58}$$

Note the structure of the k^{th} moment of the PE here is same as the Scrooge ensemble - location of the non-zero matrix elements are the same. However the matrix element for the Scrooge ensemble in Eq. 5.46 can be written as

$$\varrho^{(k)}_{\text{Scr},Z_A} = \prod_{i=1}^{k} p(z^{(i)}_A) \ \times \ \int \left(\prod_{z_A} dx_{z_A} \ e^{-x_{z_A}} \right) \frac{\prod_{i=1}^{k} x_{z^{(i)}_A}}{(\sum_{z_A} x_{z_A} p(z_A))^{k-1}} \, . \tag{5.59}$$

Note that the expressions in Eq. 5.58 and Eq. 5.59 are obviously different in general from each other for general $\{p(z_A)\}_{z_A}$, which are set by the initial state, as the integral in the RHS of the above equation does not evaluate to unity in general.

6

Quantum Chaos on Erdős–Rényi Random Graphs

The arc traced by the preceding sections, beginning with expectation values and linear response in Sec. 1.3.3, moving through the full distribution of a single observable via full counting statistics in Sec. 1.6, and arriving at the full distribution of conditional states via the projected ensemble in Sec. 1.8, has been one of progressively finer statistical resolution, with each step refining the one before. The full counting statistics refines an expectation value into its full distribution, and the projected ensemble contains every full counting statistics as a marginal. Chapter 6 completes the thesis through a complementary move. Rather than adding a further layer of resolution on a single diagnostic, it deploys several *independent* probes simultaneously on one tunable system. The projected ensemble , the partial spectral form factor, Krylov complexity, and the quantum Mpemba effect applied to the Ising model on Erdős–Rényi random graphs, whose mean connectivity interpolates smoothly between a one-dimensional integrable limit and a fully-connected chaotic one.

The alignment with present-day programmable quantum simulators is deliberate. Each diagnostic reduces, at the experimental level, to statistics of projective measurements in a product basis: bit-string frequencies for the projected-ensemble moments and the pSFF. Krylov complexity, while experimentally chalenging to access at present works as a proxy to closely related qunatities that have been experimentally accessed. The graph-Ising Hamiltonian itself sits close to the native geometry of reconfigurable neutral-atom arrays, on which transverse-field Ising models have been realised on programmable graphs with hundreds of sites [231, 232], and of trapped-ion platforms with site-resolved readout and tunable long-range couplings [233]. In Chapter 6 we exploit this confluence of tunable system and experimentally accessible probes to locate the chaos–integrability transition by *cross-validation*: each diagnostic is sensitive to a different facet of the dynamics, and the connectivity threshold at which they agree pins the transition down more sharply than any one of them in isolation.

This chapter is adapted from the publication: G. J. Sreejith and **Sandipan Manna**, "Signatures of quantum chaos and complexity in the Ising model on random graphs," Phys. Rev. B 113, 214322 (2026).

6.1 Introduction

Quantum Ising models have played a central role in the many-body physics of quantum phase transitions [234, 235, 236], arising naturally in both lattice systems and disordered, glassy settings [237, 238, 239]. They also serve as the framework for quantum annealing (QAA) and variational quantum algorithms (VQA), which encode classical optimization problems in an Ising Hamiltonian and use quantum fluctuations to search for low-energy solutions [240, 241, 242, 243, 244, 245, 246]. Hardware connectivity constraints [247, 248] as well as the need to encode general graph optimization problems [232, 249, 250] make the dynamics of these models on random graphs a question of direct practical relevance. Performance of related optimizer circuits [251, 252, 253] has been shown, in specific instances, to correlate with chaos diagnostics such as operator spreading [254, 255, 256] and information scrambling [257, 258, 259, 260, 261, 262, 263]. While these characteristics have been investigated extensively in regular lattice systems [256, 259, 264, 265, 266, 267], studies on irregular graphs remains largely unexplored.

In QAA, the instantaneous Hamiltonian interpolating between a transverse-field driver and an Ising problem Hamiltonian encoded on a random graph can exhibit chaotic dynamics for initial states with finite excitation energy density. While ideal adiabatic evolution remains confined to the low-energy sector and is therefore insensitive to bulk spectral statistics, it has been shown that adding a chaotic perturbation at intermediate times can improve QAA performance by enhancing the bottleneck gap and delocalizing low-energy states in hard optimization instances [252, 251].

An alternate optimization scheme is the Quantum Approximate Optimization Algorithm (QAOA) [268, 241] which resembles a Trotterization of the QAA. The state is evolved under an alternating sequence of transverse field (H_{x}) and cost Hamiltonian (H_{c}), with $\{\gamma_k, \beta_k\}$ as variational parameters of the quantum optimizer circuit, optimized to minimize $\langle H_{\mathrm{c}} \rangle$ on the final state. Unlike QAA, the intermediate states of a QAOA circuit are not constrained to the low-energy sector. Consequently, eigenstates drawn from the bulk of the spectrum of H_{c} or H_{x} may be transiently populated, making bulk spectral properties directly relevant to the circuit dynamics. In simulations of randomly picked finite-size problem instances, we show (Sec. 6.2) that a three-term ansatz with H_{c}, H_{x}, and an additional term H_{d} achieves a better approximation ratio than the standard two-term QAOA when H_{d} exhibits signatures of chaos. However, chaotic intermediate dynamics can also be detrimental: they may exacerbate barren plateaus by suppressing parameter gradients at shallow circuit depths [269, 270, 271]. Quantum chaos has also been identified as a key resource in quantum reservoir computing. In an random-graph Ising setup closely related to the one studied here, it was found that optimal learning performance of a quantum reservoir is achieved at the boundary between the chaotic and localized phases [253]. Thus, a refined understanding and control of the onset of chaos in finite-size random-graph Hamiltonians can provide valuable insights into the development of various proposed use cases for NISQ devices.

In this chapter, we present an investigation of quantum dynamics in the Ising model on Erdős-Rényi (ER) graphs with a mixed field, focusing on how graph connectivity shapes the onset of quantum chaos. We parameterize graph connectivity using the connectance ($\tilde{M}$), which is the fraction of connected edges among all possible edges. For simplicity, we consider the case where Ising coupling strengths are held fixed; disorder in our model arises from the

connectivity pattern and not from randomness in the coupling strengths or the external field. Level spacing distributions, level velocities, and spectral correlations in this model were studied in Ref. [272], where chaotic spectral properties were found to emerge in the intermediate $\tilde{M}$ regime. These are spectral diagnostics as they characterize quantum chaos through eigenvalue correlations alone, and carry no direct information about eigenvector structure. et dynamical processes that are experimentally accessible, such as information scrambling, operator growth, and thermalization, are sensitive to eigenvector structure. To build a more complete picture, we employ diagnostics that probe signatures of chaos in projective measurement outcomes, eigenstate structure, operator spreading, and the growth of complexity under unitary evolution — namely, the projected ensemble statistics, partial spectral form factor, and Krylov complexity. These quantities are more directly connected to dynamical and experimentally accessible observables, and together provide a perspective on quantum chaos that is distinct from, and complementary to, the spectral statistics studied previously.

Conventional studies of quantum thermalization focus on quantities governed by the Eigenstate Thermalization Hypothesis (ETH)-specifically, expectation values of local observables [8, 9, 204]. The projected ensemble (PE) [16, 17] offers a finer characterization by unraveling the density matrix into an ensemble of pure quantum states, enabling analysis beyond the average captured by the density matrix alone. For systems without conserved charges, the PE of a time-evolved state is expected to converge to the Haar ensemble, a condition known as *deep thermalization*. We show that the distance between PE and Haar distribution decays faster with the system size at intermediate $\tilde{M}$. In contrast, in sparse and dense limits ($\tilde{M} \to 0, 1$), the trace distance shows a slow decay with the system size. Next, we focus on the partial spectral form factor (pSFF), which extends the spectral form factor (SFF) to capture correlations between eigenstates and eigenvalues within the subsystem. We empirically demonstrate distinct signatures in the pSFF across different connectivity regimes. Measurements of PE and pSFF have already been experimentally demonstrated in $5 - 25$ qubit systems in various platforms [67, 273, 274, 17, 275]. While our numerical studies are restricted to 15 qubits, quantum devices can be used to extend this investigation to larger systems in the near future.

Heisenberg evolution under a chaotic Hamiltonian drives rapid growth of local operators, both in real space and in operator space [276]. To probe the crossover from an operator-spreading perspective, we compute the Krylov complexity (KC) and its late-time saturation as a function of $\tilde{M}$. In the Krylov subspace, an initial local operator spreads over a set of orthogonal basis states generated by Lanczos tridiagonalization of the Liouvillian superoperator, analogous to a particle propagating on a tight-binding chain with nearest-neighbor hopping. KC quantifies this by measuring the average position of the wave packet in the chain. We observe that the Lanczos coefficients, which correspond to the hopping parameters in the tight-binding interpretation, exhibit enhanced fluctuations near the integrable and localized limits (for finite system sizes). Most importantly, the KC saturation values are significantly larger (and grow faster with system size) in the chaotic regime compared to the localized and integrable regimes.

The crossover from chaotic to integrable and localized regimes is associated with the emergence of approximate conservation laws and local integrals of motion [277, 278, 279]. In the model studied here, this takes two distinct forms: at $\tilde{M} \to 0$, disconnected clusters yield trivial local

conserved charges, while at $\tilde{M} = 1$, a permutation symmetry fragments the Hilbert space (Sec. 6.2). At intermediate $\tilde{M}$, this fragmentation is weakly broken, leaving projections onto Hilbert space fragments as approximate conservation laws that partially obstruct thermalization.

All three diagnostics used in this chapter, i.e., the projected ensemble, the partial spectral form factor, and the Krylov complexity, probe how these conservation laws suppress quantum information scrambling, but from complementary vantages. PE deviates from the Haar ensemble in the presence of conserved quantities, instead approaching an ensemble constrained by the charges. This was demonstrated in the case of $U(1)$ charges [280, 215] and kinetic constraints [219]. The universal ensemble approached under dynamics with more complex or approximate charges has not been studied extensively, and is expected to deviate from the Haar ensemble. The pSFF, an experimentally accessible proxy for the SFF, captures the resulting effect in eigenvalue and eigenstate correlations [281, 282]. Krylov complexity tracks the restricted growth of local operators along symmetry-protected directions in operator space, with lower saturation values in integrable settings. A central finding of this chapter is that all three consistently identify the same connectivity-driven crossover, providing a unified picture of how approximate conservation laws govern the onset of chaos across these complementary facets of quantum dynamics.

This chapter is organized as follows. Section 6.2 provides a brief introduction to the model and its symmetries. We also briefly discuss the QAOA protocol and demonstrate the performance of random graph Ising model as a component in circuit ansatz at various graph connectivity. We utilize the projected ensemble protocol to examine deep thermalization through higher-order moments of quantum state ensembles in Sec. 6.3. In Sec. 6.4, we study the partial spectral form factor (pSFF) of subsystems to identify characteristic signatures of chaotic behavior and its implications in the context of experiments. We also explore the effect of the choice of subsystem on pSFF. Section 6.5 presents results on operator delocalization through Krylov complexity. Finally, Sec. 6.6 discusses the limitations and potential extensions of our study.

6.2 Ising Model on random graphs

In this study, we consider the mixed-field quantum Ising model whose Hamiltonian is given by

$$H = \frac{J}{M} H_{\mathrm{p}} + \frac{g}{L} H_{\mathrm{x}} + \frac{h}{L} H_{\mathrm{z}} \ , \tag{6.1}$$
$$H_{\mathrm{p}} = -\sum_{i,j} A_{ij} Z_i Z_j, \quad H_{\mathrm{x}} = -\sum_i X_i, \quad H_{\mathrm{z}} = -\sum_i Z_i \ .$$

$\{X_i, Y_i, Z_i\}$ are Pauli matrices acting on site i and g, h are the strengths of the transverse and longitudinal field, respectively. A_{ij} is the adjacency matrix of the underlying graph, where spins are the nodes. $A_{ij} = 1(0)$ if there is a coupling (no coupling) between spins i and j. We take $J = 1$ throughout this chapter. The adjacency matrices are chosen to represent random ER graphs [283] $\mathcal{G}(L, M)$ where L and M denote the number of nodes and edges, respectively. M can be obtained as $M = \frac{1}{2}\sum_{i,j} A_{ij}$. The denominators L, M in Eq. 6.1 ensure that the bandwidth of the energy spectrum scales as $\approx O(JL^0M^0)$. For $g = 0$, there is a global $U(1)$ symmetry. For generic g, at $h = 0$, the model has a global parity symmetry given by, $\mathcal{P} = \prod_{i=1}^{L} X_i$. All edges have equal strength (J) and graph-to-graph variation arises entirely from the adjacency

matrix. For L sites, the maximum possible number edges is $M_{\max} = \binom{L}{2}$. We define the connectance $\tilde{M} = M/M_{\max}$ to characterize the graphs. For each $\tilde{M}$ we sample graphs with $\tilde{M}M_{\max}$ edges with uniform probability. $\tilde{M} = 0$ and 1 correspond to the non-interacting and

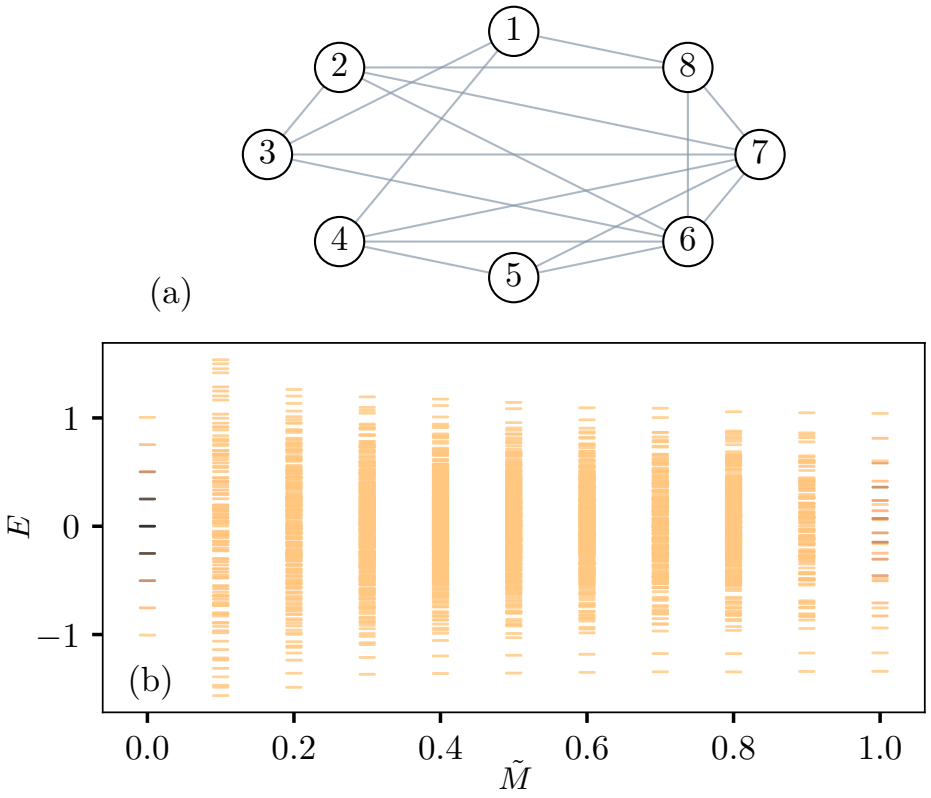

Figure 6.1: (a) A single realization of Erdos-Renyi graph with $L = 8$ nodes and connectance, $\tilde{M} = 0.6$ which implies number of connected edges, $M = 17$. Interacting pairs are represented by connected edges. (b) Eigen-spectrum of Hamiltonian in Eq. 6.1 for an instance at each $\tilde{M}$ with $L = 8$. We have used darker shades to indicate degeneracy.

integrable LMG (Lipkin–Meshkov–Glick model [284]) limits, respectively (the presence of a small longitudinal field causes deviation in spectral characteristics from the LMG model in finite systems). Figure 6.1(a) shows one realization of such a lattice. We take $J = 1$ and $g = 1$, thus working with a ferromagnetic Hamiltonian. h is taken to be a small positive value in subsequent sections to break the model's parity symmetry. The dynamical properties studied in this chapter characterize the bulk of the spectrum, which is expected to be independent of the ferromagnetic or anti-ferromagnetic nature of the ground state, i.e., the sign of J.

The onset of chaos with $\tilde{M}$ in this model (with $h = 0$) was studied in Ref. [272] using level spacing statistics, level velocity, and spectral form factor. The system exhibits chaotic behavior at intermediate connectivity, with spectral features matching Wigner-Dyson (WD) statistics, and shows deviations at extreme $\tilde{M}$ in finite-system studies. Figure 6.1(b) shows the eigenvalue spectrum of this Hamiltonian at $L = 8, g = 1.0$ and $h = 0.1$ for a representative realization at each $\tilde{M}$. For intermediate $\tilde{M}$, the level-spacing distribution in the unfolded spectrum is close to the WD distribution for numerically accessible systems. It approaches the WD distribution with

increasing L for $\tilde{M}$ close to 1 and 0 when g takes a value in $0.5J < g < 4J$. Thus, at large enough L, and intermediate values of g, the level spacing ratio is expected to be WD for all $\tilde{M} \neq 0, 1$. At very large and small values of g, the system is nearly non-interacting, with eigenstates given by simple product states to a good approximation; thus, the level-spacing ratio deviates from WD.

We choose $g = 1$ throughout to retain the possibility of chaotic behavior in the system sizes studied ($6 \leq L \leq 15$). Next, we discuss the symmetries of this Hamiltonian at extremal $\tilde{M}$.

6.2.1 Symmetries and conservation laws near $\tilde{M} = 0$ and 1

At small $\tilde{M}$ and finite system sizes, ER graphs consist of weakly connected clusters. The Hamiltonian then decomposes effectively into smaller blocks with support only within individual clusters, leading to a breakdown of ergodicity. Consequently, eigenstates in this regime are weakly entangled, with bipartite entanglement entropy across a real-space cut remaining well below the volume-law value expected for chaotic systems, a trend we confirm for $\tilde{M} < 0.3$ (Fig. 6.14 in Appendix 6.A). However, the percolation threshold for ER graphs is $\tilde{M}_c \sim 1/L$, so for any fixed small $\tilde{M} > 0$, increasing the system size L eventually drives the graph past this threshold, beyond which a giant component of size $\mathcal{O}(L)$ emerges [285]. Equivalently, at fixed L, chaotic behavior sets in once $\tilde{M}$ exceeds $\mathcal{O}(1/L)$. This structural crossover in the $(\tilde{M}, L)$ plane underlies the system-size-dependent onset of chaos observed in our study at small $\tilde{M}$.

At $\tilde{M} = 1$ and $h = 0$, the Hamiltonian in Eq. 6.1 can be rewritten as

$$H = \frac{1}{2M} S_z^2 + \frac{1}{L} S_x, \tag{6.2}$$

up to an additive constant, where $S_x = \sum_i X_i$ and $S_z = \sum_i Z_i$. The Hamiltonian is symmetric under the permutation group S_L (relabeling of spin indices) and commutes with the total spin squared $S^2 \equiv S_x^2 + S_y^2 + S_z^2$. As a consequence, the vector space can therefore be decomposed into

$$V = \sum_{S=S_{\min}}^{L/2} V_S \otimes V_P, \tag{6.3}$$

where $S_{\min} = 0(1/2)$ if L is even (odd). V_S forms a spin S irrep of $SU(2)$ and V_P is some irrep of S_L representing the multiplicity of the S representation. On this decomposition, H acts as $\sum_S^{\oplus} H_S \otimes \mathbb{I}_{V_P}$. To explicitly see this, we can use the following three-spin/qubit example. The space decomposes into irreps of $SU(2)$ as $\frac{3}{2} \oplus \frac{1}{2} \oplus \frac{1}{2}$. In the following basis

$$\begin{gathered}
|\tfrac{3}{2}, m - \tfrac{3}{2}\rangle \propto S_+^m |000\rangle;\ m = 0, 1, \ldots 3 \\
|\tfrac{1}{2}, -\tfrac{1}{2}, \alpha = 0\rangle \propto (|01\rangle - |10\rangle)|0\rangle \\
|\tfrac{1}{2}, +\tfrac{1}{2}, \alpha = 0\rangle \propto (|01\rangle - |10\rangle)|1\rangle \\
|\tfrac{1}{2}, \tfrac{1}{2}, \alpha = 1\rangle \propto \sqrt{\tfrac{2}{3}}\,|110\rangle - \tfrac{1}{\sqrt{6}}(|101\rangle + |011\rangle) \\
|\tfrac{1}{2}, -\tfrac{1}{2}, \alpha = 1\rangle \propto \tfrac{1}{\sqrt{6}}(|100\rangle + |010\rangle) - \sqrt{\tfrac{2}{3}}\,|001\rangle
\end{gathered}$$

where the α index represents the multiplicity sector, S_+ is the collective spin raising operator,

Hamiltonian has the form

$$H = \begin{bmatrix} H_{\frac{3}{2}} & 0 & 0 \\ 0 & H_{\frac{1}{2}} & 0 \\ 0 & 0 & H_{\frac{1}{2}} \end{bmatrix} \equiv H_{\frac{3}{2}} \oplus H_{\frac{1}{2}} \otimes \mathbb{I}_2 \tag{6.4}$$

In a similar way, the $L = 4$ case decomposes as $H_2 \oplus H_0 \otimes \mathbb{I}_2 \oplus H_1 \otimes \mathbb{I}_3$.

The permutation symmetry and the commutation with S^2 lead to extensive Hilbert space fragmentation with maximal fragment size upper bound by $L + 1$ (corresponding to the $S = \frac{L}{2}$ sector). Less important here, the permutation symmetry guarantees extensive degeneracy from the multiplicity space acting as a zero mode. The small fragments imply that the initial states undergo very restricted expansion in the Hilbert space, resulting in the absence of thermalization. As the bonds are removed when $\tilde{M} < 1$, the symmetries are lost, resulting in weak coupling of the sectors. Eigenstates still have large weights in one block, resulting in an eigenstate ordering inherited from the nearby $\tilde{M} = 1$ point.

When $\tilde{M} = 1 - \epsilon$ for small $\epsilon > 0$, i.e., just below the maximally connected limit, the Hamiltonian can be viewed as a perturbation of the LMG model by a term

$$V = \frac{2J}{L(L-1)\tilde{M}} \sum_{\langle ij \rangle_{\text{del}}} Z_i Z_j, \tag{6.5}$$

where the sum runs over the $\epsilon L(L-1)/2$ deleted bonds. Before the perturbation, the LMG energy eigenvalues depend only on the S^2 eigenvalue, $E = E(s)$. The perturbation introduces off-diagonal blocks coupling different s sectors. For s away from the fully polarized limits, each s sector is exponentially degenerate, with multiplicity

$$m(s) = \frac{2s+1}{L/2+s+1} \binom{L}{L/2-s}. \tag{6.6}$$

Treating the degenerate eigenstates as random vectors in the computational basis with typical coefficient magnitude $\sim 2^{-L/2}$, the off-diagonal blocks coupling sectors s and s' have dimensions $m(s) \times m(s')$ (exponentially large in L) and matrix elements of order $\langle s|V|s'\rangle \sim \mathcal{O}(\sqrt{\epsilon}/2^{L/2})$. Although individual matrix elements are exponentially small, the coupling between exponentially large degenerate blocks leads to a lifting of the block-diagonal structure and mixing of eigenstates at large L. While this constitutes only a plausibility argument for the emergence of chaos at any finite ϵ, our numerical results are consistent with this picture.

While an atypical initial state, such as a direct product state, will have overlap with an extensive number of energy eigenstates, taking it to an infinite temperature diagonal ensemble at equilibration, the eigenstate ordering results in overlaps with only a restricted set of eigenstates, resulting in the diagonal ensemble deviating from the infinite temperature ensemble. We explicitly show this distinction through the inverse participation ratio (IPR) of such product state in the basis of eigenstates (Fig. 6.15 in Appendix 6.A).

In the rest of this section, we demonstrate that chaotic dynamics in such a Hamiltonian can affect QAOA performance when this Hamiltonian is employed as an additional term in QAOA protocol.

6.2.2 QAOA with random Ising driver

Here, we empirically demonstrate, in the specific setting of QAOA, that chaos in the instantaneous Hamiltonian can be relevant to the circuit performance. We consider the problem of minimizing a classical Ising cost Hamiltonian of the form

$$H_{\mathrm{c}} = \sum_{i,j \in C} W_{ij} Z_i Z_j, \tag{6.7}$$

defined on a random graph C with L nodes. Several difficult classical optimization problems [286], such as MAXCUT and SAT, can be cast as ground-state search of such an Ising Hamiltonian [242]. For the numerical demonstrations in this section, we sample the graph C from a set of ER graphs and sample the edge weights W_{ij} uniformly from $\{+1, -1\}$. The standard QAOA ansatz alternates between the cost unitary $e^{\imath\gamma_k H_{\mathrm{c}}}$ and a mixer unitary $e^{\imath\beta_k H_{\mathrm{x}}}$ where γ_k, β_k are variational parameters associated with the k-th layer which are to be optimized. The entire circuit consists of p such layers. Here, we modify this QAOA protocol by adding an additional driver unitary $e^{\imath\alpha_k H_{\mathrm{d}}}$ in each layer as illustrated in Fig. 6.2. H_{d} is a mixed-field Ising model on an ER graph

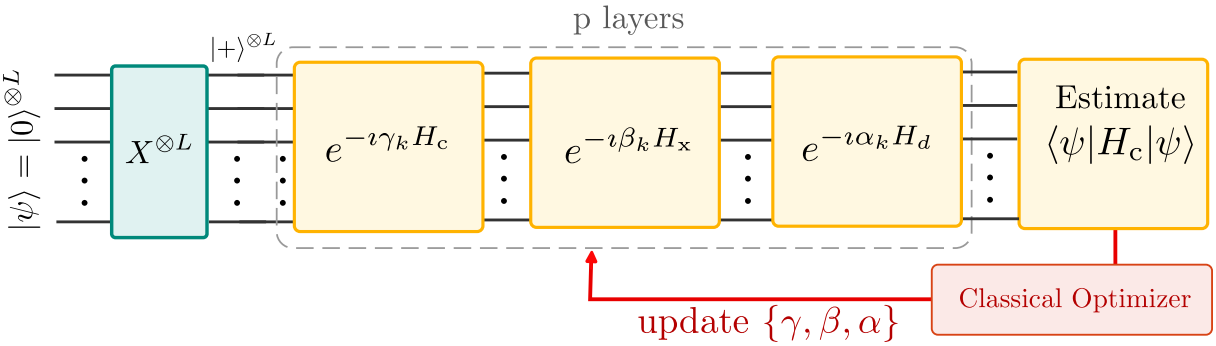

Figure 6.2: An outline of QAOA protocol. The three-term variational circuit is parameterized by $\{\alpha_k, \beta_k, \gamma_k\}$. The entire circuit consists of p such layers. The input state of the ansatz is taken as $|+\rangle^{\otimes L}$. The energy of the cost function is optimized with a classical optimizer and the parameters are iteratively updated using gradient descent.

with Pauli-YY interaction given as,

$$H_{\mathrm{d}}^{YY} = -\frac{JL}{M} \sum_{i,j} A_{ij} Y_i Y_j - g \sum_i X_i. \tag{6.8}$$

Its spectral properties are identical to those of the annealing Hamiltonian (Eq. 6.1 with $h = 0$ for simplicity), and its chaotic character is therefore tunable through $\tilde{M}$. Note that the adjacency matrices C (of H_{c}) and A (of H_{d}) are chosen independently. We take the initial state for the ansatz as $|+\rangle^{\otimes L}$ and set $J = g = 1$. The values of α, β, γ are optimized such that $\langle H_{\mathrm{c}} \rangle$ is minimized. These unitaries need to be implemented on quantum devices using a Trotterized approach [287, 288].

To understand the state evolution in such a circuit, we examine the trajectory of the energy expectation value of the instantaneous state at each step of a 4-layer QAOA ansatz (Fig. 6.3). The background horizontal lines show the instantaneous eigenspectrum, colored by the overlap with the optimized state $|\psi_{\mathrm{opt}}\rangle$; the darkest lines, concentrated at the low-energy end of H_c,

indicate that $|\psi_{\text{opt}}\rangle$ is strongly supported on low-energy computational basis states. For optimized parameters (black line), the trajectory navigates through intermediate states with finite energy density, with significant overlap with mid-spectrum eigenstates of H_d at intermediate steps. This is qualitatively distinct from adiabatic evolution, in which the state remains confined to the low-energy manifold at all times. Nevertheless, the optimized circuit successfully drives the final state to near-ground-state energy, as indicated by the diamond marker ($\langle\psi_{\text{opt}}|H_c|\psi_{\text{opt}}\rangle \approx -1$). For randomly chosen parameters (red dashed line), the energy expectation value shows no systematic drift toward low energy, fluctuating throughout the bulk of the instantaneous spectrum.

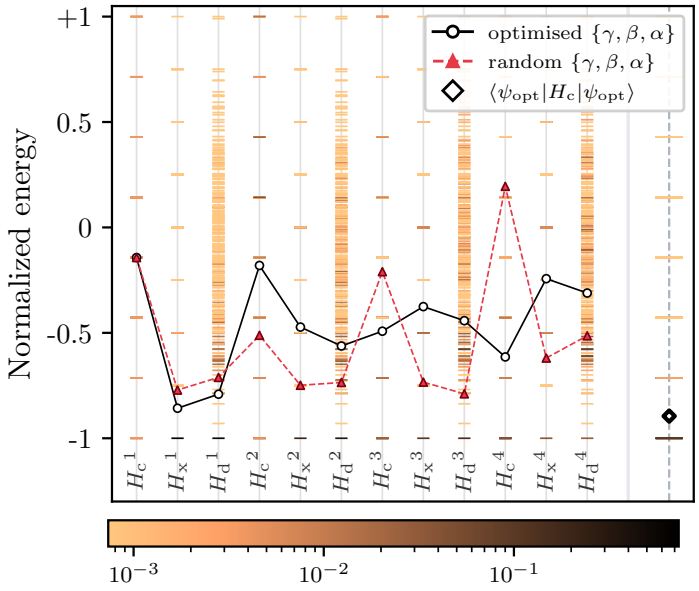

Figure 6.3: Trajectory of energy expectation value of instantaneous state in QAOA dynamics through the eigen-spectrum of instantaneous QAOA Hamiltonian. The thickness of dashes is proportional to the degeneracy of the eigenstates. The ansatz is a 4-layer quantum circuit. The label at the bottom of each stack shows the instantaneous Hamiltonian and the corresponding layer (in superscript). The marker in the right-most stack marks the final energy expectation value of the optimized state, i.e., $\langle\psi_{\text{opt}}|H_c|\psi_{\text{opt}}\rangle$. The color indicates the overlap between the optimized state and the instantaneous eigenspectrum. $L = 8$. The problem graph has a connectivity $\tilde{M}_c = 0.4$.

We now assess the performance of this three-term QAOA protocol as a function of $\tilde{M}$. We show the results for two randomly picked instances of the classical Ising Hamiltonian H_c (Eq. 6.7) on a random ER graph of $L = 8$ sites with $\tilde{M}_c = 0.4$. Keeping H_c fixed, we sample 1000 different realizations of H_d (Eq. 6.8) and optimize a circuit of $p = 2, 3$ layers. In each case, 600 ADAM [289] gradient-descent steps were performed to minimize the cost function $E_{\text{QAOA}} = \langle\psi|H_c|\psi\rangle$ (energy expectation value of the final state with respect to the cost Hamiltonian). E_{QAOA} is evaluated numerically exactly and the gradient is obtained using finite difference method. To gauge the distribution of performance of the optimized QAOA, we compute the approximation ratio for each of the 1000 instances as defined below,

$$\mathcal{R} = \frac{E_{\text{max}} - E_{\text{QAOA}}}{E_{\text{max}} - E_{\text{GS}}} \leq 1 \tag{6.9}$$

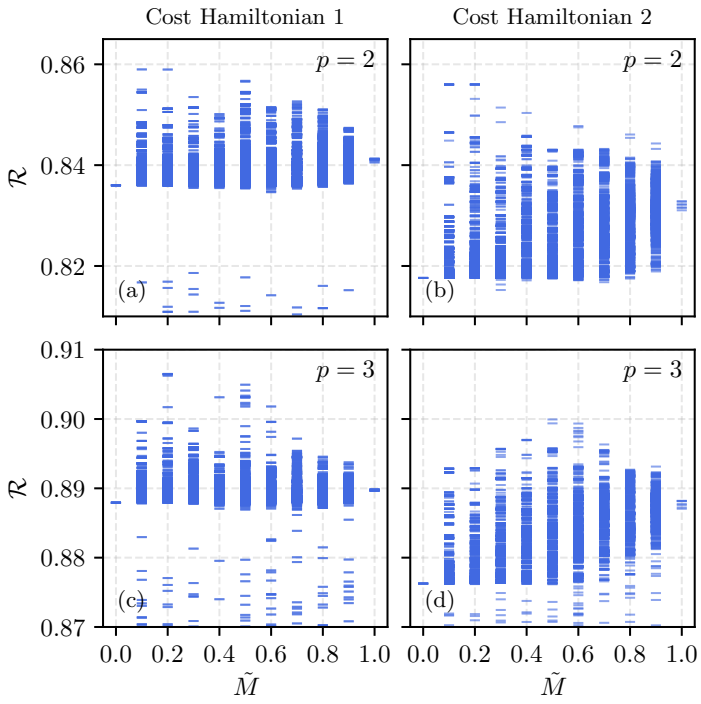

Figure 6.4: Approximation ratio of the optimized state for a QAOA circuit with $L = 8, p = 2$ (a,b) and $L = 8, p = 3$ (c,d). Keeping the problem H_c fixed, for each $\tilde{M}$, we show the QAOA optimized approximation ratio for 1000 random choices of H_d at that $\tilde{M}$. The two columns describe data for two independently sampled problems H_c with $\tilde{M}_c = 0.4$.

Higher $\mathcal{R}$ implies better optimization performance. Here, E_{GS} and E_{max} are the ground state and maximum eigenvalue of H_c respectively. Figure 6.4 shows the distribution of $\mathcal{R}$ values for the two cost Hamiltonians. Two features are particularly notable. First, $\mathcal{R}$ is higher at $\tilde{M} > 0$ compared to the standard transverse-field mixer ($\tilde{M} = 0$) for the majority of driver instances, confirming that the additional Ising mixer improves QAOA performance. Further, the approximation ratio is almost always larger at intermediate $\tilde{M}$, where H_d exhibits chaotic spectral statistics. Note that the spread in $\mathcal{R}$ at $\tilde{M} = 1$ is due to the variation in initial parameter value across multiple gradient-descent optimizations. This correlation suggests possible influence of the chaotic dynamics of H_d on QAOA performance, similar to what was observed for QAA [252] (see Appendix 6.B for additional numerical examples for system size up to $L = 10$).

The improvement in QAOA performance observed with H_d containing YY term can potentially be attributed to two distinct factors: the chaotic nature of H_d, and the presence of terms that scatter between computational basis states with Hamming distance 2, enabling broader exploration of the solution space. To decouple these two contributions, we consider in Appendix 6.B an alternative driver Hamiltonian with Pauli-ZZ coupling,

$$H_d^{ZZ} = -\frac{JL}{M} \sum_{i,j} A_{ij} Z_i Z_j - g \sum_i X_i, \tag{6.10}$$

in which the interaction term is diagonal in the computational basis but have identical spectral properties. We qualitatively obtain the same results, suggesting that the chaotic character of the

entire H_d, rather than the nature of its individual terms, leads to improved performance of the modified QAOA.

Having demonstrated a potential connection between circuit performance and chaos in the dynamics, in the subsequent sections, we present a thorough investigation of the dynamical properties of H_{d}^{ZZ} utilizing multiple complementary probes.

6.3 Projected ensemble and emergence of deep thermalization

ETH predicts that the reduced density matrix of any small subsystem of an isolated quantum system evolving under a generic Hamiltonian relaxes to a Gibbs state determined solely by the initial energy density. This relaxation follows from the delocalization of initial local information across the many-body system, with scrambling as the underlying dynamical mechanism. The subsystem's complement serves as an effective bath, whose degrees of freedom are traced out to yield the reduced density matrix. Under chaotic dynamics satisfying ETH, the resulting reduced state relaxes to a Gibbs ensemble, and all memory of the initial state is effectively erased from local observables. This framework is sufficient to predict expectation values of local subsystem observables. However, modern quantum simulator platforms can track all degrees of freedom simultaneously [210, 231, 233], rendering the system-bath distinction artificial. Access to the bath state allows one to obtain pure states of the subsystem conditioned on the measurement outcome of the bath. The ensemble of such conditional pure states is the Projected Ensemble (PE), and constitutes a physically natural unraveling of the reduced density matrix. While a density matrix admits infinitely many unravelings, the restriction to projective measurements selects a physically motivated one. Unlike the density matrix, which encodes only the first moment of the state ensemble, the PE encodes the full distribution of quantum states in the Hilbert space, providing access to all higher moments and thereby to fluctuations beyond mean observable values. This motivates a distinction between thermalization at the level of local expectation values and the more fundamental notion of *deep thermalization*, which concerns convergence of the underlying quantum state distribution in the projected ensemble to the Haar measure [218, 217, 215, 290, 291, 219, 280, 292, 293, 294].

Consider a system of L sites partitioned into two subsystems, A and B, with $L = L_A + L_B$. Under unitary evolution, the entire system is described by a pure state, $|\psi_{AB}\rangle \in \mathcal{H}_A \otimes \mathcal{H}_B$ at all times. We consider initial states of the form

$$|\psi_{AB}(t=0)\rangle = \frac{1}{\sqrt{2^L}} \bigotimes_{i=0}^{L} (|0\rangle + \imath|1\rangle), \tag{6.11}$$

evolved under the Hamiltonian in Eq. 6.1 (with $J = 1, g = 1$ and $h = 0.1$). The state has 0 energy expectation for this Hamiltonian. In the absence of any conserved charges (other than energy), the subsystem properties are expected to relax to those of a Gibbs ensemble $e^{-\frac{1}{T}H}$ where T is the effective temperature of the initial state. As the Hamiltonian is traceless, $T = \infty$, and the subsystem properties of the time-evolved states (with Eq. 6.11 as initial state) relax to that of the identity density matrix.

We perform simultaneous projective measurements of Pauli-Z on all qubits in subsystem B

on copies of $|\psi_{AB}\rangle$ and collect the corresponding pure state $|\psi_A(b_i)\rangle$ in A conditioned on the measurement outcome b_i,

$$|\psi_{A,b_i}\rangle = \frac{1}{\sqrt{p(b_i)}}\Pi_{b_i}|\psi_{AB}\rangle = |\psi_A(b_i)\rangle \otimes |b_i\rangle, \tag{6.12}$$

where $\Pi_{b_i} = \mathbb{I} \otimes |b_i\rangle\langle b_i|$ and $p(b_i) = \langle\psi_{AB}|\Pi_{b_i}|\psi_{AB}\rangle$. The state $|\psi_{A,b_i}\rangle$ arises with probability $p(b_i)$ and the ensemble of these states, described by $\mathcal{E}_{\rm PE} = \{p(b_i), |\psi_{A,b_i}\rangle\}$, is the PE. When seen as an ensemble of the states in A, its distribution over the Hilbert space of A can be characterized by its k-th moment as, $\rho_{\rm PE}^{(k)} = \sum_{b_i} p(b_i)(|\psi_A(b_i)\rangle\langle\psi_A(b_i)|)^{\otimes k}$. Given the PE, these can be computed using the b_i labels on the ensemble states. The kth moment of any observable's expectation value can be obtained as $\langle\hat{O}^{\otimes k}\rangle_{\rm PE} = {\rm Tr}[\rho_{\rm PE}^{(k)}\hat{O}^{\otimes k}]$.

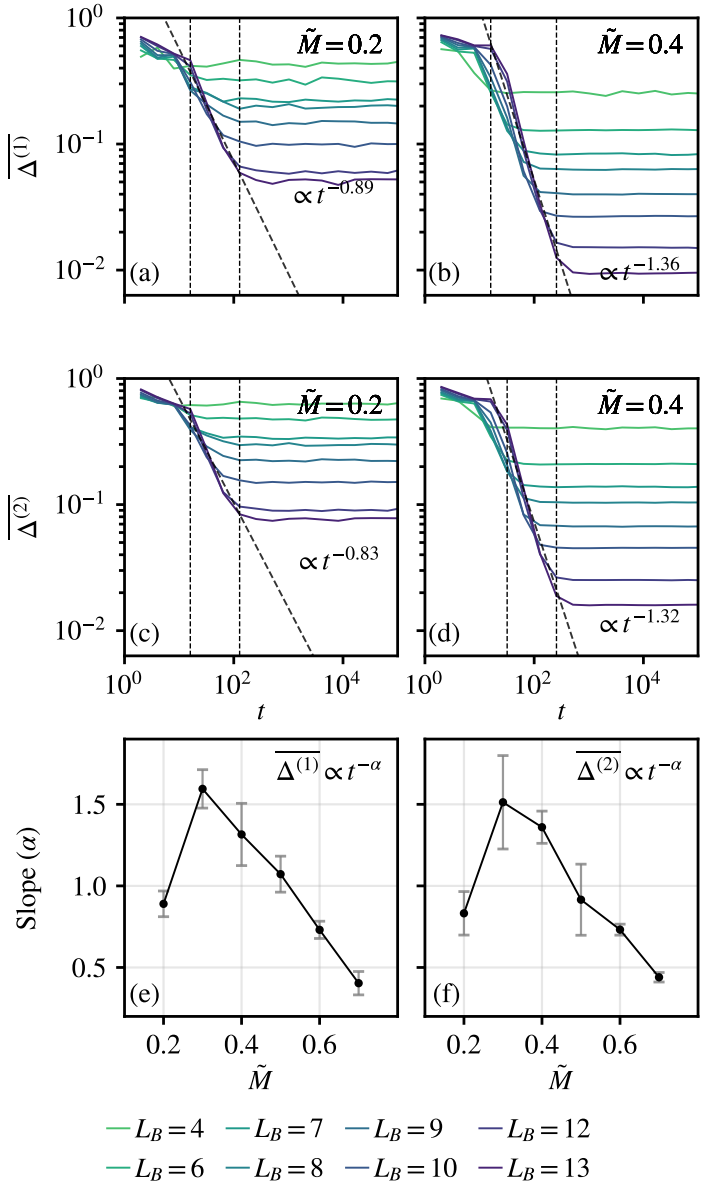

Figure 6.5: (a)-(b) Evolution of $\overline{\Delta^{(1)}}$ with time for $\tilde{M} = 0.2$ and 0.4, respectively. (c)-(d) Evolution of $\overline{\Delta^{(2)}}$ with time for $\tilde{M} = 0.2$ and 0.4, respectively. All data represented here are averaged over 500 graphs. Power-law fits for $L = 14$ are shown with black dashed lines, and the corresponding exponents are noted in the plot. Vertical black dotted lines indicate the region where the fitting was done to obtain the power-law exponents. (e)-(f) The slope of trace distance with time across $\tilde{M}$ (with estimated error in slope indicated). $L_A = 2$. The parameters for Hamiltonian (Eq. 6.1) are taken as $g = 1.0, h = 0.1$.

To characterize deep thermalization, one must identify the universal ensemble toward which the PE converges in the limit of large system sizes L and long times. Under unitary evolution with H from the initial state in Eq. 6.11, if H is chaotic, the PE asymptotically (in L, t) approaches the Haar ensemble [16, 17, 214, 56]. The choice of the measurement basis does not affect the convergence of the PE in this case [280, 215]. In the presence of conservation laws or constraints, the asymptotic projected ensemble reached at $L, t \to \infty$ deviates from the Haar ensemble and is determined by the charges of the initial state [280, 217, 215] as well as any correlation between measurement outcomes and the conserved charges. The degree of deep thermalization is thus quantified by the deviation of the PE moments from those of the Haar ensemble.

To compare the Haar ensemble and the PE, we use the trace distance between corresponding moments. Given two ensembles, we define the trace distance between their k-th moments as,

$$\Delta^{(k)}(\mathcal{E}, \mathcal{E}') = \frac{1}{2}\mathrm{Tr}\sqrt{(\rho_{\mathcal{E}}^{(k)} - \rho_{\mathcal{E}'}^{(k)})(\rho_{\mathcal{E}}^{(k)} - \rho_{\mathcal{E}'}^{(k)})^\dagger} \tag{6.13}$$

We will denote quantities averaged over multiple graph realizations with overbar. The results presented here are averages over 500 graph realizations. Figure 6.5 (a-d) show the evolution of trace distances $\Delta^{(1)}(\mathcal{E}, \mathcal{E}_{\mathrm{Haar}})$ and $\Delta^{(2)}(\mathcal{E}, \mathcal{E}_{\mathrm{Haar}})$ with time for different $\tilde{M}$. The distances decay with time in all cases, ultimately saturating to a system-size-dependent asymptotic value, $\overline{\Delta^{(k)}}(t \to \infty)$. Figure 6.6 shows the dependence of the asymptotic distance on the system size. Both the initial decay with time and the L dependence of the asymptotic distance show clear dependence on $\tilde{M}$.

Convergence of PE to the Haar ensemble with time: For intermediate $\tilde{M}$, the trace distance between the PE and the Haar ensemble decays as a power law in time, with an $\tilde{M}$-dependent exponent α (Fig. 6.5(a)–(d)). The convergence is fastest in the chaotic regime, with the largest exponent ($\alpha \approx 1.6$) occurring at $\tilde{M} \approx 0.3$ (Fig. 6.5(e)–(f)). For comparison, the nearest-neighbor mixed-field Ising model at a specific chaotic parameter point (where it is expected to be chaotic) exhibits an exponent of ≈ 1.2 [16]. The exponent decreases on either side of $\tilde{M} \approx 0.3$, toward both the sparse and dense limits. The power-law exponent is consistent within error bars across both the first and second moments of the PE, indicating that the thermalization rate is independent of the moment order, a feature previously reported in Refs. [16, 218]. At extremal values ($\tilde{M} \leq 0.1$, $\tilde{M} \geq 0.8$), the trace distance exhibits a slower approach to its asymptotic value, accompanied by pronounced plateaus, suggesting that thermalization proceeds via distinct dynamical timescales in these regimes.

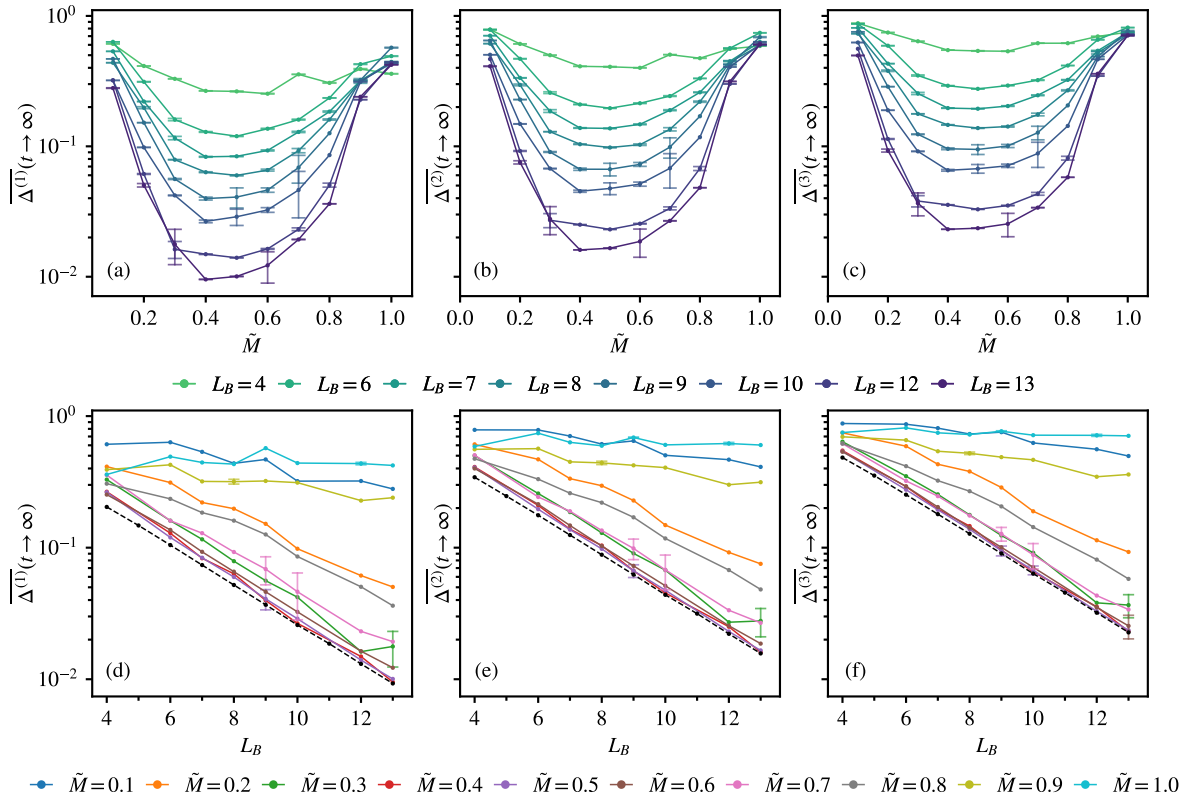

Figure 6.6: (a)-(c) Asymptotic ($t = 10^9 J^{-1}$) trace distance of first 3 moments of PE from Haar ensemble as a function of L_B. The asymptotic trace distance gets suppressed with increasing L_B for all $\tilde{M}$. Error bars represent the standard error of the mean across realizations at a fixed t. (d)-(f) The same data plotted to show the the scaling of $\overline{\Delta^{(k)}}(t \to \infty)$ with L across all $\tilde{M}$ for first 3 moments of PE. The error bars are not shown when they are comparable to the marker size. Each data point shown represents an average over 500 graph realizations, calculated for a subsystem of size $L_A = 2$ with Hamiltonian parameters (Eq. 6.1) $g = 1.0$ and $h = 0.1$. The black dashed line shows the trace distance of an empirical ensemble of 500 random states (sampled from Haar random states of system size L) from the corresponding moments of the Haar ensemble.

Asymptotic (late-time) trace distance, $\overline{\Delta^{(k)}}(t \to \infty)$: We compare the late-time asymptotic trace distances $\Delta^{(k)}$ for $k = 1, 2, 3$ in Fig. 6.6(a)-(c) as a function of $\tilde{M}$ for multiple L. Figure 6.6(d)-(f) show the L dependence of $\overline{\Delta^{(k)}}(t \to \infty)$.

At fixed L, the asymptotic trace distance is largest at extremal $\tilde{M}$ and decreases toward intermediate connectance, reaching a minimum at $\tilde{M} \approx 0.4$. At $\tilde{M} = 0.4$–0.5, the trace distance approaches the same obtained for Haar random states of the same system size (black dashed lines in Fig. 6.6(d)–(f)). The larger trace distance at $\tilde{M}$ away from 0.4 suggests that these Hamiltonians possess approximate conservation laws that impose structure on the eigenstates, preventing full ergodicity (as discussed in Sec. 6.2). We find no evidence of slow time-dependent drift in the asymptotic region (Fig. 6.5(a)–(d)), confirming that the trace distance has genuinely converged rather than remaining in a slow transient. On the sparse side ($\tilde{M} \ll 0.4$), disconnected clusters give rise to local conserved quantities, accounting for some of the observed deviation from chaos. On the dense side ($\tilde{M} \gtrsim 0.4$), the approximate $SU(2)$ symmetry inherited from the near-LMG structure provides the relevant approximate conservation laws that impede PE

convergence.

The asymptotic trace distance $\overline{\Delta^{(k)}}(t \to \infty)$ decays exponentially with L at intermediate $\tilde{M}$, consistent with convergence of the PE to the Haar ensemble in the thermodynamic limit and with deep thermalization in chaotic models. In contrast, at $\tilde{M} \to 0, 1$, the decay with L is significantly slower, while the fastest decay occurs at intermediate $\tilde{M}$. This qualitative behavior is consistent across the first, second, and third moments of the PE. The fact that the trace distance decays with L even at $\tilde{M} = 0.1$ and 0.9, albeit slowly, is tentative evidence that the system may be chaotic throughout, except at the integrable limits $\tilde{M} = 0, 1$, a conclusion consistent with Ref. [272].

So far in this section, we have investigated the PE's approach to the Haar ensemble for time evolutions starting from a specific zero-energy expectation-value initial state (Eq. 6.11). At $\tilde{M} = 1.0$, the Hamiltonian has a permutation symmetry which is preserved by this state, as a result of which the instantaneous state has finite overlaps with only a small number of energy eigenstates of the $\tilde{M} = 1$ Hamiltonian. However, the results shown in Fig. 6.6 stay valid even if we consider other 0 energy expectation value initial states that lack permutation symmetry. In Appendix 6.C, we show analogous results for initial direct product states with limited or no permutation symmetry, demonstrating the robustness of the results presented in Fig. 6.6.

In summary, we find that finite-system studies of the PE show a clearly faster onset of chaos (through convergence of the PE to the Haar ensemble) with increasing system size at intermediate connectivity $\tilde{M} \sim 0.4 - 0.6$. Away from this, the approach of PE to the Haar ensemble is slower, likely due to approximate conserved charges or symmetries. In the latter cases, in accessible systems, the asymptotic PE approaches the Haar ensemble as system size increases, indicating that the number of approximately conserved charges and symmetries becomes subextensive. Measurement of the projected ensemble and its higher moments has been demonstrated in quantum simulators for 1D lattice systems with up to 25 qubits [16]. Extending such protocols to random-graph connectivity presents additional experimental challenges, particularly in terms of qubit connectivity and mid-circuit measurement overhead. Nevertheless, our finite-size results suggest that the trace distance of the PE from the Haar ensemble provides a clear and resolvable diagnostic of the chaotic crossover, capturing the $\tilde{M}$-dependent convergence rate and the moment-independence of the thermalization exponent. These signatures are visible at system sizes accessible to near-term quantum devices, making this a tractable target for experimental investigation.

6.4 Partial Spectral Form Factor

Having characterized the emergence of chaos through the properties of the projected ensemble, we now turn to a complementary diagnostic: the correlations within the energy spectrum itself. To this end, we investigate the partial spectral form factor (pSFF), which generalizes the spectral form factor (SFF) to subsystems and serves as a probe of spectral correlation, a key signature of quantum chaos. Unlike the SFF, the pSFF is more readily accessible in experiments. In this section, we utilize the pSFF to study the localization-to-chaos crossover as a function of connectivity ($\tilde{M}$) and explore its dependence on both system and subsystem size in different connectivity regimes.

Before discussing the pSFF, we briefly review the SFF [295, 296, 255, 297]. The SFF is a spectral diagnostic of quantum chaos that encapsulates both short- and long-range spectral correlations, providing information beyond that contained in level-spacing statistics (which captures only adjacent level spacings). The SFF is the Fourier transform of the eigenvalue density-density correlation, defined as follows,

$$K(t) = \frac{1}{d^2} \sum_{i,j=1}^{d} e^{i(E_i - E_j)t} = \frac{1}{d^2} \mathrm{Tr}[\mathcal{T}(t)] \mathrm{Tr}[\mathcal{T}^\dagger(t)] \ , \tag{6.14}$$

where d is the Hilbert space dimension of the full system and E_i is i-th eigenvalue of the Hamiltonian. t is the Fourier variable of energy, with units of time. The time evolution unitary operator is represented as, $\mathcal{T}(t) = e^{-\imath H t}$. The prefactor ensures $K(0) = 1$. In a chaotic spectrum (obeying WD statistics), SFF decays from 1 at $t = 0$ till Thouless time $t_{Th} \approx O(\delta E^{-1})$ where δE is the mean level spacing. This results in SFF dropping to below $1/d$ at intermediate time. This is followed by a linear ramp up to saturation to $1/d$ at plateau time (the time at which the plateau in SFF begins), $t_p \approx O(2^L)$. The dip in SFF (referred to as a correlation hole) is caused by level repulsion and spectral rigidity in chaotic systems as predicted by random matrix theory (RMT). This ramp-and-plateau structure is a signature of the chaotic spectrum. For a spectrum following Poisson statistics, the SFF is expected to gradually reach its asymptotic value after an initial transient period without any correlation hole or ramp. For chaotic systems, the asymptotic SFF is given as $K(t \to \infty) = 1/d$ in the absence of any degeneracy in the eigenspectrum. Recently, SFF has been experimentally measured in a 5-qubit superconducting device using a randomized measurement protocol [273]. Ref. [272] analyzed SFF in the model studied here for $h = 0$. In the intermediate regime of both $\tilde{M}$ and g, the SFF converges with increasing L to the characteristic dip-ramp-plateau structure predicted by RMT, indicating chaotic spectra. Conversely, chaos is suppressed at the extreme limits of connectivity. In both the sparsely connected ($\tilde{M} \to 0$) and densely connected ($\tilde{M} \to 1$) regimes, the development of the correlation hole is slower with increasing L. Similarly, the correlation hole vanishes for both very small and very large g, indicating a breakdown of RMT statistics.

Despite recent experimental demonstrations of SFF measurement on superconducting qubit arrays, a significant practical challenge remains regarding the requirement of global control and site-resolved operations across the entire quantum system. In practice, implementing such fully controlled rotations on all qubits becomes resource-intensive as system size increases. The partial spectral form factor (pSFF) was recently introduced as a scalable alternative [67], which, unlike the full SFF, requires controlled operations that scale only within a smaller subsystem [67, 273]. The pSFF is described in terms of the time-evolution operator restricted to a subsystem. The pSFF can be defined as follows,

$$\begin{aligned} K_A(t) &= \frac{1}{dd_A} \sum_{i,j} e^{\imath(E_i - E_j)t} \mathrm{Tr}_B[\rho_B(E_i)\rho_B(E_j)] \\ &= \frac{1}{dd_A} \mathrm{Tr}_B[\mathrm{Tr}_A[\mathcal{T}(t)]\, \mathrm{Tr}_A[\mathcal{T}^\dagger(t)]], \end{aligned} \tag{6.15}$$

where $\rho_B(E_i) = \mathrm{Tr}_A\left[|E_i\rangle\langle E_i|\right]$ is the reduced density matrix of subsystem B for energy eigenstate

$|E_i\rangle$. pSFF captures the correlation of both eigenstates and eigenvalues. The normalization factor in Eq. 6.15 ensures $K_A(0) = 1$.

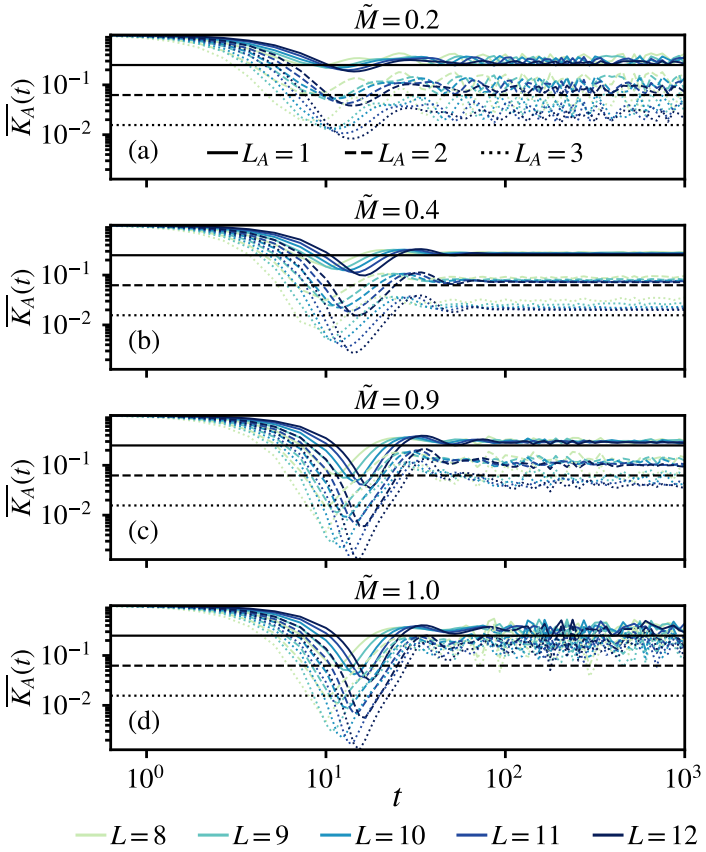

Figure 6.7: Time evolution of the pSFF, $\overline{K_A}(t)$, for various system sizes (L, different colors) and subsystem sizes (L_A, different line styles). Panels show different connectivities: (a) $\tilde{M} = 0.2$, (b) $\tilde{M} = 0.4$, (c) $\tilde{M} = 0.9$, and (d) $\tilde{M} = 1.0$. The solid, dashed, and dotted lines correspond to $L_A = 1, 2$, and 3, respectively. The horizontal black lines denote the expected asymptotic values for a chaotic system, $1/d_A^2$. All data are averaged over 500 graph realizations (denoted by an overbar) with Hamiltonian parameters (Eq. 6.1) of $g = 1.0$ and $h = 0.1$.

We now investigate pSFF for the Hamiltonian in Eq. 6.1, setting $g = 1$ and $h = 0.1$ with the goal of understanding the manifestation of localization, integrability and chaos as well as the finite-size effect in these cases. The SFF can be computed directly from the eigenvalue spectrum, allowing spectral unfolding on mid-spectrum eigenvalues to remove non-universal level-density variations. However, in an experimental setting, the full eigenspectrum is usually inaccessible, precluding spectral unfolding. In the following, we therefore compute the pSFF on the full spectrum without unfolding. In spite of this, we find that the pSFF reveals clear chaotic behavior at intermediate connectivity and distinct deviations at extremal connectivity, making the pSFF another route to investigate the model in scalable experimental systems.

We analyze the behavior of pSFF at multiple values of $\tilde{M}$ with the results presented in Fig. 6.7. In the results presented here, the pSFF is averaged over 500 ER graph realizations.

pSFF at small $\tilde{M}$: For $\tilde{M} = 0.2$, Fig. 6.7(a) shows that there is no distinct correlation hole, and the pSFF reaches its asymptotic value after a transient period. The absence of a

correlation hole indicates the lack of correlation in the eigenspectrum (consistent with Poisson statistics). There is also a persistent oscillation present at late-times, even after averaging over graph realizations. The black lines in Fig. 6.7(a) shows the asymptotic values of pSFF for a chaotic Hamiltonian. Apart from the late-time fluctuation in pSFF, the mean asymptotic value is also larger compared to the expectation for a chaotic Hamiltonian. This can be attributed to quasi-degeneracies in the eigenspectrum (when adjacent level spacing goes below δE) [272]. For $\tilde{M}$ close to 0, there is a wide fluctuation at all times due to the existence of disconnected clusters, which obscures the possible existence of any correlation hole.

pSFF at intermediate $\tilde{M}$: The pSFF shows qualitatively different behavior in the chaotic regime. In Fig. 6.7(b), the pSFF shows a dip (correlation hole) and a subsequent ramp-and-plateau structure. This correlation hole arises from energy-spectrum correlations, as expected in chaotic systems. The depth of the correlation hole increases with both L and L_A. The time at the appearance of the correlation hole, t_{Th}, increases with L for fixed L_A. For chaotic systems, RMT predicts [67] (in the absence of degeneracy) $K_A(t \to \infty) \approx K(t \to \infty) + 1/d_A^2 = 1/d + 1/d_A^2$. For $L_A \ll L$, $K_A(t \to \infty) \approx 1/d_A^2$ i.e., asymptotic pSFF shows a subsystem size (L_A) dependent shift. In Fig. 6.7, these asymptotic values (for chaotic spectra) are shown using black horizontal lines. For $\tilde{M} = 0.4$, Fig. 6.7(b) shows that the asymptotic K_A shows very little fluctuation at late-time and approaches $\approx 1/d_A^2$. Additionally, there is no significant fluctuation in pSFF at $t > t_p$ when no average over graph realizations is taken.

pSFF at large $\tilde{M}$: In the densely connected limit approaching all-to-all connectivity, i.e., $\tilde{M} = 0.9$, Fig. 6.7(c) shows a dip in pSFF. In this case, the asymptotic pSFF shows small oscillation around a plateau value larger than $1/d_A^2$. This deviation from $1/d_A^2$ is caused by approximate degeneracy in the energy spectrum close to $\tilde{M} = 1$.

pSFF at $\tilde{M} = 1.0$: At $\tilde{M} = 1.0$, i.e., where the model is expected to be almost integrable (in the presence of a small nonzero h), we observe a dip in pSFF at an intermediate time, a feature that persists even in the $h = 0$ limit. The pSFF eventually saturates to a value exceeding the RMT prediction for chaotic systems, suggesting a deviation from WD spectra.

Scaling of the plateau time : To further quantify the ramp-and-plateau behavior and its dependence on L in the chaotic regime, we study the scaling of the plateau time, t_p with L for $L_A = 2$. This time is determined numerically as the intersection of two linear fits: one to the logarithmic plot of the ramp ($t_{\text{Th}} < t < t_p$) and another to the late-time plateau ($t > t_p$). We observe a clear exponential scaling of t_p with system size L, as shown in Fig. 6.8(a), with a slope that does not strongly depend on $\tilde{M}$ within the chaotic regime. The exponential scaling of the plateau time is a feature [67, 273] of the SFF that is inherited by the pSFF. Our data in Fig. 6.8(a) quantitatively supports this behavior.

Entropy from pSFF : Another quantity related to pSFF is the purity of the subsystem averaged over eigenstates, defined as $p_B = \mathbb{E}_i[\text{Tr}(\rho_B(i)^2)]$ where $\rho_B(i)$ is the reduced density matrix of the subsystem B in the i-th eigenstate. This quantity captures the entanglement

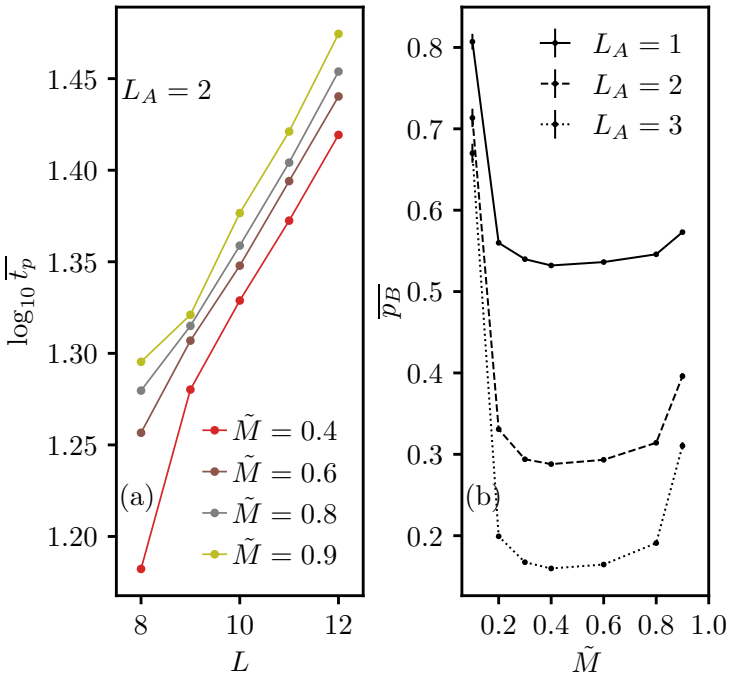

Figure 6.8: Quantitative analysis of the pSFF. (a) Scaling of the plateau time, $\log_{10} t_p$, as a function of system size L for several connectance, $\tilde{M}$, with a fixed subsystem size of $L_A = 2$. (b) The late-time subsystem purity, $\overline{p_B}$, as a function of $\tilde{M}$ for a fixed system size $L = 12$ and varying subsystem sizes, L_A. All data are averaged over 500 graph realizations (denoted by an overbar) with Hamiltonian parameters (Eq. 6.1) of $g = 1.0$ and $h = 0.1$. Here overbar denotes annealed average.

of subsystem with its complement and is related to the annealed subsystem Renyi entropy as $R_2 = -\log(p_B)$. The purity can be obtained from pSFF at $t \to \infty$ as $p_B = \lim_{t_p/t \to 0} K_A(t) d_A$. Figure 6.8(b) shows p_B as a function of $\tilde{M}$ for multiple L_A and $L = 12$. The purity is minimum at the intermediate $\tilde{M}$ i.e., subsystem B is more mixed (more entanglement with A) in the chaotic regime compared to the integrable or localized regime. At both $\tilde{M} \to 0, 1$, the purity goes up. The higher purity at $\tilde{M} \to 0, 1$ is consistent with the expectation of lower entanglement in the localized or integrable eigenstates compared to the chaotic eigenstates. The purity of B decreases (i.e., increase in subsystem entanglement) with increasing L_A.

Fluctuation in pSFF due to choice of subsystem : To complete our analysis of the pSFF, we investigate the fluctuation in pSFF due to the choice of subsystem. We compute pSFF for $L_A = 2$ subsystems over 200 graph realizations for multiple L. In each realization, we choose all possible subsystems consisting of two sites as A and the rest of the sites constitute B. Figure 6.9(a) shows the distribution of asymptotic pSFF values for $L_A = 2$ and multiple L at $\tilde{M} = 0.6$. The variance reduces with increasing L. At large L, the choice of sites constituting the subsytem does not affect the asymptotic pSFF in the chaotic regime. The peak also shows a shift toward the expected value (in chaotic spectra) $\approx 1/d_A^2$ (0.0625 for $L_A = 2$) with increasing L. This behavior contrasts sharply with the near-integrable regime ($\tilde{M} = 0.9$). Here, Fig. 6.9(b) shows a broad distribution for small L. The distribution gets sharper with L for fixed L_A. However, it is significantly broader compared to the chaotic case for the same L and L_A.

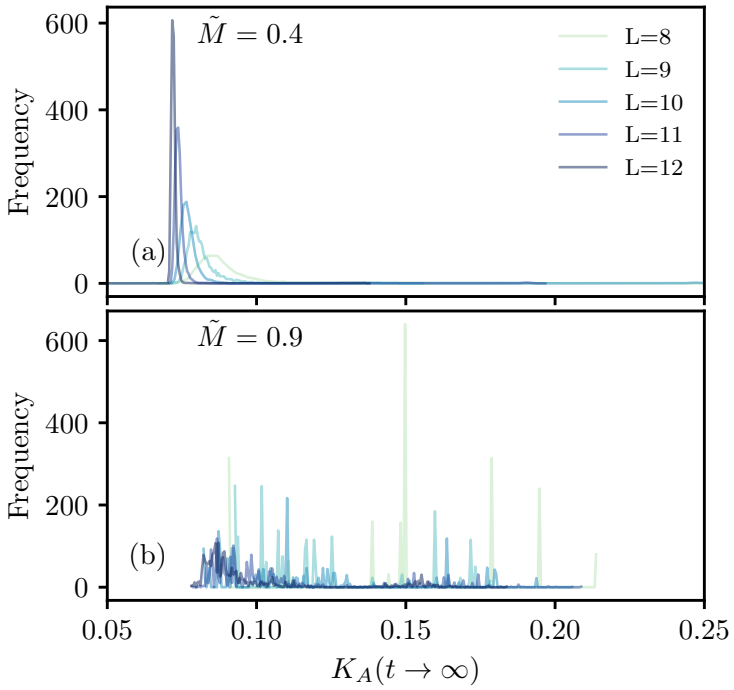

Figure 6.9: Normalized distribution of the asymptotic (late-time) pSFF, $K_A(t \to \infty)$, computed over all possible two-site subsystems for different system sizes, L. Panel (a) shows the distribution in the chaotic regime, $\tilde{M} = 0.6$. Panel (b) shows the distribution in the near-integrable regime, $\tilde{M} = 0.9$. For all calculations, the subsystem size is fixed at $L_A = 2$ and the Hamiltonian (Eq. 6.1) parameters are $g = 1.0$ and $h = 0.1$. The data is presented here for 200 graph realizations.

Experimental implications : Qualitative features of pSFF across dynamical regimes resemble those of SFF. As the pSFF can be experimentally obtained using randomized measurement (with lower resource requirement compared to SFF), we briefly comment on the number of measurements required to estimate pSFF with sufficient accuracy to capture the physics described in this section. As established in Ref. [67], the relative error, ϵ, of the pSFF measurement scales with the number of experimental shots, N_m, as $\epsilon \propto \sigma_A / K_A \sqrt{N_m}$ at each instant of time, where σ_A is the variance in the shadow estimator of pSFF. This implies that the number of measurements needed to reach a desired precision, $N_m \propto \sigma_A^2 / K_A^2$. The number of required measurement scales is inversely proportional to the instantaneous value of pSFF. This makes the estimation of the dip in pSFF (i.e., around $t = t_{\text{Th}}$) challenging for a large subsystem in a chaotic regime as $K_A(t \approx t_{\text{Th}}) = O(10^{-3})$ in our model. Compared to this, the asymptotic value of pSFF serves as a better distinguishing factor, as the magnitude is typically one order of magnitude larger here ($t > t_p$). However, obtaining plateau requires long time evolution, making it susceptible to decoherence. The correlation hole appears at an earlier time, though it requires a larger number of measurements.

The fluctuation of the late-time pSFF over time, within a single experimental realization, provides a qualitative diagnostic that distinguishes chaotic from integrable Hamiltonian dynamics. The markedly lower variance of the asymptotic pSFF over subsystem choices in the chaotic regime further implies a reduced experimental overhead, requiring fewer independent realizations for accurate estimation of the pSFF relative to its integrable counterpart.

6.5 Operator delocalization through Krylov complexity

In a closed quantum system, generic Hamiltonian evolution causes initial operators to become increasingly complex over time. While probes like out-of-time-ordered correlators (OTOCs) [258] can be studied for operator spreading, their reliance on spatial separation metric is ill-suited for random graphs that lack an inherent local structure. A locality-independent quantification of complexity can be the measure of the extent to which an operator spreads under time evolution in a basis composed of increasingly complicated operators [298, 299, 276]. In this section, we analyze the dynamics of operator spreading in the system through Krylov complexity. The time evolution of an operator is generated by applying the propagator constructed with the Liouvillian superoperator, and the resulting KC dynamics provide a diagnostic for quantifying chaos and localization.

First, we briefly review KC from the operator viewpoint (an alternative formulation for spread complexity of state has also been proposed [300]). We start with an initial operator $\mathcal{O}(0)$. In Heisenberg picture, the time-evolved operator $\mathcal{O}(t)$ can be expressed as,

$$\mathcal{O}(t) = e^{\imath Ht}\mathcal{O}(0)e^{-\imath Ht} = e^{\imath \mathcal{L}t}|\mathcal{O}(0)) \tag{6.16}$$

where the Liouvillian, $\mathcal{L} = (\mathbb{I}\otimes H - H^T \otimes \mathbb{I})$ and $|\mathcal{O}) = \text{vec}(\mathcal{O}) \in \mathcal{H}_d \otimes \mathcal{H}_d$ refers to the vectorized operator defined using,

$$\begin{aligned} \mathcal{O} &= \sum_{i,j} \mathcal{O}_{i,j}|i\rangle\langle j| \\ \implies |\mathcal{O}) &= \text{vec}\left[\sum_{i,j} \mathcal{O}_{i,j}|i\rangle\langle j|\right] = \sum_{i,j} \mathcal{O}_{i,j}|i\rangle|j\rangle. \end{aligned} \tag{6.17}$$

Here, $|i\rangle, |j\rangle$ refers to computational basis states. The action of $\mathcal{L}$ on a generic operator $\mathcal{O}$ is defined as $\mathcal{L}|\mathcal{O}) = \text{vec}([H, \mathcal{O}])$. Subsequently, we can define the Krylov subspace ($\mathcal{K}_\mathcal{O}$) of $\mathcal{L}$ associated with $\mathcal{O}$ as the minimal subspace where $\mathcal{O}$ is restricted under time-evolution with $\mathcal{L}$ and is spanned by,

$$\begin{aligned} \mathcal{K}_\mathcal{O} &= \text{span}\{\mathcal{L}^n|\mathcal{O})\}_{n=0}^{\infty} = \text{span}\{|\mathcal{O}), |\mathcal{L}\mathcal{O}), |\mathcal{L}^2\mathcal{O}), ...\} \\ &= \text{span}\{\text{vec}(\mathcal{O}), \text{vec}([H, \mathcal{O}]), \text{vec}([H, [H, \mathcal{O}]])...\}. \end{aligned} \tag{6.18}$$

The dimension of $\mathcal{K}_\mathcal{O}$ is denoted by K and bounded [301] as $1 \leq K \leq d^2 - d + 1$. Evidently, the nested commutator operators in $\mathcal{K}_\mathcal{O}$ gets wider (have larger support) with increasing order. We define an inner product on operator space as $(A|B) = \text{Tr}(A^\dagger B)$, and work with a complete orthonormal basis $\{|\mathcal{O}_n)\}_{n=0}^{K-1}$ in $\mathcal{K}_O$ obtained using Lanczos algorithm and implemented through successive full Gram-Schmidt orthogonalization (see Appendix 6.D) starting from $|\mathcal{O}_0) = \text{vec}(\mathcal{O}(0))$ i.e., the first element of the basis is the initial operator. This orthonormal basis in operator space is denoted as Krylov basis. The Liouvillian takes a tri-diagonal form

when expanded in $\{|\mathcal{O}_n)\}$,

$$\mathcal{L} = \begin{pmatrix} 0 & b_1 & & & & \\ b_1 & 0 & b_2 & & & \\ & b_2 & 0 & \ddots & & \\ & & \ddots & \ddots & b_{K-2} & \\ & & & b_{K-2} & 0 & b_{K-1} \\ & & & & b_{K-1} & 0 \end{pmatrix} \tag{6.19}$$

where diagonal elements are 0 and off-diagonal elements $(b_1, b_2, \ldots b_n)$ form an ordered set of coefficients referred to as Lanczos coefficients. Under time-evolution with $\mathcal{L}$,

$$\mathcal{O}(t) = e^{\imath \mathcal{L} t}|\mathcal{O}_0) = \sum_{n=0}^{K-1} \imath^n \phi_n |\mathcal{O}_n) \tag{6.20}$$

where ϕ_n are the expansion coefficients of $\mathcal{O}(t)$ in $\mathcal{K}_O$. The unitarity of time evolution ensures $\sum_{n=0}^{K-1} |\phi_n|^2 = 1$. The time-evolution of ϕ_n are given by a set of K coupled differential equations,

$$\partial_t \phi_n(t) = \phi_{n-1}(t) b_n - \phi_{n+1}(t) b_{n+1}, \tag{6.21}$$

where $n \in [0, K-1]$ and $\phi_n(0) = \delta_{n,0}$ is taken as initial condition, $b_0 = b_K = 0$ is the boundary condition. The form of $\mathcal{L}$ suggests an interpretation of this dynamics analogous to a particle hopping problem on a finite chain, with $\{|O_n)\}_{n=0}^{K-1}$ acting as the sites and the hopping amplitudes given by the Lanczos coefficients. To elucidate this, we can represent $\mathcal{L}$ in Krylov basis,

$$\mathcal{L} = \sum_{n=0}^{K-1} b_n (|\mathcal{O}_n)(\mathcal{O}_{n-1}| + |\mathcal{O}_{n-1})(\mathcal{O}_n|). \tag{6.22}$$

The corresponding evolution of wavefunction representing this particle, $\phi = (\phi_0, \imath\phi_1, \ldots, \imath^{K-1}\phi_{K-1})$ can be obtained by solving the set of coupled equations in 6.21. The KC is defined as,

$$\mathcal{C}(t) = \sum_{n=0}^{K-1} n |\phi_n(t)|^2, \tag{6.23}$$

measuring the particle's mean position in the Krylov chain. $|\mathcal{O}_n)$ involves n-th order nested commutators, resulting in Krylov basis elements that have increasingly larger support and more complicated structure with increasing n. KC captures the spread of a time-evolved operator in this Krylov basis. We denote the support of an operator $\mathcal{O}$ as $|\mathcal{O}|$.

The Lanczos coefficients b_n control how quickly operators spread through the Krylov basis during time evolution. The scaling of b_n with n and its fluctuation serve as a signature that can distinguish quantum chaotic dynamics from integrable or localized dynamics [302]. In the

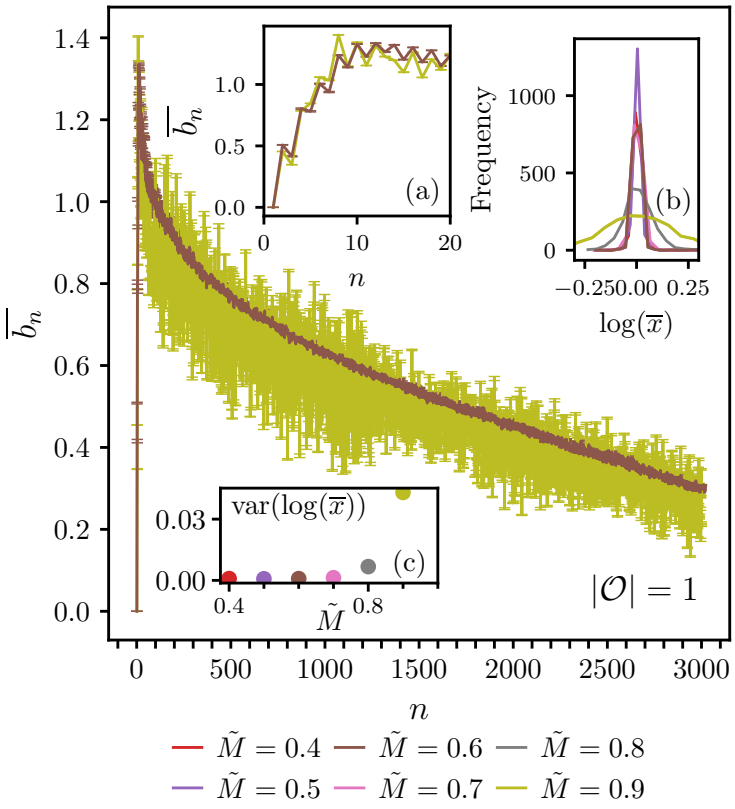

Figure 6.10: Analysis of the Lanczos coefficients, b_n, for an initial operator with support on a single site. The main panel shows the average coefficients, $\overline{b_n}$, as a function of the iteration number n for $\tilde{M} = 0.6, 0.9$. Error bars represent the standard error of the mean. (Inset)(a) shows the initial growth of $\overline{b_n}$ for the first 20 iterations. (b) shows the distribution of the logarithm of the ratio of consecutive coefficients, $\log(\overline{x})$, where $x_n = b_n/b_{n+1}$. (c) shows the variance of the $\log(\overline{x})$ distribution as a function of $\tilde{M}$. All data are for a system of size $L = 6$ with Hamiltonian parameters $g = 1.0$ and $h = 0.1$, averaged over 500 graph realizations (denoted by overbar).

following discussion, we take the initial operator in simple product form,

$$\mathcal{O}(0) = \prod_{i=1}^{|\mathcal{O}|} Y_i. \tag{6.24}$$

Here, $|\mathcal{O}|$ denotes the size of $\mathcal{O}$, i.e., the number of sites where the operator acts non-trivially. Note that we do not have any underlying spatial structure in the lattice; thus, no natural local structure can be attributed to $\mathcal{O}(0)$ when it has support larger than 1. In the rest of the section, we present the empirical observations regarding the Krylov complexity and Lanczos coefficients as well as comparisons with related similar studies and other systems.

Fluctuation in Lanczos coefficients : The sequence of Lanczos coefficients b_n has been investigated across different dynamical regimes [303, 304]. Empirically, it is found that b_n grows linearly (sub-linearly) at small n for chaotic (integrable) systems, saturates at intermediate n, and finally descends till $n = K - 1$. The inset (a) in Fig. 6.10 shows the growth and subsequent saturation of Lanczos coefficients for small n. The distinction in the scaling of Lanczos coefficients

at small n between chaotic and integrable regimes is unclear here due to the small system size ($L = 6$).

The descent region in b_n shows significantly larger fluctuations in the integrable regime than in the chaotic regime. In a single-particle picture, this translates into greater disorder in local hopping parameters. In Fig. 6.10 (main panel), we show the Lanczos sequence, $\overline{b_n}$ (averaged over ER graphs) for $\tilde{M} = 0.6$ and 0.9. The fluctuation in Lanczos amplitude at large n is significantly larger for $\tilde{M} = 0.9$ (approaching integrability) compared to $\tilde{M} = 0.6$ (chaotic). Similar large fluctuations were also observed in the sparsely connected regime (not shown). To quantify this fluctuation, we use the distribution of the ratio of consecutive Lanczos coefficients, $x_n = \left(\frac{b_n}{b_{n+1}}\right)$ averaged over graph realizations. Figure 6.10 (b) shows the distribution of $\log(\bar{x}_n)$ with n for multiple $\tilde{M}$. The distribution has a mean 0 with the variance increasing as $\tilde{M} \to 1$ (Fig. 6.10 (c)).

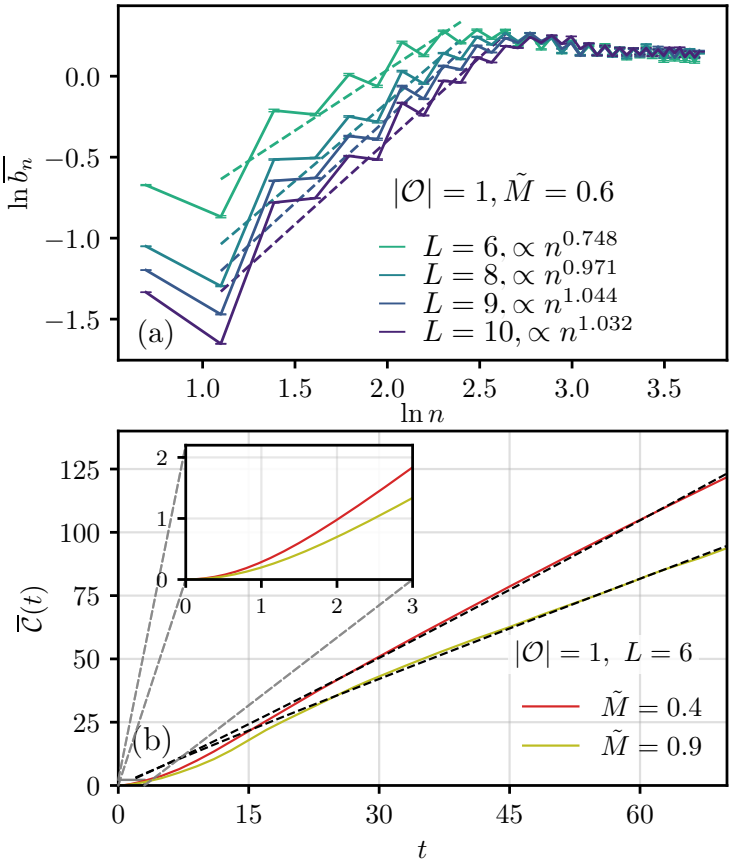

Figure 6.11: First few Lanczos coefficients and Early-time growth of Krylov complexity. (a) Log-log plot of the average Lanczos coefficients, $\overline{b_n}$, versus the iteration number n for several system sizes L at $\tilde{M} = 0.6$. Dashed lines show power-law fits, $\overline{b_n} \propto n^{\delta}$. All data points are averaged over 200 graph realizations. (b) The corresponding early-time growth of Krylov complexity, $\overline{\mathcal{C}}(t)$, for the chaotic ($\tilde{M} = 0.4$, red) and near-integrable ($\tilde{M} = 0.9$, yellow) regimes. The black dashed lines show the linear fit to late-time data. The inset shows a magnified view of the initial non-linear growth. All data are for a single-site initial operator ($|\mathcal{O}| = 1$) with Hamiltonian (Eq. 6.1) parameters $g = 1.0$ and $h = 0.1$. For KC, we performed a quenched average over 500 graph realizations (denoted by overbar).

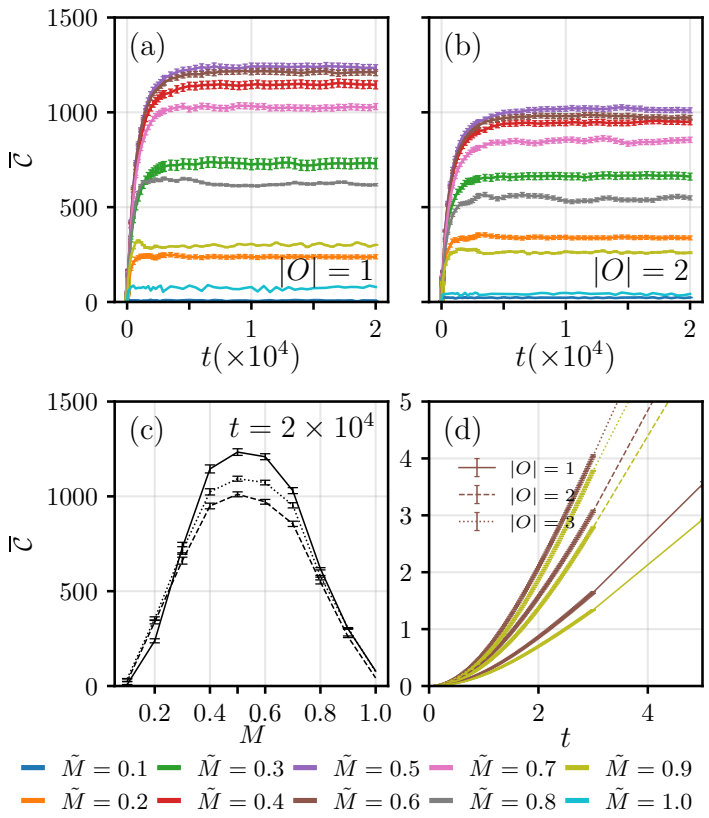

Figure 6.12: Evolution and initial growth of Krylov complexity, $\overline{\mathcal{C}}(t)$, for a system with $L = 6$. (a)-(b) The time evolution for initial operators with increasing support, $|\mathcal{O}| = 1$ and 2 with $\mathcal{O} = \prod_{i=1}^{|\mathcal{O}|} Y_i$, respectively, across multiple connectance, $\tilde{M}$. Error bars indicate the standard error of the mean. (c) The asymptotic $\overline{\mathcal{C}}$ as a function of $\tilde{M}$ for $|\mathcal{O}| = 1, 2$ and 3 (marked with solid,dashed and dotted black lines, respectively). (d) A magnified view of the initial growth for the same $|\mathcal{O}| = 1, 2$ and 3 for $\tilde{M} = 0.6$ and 0.9. All data are presented after averaging over 500 graph realizations (denoted by overbar) with Hamiltonian parameters $g = 1$ and $h = 0.1$ from Eq. 6.1.

Growth of KC : The growth of the Lanczos coefficients, b_n, directly governs the multi-stage evolution of the Krylov complexity, $\overline{\mathcal{C}}(t)$. Figure 6.11(a) shows the n dependence of $\overline{b_n}$ for a single-site initial operator, $\mathcal{O} = Y_1$ in the chaotic regime ($\tilde{M} = 0.6$). $\overline{b}_n$ is expected to grow linearly with n in the chaotic regime according to the universal operator growth hypothesis [276, 301]. Upon fitting b_n calculated in finite systems to n^δ, we find that δ approaches 1 with increasing system size L, consistent with chaotic behavior. For times $t \lesssim \log(L)$, this linear growth of b_n results in an exponentially growing KC, a feature associated with the spreading of operator support across the system [305, 306]. For $L = 6$, we find the initial growth of $\mathcal{C}(t)$ to be slower than this expected exponential behavior (Fig. 6.11(b)), likely related to sublinear growth of b_n with n in smaller systems (Fig. 6.11(a)).

This initial phase is followed by a robust linear growth, indicated by the linear fits (dashed lines) in Fig. 6.11(b), during which the operator spreads through the higher-order elements of the Krylov basis. Finally, at late-times, the finite-size of the system halts this spread, causing the complexity to saturate. These qualitative features i.e., initial non-linear growth that transitions

into a linear region in KC, and saturation at late-time due to finite L are present in both the chaotic and near-integrable regimes, though the initial growth rate of KC slows down near integrability (Fig. 6.11(b) inset).

We observe an even-odd fluctuation about the linear trend in $\overline{b_n}$ similar to what has been observed in quantum field theories and Hamiltonian systems [307, 308, 302, 309]. The precise form of the subleading corrections to the linear growth relates the long-time decay of the operator autocorrelation. Corrections with an odd-even structure of the form $(-1)^n(\ln n)^{-a}$ have been shown to imply a power-law decay of the autocorrelation [276, 309]. In the finite data in Fig. 6.11(a), it is unclear if the corrections scale this way.

Saturation value of KC: Among the features in the time evolution of KC, late-time saturation value $\overline{\mathcal{C}}(t \to \infty)$, is the clearest indicator of chaos. The saturation value is expected to be higher for chaotic systems compared to integrable or localized systems, hinting at the emergence of more complex operators at late-times where dynamics are not hindered by constraints or approximate conserved charges. This is evident in Fig. 6.12(a)-(b), where the KC saturates to a significantly larger value (in the range of $1000 - 1400$) for intermediate $\tilde{M}$, compared to the extreme $\tilde{M}$ where $\overline{\mathcal{C}}(t \to \infty) \approx 5 - 200$ for all operator sizes $|\mathcal{O}_0|$. Figure 6.12(c) shows the KC value at saturation as a function of $\tilde{M}$, clearly indicating the distinct nature of operator spreading in the chaotic and integrable/localized regimes. The saturation to a value below the theoretical maximum of $K/2$ can be attributed to finite system size and potential degeneracies in the spectrum.

Effect of initial operator size: Figure 6.12(d) shows that the initial growth rate increases with the support of the initial operator, $|\mathcal{O}_0|$. This is physically plausible, as an operator with a larger initial support has already "explored" a larger part of the system's real space. This feature holds in both chaotic and near-integrable regimes.

We do not observe a simple monotonic dependence of the KC saturation value on the initial operator support $|\mathcal{O}|$, and these results do not change qualitatively for other initial operators, as shown in Appendix 6.E. In contrast, in studies on SYK_2 (a free model), the growth of $\mathcal{C}(t)$ was found to depend on initial operator size [310].

Wavefunction spread in Krylov space: The analogy of a particle hopping on the Krylov chain can be made more direct by examining the probability distribution of the particle's position, given by the Krylov wavefunction, $|\phi_n|^2$. This is reported in Fig. 6.13 for multiple $\tilde{M}$ at a late-time of $t \approx 2 \times 10^5$. Finite $|\phi_n|^2$ even at large n indicates that $\mathcal{O}(t)$ involves high-complexity operators in the Krylov basis. We observe that $|\phi_n|^2$ decays rapidly with n at large $\tilde{M}$, indicating that the operator remains localized near the beginning of the Krylov chain. In contrast, it shows a much slower decay with n in the chaotic regime, signifying delocalization across the chain. The qualitative trend holds for all operator sizes $|\mathcal{O}|$.

Experimental access to late-time Krylov complexity is challenging, and the development of scalable experimental protocols is still in the nascent stage [311, 304]. Thus even though asymptotic values of Krylov complexity shows clear signatures of chaos as seen in Fig. 6.12 experimentally reproducing them or obtaining a clear scaling is difficult. However early time behavior of Krylov complexity can be captured in current devices by measuring two-point

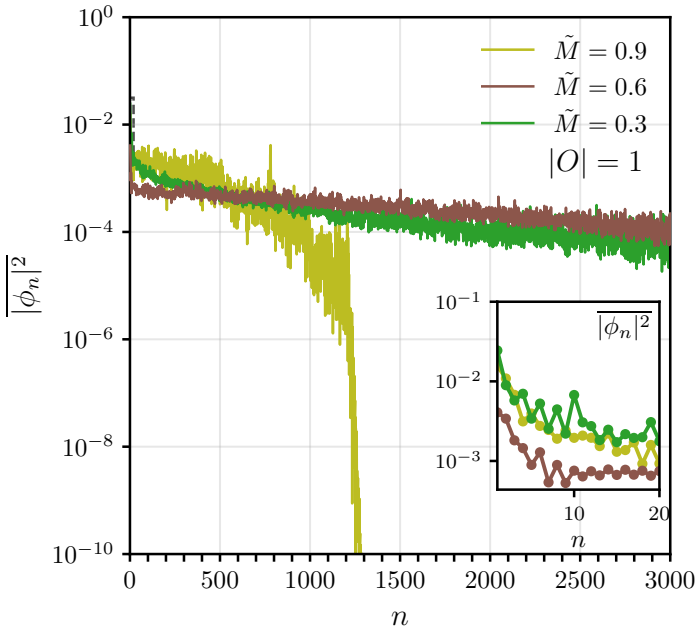

Figure 6.13: The late-time Krylov wavefunction, $|\phi_n(t)|^2$, shown at $t = 2 \times 10^5$ for several connectance, $\tilde{M}$. (Inset) A magnified view of the occupancy for the first few Krylov basis states at the late-time. All data are for a single-site initial operator ($\mathcal{O} = Y_1$) on a system of size $L = 6$ with Hamiltonian parameters $g = 1.0$ and $h = 0.1$, averaged over 500 graph realizations (denoted by overbar).

correlator $F(t) = \langle \mathcal{O}(t)\mathcal{O}(0) \rangle$. Since $F(t)$ is an even function of time (due to cyclicity of trace), it can be expanded in even powers of t as

$$F(t) = \sum_{n=0}^{\infty} \frac{(-1)^n t^{2n}}{(2n)!} \mu_{2n}, \tag{6.25}$$

where the 'moments' μ_{2n} are related to the adjoint action of the Liouvillian on the operators as $\frac{\mathrm{Tr}(\mathcal{O}\mathcal{L}^{2n}\mathcal{O})}{\mathrm{Tr}(\mathcal{O}^2)}$ are the moments of the correlation function. The Lanczos coefficients $\{b_n\}$, which govern the growth of the operator in Krylov space, are entirely determined by these moments via a Gram-Schmidt orthogonalization of the sequence $\{\mathcal{O}, \mathcal{L}\mathcal{O}, \mathcal{L}^2\mathcal{O}, \ldots\}$, meaning that $F(t)$ encodes, in principle, all the information needed to extract $\{b_n\}$ [276]. Since the polynomial fit requires accurate estimation of the autocorrelation function, which becomes challenging at large t due to decoherence in the experimental setup, only early time KC estimation is likely to be accessible. These still can capture certain distinguishing characteristics of chaotic dynamics (Fig. 6.11).

6.6 Conclusion and Outlook

In this chapter, we have investigated the emergence of quantum chaos and complexity in the mixed-field Ising model defined on Erdős–Rényi graphs, and studied how the connectivity $\tilde{M}$ governs the onset of chaos. Hamiltonians of similar structure appear naturally in quantum circuits related to optimization tasks, and careful use of such Hamiltonian terms can have a catalytic

effect in improving the performance of QAOA and annealing algorithms (Sec. 6.2, also see Ref. [252]). Using a combination of diagnostics – deep thermalization of the projected ensemble, the partial spectral form factor, and Krylov complexity, we provide a detailed characterization of the localized-to-chaotic-to-integrable crossover driven by changes in connectance. All metrics consistently point to the onset of chaotic behavior at intermediate $\tilde{M}$, even for modest system sizes. With increasing L, the chaotic region in the space of $\tilde{M}$ expands, and we expect that in the thermodynamic limit, the model is chaotic everywhere except at $\tilde{M} = 0$ and 1.

Deep thermalization of the projected ensemble reveals a rapid approach of PE to Haar ensemble with system-size at intermediate $\tilde{M} \sim 0.4 - 0.7$ indicating chaotic dynamics. Away from intermediate $\tilde{M}$, the metrics of deep thermalization, namely the trace distance of PE moments from that of the Haar ensemble, show a smooth crossover from chaotic to integrable/localized features. This is reflected in the time dependence of the trace distances as well as the system size dependence of the asymptotic plateau in the trace distance. The $\tilde{M} \sim 0$ systems have disconnected or weakly connected clusters, which result in local integrals of motion. At $\tilde{M} = 1$, i.e., the LMG limit, the system commutes with the total spin operator S^2 as well as has a large number of permutation symmetries, causing fragmentation of the Hilbert space into fragments of sizes at most $L + 1$. Away from this limit, the deletion of a finite density of bonds on the LMG model results in weak mixing of these fragments. Thus, just away from the extreme limits, we expect approximate conservation laws that cause slow relaxation. These also cause non-ergodic eigenstates, which are reflected in the asymptotic trace distance plateau being different from that of the maximally chaotic $\tilde{M} \sim 0.4$. These diagnostics can be scaled up in currently accessible quantum simulators, making our finite-size results a baseline for such an experimental effort. Construction of the projected ensemble, estimation of its higher moments, and behavior of deep thermalization measures have already been demonstrated on quantum simulator platforms with up to 25 qubits in both neutral-atom arrays [17] and superconducting architectures [16]. The finite-size signatures of deep thermalization reported here, such as the $\tilde{M}$-dependent exponent in the time-dependent decay of the trace distance, are within reach of current systems. With improvements in coherence time, larger system sizes will become accessible on quantum devices, enabling extrapolations toward the thermodynamic limit.

We have shown that the partial spectral form factor also provides a clear characterization of the chaotic dynamics of the random graph Hamiltonian, similar to what has been achieved using the spectral form factor. The intermediate $\tilde{M}$ graphs agree well with the chaos imprints exhibiting a correlation hole, a ramp, and a plateau structure. The localizing Hamiltonian in the small $\tilde{M}$ regime has a pSFF without a correlation-hole structure. Both $\tilde{M} \sim 1$ and $\tilde{M} \sim 0$ systems show larger fluctuations and differ in the mean value of the late-time plateau of the pSFF. Overall, the behavior of the pSFF in the localizing, integrable, and chaotic regimes is qualitatively similar to that of the spectral form factor. While SFF and pSFF can be estimated using randomized measurements, pSFF requires measurements and controlled unitaries only at a small subsystem level [67, 273]. The better experimental scalability makes pSFF a valuable tool for investigating the emergence of chaos in larger systems using quantum simulators. Realizing the full ramp-and-plateau structure of the pSFF does, however, require long coherence times to evolve the system to $t \sim t_p$, which scales exponentially with L. The correlation hole appears

considerably earlier t_{Th} and serves as a potential discriminator between chaotic and non-chaotic regimes.

The relaxation dynamics studied in Appendix 6.F also show distinct long-time behavior in the different connectance regimes. While the chaotic regime shows anomalous thermalization behavior reminiscent of the quantum Mpemba effect, the integrable regime shows persistent oscillations in the late-time trace distance from the equilibrium density matrix.

Krylov complexity provides the cleanest distinction of dynamical regimes, showing clearly larger values at intermediate connectance consistent with chaos (Fig. 6.12(c)). However, estimating KC experimentally is challenging at present. Experimentally measurable proxies have been proposed for KC; these can help scale up the study of the emergence of chaos from an information scrambling perspective. An analogous investigation applicable directly to the quantum annealing setting requires analysis of the low-energy sector of the spectrum using probes such as an energy-density-specific Krylov complexity, as the performance of quantum annealing is sensitive to the localization of low-lying eigenstates [251]. Overall, our results provide a comprehensive and experimentally relevant characterization of the connectivity-driven onset of quantum chaos, offering benchmarks and insights for controlling the performance of variational quantum algorithms and reservoir computing [253].

Appendix 6.A Eigenstate Localization and Entanglement

Here, we briefly discuss the eigenstate properties of the Hamiltonian in Eq. 6.1 with $g = 1$ and $h = 0.1$ for a $L = 10$. We take a single realization of the Hamiltonian at each $\tilde{M}$ and compute the bipartite entanglement entropy of each eigenstate. We quantify the entanglement entropy with Von-Neumann entropy, $R_1^A = -\sum_i \lambda_i \log \lambda_i$, where λ_i are the squared singular values of the subsystem reduced density matrix. The result is presented in Fig. 6.14 for a range of connectivities. The maximum entanglement is bounded by Page value, $R_1^{\mathrm{A,Page}} = (L/2)\log 2 - 0.5$ and is marked with the black dashed line. The entanglement is smaller than Page value even for the mid-spectrum states at $\tilde{M}$ close to 0. For $\tilde{M} \approx 0.3 - 0.7$, the entanglement entropy of most of the bulk eigenstates approaches the Page value. As $\tilde{M} \to 1.0$, some fraction of mid-spectrum eigenstates show lower entanglement entropy. At $\tilde{M} = 1.0$, signs of fragmentation appear, with eigenstate entanglement values clustering.

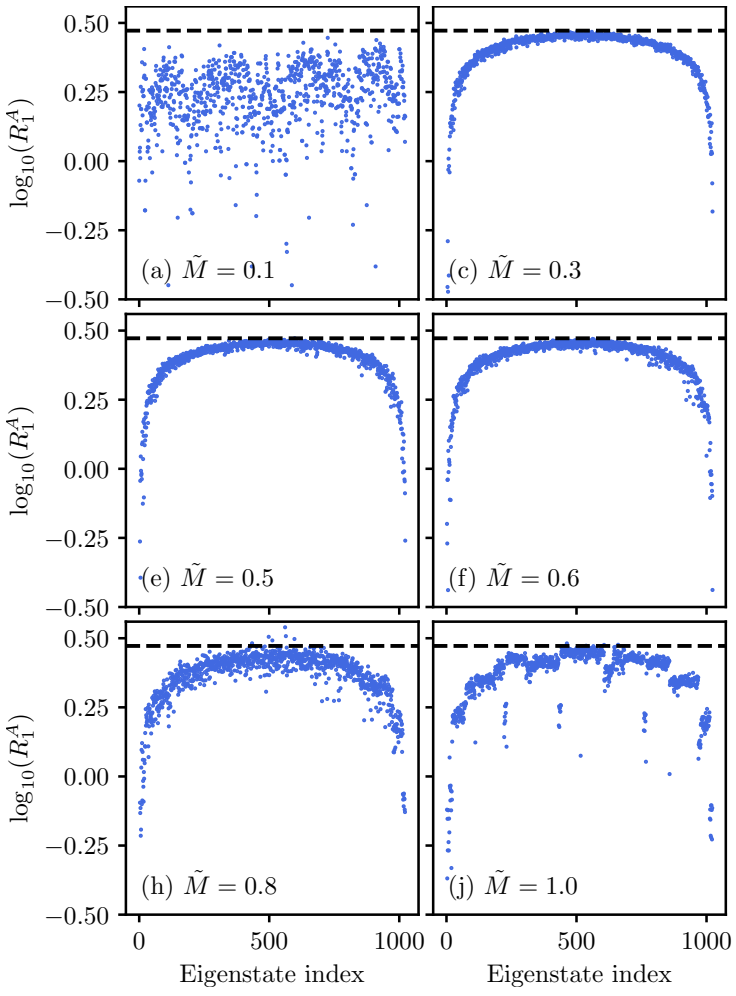

Figure 6.14: The bipartite entanglement entropy for a single instance of the Ising problem on an ER graph of $L = 10$ sites with $L_A = 5$. The black dashed line shows the Page value.

Next, we examine the localization of simple product states in the eigenstate basis. We

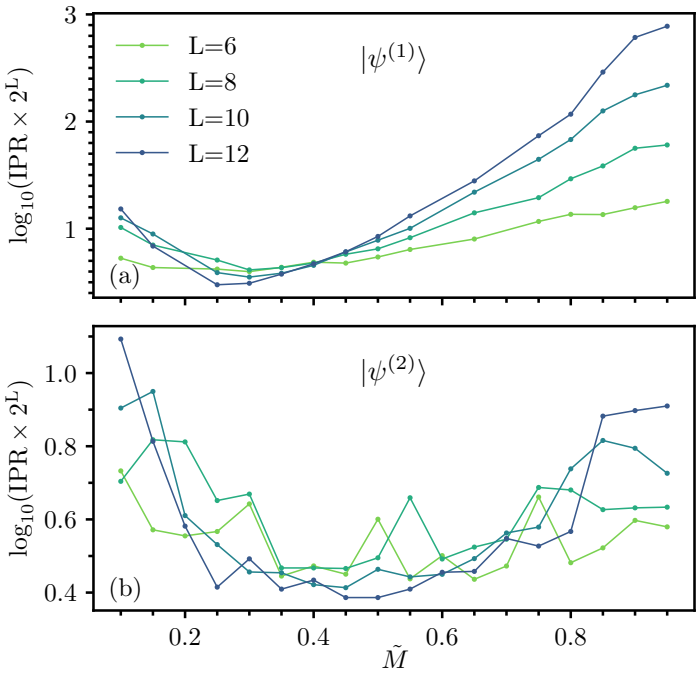

Figure 6.15: The IPR of product states (a) $|\psi^{(1)}\rangle$ (b) $|\psi^{(2)}\rangle$. All data points are averaged over 100 graph instances (and initial state in the case of (b))

measure this quantity with inverse participation ratio (IPR), defined as

$$\mathrm{IPR}(\psi) = \sum_{i=1}^{d} |\langle E_i|\psi\rangle|^4, \tag{6.26}$$

where E_i are Hamiltonian eigenstates. IPR is 1 for perfectly localized state and $1/2^L$ for maximally delocalized states. We compute the IPR for two classes of initial product states,

$$|\psi^{(1)}\rangle = \frac{1}{\sqrt{2^L}} \bigotimes_{i=0}^{L} (|0\rangle + \imath|1\rangle), \tag{6.27}$$

These states (same as Eq. 6.11) have 0 energy and are permutation-invariant. Next, we consider a class of states that lack the permutation invariance. Consider each site i is prepared in an equatorial state on the Bloch sphere,

$$|\psi^{(2)}\rangle = \bigotimes_{i=1}^{L} |\phi_i\rangle, \qquad |\phi_i\rangle = \frac{|0\rangle + e^{i\phi_i}|1\rangle}{\sqrt{2}}, \tag{6.28}$$

where $|0\rangle$ and $|1\rangle$ are the eigenstates of Z. The angles $\{\phi_i\}$ are drawn from antipodal pairs to ensure zero energy. Specifically, $L/2$ angles $\alpha_k \sim \mathrm{Uniform}[0, 2\pi)$ are sampled independently, giving the set

$$\{\phi_i\}_{i=1}^{L} = \{\alpha_1,\ \alpha_1 + \pi,\ \alpha_2,\ \alpha_2 + \pi,\ \ldots,\ \alpha_{L/2},\ \alpha_{L/2} + \pi\}, \tag{6.29}$$

randomly assigned across sites. The zero-energy condition follows from the cancellation within

each antipodal pair,

$$\langle H\rangle = -g\sum_{i=1}^{L}\cos\phi_i = -g\sum_{k=1}^{L/2}\Big(\cos\alpha_k + \cos(\alpha_k+\pi)\Big) = 0, \tag{6.30}$$

where the J_z and h_z terms vanish identically since $\langle\sigma_i^z\rangle = 0$ for all equatorial states. The special case $\alpha_k = \pi/2$ for all k recovers the uniform $|+y\rangle^{\otimes L}$ initial state used in the main text in Eq. 6.11. Fig. 6.15(a) shows the IPR for $|\psi^{(1)}\rangle$ averaged over 100 Hamiltonians. The IPR is minimum near $\tilde{M} = 0.3$, indicating the state is maximally spread among the eigenstates compared to the case of other $\tilde{M}$. Incidentally, $\Delta^{(k)}$ attains its minimum value around this $\tilde{M}$ in Fig. 6.6. The IPR goes up (the product state is localized in the eigenbasis of the Hamiltonian) at extremal values of $\tilde{M}$.

For $|\psi^{(2)}\rangle$, we average over both initial state and Hamiltonians at each $\tilde{M} = 0.3$. As shown in Fig. 6.15(b), for larger systems, there is a clear minimum in IPR at $\tilde{M} = 0.5$. At very small systems ($L = 6$), this distinction gets weak.

Appendix 6.B Additional data on QAOA with random Ising mixer

In Sec. 6.2.2, we provided an illustrative example demonstrating the effect of the additional mixer Hamiltonian on QAOA performance for $L = 8$ and $\tilde{M}_c = 0.4$. Here, we present the QAOA performance for an random Ising problem instance on an ER graph with $L = 10$ and $\tilde{M}_c = 0.3$ to validate the results on larger system. The H_d was taken with Pauli-YY coupling (Eq. 6.8). This YY term can scatter among computational basis states with Hamming distance 2 compared to just the transverse field mixer which scatters among states with Hamming distance 1. We demonstrate the numerical results in Fig. 6.16 for 500 random instances of H_d at each $\tilde{M}$. Here, we first define a baseline for performance comparison. We consider the best E_{QAOA} obtained with $\tilde{M} \in \{0, 1\}$ as $E^{\mathrm{ref}}_{\mathrm{QAOA}}$. The red line denotes the fraction of instances where the energy obtained with QAOA protocol is lower compared to $E^{\mathrm{ref}}_{\mathrm{QAOA}}$. The fraction of instances surpassing the baseline energy shows two distinct trends: at fixed p, it is maximized at intermediate $\tilde{M}$, confirming that the chaotic regime provides a favorable landscape for QAOA optimization; additionally, at any fixed $\tilde{M}$, this fraction grows with p, indicating that deeper circuits with more applications of the chaotic driver Hamiltonian progressively improve the ability to explore the energy landscape and find lower-energy solutions. The latter trend is consistent with the expectation that repeated application of a chaotic driver generates more complex quantum superpositions, allowing QAOA to access a larger portion of the Hilbert space with increasing circuit depth. This trend empirically holds for circuits with up to $p = 3$ layers that we have studied in this chapter. However, very deep quantum circuits suffer from barren plateaus where the cost function gradient vanishes exponentially with system size, making classical parameter optimization intractable.

As discussed in Sec . 6.2, the improvement in QAOA performance observed with the H^{YY} driver could stem from the chaotic nature of H_{d}, and the presence of terms that scatter among computational basis states more efficiently. We consider an alternative driver Hamiltonian with Pauli-ZZ coupling,

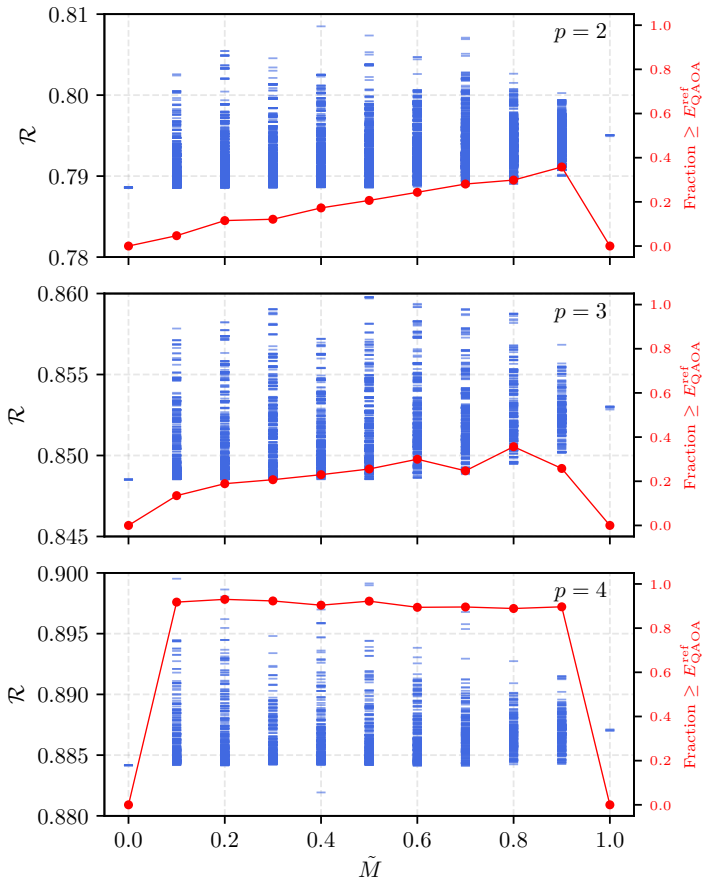

Figure 6.16: The approximation ratio for an Ising problem on an ER graph of $L = 10$ sites with $\tilde{M}_c = 0.3$. The red line shows the fraction of QAOA instances where the corresponding connectivity performs better than the baseline.

$$H_{\text{d}} = -\frac{JL}{M}\sum_{i,j} A_{ij} Z_i Z_j - g\sum_i X_i, \tag{6.31}$$

which is diagonal in the computational basis and therefore induces no scattering among basis states. Taking the same problem instance H_{c} as in Fig. 6.4(a),(c) (Problem 1), we present the distribution of QAOA performance for $p = 2, 3$ and 4 in Fig. 6.17. The improvement in performance with intermediate $\tilde{M}$ persists with the ZZ driver, despite the absence of any Hamming distance 2 scattering. This establishes that the chaotic structure of H_{d}, rather than the specific scattering properties of the mixer, is the primary driver of the observed improvement in QAOA.

Appendix 6.C PE from a Permutation-Symmetry-Breaking Initial State

The initial state is chosen to be a product state $\psi^{(2)}$ (Eq. 6.28 with zero energy expectation value, $\langle\psi_0|H|\psi_0\rangle = 0$ and without permutation symmetry.

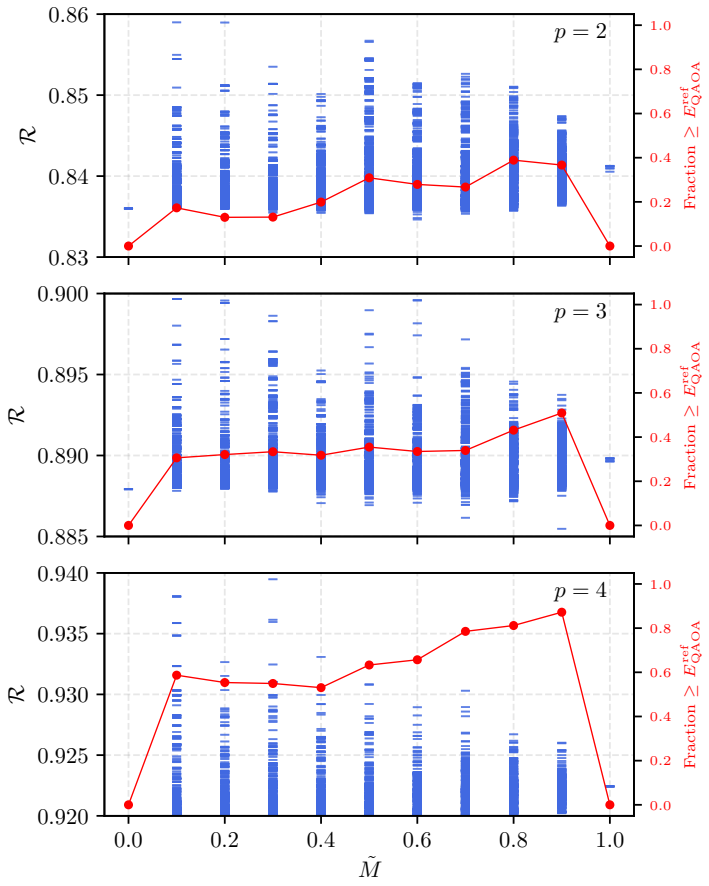

Figure 6.17: The approximation ratio for an Ising problem on an ER graph of $L = 8$ sites with $\tilde{M}_c = 0.4$ (same H_c as Problem 1 in Fig. 6.2.2). The red line shows the fraction of QAOA instances where the corresponding connectivity performs better than the baseline.

Figure 6.18 shows the scaling of trace distance between the first 3 moments of PE and Haar ensemble across connectivity and system size. The initial state is taken as a random direct product state (Eq. 6.28) with energy expectation value 0. The data is presented for 500 random initial states and ER graphs. The qualitative behavior is similar to Fig. 6.6.

Appendix 6.D Lanczos algorithm

In the main text, we used the Lanczos algorithm to generate a basis for the Krylov space. The Lanczos algorithm is an iterative method for constructing the orthonormal basis of the Krylov subspace, $\mathcal{K}_{\mathcal{O}}$. The conventional implementation of the algorithm relies on a computationally efficient three-term recurrence relation, in which each new vector is made orthogonal only to the two preceding vectors. While theoretically exact, this procedure is numerically unstable when implemented with finite-precision arithmetic, as rounding errors accumulate, gradually leading to a loss of orthogonality among the basis vectors.

To circumvent this issue, we employ the more robust, albeit computationally intensive, Lanczos with Full Orthogonalization [312, 301]. In this scheme, each new candidate vector is explicitly made orthogonal to *all* previously generated basis vectors using a Gram-Schmidt

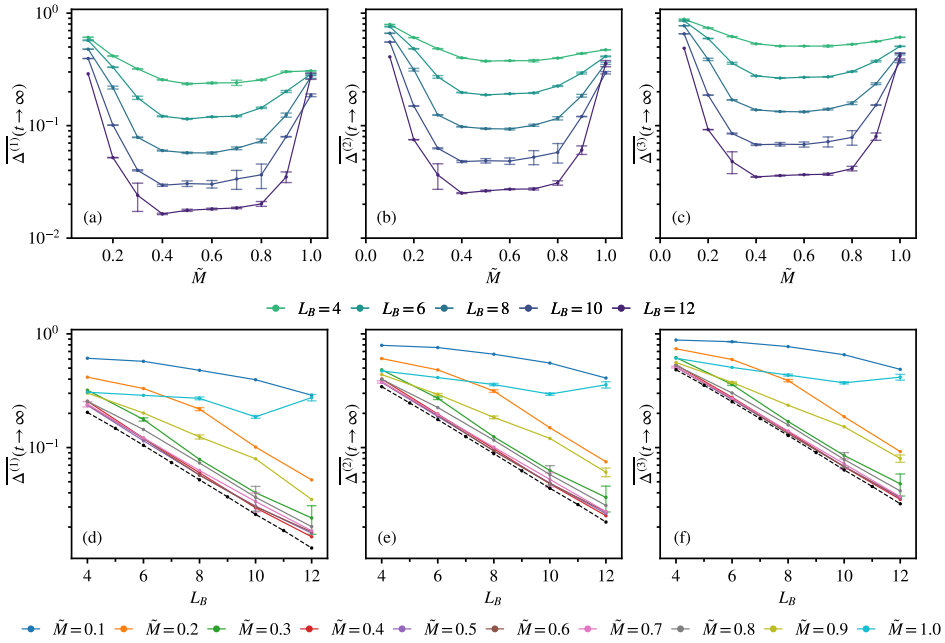

Figure 6.18: (a)-(c) Asymptotic ($t = 10^9 J^{-1}$) trace distance of first 3 moments of PE from Haar ensemble as a function of L_B. The asymptotic trace distance gets suppressed with increasing L_B for all $\tilde{M}$. Error bars represent the standard error of the mean across realizations at a fixed t. (d)-(f) The same data plotted to show the the scaling of $\overline{\Delta^{(k)}}(t \to \infty)$ with L across all $\tilde{M}$ for first 3 moments of PE. The error bars are not shown when they are comparable to the marker size. Each data point shown represents an average over 500 graph realizations and random direct product initial states (Eq. 6.28), calculated for a subsystem of size $L_A = 2$ with Hamiltonian parameters (Eq. 6.1) $g = 1.0$ and $h = 0.1$. The black dashed line shows the trace distance of an empirical ensemble of 500 random states (sampled from Haar random states of system size L) from the corresponding moments of the Haar ensemble.

procedure. This ensures a numerically stable orthonormal basis (up to machine precision) at the cost of increased computational complexity, as the number of required inner products scales with the iteration number n, rather than being constant. However, for small system sizes, this cost is manageable. The procedure we implement is as follows:

1. **Initialization:** Start with the vectorized initial operator, $|\tilde{\mathcal{O}}_0) = \text{vec}(\tilde{\mathcal{O}}_0)$. Normalize it to obtain the first basis vector of the Krylov basis:

$$|\mathcal{O}_0) = \frac{|\tilde{\mathcal{O}}_0)}{\sqrt{(\tilde{\mathcal{O}}_0|\tilde{\mathcal{O}}_0)}}$$

2. **Iteration (for n = 0, 1, 2, ...):**

   First, generate a new candidate vector by applying the Liouvillian to the most recently generated basis vector:

$$|w_{n+1}) = \mathcal{L}|\mathcal{O}_n)$$

   Next, enforce orthogonality. To ensure the new vector is orthogonal to all previously found basis vectors, explicitly subtract the projection onto each of them. For numerical stability,

this process is repeated twice (double orthogonalization):

$$|w'_{n+1}) = |w_{n+1}) - \sum_{j=0}^{n} (\mathcal{O}_j|w_{n+1})|\mathcal{O}_j)$$

The next Lanczos coefficient, b_{n+1}, is the norm of this fully orthogonalized vector:

$$b_{n+1} = \sqrt{(w'_{n+1}|w'_{n+1})}$$

If b_{n+1} is smaller than a numerical tolerance (e.g., 10^{-13}), the Krylov subspace is exhausted, and the algorithm terminates constructing a Krylov subspace of dimension K such that $b_K < 10^{-13}$. Otherwise, the next orthonormal basis vector is found by normalizing:

$$|\mathcal{O}_{n+1}) = \frac{|w'_{n+1})}{b_{n+1}}$$

This iterative process yields the set of orthonormal basis operators $\{|O_n))\}_{n=0}^{K-1}$ and the real, positive Lanczos coefficients $\{b_n\}_{n=1}^{K-1}$ that define the tri-diagonal hermitian matrix representation of $\mathcal{L}$.

A key feature of the resulting tridiagonal matrix for $\mathcal{L}$ is that its diagonal elements, $a_n = (\mathcal{O}_n|\mathcal{L}|\mathcal{O}_n)$, are identically zero. This arises from the definition of the Liouvillian and the cyclic property of the trace. Assuming the basis operators $|\mathcal{O}_n))$ are Hermitian (which is the case if the initial operator is Hermitian), we have:

$$\begin{aligned} a_n &= (\mathcal{O}_n|\mathcal{L}|\mathcal{O}_n) \\ &= \mathrm{Tr}(\mathcal{O}_n^\dagger[H, \mathcal{O}_n]) \\ &= \mathrm{Tr}(\mathcal{O}_n(H\mathcal{O}_n - \mathcal{O}_n H) \\ &= \mathrm{Tr}(\mathcal{O}_n H \mathcal{O}_n) - \mathrm{Tr}(\mathcal{O}_n \mathcal{O}_n H) = 0 \end{aligned}$$

This cancellation ensures that the Liouvillian is purely off-diagonal in the Krylov basis, simplifying the resulting dynamics to a hopping problem on a chain without any on-site potential.

Appendix 6.E Krylov complexity for random single-site operators

In Sec. 6.5, we discussed the Krylov complexity for a simple initial operator (Pauli Y). We also saw the effect of the initial size of the operator on its growth. A natural question arises regarding the dependence of the behavior on the choice of operator. Here, we take a random single-site operator as,

$$\mathcal{O}_i = r_0\mathbb{I} + r_1 X_i + r_2 Y_i + r_3 Z_i. \tag{6.32}$$

Here, $\{r_0, r_1, r_2, r_3\}$ are random numbers sampled from a normal distribution. The operator is normalized such that it has a norm of $\sqrt{2}$ (i.e., equal to Pauli operators). In Fig 6.19, we

present the results after averaging over 500 graphs. For each graph realization, we take a different random initial operator. Averaging is done over both graph realizations and the initial operator. The trend with $\tilde{M}$ holds here as well as shown in Fig 6.19(a). We compare the asymptotic KC obtained after averaging over random graphs and operators with the scenario where averaging is done only over graphs in Fig. 6.19(b). The asymptotic KC is smaller for random operators, but the qualitative trend is the same. The time-evolved Krylov wavefunction is shown in Fig. 6.19(c). The wavefunction shows a clear sign of localization for $\tilde{M} = 0.9$. The distribution of Lanczos coefficients is also consistent with the qualitative characteristics observed earlier in Sec. 6.5.

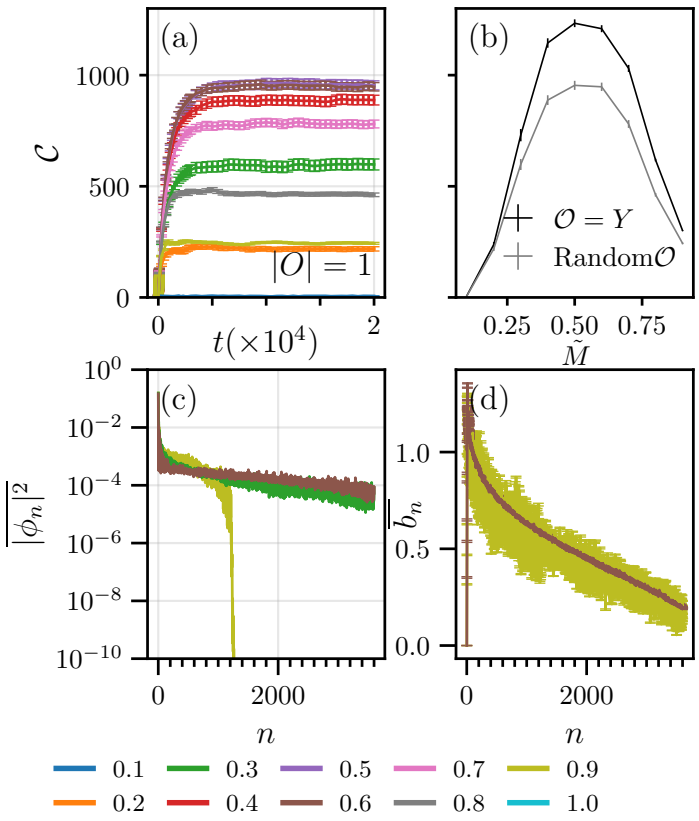

Figure 6.19: (a) Time evolution of KC and its asymptotic value across multiple $\tilde{M}$. (b) Comparison of asymptotic Krylov complexity as a function of $\tilde{M}$ for random single-site operator and Pauli-Y operator. (c) The asymptotic Krylov wavevector (d) The distribution of Lanczos coefficients. $L = 6$ Error bars are shown as the standard error of the mean. All results are presented after averaging over 500 random graphs and operators.

Appendix 6.F Anomalous relaxation of initial product states

In this appendix, we analyze the dynamical relaxation of quantum states under unitary time evolution. In closed quantum many-body systems, a subsystem's approach to equilibrium is driven by the scrambling of local information, a process whose efficiency was characterized in Sec. 6.5 via Krylov complexity. Here, we focus on how certain simple initial states relax under this unitary dynamics. An intuitive expectation for individual states is that the time to reach equilibrium should monotonically increase with the initial state's "distance" from the equilibrium

ensemble. In a classical context, a "hotter" system is farther from ambient temperature compared to a "cooler" system. So, we can expect that a "cooler" state, being "closer" to equilibrium, would relax faster than a "hotter" one. However, it has been found that certain initial conditions can defy this intuition, giving rise to anomalous thermalization behaviors. Broadly, this phenomenon is studied as the Mpemba effect, first reported in water [313], where initially hotter systems freeze faster than cooler ones under a quench.

Recently, the quantum Mpemba effect, a quantum analogue of the counterintuitive classical phenomenon, has been studied. The QME was first proposed for open quantum systems, where a system's coupling to a thermal bath induces irreversible dynamics [314, 315, 316, 317]. In this setting, the effect is understood to arise from the spectral properties of the system's dissipative Liouvillian. An initial state can be designed such that its overlap with the slowest eigenmode of the Liouvillian is suppressed, allowing it to equilibrate anomalously fast. This open-system QME was recently experimentally demonstrated [318].

Subsequently, the QME has been extended to isolated systems with global symmetry undergoing unitary evolution, where thermalization is observed at the subsystem level [319, 320, 321, 322, 323]. In such closed systems, the "distance" from equilibrium is typically inferred from the off-diagonal blocks in the symmetry-imposed subsystem reduced density matrix at equilibrium after a quench from an initial state which is not an eigenstate of the global symmetry. Recently, QME has been studied in spin chains and Floquet systems where global symmetries are absent [323] as well as systems with disorder [324].

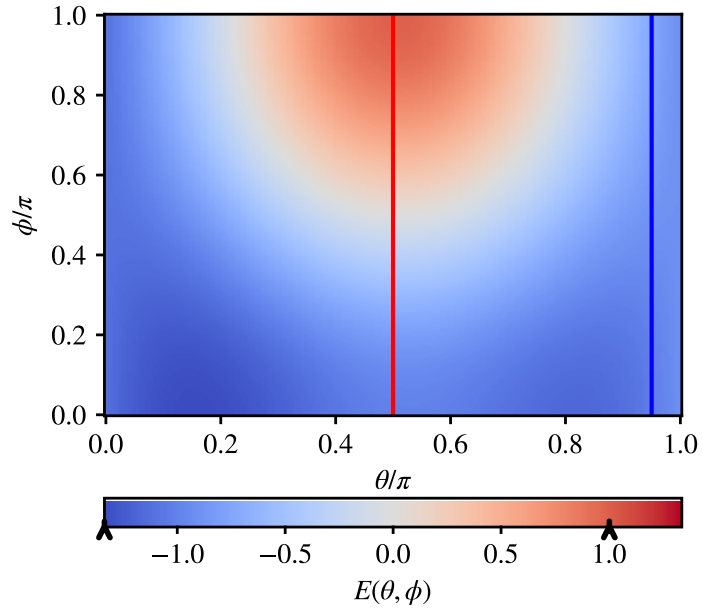

Figure 6.20: Distribution of energy of the initial state as a function of (θ, ϕ). $L_A = 4, L = 12$. The initial states are of the form in Eq. 6.34. The markers on the colorbar indicate the bandwidth of the eigen spectrum.

To investigate the presence of QME in this random graph system, we first establish a quench protocol and a metric to quantify the thermalization. Unlike studies that track the restoration of a global symmetry, our Hamiltonian (Eq. 6.1) with $h \neq 0$ lacks such a conserved quantity. We

therefore adopt a more direct approach [323] to quantify relaxation. Our metric is the trace distance, $\Delta^{(1)}$ (Eq. 6.13), between the time-evolved reduced density matrix and its corresponding diagonal ensemble. This diagonal ensemble represents the infinite-time equilibrium ensemble ($\rho_A(\infty)$) given as,

$$\rho_A(\infty) = \mathrm{Tr}_B(\mathcal{U}\mathrm{diag}(|\mathcal{U}\psi\rangle|^2)\mathcal{U}^\dagger), \tag{6.33}$$

where $H = \mathcal{U}\tilde{E}U^\dagger$ for Hamiltonian H and $\tilde{E}$ is a diagonal matrix containing the eigenvalues of H. B indicates the complement of subsystem A. To simplify the parameter space of the initial state, we prepare a family of permutation-invariant product states $\psi(\theta, \phi)$ in real space as,

$$\psi(\theta,\phi) = \otimes_{i=0}^{L}\left(\cos\left(\frac{\theta}{2}\right)|0\rangle + e^{\imath\phi}\sin\left(\frac{\theta}{2}\right)|1\rangle\right). \tag{6.34}$$

The initial state energy $E(\theta, \phi)$ is a smooth function of θ, ϕ and given as,

$$E(\theta,\phi) = -(\cos\theta)^2 - g\sin\theta\cos\phi - h\cos\theta. \tag{6.35}$$

$E(\theta, \phi)$ depends only on the coupling parameters of the Hamiltonian but not on the connectance (This is due to the normalization factors in the denominator of Eq. 6.1). The distribution of initial state energy as a function of (θ, ϕ) is shown in Fig. 6.20. The red and blue region shows high and low energy states, respectively, with a crossover region near 0 energy where states correspond to infinite temperature. Consider two initial states $\psi(\theta_1, \phi_1)$ and $\psi(\theta_2, \phi_2)$ such that $\Delta^{(1)}_{\theta_1,\phi_1}(t = 0) > \Delta^{(1)}_{\theta_2,\phi_2}(t = 0)$ where trace distance is always taken from the respective diagonal ensembles. Existence of QME implies for $t > t_M$, $\Delta^{(1)}_{\theta_1,\phi_1}(t) < \Delta^{(1)}_{\theta_2,\phi_2}(t)$, where t_M is referred to Mpemba time. Here, $\Delta^{(1)}_{\theta_1,\phi_1}(t = 0)$ is the initial "hotter" state due to the higher trace distance of the subsystem reduced density matrix from the corresponding equilibrium ensemble.

Our analysis focuses on two distinct classes of initial states (Eq. 6.34), parametrized by θ and marked in Fig. 6.20. The first class, with $\theta = 0.5\pi$, spans a wide range of initial energies as ϕ is varied. In contrast, the second class, with $\theta = 0.95\pi$, consists of nearly-polarized states whose initial energies are only weakly dependent of ϕ.

Starting with these two classes of initial states (identified by θ), we time evolve with a specific graph realization of Hamiltonian in Eq. 6.1 with $h = 0.1, g = 1$. We first consider $\tilde{M} = 0.4$, where the model is expected to be chaotic. Figure 6.21(b) and (d) shows time evolution of $\overline{\Delta^{(1)}}$ for $\theta = 0.5\pi$ and $\theta = 0.95\pi$, respectively. All data are presented after averaging over 500 graph realizations starting with the same set of initial states. We observe a clear crossing in $\Delta^{(1)}$ in Fig. 6.21(d) where the initial states are taken such that $\theta = 0.5\pi$. Such crossing is absent in Fig. 6.21(b) where $\theta = 0.95\pi$ and relaxation to equilibrium looks almost independent of the initial state at the late-time.

The observed differences in the late-time relaxation dynamics can be qualitatively understood by considering how the initial states are represented in the energy eigenbasis. $\Delta^{(1)}$ can be expressed in terms of the overlap of the initial state with energy eigenstates as,

$$\Delta^{(1)}(t) = \frac{1}{2}\left\|\sum_{n\neq m} c_n c_m^* e^{-i(E_n-E_m)t}\mathrm{Tr}_\mathrm{B}(|E_n\rangle\langle E_m|)\right\|_1 \tag{6.36}$$

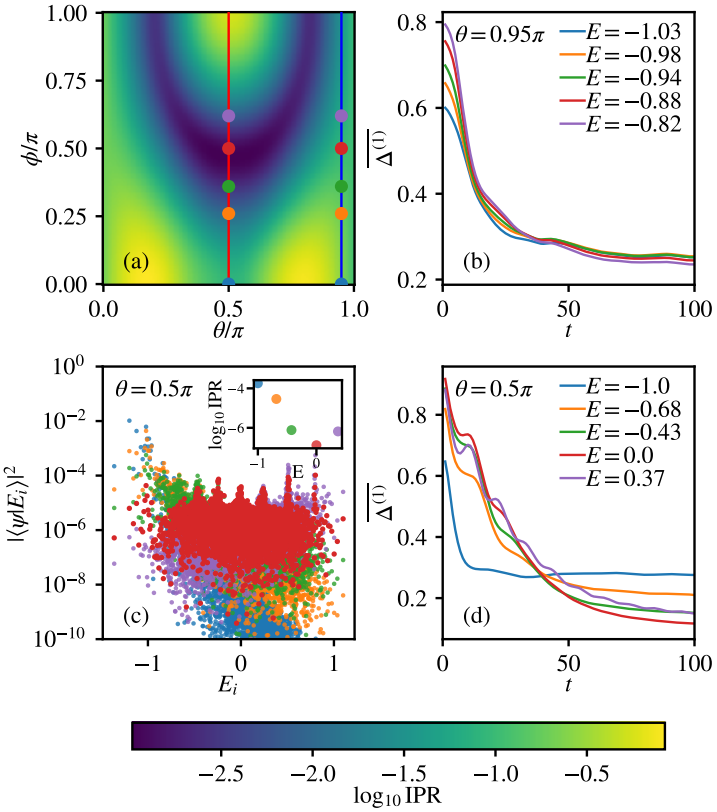

Figure 6.21: Anomalous relaxation in the chaotic regime at $\tilde{M} = 0.4$ for a system with $L = 12$. (a) The Inverse Participation Ratio (IPR) as a function of the initial state parameters (θ, ϕ). The red and blue vertical lines at $\theta = 0.5\pi$ and $\theta = 0.95\pi$ indicate the two classes of states studied. (b) Relaxation dynamics, measured by the trace distance $\Delta^{(1)}(t)$ from the diagonal ensemble, for the nearly-polarized states ($\theta = 0.95\pi$). (c) The distribution of overlaps, $|\langle E_n|\psi\rangle|^2$, with energy eigenstates for several initial states from the $\theta = 0.5\pi$ class. The inset shows the corresponding IPR for each state. (d) Relaxation dynamics for the $\theta = 0.5\pi$ class, showing a clear crossing indicative of the QME. For all plots, the subsystem size is $L_A = 4$, and all data are averaged over 500 graph realizations (denoted by overbar) using the Hamiltonian in Eq. 6.1 with $g = 1.0$ and $h = 0.1$.

where $c_n = \langle\psi|E_n\rangle$. At $t = 0$, $\Delta^{(1)}(0) = \frac{1}{2}\left\|\sum_{n\neq m} c_n c_m^* \mathrm{Tr}_B(|E_n\rangle\langle E_m|)\right\|_1$ i.e., the trace distance contains $O(d^2)$ terms weighted by the overlaps of initial state with eigenstates. As was pointed out in Ref. [323], the relaxation rate of states can be related to the number of nonzero coefficients c_n, quantified by the inverse participation ratio (IPR) given as,

$$\mathrm{IPR}(\psi) = \sum_{i=1}^{d} |\langle E_i|\psi\rangle|^4. \tag{6.37}$$

If the initial state ψ is a generic state (with energy close to 0, i.e., analogous to a mid-spectrum eigenstate), $c_n \approx O(1/\sqrt{d})$ in Eq. 6.36, corresponding to a smaller IPR.

$|\Delta^{(1)}(t)|^2$ is the sum of squared norms of the matrix elements of $(\rho_A - \rho_A(\infty))$. For an initial state ψ which has overlap with a large number of energy eigenstates (i.e., smaller IPR), there is a large number of nonzero c_ns. Each c_n is small due to normalization of the initial state and, at the same time, there are a larger number of fluctuating phases in the expansion of each

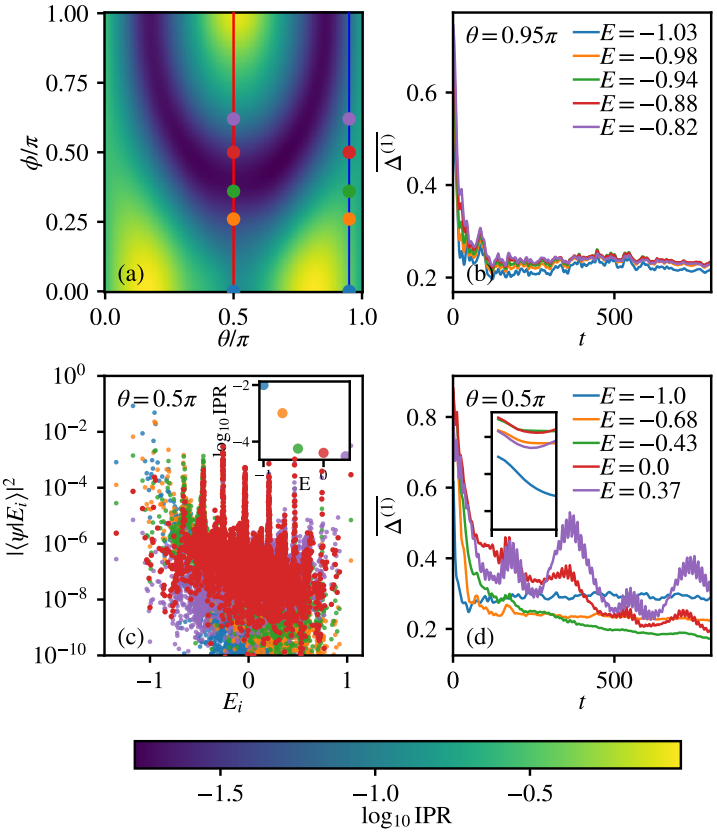

Figure 6.22: Anomalous relaxation in the near-integrable regime at $\tilde{M} = 0.8$ for a system with $L = 12$. (a) The IPR as a function of the initial state parameters (θ, ϕ). The red and blue vertical lines indicate the two classes of states studied. (b) Relaxation dynamics, $\Delta^{(1)}(t)$, for the nearly-polarized states ($\theta = 0.95\pi$). (c) The distribution of overlaps, $|\langle E_n|\psi\rangle|^2$, with energy eigenstates for several initial states from the $\theta = 0.5\pi$ class. (d) Relaxation dynamics for the $\theta = 0.5\pi$ class, showing persistent oscillations and multiple crossings. The inset provides a zoomed-in view of the initial relaxation ($t = 0 - 10(J)$). For all plots, the subsystem size is $L_A = 4$, and all data are averaged over 500 graph realizations (denoted by overbar) using the Hamiltonian in Eq. 6.1 with $g = 1.0$ and $h = 0.1$.

matrix element of $(\rho_A - \rho_A(\infty))$. As a result, the temporal fluctuation in trace distance as the system relaxes is weaker in the case where IPR is smaller. For states with high IPR, a larger number of c_ns will be close to 0, which results in large temporal oscillations in trace distance from equilibrium. This causes a slower equilibration.

In Fig. 6.21, for the "cooler" initial states, the initial distance from the diagonal ensemble is lower as compared to "hotter" states. Though we can not prove this, we attempt to provide a plausibility argument. First, we consider the low IPR states. These states have a finite expectation value for Pauli observables. The diagonal ensemble constructed with this initial state will be a mixture of highly entangled mid-spectrum eigenstates. However, the diagonal ensemble will have 0 expectation value of such observables (as it is an almost uniform mixture of mid-spectrum eigenstates, which resemble infinite temperature states according to ETH). This suggests that the diagonal ensemble is not a good approximation at the initial time for the direct product state, resulting in a large initial trace distance. Note that, states close to the ground state are being approximated by a diagonal ensemble which, consists of low-lying eigenstates

that can have finite local expectation values.

We present IPR as a function of initial state parameters in Fig. 6.21(a). Interestingly, IPR shows a clear correlation with energy (Fig. 6.20). The states with energy close to 0 (i.e, they are similar to mid-spectrum states) have a lower IPR (i.e., delocalized in the eigenspectrum). The states away from the middle of the spectrum have higher IPR (i.e., localized in the eigenspectrum). The states considered for time evolution are marked in parameter space with dots. The states with $\theta = 0.5\pi$ show a spread in their IPR values. The IPR distribution is consistent with the observation in Fig. 6.21(d). The states with smaller IPR decay faster in spite of having a larger initial trace distance from their equilibrium density matrix compared to states that have a larger IPR. A smaller IPR signifies a larger number of fluctuating phases in Eq. 6.36, which explains the faster relaxation. Further, we look at the overlap of the initial states taken in Fig. 6.21(b) with individual energy eigenstates and present them in Fig. 6.21(c). The state having energy close to 0 has an almost uniform distribution of overlaps (with eigenstates). The state away from the energy 0 show a larger concentration of overlap at the edge of the spectrum. The inset in Fig. 6.21(c) shows the IPR for these states. In the states where $\theta = 0.95\pi$, the IPR shows very minor dependence on ϕ (similar to what is observed in energy). This explains the absence of a clear QME for this set of states.

The clear observation of the QME in the chaotic regime is driven by the broad delocalization of initial states across the energy spectrum. A natural question is how this phenomenon behaves as the system approaches the integrable limit at high connectance ($\tilde{M} \to 1$), where the eigenspectrum deviates from chaotic WD statistics. We investigate this interplay at $\tilde{M} = 0.8$ (Fig. 6.22). While the correlation between IPR and energy persists (Fig. 6.20 and 6.22(a)), the overall range of IPR values is smaller, indicating that the initial states are more localized in the eigenbasis as $\tilde{M} \to 1$. Consequently, the nearly-polarized $\theta = 0.95\pi$ states still show no strong signature of the QME (Fig. 6.22(b)). For the $\theta = 0.5\pi$ states, however, the dynamics are markedly different from the chaotic case. Instead of a smooth decay, the trace distance exhibits persistent late-time oscillations, as seen in Fig. 6.22(d). We expect this to be caused by the emergence of symmetry constraints and (approximate) Hilbert space fragmentation close to an integrable point. In integrable models, quenching from the ground state results in coherent propagation of stable quasiparticles, which manifests as persistent oscillations and multiple crossings in the relaxation curves [320, 325]. For a near-integrable system, our results show multiple crossings and oscillatory behavior in trace distance for a finite system within the timescale studied (Fig. 6.22(d)).

7

Conclusion and Outlook

Strongly interacting quantum many-body systems are difficult. The Hilbert space dimension grows exponentially in the number of degrees of freedom, exact diagonalization reaches only modest sizes, and the analytical tools that work in the non-interacting case rarely survive the introduction of generic interactions. There is no single method that handles all of this, and progress is usually through the discovery of structural features that make some particular strongly interacting regime tractable. Integrability, emergent conserved quantities in disordered systems, exact solutions in certain strongly interacting regimes in presence of symmetries are examples of such features. Each gives a foothold that lets quantitative work proceed where it would otherwise stall.

This thesis has been an attempt to identify and make quantitative use of such structural features in four physically distinct settings, and to use them to go beyond conventional expectation values into the finer statistical structure of the dynamics. In every case the system is strongly interacting. None of the models studied is free, and, none yields to perturbation theory in a small parameter. What allowed quantitative progress was the presence of additional structure of one kind or another. The structures differ from chapter to chapter. The chiral clock chain and the XXZ chain are Bethe-ansatz integrable. The disordered chain of Chapter 5 is many-body localized, with a full set of emergent local integrals of motion. The random-graph Ising model of Chapter 6 has no integrability of either type, but tuning its connectivity allows us to interpolates between an integrable/localized limit and a chaotic regime. Different features, but each sufficient to push the analysis well beyond what generic interacting models permit.

The chiral clock chain studied in Chapter 3 is strongly interacting and analytically intricate, and numerical exact diagonalization alone would not afford sufficiently large system sizes to characterize its transport. The Bethe-ansatz structure supplies a hierarchy of conserved charges, and those charges carry a direct imprint on thermal transport. The Mazur bound constructed from their overlaps with the energy current saturates the thermal Drude weight at every accessible temperature, providing an independent verification of the numerically obtained Drude weight from the current-current correlator. More importantly, the analysis of conserved charges provides a microscopic understanding of transport in this specific strongly interacting system.

The Mazur-bound calculation was carried out at the time-reversal-symmetric point. The

chiral clock model has a richer parameter space in which the chiral phase breaks time-reversal symmetry and may introduce a qualitatively different character to the conserved-charge structure. Studying the nature of the conserved charges and the features of transport in the absence of time-reversal symmetry is therefore a natural extension of the present work. A complementary direction is the formalization of generalized hydrodynamics for the chiral clock model. For the XXZ chain, GHD predictions for Drude weights in terms of dressed velocities and occupation functions are well established, and extending this framework to the chiral clock model would both deepen the theoretical understanding and push the analysis of ballistic transport to the thermodynamic limit, where finite-size Bethe-ansatz calculations become costly. Finally, moving away from the integrable point and studying how transport crosses over from the ballistic to the diffusive regime, and how the conserved charges break down in that process, remains an interesting open question.

Chapter 4 takes the same integrable structure into a qualitatively different regime. Where the clock chain analysis characterizes thermal transport through equilibrium linear response, the question here is what the conserved charges of the boundary-driven XXZ spin chain imply for the full statistics of the current far from equilibrium, in the long-time nonequilibrium steady state. This is a sharper probe of the same underlying structure: rather than a single transport coefficient, the full counting statistics encodes the entire probability distribution of transferred charge, and the large-deviation rate function governs the exponentially rare current fluctuations that a mean-current measurement cannot resolve. The transfer-matrix structure inherited from integrability makes this calculation tractable. At the free point the scaled cumulant generating function is obtained in closed form; in the interacting regime the same transfer-matrix framework reaches numerical precision for the full distribution. Large deviation framework provides an universal structure for the full distribution of obseravbles obtained in this chapter. From an experimental viewpoint, shadow snapshots of the NESS directly sample the full counting statistics of any diagonal observable, providing experimental access to the entire current distribution at no additional measurement cost beyond what state tomography already requires.

Several directions remain open. The calculations in this chapter were performed under maximal boundary bias, which simplifies the transfer-matrix construction but represents a special corner of the full nonequilibrium phase diagram. Moving to non-maximal bias would probe the crossover from linear to nonlinear response. A parallel direction concerns the range of models for which the FCS can be obtained exactly [326]. Additionally, there can be implications on quantum tomography from this FCS calculations and their experimental measurements.

The structural input in Chapter 5 was of a qualitatively different kind. A many-body localized system supports a set of local integrals of motion, and we chose a setting where these are strictly one-local, allowing the projected ensemble to be constructed and analyzed in a controlled fashion. We found that the limiting ensemble lay in the Scrooge family when the measurement basis was aligned with the local integrals of motion, and that misalignment moved the ensemble continuously towards the Haar limit. The existence of localized charges in disordered systems is by now well established; what our study revealed is their imprint on a comparatively delicate object, namely the deep-thermalization ensemble of a small subsystem, which probes wavefunction structure beyond what any finite expectation value could resolve. The asymptotic ensemble

reached by the projected ensemble extends the idea of the Gibbs ensemble to the level of the quantum state distribution itself, with direct implications for quantum state designs. Much of the existing literature on deep thermalization is restricted to settings with Abelian conserved charges, and it is natural to ask how the picture changes in the presence of non-Abelian charges, where the charges do not mutually commute and the structure of the invariant ensemble is richer. A separate but related extension concerns symmetry sectors: it has recently been argued that in systems with symmetry, deep thermalization should proceed to individual Scrooge ensembles within each symmetry sector [215], and working this out explicitly in a concrete model remains an interesting open problem.

Chapter 6 carried the same strategy into a setting that resembles practical quantum devices. The Ising model on an Erdős–Rényi random graph possesses no Bethe-ansatz structure, yet its geometry supports the emergence of approximate conservation laws in specific limits. Its connectivity is controlled by a single effective parameter $\tilde{M}$ that tunes the Hamiltonian continuously between an integrable/localized limit and a chaotic regime. Rather than relying on a single diagnostic, we deployed several complementary probes of chaos, including the spectral form factor, Krylov complexity, and projected-ensemble convergence, on the same Hamiltonian and analyzed how they reveal different aspect of dynamical characteristics. We further demonstrated that this dynamical structure has direct consequences for quantum optimization.

While the connection between dynamical properties and optimization performance has begun to attract attention [327, 262, 252], a systematic understanding of how specific features of the chaos-to-integrability crossover, such as the onset of the chaotic window or the breakdown of approximate conservation laws, translate into concrete changes in algorithmic performance remains largely open. Whether the diagnostics deployed here can serve as practical predictors of optimization hardness, and whether tuning a physical system toward or away from the chaotic regime can be used to improve convergence of variational algorithms [268, 328], are questions that the present analysis motivates.

The four chapters of this thesis are unified by a common premise: strongly interacting quantum systems are generically intractable, and progress requires the identification of structural features that make specific regimes analytically or numerically accessible.

What emerges from these studies is a salient pattern. Strongly interacting models that look forbidding at the first glance often carry hidden structure that allows analysis at the level of detailed statistical features of the dynamics. The Drude weight depends on a handful of charges. The full counting statistics is set by an entire transfer-matrix spectrum. The projected ensemble responds to whether the measurement basis sees the conserved charges. Krylov complexity reads operator growth, thus distinguishing the dynamical regimes in a locality-independent way. Each of these probes asks a slightly different question, and the answers are accessible when the system has certain features that make them tractable even in the presence of strong interaction. Choosing the observables that probe beyond the local expectation values and two-point correlators reveal deeper structures in the underlying universal behavior of such strongly interacting systems. Advent of modern quantum simulators make such finer questions particularly relevant. Matrix product states recurred throughout, both as a numerical engine and as analytical objects in their own right, with the exact NESS ansatz of Chapter 4 being the cleanest example.

What does seem clear from the calculations presented here is that strongly interacting quantum systems, despite their generic intractability, retain enough structure in the specific cases we considered to permit detailed statistical statements about their dynamics. The reach of the analytical and numerical tools available now is broader than the conventional toolbox of expectation values, susceptibilities, and transport coefficients would suggest, provided one is willing to look at finer features. This thesis is an effort to use that broader reach in four specific settings. The four are a small sample of a much larger class of problems to which similar arguments should apply.

Bibliography

[1] Ryogo Kubo. "Statistical-Mechanical Theory of Irreversible Processes. I. General Theory and Simple Applications to Magnetic and Conduction Problems". *Journal of the Physical Society of Japan* 12.6 (1957), pp. 570–586.

[2] J. M. Luttinger. "Theory of Thermal Transport Coefficients". *Physical Review* 135.6A (1964), A1505–A1514.

[3] Dieter Forster. *Hydrodynamic Fluctuations, Broken Symmetry, and Correlation Functions*. Frontiers in Physics. Reading, Massachusetts: W. A. Benjamin, 1975.

[4] Benjamin Doyon. "Lecture notes on Generalised Hydrodynamics". *SciPost Phys. Lect. Notes* (2020), p. 18.

[5] P. Mazur. "Non-Ergodicity of Phase Functions in Certain Systems". *Physica* 43.4 (1969), pp. 533–545.

[6] Masuo Suzuki. "Ergodicity, Constants of Motion, and Bounds for Susceptibilities". *Physica* 51.2 (1971), pp. 277–291.

[7] X. Zotos, F. Naef, and P. Prelovšek. "Transport and Conservation Laws". *Physical Review B* 55.17 (1997), pp. 11029–11032.

[8] J. M. Deutsch. "Quantum Statistical Mechanics in a Closed System". *Physical Review A* 43.4 (1991), pp. 2046–2049.

[9] Mark Srednicki. "Chaos and Quantum Thermalization". *Physical Review E* 50.2 (1994), pp. 888–901.

[10] G. Lindblad. "On the Generators of Quantum Dynamical Semigroups". *Communications in Mathematical Physics* 48.2 (1976), pp. 119–130.

[11] Tomaž Prosen. "Exact nonequilibrium steady state of a strongly driven open XXZ chain". *Physical review letters* 107.13 (2011), p. 137201.

[12] Jürgen Gärtner. "On Large Deviations from the Invariant Measure". *Theory of Probability & Its Applications* 22.1 (1977), pp. 24–39.

[13] Richard S Ellis. "Large deviations for a general class of random vectors". *The Annals of Probability* 12.1 (1984), pp. 1–12.

[14] Ewan McCulloch, Jacopo De Nardis, Sarang Gopalakrishnan, and Romain Vasseur. "Full Counting Statistics of Charge in Chaotic Many-Body Quantum Systems". *Phys. Rev. Lett.* 131 (21 Nov. 2023), p. 210402.

[15] Sarang Gopalakrishnan, Alan Morningstar, Romain Vasseur, and Vedika Khemani. "Distinct universality classes of diffusive transport from full counting statistics". *Physical Review B* 109.2 (2024), p. 024417.

[16] Jordan S. Cotler, Daniel K. Mark, Hsin-Yuan Huang, Felipe Hernández, Joonhee Choi, Adam L. Shaw, Manuel Endres, and Soonwon Choi. "Emergent Quantum State Designs from Individual Many-Body Wave Functions". *PRX Quantum* 4.1 (2023), p. 010311.

[17] Joonhee Choi, Adam L. Shaw, Ivaylo S. Madjarov, Xin Xie, Ran Finkelstein, Jacob P. Covey, Jordan S. Cotler, Daniel K. Mark, Hsin-Yuan Huang, Anant Kale, Hannes Pichler, Fernando G. S. L. Brandão, Soonwon Choi, and Manuel Endres. "Preparing Random States and Benchmarking with Many-Body Quantum Chaos". *Nature* 613.7944 (2023), pp. 468–473.

[18] Gerald D. Mahan. *Many-Particle Physics*. Springer US, 2000.

[19] R. Kubo. "The Fluctuation-Dissipation Theorem". *Reports on Progress in Physics* 29.1 (1966), pp. 255–284.

[20] R. Haag, N. M. Hugenholtz, and M. Winnink. "On the Equilibrium States in Quantum Statistical Mechanics". *Communications in Mathematical Physics* 5.3 (1967), pp. 215–236.

[21] Herbert B. Callen and Theodore A. Welton. "Irreversibility and Generalized Noise". *Physical Review* 83.1 (1951), pp. 34–40.

[22] J. M. Luttinger. "Fermi Surface and Some Simple Equilibrium Properties of a System of Interacting Fermions". *Phys. Rev.* 119 (1960), p. 1153.

[23] B. Sriram Shastry. "Sum Rule for Thermal Conductivity and Dynamical Thermal Transport Coefficients in Condensed Matter". *Physical Review B* 73.8 (2006), p. 085117.

[24] W. Kohn. "Theory of the Insulating State". *Physical Review* 133.1A (1964), A171–A181.

[25] H. Castella, X. Zotos, and P. Prelovšek. "Integrability and Ideal Conductance at Finite Temperatures". *Physical Review Letters* 74.6 (1995), pp. 972–975.

[26] Tomaž Prosen and Enej Ilievski. "Families of Quasilocal Conservation Laws and Quantum Spin Transport". *Physical Review Letters* 111.5 (2013), p. 057203.

[27] Tomaž Prosen. "Quasilocal Conservation Laws in XXZ Spin-1/2 Chains: Open, Periodic and Twisted Boundary Conditions". *Nuclear Physics B* 886 (2014), pp. 1177–1198.

[28] H. Bethe. "Zur Theorie der Metalle". *Zeitschrift für Physik* 71.3–4 (1931), pp. 205–226.

[29] Minoru Takahashi. *Thermodynamics of One-Dimensional Solvable Models*. Cambridge: Cambridge University Press, 1999.

[30] C. N. Yang. "Some Exact Results for the Many-Body Problem in One Dimension with Repulsive Delta-Function Interaction". *Physical Review Letters* 19.23 (1967), pp. 1312–1315.

[31] R. J. Baxter. "Partition Function of the Eight-Vertex Lattice Model". *Annals of Physics* 70.1 (1972), pp. 193–228.

[32] V. E. Korepin, N. M. Bogoliubov, and A. G. Izergin. *Quantum Inverse Scattering Method and Correlation Functions*. Cambridge: Cambridge University Press, 1993.

[33] M. G. Tetel'man. "Lorentz Group for Two-Dimensional Integrable Lattice Systems". *Soviet Physics JETP* 55.2 (1982), pp. 306–310.

[34] Kiyoshi Sogo and Miki Wadati. "Boost Operator and Its Application to Quantum Gelfand–Levitan Equation for Heisenberg–Ising Chain with Spin One-Half". *Progress of Theoretical Physics* 69.2 (1983), pp. 431–450.

[35] M. P. Grabowski and P. Mathieu. "Structure of the Conservation Laws in Quantum Integrable Spin Chains with Short Range Interactions". *Annals of Physics* 243.2 (1995), pp. 299–371.

[36] C. N. Yang and C. P. Yang. "Thermodynamics of a One-Dimensional System of Bosons with Repulsive Delta-Function Interaction". *Journal of Mathematical Physics* 10.7 (1969), pp. 1115–1122.

[37] Olalla A. Castro-Alvaredo, Benjamin Doyon, and Takato Yoshimura. "Emergent Hydrodynamics in Integrable Quantum Systems out of Equilibrium". *Physical Review X* 6.4 (2016), p. 041065.

[38] Bruno Bertini, Mario Collura, Jacopo De Nardis, and Maurizio Fagotti. "Transport in Out-of-Equilibrium XXZ Chains: Exact Profiles of Charges and Currents". *Physical Review Letters* 117.20 (2016), p. 207201.

[39] X. Zotos. "Finite Temperature Drude Weight of the One-Dimensional Spin-1/2 Heisenberg Model". *Physical Review Letters* 82.9 (1999), pp. 1764–1767.

[40] C. Karrasch, J. H. Bardarson, and J. E. Moore. "Finite-Temperature Dynamical Density Matrix Renormalization Group and the Drude Weight of Spin-1/2 Chains". *Physical Review Letters* 108.22 (2012), p. 227206.

[41] Heinz-Peter Breuer and Francesco Petruccione. *The Theory of Open Quantum Systems*. Oxford: Oxford University Press, 2002.

[42] V. Gorini, A. Kossakowski, and E. C. G. Sudarshan. "Completely Positive Dynamical Semigroups of N-Level Systems". *Journal of Mathematical Physics* 17.5 (1976), pp. 821–825.

[43] R. Alicki. "On the Detailed Balance Condition for Non-Hamiltonian Systems". *Reports on Mathematical Physics* 10.2 (1976), pp. 249–258.

[44] Tomaž Prosen. "Open XXZ Spin Chain: Nonequilibrium Steady State and a Strict Bound on Ballistic Transport". *Physical Review Letters* 106.21 (2011), p. 217206.

[45] Hugo Touchette. "The Large Deviation Approach to Statistical Mechanics". *Physics Reports* 478.1–3 (2009), pp. 1–69.

[46] Luca D'Alessio, Yariv Kafri, Anatoli Polkovnikov, and Marcos Rigol. "From Quantum Chaos and Eigenstate Thermalization to Statistical Mechanics and Thermodynamics". *Advances in Physics* 65.3 (2016), pp. 239–362.

[47] Mark Srednicki. "The approach to thermal equilibrium in quantized chaotic systems". *Journal of Physics A: Mathematical and General* 32.7 (Jan. 1999), 1163–1175.

[48] Marcos Rigol, Vanja Dunjko, Vladimir Yurovsky, and Maxim Olshanii. "Relaxation in a Completely Integrable Many-Body Quantum System: An Ab Initio Study of the Dynamics of the Highly Excited States of 1D Lattice Hard-Core Bosons". *Physical Review Letters* 98.5 (2007), p. 050405.

[49] Lev Vidmar and Marcos Rigol. "Generalized Gibbs Ensemble in Integrable Lattice Models". *Journal of Statistical Mechanics: Theory and Experiment* 2016.6 (2016), p. 064007.

[50] Rahul Nandkishore and David A. Huse. "Many-Body Localization and Thermalization in Quantum Statistical Mechanics". *Annual Review of Condensed Matter Physics* 6 (2015), pp. 15–38.

[51] Dmitry A. Abanin, Ehud Altman, Immanuel Bloch, and Maksym Serbyn. "Colloquium: Many-Body Localization, Thermalization, and Entanglement". *Reviews of Modern Physics* 91.2 (2019), p. 021001.

[52] D. M. Basko, I. L. Aleiner, and B. L. Altshuler. "Metal–Insulator Transition in a Weakly Interacting Many-Electron System with Localized Single-Particle States". *Annals of Physics* 321.5 (2006), pp. 1126–1205.

[53] David A. Huse, Rahul Nandkishore, and Vadim Oganesyan. "Phenomenology of Fully Many-Body-Localized Systems". *Physical Review B* 90.17 (2014), p. 174202.

[54] Maksym Serbyn, Z. Papić, and D. A. Abanin. "Local Conservation Laws and the Structure of the Many-Body Localized States". *Physical Review Letters* 111.12 (2013), p. 127201.

[55] Maksym Serbyn, Z. Papić, and D. A. Abanin. "Quantum Quenches in the Many-Body Localized Phase". *Physical Review B* 90.17 (2014), p. 174302.

[56] Karol Życzkowski and Hans-Jürgen Sommers. "Induced Measures in the Space of Mixed Quantum States". *Journal of Physics A: Mathematical and General* 34.35 (2001), pp. 7111–7125.

[57] Don N. Page. "Average Entropy of a Subsystem". *Physical Review Letters* 71.9 (1993), pp. 1291–1294.

[58] Christoph Dankert, Richard Cleve, Joseph Emerson, and Etera Livine. "Exact and Approximate Unitary 2-Designs and Their Application to Fidelity Estimation". *Physical Review A* 80.1 (2009), p. 012304.

[59] Fernando G. S. L. Brandão, Aram W. Harrow, and Michał Horodecki. "Local Random Quantum Circuits are Approximate Polynomial- Designs". *Communications in Mathematical Physics* 346.2 (2016), pp. 397–434.

[60] C. E. Porter and R. G. Thomas. "Fluctuations of Nuclear Reaction Widths". *Physical Review* 104.2 (1956), pp. 483–491.

[61] M. L. Mehta. *Random Matrices*. 3rd. Amsterdam: Elsevier, 2004.

[62] Sheldon Goldstein, Joel L. Lebowitz, Roderich Tumulka, and Nino Zanghì. "Canonical Typicality". *Physical Review Letters* 96.5 (2006), p. 050403.

[63] Richard Jozsa, Daniel Robb, and William K. Wootters. "Lower Bound for Accessible Information in Quantum Mechanics". *Physical Review A* 49.2 (1994), pp. 668–677.

[64] Fritz Haake. *Quantum Signatures of Chaos*. 3rd. Berlin: Springer, 2010.

[65] B. Bertrand and A. M. García-García. "Anomalous Thouless energy and critical statistics on the metallic side of the many-body localization transition". *Phys. Rev. B* 94.14 (2016), p. 144201.

[66] Pavel Kos, Marko Ljubotina, and Tomaž Prosen. "Many-Body Quantum Chaos: Analytic Connection to Random Matrix Theory". *Phys. Rev. X* 8.2 (2018), p. 021062.

[67] Lata Kh. Joshi, Andreas Elben, Amit Vikram, Benoît Vermersch, Victor Galitski, and Peter Zoller. "Probing Many-Body Quantum Chaos with Quantum Simulators". *Physical Review X* 12.1 (2022), p. 011018.

[68] Amos Chan, Andrea De Luca, and J. T. Chalker. "Solution of a Minimal Model for Many-Body Quantum Chaos". *Phys. Rev. X* 8.4 (2018), p. 041019.

[69] Ulrich Schollwöck. "The density-matrix renormalization group in the age of matrix product states". *Annals of Physics* 326.1 (2011), pp. 96–192.

[70] Román Orús. "A practical introduction to tensor networks: Matrix product states and projected entangled pair states". *Annals of Physics* 349 (Oct. 2014), 117–158.

[71] J. Ignacio Cirac, David Pérez-García, Norbert Schuch, and Frank Verstraete. "Matrix product states and projected entangled pair states: Concepts, symmetries, theorems". *Reviews of Modern Physics* 93.4 (Dec. 2021).

[72] M. B. Hastings. "An area law for one-dimensional quantum systems". *Journal of Statistical Mechanics: Theory and Experiment* 2007.08 (2007), P08024.

[73] I. V. Oseledets. "Tensor-Train Decomposition". *SIAM Journal on Scientific Computing* 33.5 (2011), pp. 2295–2317.

[74] B. Pirvu, V. Murg, J. I. Cirac, and F. Verstraete. "Matrix product operator representations". *New Journal of Physics* 12.2 (2010), p. 025012.

[75] Ian P. McCulloch. "Infinite size density matrix renormalization group, revisited". *arXiv preprint arXiv:0804.2509* (2008).

[76] Gregory M. Crosswhite, A. C. Doherty, and Guifré Vidal. "Applying matrix product operators to model systems with long-range interactions". *Physical Review B* 78.3 (2008), p. 035116.

[77] Gregory M. Crosswhite and Dave Bacon. "Finite automata for caching in matrix product algorithms". *Physical Review A* 78.1 (2008), p. 012356.

[78] C. Hubig, I. P. McCulloch, and U. Schollwöck. "Generic construction of efficient matrix product operators". *Physical Review B* 95.3 (2017), p. 035129.

[79] Daniel E. Parker, Xiangyu Cao, and Michael P. Zaletel. "Local matrix product operators: Canonical form, compression, and control theory". *Physical Review B* 102.3 (2020), p. 035147.

[80] Steven R. White. "Density matrix formulation for quantum renormalization groups". *Physical Review Letters* 69.19 (1992), pp. 2863–2866.

[81] C. Hubig, I. P. McCulloch, U. Schollwöck, and F. A. Wolf. "Strictly single-site DMRG algorithm with subspace expansion". *Physical Review B* 91.15 (2015), p. 155115.

[82] Pasquale Calabrese and John Cardy. "Evolution of entanglement entropy in one-dimensional systems". *Journal of Statistical Mechanics: Theory and Experiment* 2005.04 (2005), P04010.

[83] Jutho Haegeman, J. Ignacio Cirac, Tobias J. Osborne, Iztok Pižorn, Henri Verschelde, and Frank Verstraete. "Time-Dependent Variational Principle for Quantum Lattices". *Physical Review Letters* 107.7 (2011), p. 070601.

[84] Jutho Haegeman, Christian Lubich, Ivan Oseledets, Bart Vandereycken, and Frank Verstraete. "Unifying time evolution and optimization with matrix product states". *Physical Review B* 94.16 (2016), p. 165116.

[85] Mingru Yang and Steven R. White. "Time-dependent variational principle with ancillary Krylov subspace". *Physical Review B* 102.9 (Sept. 2020).

[86] Norbert Schuch, Michael M. Wolf, Frank Verstraete, and J. Ignacio Cirac. "Entropy Scaling and Simulability by Matrix Product States". *Physical Review Letters* 100.3 (2008), p. 030504.

[87] Christopher David White, Michael Zaletel, Roger S. K. Mong, and Gil Refael. "Quantum dynamics of thermalizing systems". *Physical Review B* 97.3 (2018), p. 035127.

[88] A. J. Daley, C. Kollath, U. Schollwöck, and G. Vidal. "Time-dependent density-matrix renormalization-group using adaptive effective Hilbert spaces". *Journal of Statistical Mechanics: Theory and Experiment* 2004.04 (2004), P04005.

[89] Steven R. White and Adrian E. Feiguin. "Real-Time Evolution Using the Density Matrix Renormalization Group". *Physical Review Letters* 93.7 (2004), p. 076401.

[90] Guifré Vidal. "Efficient Simulation of One-Dimensional Quantum Many-Body Systems". *Physical Review Letters* 93.4 (2004), p. 040502.

[91] H. F. Trotter. "On the product of semi-groups of operators". *Proceedings of the American Mathematical Society* 10.4 (1959), pp. 545–551.

[92] Masuo Suzuki. "Generalized Trotter's formula and systematic approximants of exponential operators and inner derivations with applications to many-body problems". *Communications in Mathematical Physics* 51.2 (1976), pp. 183–190.

[93] Masuo Suzuki. "Fractal decomposition of exponential operators with applications to many-body theories and Monte Carlo simulations". *Physics Letters A* 146.6 (1990), pp. 319–323.

[94] Michael P. Zaletel, Roger S. K. Mong, Christoph Karrasch, Joel E. Moore, and Frank Pollmann. "Time-evolving a matrix product state with long-ranged interactions". *Physical Review B* 91.16 (2015), p. 165112.

[95] Adrian E. Feiguin and Steven R. White. "Finite-temperature density matrix renormalization using an enlarged Hilbert space". *Physical Review B* 72.22 (2005), 220401(R).

[96] Sebastian Paeckel, Thomas Köhler, Andreas Swoboda, Salvatore R. Manmana, Ulrich Schollwöck, and Claudius Hubig. "Time-evolution methods for matrix-product states". *Annals of Physics* 411 (2019), p. 167998.

[97] Thomas Barthel. "Precise evaluation of thermal response functions by optimized density matrix renormalization group schemes". *New Journal of Physics* 15.7 (2013), p. 073010.

[98] Bruno Bertini, Fabian Heidrich-Meisner, Christoph Karrasch, Tomaž Prosen, R Steinigeweg, and Marko Žnidarič. "Finite-temperature transport in one-dimensional quantum lattice models". *Reviews of Modern Physics* 93.2 (2021), p. 025003.

[99] Tomaž Prosen and Marko Žnidarič. "Matrix product simulations of non-equilibrium steady states of quantum spin chains". *Journal of Statistical Mechanics: Theory and Experiment* 2009.02 (Feb. 2009), P02035.

[100] Inés de Vega and Mari-Carmen Bañuls. "Thermofield-based chain-mapping approach for open quantum systems". *Phys. Rev. A* 92 (5 Nov. 2015), p. 052116.

[101] C Karrasch, JH Bardarson, and JE Moore. "Reducing the numerical effort of finite-temperature density matrix renormalization group calculations". *New Journal of Physics* 15.8 (2013), p. 083031.

[102] Alexander Vasiliev, Olga Volkova, Elena Zvereva, and Maria Markina. "Milestones of low-D quantum magnetism". *npj Quantum Materials* 3.1 (2018), p. 18.

[103] A.A Belik, M Azuma, and M Takano. "Characterization of quasi-one-dimensional S=1/2 Heisenberg antiferromagnets Sr2Cu(PO4)2 and Ba2Cu(PO4)2 with magnetic susceptibility, specific heat, and thermal analysis". *Journal of Solid State Chemistry* 177.3 (2004), pp. 883–888.

[104] Toshiya Kinoshita, Trevor Wenger, and David S Weiss. "A quantum Newton's cradle". *Nature* 440.7086 (2006), pp. 900–903.

[105] Immanuel Bloch, Jean Dalibard, and Sylvain Nascimbene. "Quantum simulations with ultracold quantum gases". *Nature Physics* 8.4 (2012), pp. 267–276.

[106] Walter Hofstetter and Tao Qin. "Quantum simulation of strongly correlated condensed matter systems". *Journal of Physics B: Atomic, Molecular and Optical Physics* 51.8 (2018), p. 082001.

[107] Hannes Bernien, Sylvain Schwartz, Alexander Keesling, Harry Levine, Ahmed Omran, Hannes Pichler, Soonwon Choi, Alexander S Zibrov, Manuel Endres, Markus Greiner, et al. "Probing many-body dynamics on a 51-atom quantum simulator". *Nature* 551.7682 (2017), pp. 579–584.

[108] Marlon Brenes, Eduardo Mascarenhas, Marcos Rigol, and John Goold. "High-temperature coherent transport in the XXZ chain in the presence of an impurity". *Physical Review B* 98.23 (2018), p. 235128.

[109] Marlon Brenes, Tyler LeBlond, John Goold, and Marcos Rigol. "Eigenstate thermalization in a locally perturbed integrable system". *Physical review letters* 125.7 (2020), p. 070605.

[110] Jacopo De Nardis, Sarang Gopalakrishnan, Romain Vasseur, and Brayden Ware. "Subdiffusive hydrodynamics of nearly integrable anisotropic spin chains". *Proceedings of the National Academy of Sciences* 119.34 (2022), e2202823119.

[111] Christoph Karrasch, Tomaž Prosen, and Fabian Heidrich-Meisner. "Proposal for measuring the finite-temperature Drude weight of integrable systems". *Physical Review B* 95.6 (2017), 060406(R).

[112] P Prelovšek, M Mierzejewski, and J Herbrych. "Coexistence of diffusive and ballistic transport in integrable quantum lattice models". *Physical Review B* 104.11 (2021), p. 115163.

[113] Christoph Karrasch, DM Kennes, and F Heidrich-Meisner. "Spin and thermal conductivity of quantum spin chains and ladders". *Physical Review B* 91.11 (2015), p. 115130.

[114] Stephan Langer, Markus Heyl, Ian P McCulloch, and Fabian Heidrich-Meisner. "Real-time energy dynamics in spin-1 2 Heisenberg chains". *Physical Review B* 84.20 (2011), p. 205115.

[115] Marko Ljubotina, Marko Žnidarič, and Tomaž Prosen. "Spin diffusion from an inhomogeneous quench in an integrable system". *Nature communications* 8.1 (2017), pp. 1–6.

[116] Andrew Urichuk, Yahya Oez, Andreas Klümper, and Jesko Sirker. "The Spin Drude Weight of the XXZ Chain and Generalized Hydrodynamics". *SciPost Physics* 6.1 (2019), p. 005.

[117] B. N. Narozhny, A. J. Millis, and N. Andrei. "Transport in the XXZ model". *Phys. Rev. B* 58 (6 Aug. 1998), R2921–R2924.

[118] NMR Peres, PD Sacramento, DK Campbell, and JMP Carmelo. "Curvature of levels and charge stiffness of one-dimensional spinless fermions". *Physical Review B* 59.11 (1999), p. 7382.

[119] J. Herbrych, P. Prelovšek, and X. Zotos. "Finite-Temperature Drude Weight within the Anisotropic Heisenberg Chain". *Physical Review B* 84.15 (2011), p. 155125.

[120] David A Rabson, BN Narozhny, and AJ Millis. "Crossover from Poisson to Wigner-Dyson level statistics in spin chains with integrability breaking". *Physical Review B* 69.5 (2004), p. 054403.

[121] P Prelovšek, S El Shawish, X Zotos, and Martin Long. "Anomalous scaling of conductivity in integrable fermion systems". *Physical Review B* 70.20 (2004), p. 205129.

[122] J Sirker, Rodrigo Gonçalves Pereira, and I Affleck. "Conservation laws, integrability, and transport in one-dimensional quantum systems". *Physical Review B* 83.3 (2011), p. 035115.

[123] Kazumitsu Sakai and Andreas Klümper. "Non-dissipative thermal transport in the massive regimes of the XXZ chain". *Journal of Physics A: Mathematical and General* 36.46 (2003), p. 11617.

[124] F Heidrich-Meisner, A Honecker, and W Brenig. "Thermal transport of the X X Z chain in a magnetic field". *Physical Review B* 71.18 (2005), p. 184415.

[125] Andreas Klümper and Kazumitsu Sakai. “The thermal conductivity of the spin-1/2 XXZ chain at arbitrary temperature”. *Journal of Physics A: Mathematical and General* 35.9 (2002), p. 2173.

[126] Shigeru Ajisaka, Felipe Barra, Carlos Mejía-Monasterio, and Tomaž Prosen. “Nonequilibrium particle and energy currents in quantum chains connected to mesoscopic Fermi reservoirs”. *Physical Review B* 86.12 (2012), p. 125111.

[127] Marko Žnidarič. “Spin transport in a one-dimensional anisotropic Heisenberg model”. *Physical Review Letters* 106.22 (2011), p. 220601.

[128] JJ Mendoza-Arenas, S Al-Assam, SR Clark, and D Jaksch. “Heat transport in the XXZ spin chain: from ballistic to diffusive regimes and dephasing enhancement”. *Journal of Statistical Mechanics: Theory and Experiment* 2013.07 (2013), P07007.

[129] Juan Jose Mendoza-Arenas, M Žnidarič, Vipin Kerala Varma, John Goold, Stephen R Clark, and Antonello Scardicchio. “Asymmetry in energy versus spin transport in certain interacting disordered systems”. *Physical Review B* 99.9 (2019), p. 094435.

[130] Naveen Nishad and GJ Sreejith. “Energy transport in chiral clock model”. *New Journal of Physics* 24.1 (2022), p. 013035.

[131] Leonardo Mazza, Jacopo Viti, Matteo Carrega, Davide Rossini, and Andrea De Luca. “Energy transport in an integrable parafermionic chain via generalized hydrodynamics”. *Phys. Rev. B* 98 (7 Aug. 2018), p. 075421.

[132] Christoph Karrasch, Roni Ilan, and JE Moore. “Nonequilibrium thermal transport and its relation to linear response”. *Physical Review B* 88.19 (2013), p. 195129.

[133] Yuji Nozawa and Hirokazu Tsunetsugu. “Generalized hydrodynamic approach to charge and energy currents in the one-dimensional Hubbard model”. *Physical Review B* 101.3 (2020), p. 035121.

[134] Márton Kormos. “Inhomogeneous quenches in the transverse field Ising chain: scaling and front dynamics”. *SciPost Physics* 3.3 (2017), p. 020.

[135] Xenophon Zotos. “A TBA approach to thermal transport in the XXZ Heisenberg model”. *Journal of Statistical Mechanics: Theory and Experiment* 2017.10 (2017), p. 103101.

[136] Bruno Bertini and Maurizio Fagotti. “Determination of the nonequilibrium steady state emerging from a defect”. *Physical Review Letters* 117.13 (2016), p. 130402.

[137] Benjamin Doyon and Herbert Spohn. “Drude weight for the Lieb-Liniger Bose gas”. *SciPost Physics* 3.6 (2017), p. 039.

[138] S. Langer, F. Heidrich-Meisner, J. Gemmer, I. P. McCulloch, and U. Schollwöck. “Real-time study of diffusive and ballistic transport in spin-$\frac{1}{2}$ chains using the adaptive time-dependent density matrix renormalization group method”. *Phys. Rev. B* 79 (21 June 2009), p. 214409.

[139] C Karrasch, JE Moore, and F Heidrich-Meisner. “Real-time and real-space spin and energy dynamics in one-dimensional spin-1 2 systems induced by local quantum quenches at finite temperatures”. *Physical Review B* 89.7 (2014), p. 075139.

[140] Simon Jesenko and Marko Žnidarič. "Finite-temperature magnetization transport of the one-dimensional anisotropic Heisenberg model". *Physical Review B* 84.17 (2011), p. 174438.

[141] X Zotos and Peter Prelovšek. "Evidence for ideal insulating or conducting state in a one-dimensional integrable system". *Physical Review B* 53.3 (1996), p. 983.

[142] João S. Ferreira and Michele Filippone. "Ballistic-to-diffusive transition in spin chains with broken integrability". *Phys. Rev. B* 102 (18 Nov. 2020), p. 184304.

[143] F Heidrich-Meisner, A Honecker, Daniel Carlos Cabra, and W Brenig. "Transport in dimerized and frustrated spin systems". *Journal of magnetism and magnetic materials* 272 (2004), pp. 890–891.

[144] Alexandros Metavitsiadis, Angelo Pidatella, and Wolfram Brenig. "Thermal transport in a two-dimensional Z 2 spin liquid". *Physical Review B* 96.20 (2017), p. 205121.

[145] Steven Howes, Leo P Kadanoff, and Marcel Den Nijs. "Quantum model for commensurate-incommensurate transitions". *Nuclear Physics B* 215.2 (1983), pp. 169–208.

[146] Paul Fendley. "Parafermionic edge zero modes in Zn-invariant spin chains". *Journal of Statistical Mechanics: Theory and Experiment* 2012.11 (2012), P11020.

[147] S Ostlund. "Incommensurate and commensurate phases in asymmetric clock models". *Physical Review B* 24.1 (1981), p. 398.

[148] David A Huse. "Simple three-state model with infinitely many phases". *Physical Review B* 24.9 (1981), p. 5180.

[149] Ye Zhuang, Hitesh J Changlani, Norm M Tubman, and Taylor L Hughes. "Phase diagram of the Z 3 parafermionic chain with chiral interactions". *Physical Review B* 92.3 (2015), p. 035154.

[150] Naveen Nishad, M. Santhosh, and G. J. Sreejith. "Postquench entropy growth in a chiral clock model". *Phys. Rev. B* 103 (19 May 2021), p. 195141.

[151] Adam S Jermyn, Roger SK Mong, Jason Alicea, and Paul Fendley. "Stability of zero modes in parafermion chains". *Physical Review B* 90.16 (2014), p. 165106.

[152] Paul Fendley, Krishnendu Sengupta, and Subir Sachdev. "Competing density-wave orders in a one-dimensional hard-boson model". *Physical Review B* 69.7 (2004), p. 075106.

[153] Helen Au-Yang, Barry M McCoy, Jacques H. H. Perk, Shuang Tang, and Mu lin Yan. "Commuting transfer matrices in the chiral Potts models: Solutions of star-triangle equations with genus > 1". *Physics Letters A* 123 (1987), pp. 219–223.

[154] MW Long, P Prelovšek, S El Shawish, J Karadamoglou, and X Zotos. "Finite-temperature dynamical correlations using the microcanonical ensemble and the Lanczos algorithm". *Physical Review B* 68.23 (2003), p. 235106.

[155] Robin Steinigeweg, Jochen Gemmer, and Wolfram Brenig. "Spin-current autocorrelations from single pure-state propagation". *Physical Review Letters* 112.12 (2014), p. 120601.

[156] Fabián Heidrich-Meisner, Andreas Honecker, Daniel Carlos Cabra, and Wolfram Brenig. "Thermal conductivity of anisotropic and frustrated spin-1 2 chains". *Physical Review B* 66.14 (2002), 140406(R).

[157] F Heidrich-Meisner, A Honecker, DC Cabra, and W Brenig. "Zero-frequency transport properties of one-dimensional spin-1 2 systems". *Physical Review B* 68.13 (2003), p. 134436.

[158] C Karrasch, DM Kennes, and JE Moore. "Transport properties of the one-dimensional Hubbard model at finite temperature". *Physical Review B* 90.15 (2014), p. 155104.

[159] HU Everts and H Roder. "Transfer matrix study of the chiral clock model in the Hamiltonian limit". *Journal of Physics A: Mathematical and General* 22.13 (1989), p. 2475.

[160] Johannes Motruk, Erez Berg, Ari M. Turner, and Frank Pollmann. "Topological phases in gapped edges of fractionalized systems". *Phys. Rev. B* 88 (8 Aug. 2013), p. 085115.

[161] Rhine Samajdar, Soonwon Choi, Hannes Pichler, Mikhail D. Lukin, and Subir Sachdev. "Numerical study of the chiral $\mathbb{Z}_3$ quantum phase transition in one spatial dimension". *Phys. Rev. A* 98 (2 Aug. 2018), p. 023614.

[162] Giuseppe Albertini, Barry M McCoy, and Jacques HH Perk. "Commensurate-incommensurate transition in the ground state of the superintegrable chiral Potts model". *Physics Letters A* 135.3 (1989), pp. 159–166.

[163] Barry M McCoy and Shi-shyr Roan. "Excitation spectrum and phase structure of the chiral Potts model". *Physics Letters A* 150.8-9 (1990), pp. 347–354.

[164] Jesko Sirker. "Transport in one-dimensional integrable quantum systems". *SciPost Physics Lecture Notes* (2020), p. 17.

[165] Anjan Kundu. *Quantum Integrable Systems: Construction, Solution, Algebraic Aspect.* 1996.

[166] Johannes Hauschild, Eyal Leviatan, Jens H Bardarson, Ehud Altman, Michael P Zaletel, and Frank Pollmann. "Finding purifications with minimal entanglement". *Physical Review B* 98.23 (2018), p. 235163.

[167] DM Kennes and Christoph Karrasch. "Extending the range of real time density matrix renormalization group simulations". *Computer Physics Communications* 200 (2016), pp. 37–43.

[168] C. Karrasch, J. Hauschild, S. Langer, and F. Heidrich-Meisner. "Drude Weight of the Spin-1/2 XXZ Chain: Density Matrix Renormalization Group versus Exact Diagonalization". *Physical Review B* 87.24 (2013), p. 245128.

[169] Matthew Fishman, Steven R. White, and E. Miles Stoudenmire. "The ITensor Software Library for Tensor Network Calculations". *SciPost Phys. Codebases* (2022), p. 4.

[170] Matthew Fishman, Steven R. White, and E. Miles Stoudenmire. "Codebase release 0.3 for ITensor". *SciPost Phys. Codebases* (2022), 4–r0.3.

[171] Thomas Barthel, Ulrich Schollwöck, and Steven R White. "Spectral functions in one-dimensional quantum systems at finite temperature using the density matrix renormalization group". *Physical Review B* 79.24 (2009), p. 245101.

[172] Jakob Unfried, Johannes Hauschild, and Frank Pollmann. "Fast time evolution of matrix product states using the QR decomposition". *Physical Review B* 107.15 (2023), p. 155133.

[173] Curt Von Keyserlingk, Frank Pollmann, and Tibor Rakovszky. "Operator backflow and the classical simulation of quantum transport". *Physical Review B* 105.24 (2022), p. 245101.

[174] Robert W Cherng and Eugene Demler. "Quantum noise analysis of spin systems realized with cold atoms". *New Journal of Physics* 9.1 (2007), p. 7.

[175] Israel Klich and Leonid Levitov. "Quantum noise as an entanglement meter". *Physical review letters* 102.10 (2009), p. 100502.

[176] Izabella Lovas, Balázs Dóra, Eugene Demler, and Gergely Zaránd. "Full counting statistics of time-of-flight images". *Physical Review A* 95.5 (2017), p. 053621.

[177] Maksims Arzamasovs and Dimitri M Gangardt. "Full counting statistics and large deviations in a thermal 1D Bose gas". *Physical review letters* 122.12 (2019), p. 120401.

[178] Marko Žnidarič. "Exact solution for a diffusive nonequilibrium steady state of an open quantum chain". *Journal of Statistical Mechanics: Theory and Experiment* 2010.05 (2010), p. L05002.

[179] Marko Žnidarič. "Exact large-deviation statistics for a nonequilibrium quantum spin chain". *Physical review letters* 112.4 (2014), p. 040602.

[180] Berislav Buča and Tomaž Prosen. "Exactly solvable counting statistics in open weakly coupled interacting spin systems". *Physical Review Letters* 112.6 (2014), p. 067201.

[181] Vladislav Popkov, Tomaž Prosen, and Lenart Zadnik. "Exact nonequilibrium steady state of open XXZ/XYZ spin-1/2 chain with Dirichlet boundary conditions". *Physical review letters* 124.16 (2020), p. 160403.

[182] Vladislav Popkov, Tomaž Prosen, and Lenart Zadnik. "Inhomogeneous matrix product ansatz and exact steady states of boundary-driven spin chains at large dissipation". *Physical Review E* 101.4 (2020), p. 042122.

[183] Tomaž Prosen. "Exact nonequilibrium steady state of an open Hubbard chain". *Physical review letters* 112.3 (2014), p. 030603.

[184] Marko Žnidarič. "Solvable quantum nonequilibrium model exhibiting a phase transition and a matrix product representation". *Physical Review E* 83.1 (2011), p. 011108.

[185] Colin Rylands and Natan Andrei. "Quantum work of an optical lattice". *Physical Review B* 100.6 (2019), p. 064308.

[186] Gabriele Perfetto, Lorenzo Piroli, and Andrea Gambassi. "Quench action and large deviations: Work statistics in the one-dimensional Bose gas". *Physical Review E* 100.3 (2019), p. 032114.

[187] Alvise Bastianello and Lorenzo Piroli. "From the sinh-Gordon field theory to the one-dimensional Bose gas: exact local correlations and full counting statistics". *Journal of Statistical Mechanics: Theory and Experiment* 2018.11 (2018), p. 113104.

[188] Mario Collura, Fabian HL Essler, and Stefan Groha. "Full counting statistics in the spin-1/2 Heisenberg XXZ chain". *Journal of Physics A: Mathematical and Theoretical* 50.41 (2017), p. 414002.

[189] Chang-Yan Wang, Tian-Gang Zhou, Yi-Neng Zhou, and Pengfei Zhang. "Distinguishing Quantum Phases through Cusps in Full Counting Statistics". *Phys. Rev. Lett.* 133 (8 Aug. 2024), p. 083402.

[190] Mario Collura and Fabian HL Essler. "How order melts after quantum quenches". *Physical Review B* 101.4 (2020), p. 041110.

[191] Pasquale Calabrese, Mario Collura, Giuseppe Di Giulio, and Sara Murciano. "Full counting statistics in the gapped XXZ spin chain". *Europhysics Letters* 129.6 (2020), p. 60007.

[192] Riccardo Senese, Jacob H. Robertson, and Fabian H. L. Essler. "Out-of-equilibrium full counting statistics in Gaussian theories of quantum magnets". *SciPost Phys.* 17 (2024), p. 139.

[193] Filiberto Ares, MA Rajabpour, and Jacopo Viti. "Exact full counting statistics for the staggered magnetization and the domain walls in the XY spin chain". *Physical Review E* 103.4 (2021), p. 042107.

[194] Khadijeh Najafi and MA Rajabpour. "Full counting statistics of the subsystem energy for free fermions and quantum spin chains". *Physical Review B* 96.23 (2017), p. 235109.

[195] Jean-Marie Stephan and Frank Pollmann. "Full counting statistics in the Haldane-Shastry chain". *Physical Review B* 95.3 (2017), p. 035119.

[196] Nishan Ranabhat and Mario Collura. "Thermalization of long range Ising model in different dynamical regimes: A full counting statistics approach". *SciPost Physics Core* 7.2 (2024), p. 017.

[197] Riccardo Javier Valencia Tortora, Pasquale Calabrese, and Mario Collura. "Relaxation of the order-parameter statistics and dynamical confinement". *Europhysics Letters* 132.5 (2020), p. 50001.

[198] Guillaume Cecile, Hugo Lóio, and Jacopo De Nardis. "Measurement-induced phase transitions by matrix product states scaling". *Phys. Rev. Res.* 6 (3 Aug. 2024), p. 033220.

[199] Utkarsh Agrawal, Aidan Zabalo, Kun Chen, Justin H Wilson, Andrew C Potter, JH Pixley, Sarang Gopalakrishnan, and Romain Vasseur. "Entanglement and charge-sharpening transitions in U (1) symmetric monitored quantum circuits". *Physical Review X* 12.4 (2022), p. 041002.

[200] Rhine Samajdar, Ewan McCulloch, Vedika Khemani, Romain Vasseur, and Sarang Gopalakrishnan. "Quantum Turnstiles for Robust Measurement of Full Counting Statistics". *Phys. Rev. Lett.* 133 (24 Dec. 2024), p. 240403.

[201] Naveen Nishad and G J Sreejith. "Energy transport in Z3 chiral clock model". *New Journal of Physics* 24.1 (Jan. 2022), p. 013035.

[202] Marko Žnidarič. "Relaxation times of dissipative many-body quantum systems". *Physical Review E* 92.4 (2015), p. 042143.

[203] Toma ž Prosen. “Quantum Phase Transition in a Far-from-Equilibrium Steady State of an XY Spin Chain”. *Phys. Rev. Lett.* 101 (10 Sept. 2008), p. 105701.

[204] Marcos Rigol, Vanja Dunjko, and Maxim Olshanii. “Thermalization and its mechanism for generic isolated quantum systems”. *Nature* 452.7189 (10 Sept. 2008), pp. 854–858.

[205] Elmar Haller, James Hudson, Andrew Kelly, Dylan A Cotta, Bruno Peaudecerf, Graham D Bruce, and Stefan Kuhr. “Single-atom imaging of fermions in a quantum-gas microscope”. *Nature Physics* 11.9 (10 Sept. 2015), pp. 738–742.

[206] Charles Neill, P Roushan, M Fang, Y Chen, M Kolodrubetz, Z Chen, A Megrant, R Barends, B Campbell, B Chiaro, et al. “Ergodic dynamics and thermalization in an isolated quantum system”. *Nature Physics* 12.11 (10 Sept. 2016), pp. 1037–1041.

[207] Sepehr Ebadi, Tout T Wang, Harry Levine, Alexander Keesling, Giulia Semeghini, Ahmed Omran, Dolev Bluvstein, Rhine Samajdar, Hannes Pichler, Wen Wei Ho, et al. “Quantum phases of matter on a 256-atom programmable quantum simulator”. *Nature* 595.7866 (10 Sept. 2021), pp. 227–232.

[208] Alexander Opremcak, CH Liu, C Wilen, K Okubo, BG Christensen, D Sank, TC White, A Vainsencher, M Giustina, A Megrant, et al. “High-fidelity measurement of a superconducting qubit using an on-chip microwave photon counter”. *Physical Review X* 11.1 (10 Sept. 2021), p. 011027.

[209] Adam L. Shaw, Daniel K. Mark, Joonhee Choi, Ran Finkelstein, Pascal Scholl, Soonwon Choi, and Manuel Endres. “Experimental Signatures of Hilbert-Space Ergodicity: Universal Bitstring Distributions and Applications in Noise Learning”. *Physical Review X* 15.3 (10 Sept. 2025), p. 031001.

[210] Waseem S Bakr, Jonathon I Gillen, Amy Peng, Simon Fölling, and Markus Greiner. “A quantum gas microscope for detecting single atoms in a Hubbard-regime optical lattice”. *Nature* 462.7269 (10 Sept. 2009), pp. 74–77.

[211] Adam M Kaufman, M Eric Tai, Alexander Lukin, Matthew Rispoli, Robert Schittko, Philipp M Preiss, and Markus Greiner. “Quantum thermalization through entanglement in an isolated many-body system”. *Science* 353.6301 (10 Sept. 2016), pp. 794–800.

[212] Lane P. Hughston, Richard Jozsa, and William K. Wootters. “A complete classification of quantum ensembles having a given density matrix”. *Physics Letters A* 183.1 (10 Sept. 1993), pp. 14–18.

[213] Aram W Harrow and Saeed Mehraban. “Approximate unitary t-designs by short random quantum circuits using nearest-neighbor and long-range gates”. *Communications in Mathematical Physics* 401.2 (10 Sept. 2023), pp. 1531–1626.

[214] Aram W Harrow. “The church of the symmetric subspace”. *arXiv preprint arXiv:1308.6595* 101 (10 Sept. 2013), p. 105701.

[215] Daniel K Mark, Federica Surace, Andreas Elben, Adam L Shaw, Joonhee Choi, Gil Refael, Manuel Endres, and Soonwon Choi. “Maximum entropy principle in deep thermalization and in hilbert-space ergodicity”. *Physical Review X* 14.4 (10 Sept. 2024), p. 041051.

[216] Sheldon Goldstein, Joel L Lebowitz, Roderich Tumulka, and Nino Zanghi. "On the distribution of the wave function for systems in thermal equilibrium". *Journal of statistical physics* 125.5-6 (10 Sept. 2006), pp. 1193–1221.

[217] Rui-An Chang, Harshank Shrotriya, Wen Wei Ho, and Matteo Ippoliti. "Deep thermalization under charge-conserving quantum dynamics". *PRX Quantum* 6.2 (10 Sept. 2025), p. 020343.

[218] Maxime Lucas, Lorenzo Piroli, Jacopo De Nardis, and Andrea De Luca. "Generalized deep thermalization for free fermions". *Physical Review A* 107.3 (10 Sept. 2023), p. 032215.

[219] Tanmay Bhore, Jean-Yves Desaules, and Zlatko Papić. "Deep thermalization in constrained quantum systems". *Physical Review B* 108.10 (10 Sept. 2023), p. 104317.

[220] Saúl Pilatowsky-Cameo, Ceren B Dag, Wen Wei Ho, and Soonwon Choi. "Complete Hilbert-space ergodicity in quantum dynamics of generalized Fibonacci drives". *Physical Review Letters* 131.25 (10 Sept. 2023), p. 250401.

[221] Matteo Ippoliti and Wen Wei Ho. "Dynamical purification and the emergence of quantum state designs from the projected ensemble". *PRX Quantum* 4.3 (10 Sept. 2023), p. 030322.

[222] Harshank Shrotriya and Wen Wei Ho. "Nonlocality of deep thermalization". *arXiv preprint arXiv:2305.08437* 101 (10 Sept. 2023), p. 105701.

[223] D. A. Abanin and Z. Papić. "Recent progress in many-body localization". *Annalen der Physik* 529.7 (10 Sept. 2017), p. 1700169.

[224] Piotr Sierant, Maciej Lewenstein, Antonello Scardicchio, Lev Vidmar, and Jakub Zakrzewski. *Many-Body Localization in the Age of Classical Computing*. Sept. 2024.

[225] J. Z. Imbrie, V. Ros, and A. Scardicchio. "Local integrals of motion in many-body localized systems". *Annalen der Physik* 529.7 (10 Sept. 2017), p. 1600278.

[226] V. Ros, M. Müller, and A. Scardicchio. "Integrals of motion in the many-body localized phase". *Nucl. Phys. B* 891 (10 Sept. 2015), pp. 420–465.

[227] J. H. Bardarson, F. Pollmann, and J. E. Moore. "Unbounded Growth of Entanglement in Models of Many-Body Localization". *Phys. Rev. Lett.* 109 (1 July 2012), p. 017202.

[228] Maksym Serbyn, and Dmitry A. Abanin. "Universal Slow Growth of Entanglement in Interacting Strongly Disordered Systems". *Phys. Rev. Lett.* 110 (26 June 2013), p. 260601.

[229] Liangsheng Zhang, Vedika Khemani, and David A. Huse. "A Floquet model for the many-body localization transition". *Phys. Rev. B* 94 (22 Dec. 2016), p. 224202.

[230] Manju C, Arul Lakshminarayan, and Uma Divakaran. "Chaos controlled and disorder driven phase transitions induced by breaking permutation symmetry". *Scientific Reports* 15.1 (26 Oct. 2025), p. 260601.

[231] Antoine Browaeys and Thierry Lahaye. "Many-body physics with individually controlled Rydberg atoms". *Nature Physics* 16.2 (26 June 2020), pp. 132–142.

[232] Minh-Thi Nguyen, Jin-Guo Liu, Jonathan Wurtz, Mikhail D Lukin, Sheng-Tao Wang, and Hannes Pichler. "Quantum optimization with arbitrary connectivity using Rydberg atom arrays". *PRX Quantum* 4.1 (26 June 2023), p. 010316.

[233] Christopher Monroe, Wes C Campbell, L-M Duan, Z-X Gong, Alexey V Gorshkov, Paul W Hess, Rajibul Islam, Kihwan Kim, Norbert M Linke, Guido Pagano, et al. "Programmable quantum simulations of spin systems with trapped ions". *Reviews of Modern Physics* 93.2 (26 June 2021), p. 025001.

[234] Subir Sachdev. *Quantum phases of matter*. Vol. 110. Cambridge University Press, June 2023, p. 260601.

[235] Henk WJ Blöte and Youjin Deng. "Cluster Monte Carlo simulation of the transverse Ising model". *Physical Review E* 66.6 (26 June 2002), p. 066110.

[236] Amit Dutta, Gabriel Aeppli, Bikas K. Chakrabarti, Uma Divakaran, Thomas F. Rosenbaum, and Diptiman Sen. *Quantum Phase Transitions in Transverse Field Spin Models: From Statistical Physics to Quantum Information*. Vol. 110. Cambridge University Press, June 2015, p. 260601.

[237] David Sherrington and Scott Kirkpatrick. "Solvable Model of a Spin-Glass". *Phys. Rev. Lett.* 35 (26 Dec. 1975), pp. 1792–1796.

[238] K. Binder and A. P. Young. "Spin glasses: Experimental facts, theoretical concepts, and open questions". *Rev. Mod. Phys.* 58 (4 Oct. 1986), pp. 801–976.

[239] Giuseppe E Santoro, Roman Martonák, Erio Tosatti, and Roberto Car. "Theory of quantum annealing of an Ising spin glass". *Science* 295.5564 (26 June 2002), pp. 2427–2430.

[240] Tameem Albash and Daniel A Lidar. "Adiabatic quantum computation". *Reviews of Modern Physics* 90.1 (26 June 2018), p. 015002.

[241] Leo Zhou, Sheng-Tao Wang, Soonwon Choi, Hannes Pichler, and Mikhail D Lukin. "Quantum approximate optimization algorithm: Performance, mechanism, and implementation on near-term devices". *Physical Review X* 10.2 (26 June 2020), p. 021067.

[242] Andrew Lucas. "Ising formulations of many NP problems". *Frontiers in physics* 2 (26 June 2014), p. 74887.

[243] Tadashi Kadowaki and Hidetoshi Nishimori. "Quantum annealing in the transverse Ising model". *Physical Review E* 58.5 (26 June 1998), p. 5355.

[244] Edward Farhi, Jeffrey Goldstone, Sam Gutmann, Joshua Lapan, Andrew Lundgren, and Daniel Preda. "A Quantum Adiabatic Evolution Algorithm Applied to Random Instances of an NP-Complete Problem". *Science* 292.5516 (26 June 2001), pp. 472–475.

[245] Arnab Das and Bikas K. Chakrabarti. "Colloquium: Quantum annealing and analog quantum computation". *Rev. Mod. Phys.* 80 (3 Sept. 2008), pp. 1061–1081.

[246] Philipp Hauke, Helmut G Katzgraber, Wolfgang Lechner, Hidetoshi Nishimori, and William D Oliver. "Perspectives of quantum annealing: Methods and implementations". *Reports on Progress in Physics* 83.5 (26 June 2020), p. 054401.

[247] Matthew P Harrigan, Kevin J Sung, Matthew Neeley, Kevin J Satzinger, Frank Arute, Kunal Arya, Juan Atalaya, Joseph C Bardin, Rami Barends, Sergio Boixo, et al. "Quantum approximate optimization of non-planar graph problems on a planar superconducting processor". *Nature Physics* 17.3 (26 June 2021), pp. 332–336.

[248] Philip Krantz, Morten Kjaergaard, Fei Yan, Terry P Orlando, Simon Gustavsson, and William D Oliver. "A quantum engineer's guide to superconducting qubits". *Applied physics reviews* 6.2 (26 June 2019), p. 260601.

[249] Rebekah Herrman, Lorna Treffert, James Ostrowski, Phillip C Lotshaw, Travis S Humble, and George Siopsis. "Impact of graph structures for QAOA on MaxCut". *Quantum Information Processing* 20.9 (26 June 2021), p. 289.

[250] Itay Hen and Federico M. Spedalieri. "Quantum Annealing for Constrained Optimization". *Phys. Rev. Appl.* 5 (3 Mar. 2016), p. 034007.

[251] Madelyn Cain, Sambuddha Chattopadhyay, Jin-Guo Liu, Rhine Samajdar, Hannes Pichler, and Mikhail D Lukin. "Quantum speedup for combinatorial optimization with flat energy landscapes". *arXiv preprint arXiv:2306.13123* 110 (26 June 2023), p. 260601.

[252] Henning Schlömer and Subir Sachdev. "Quantum annealing with chaotic driver Hamiltonians". *Annals of Physics* 479 (26 Aug. 2025), p. 170042.

[253] Moein N. Ivaki, Achilleas Lazarides, and Tapio Ala-Nissila. "Quantum reservoir computing on random regular graphs". *Phys. Rev. A* 112 (1 July 2025), p. 012622.

[254] Sergey Bravyi, Matthew B Hastings, and Frank Verstraete. "Lieb-Robinson bounds and the generation of correlations and topological quantum order". *Physical review letters* 97.5 (26 June 2006), p. 050401.

[255] Jan Šuntajs, Janez Bonča, Tomaž Prosen, and Lev Vidmar. "Quantum chaos challenges many-body localization". *Physical Review E* 102.6 (26 June 2020), p. 062144.

[256] Petr Braun, Daniel Waltner, Maram Akila, Boris Gutkin, and Thomas Guhr. "Transition from quantum chaos to localization in spin chains". *Physical Review E* 101.5 (26 June 2020), p. 052201.

[257] Yasuhiro Sekino and L. Susskind. "Fast scramblers". *Journal of High Energy Physics* 2008.10 (26 Oct. 2008), p. 065.

[258] Juan Maldacena, Stephen H. Shenker, and Douglas Stanford. "A bound on chaos". *Journal of High Energy Physics* 2016 (26 Aug. 2016), p. 106.

[259] Yichen Huang, Yong-Liang Zhang, and Xie Chen. "Out-of-time-ordered correlators in many-body localized systems". *Annalen der Physik* 529.7 (26 June 2017), p. 1600318.

[260] Eiki Iyoda and Takahiro Sagawa. "Scrambling of quantum information in quantum many-body systems". *Physical Review A* 97.4 (26 June 2018), p. 042330.

[261] Zehua Tian, Yiheng Lin, Uwe R Fischer, and Jiangfeng Du. "Testing the upper bound on the speed of scrambling with an analogue of Hawking radiation using trapped ions". *The European Physical Journal C* 82.3 (26 June 2022), p. 212.

[262] Manuel H Muñoz-Arias and Pablo M Poggi. "Quantum ergodicity and scrambling in quantum annealers". *arXiv preprint arXiv:2411.12625* 110 (26 June 2024), p. 260601.

[263] Xiao Mi, Pedram Roushan, Chris Quintana, Salvatore Mandra, Jeffrey Marshall, Charles Neill, Frank Arute, Kunal Arya, Juan Atalaya, Ryan Babbush, et al. "Information scrambling in quantum circuits". *Science* 374.6574 (26 June 2021), pp. 1479–1483.

[264] Ian MacCormack, Mao Tian Tan, Jonah Kudler-Flam, and Shinsei Ryu. "Operator and entanglement growth in nonthermalizing systems: Many-body localization and the random singlet phase". *Phys. Rev. B* 104 (21 Dec. 2021), p. 214202.

[265] Myeonghyeon Kim and Dong-Hee Kim. "Slowest and fastest information scrambling in the strongly disordered XXZ model". *Phys. Rev. B* 107 (22 June 2023), p. L220203.

[266] Vedika Khemani, Ashvin Vishwanath, and David A. Huse. "Operator Spreading and the Emergence of Dissipative Hydrodynamics under Unitary Evolution with Conservation Laws". *Phys. Rev. X* 8 (3 Sept. 2018), p. 031057.

[267] Subhayan Sahu, Shenglong Xu, and Brian Swingle. "Scrambling Dynamics across a Thermalization-Localization Quantum Phase Transition". *Phys. Rev. Lett.* 123 (16 Oct. 2019), p. 165902.

[268] Edward Farhi, Jeffrey Goldstone, and Sam Gutmann. "A quantum approximate optimization algorithm". *arXiv preprint arXiv:1411.4028* 110 (26 June 2014), p. 260601.

[269] Joonho Kim, Yaron Oz, and Dario Rosa. "Quantum chaos and circuit parameter optimization". *Journal of Statistical Mechanics: Theory and Experiment* 2023.2 (26 June 2023), p. 023104.

[270] Jarrod R McClean, Sergio Boixo, Vadim N Smelyanskiy, Ryan Babbush, and Hartmut Neven. "Barren plateaus in quantum neural network training landscapes". *Nature communications* 9.1 (26 June 2018), p. 4812.

[271] Roeland Wiersema, Cunlu Zhou, Yvette de Sereville, Juan Felipe Carrasquilla, Yong Baek Kim, and Henry Yuen. "Exploring entanglement and optimization within the Hamiltonian variational ansatz". *PRX quantum* 1.2 (26 June 2020), p. 020319.

[272] András Grabarits, Kasturi Ranjan Swain, Mahsa Seyed Heydari, Pranav Chandarana, Fernando J. Gómez-Ruiz, and Adolfo del Campo. "Quantum chaos in random Ising networks". *Phys. Rev. Res.* 7 (1 Feb. 2025), p. 013146.

[273] Hang Dong, Pengfei Zhang, Ceren B Dağ, Yu Gao, Ning Wang, Jinfeng Deng, Xu Zhang, Jiachen Chen, Shibo Xu, Ke Wang, et al. "Measuring the Spectral Form Factor in Many-Body Chaotic and Localized Phases of Quantum Processors". *Physical Review Letters* 134.1 (26 June 2025), p. 010402.

[274] Bingzhi Zhang, Peng Xu, Xiaohui Chen, and Quntao Zhuang. "Holographic deep thermalization for secure and efficient quantum random state generation". *Nature Communications* 16.1 (26 June 2025), p. 6341.

[275] Zhiguang Yan, Zi-Yong Ge, Rui Li, Yu-Ran Zhang, Franco Nori, and Yasunobu Nakamura. "Characterizing Many-body Dynamics with Projected Ensembles on a Superconducting Quantum Processor". *arXiv preprint arXiv:2506.21061* 110 (26 June 2025), p. 260601.

[276] Daniel E Parker, Xiangyu Cao, Alexander Avdoshkin, Thomas Scaffidi, and Ehud Altman. "A universal operator growth hypothesis". *Physical Review X* 9.4 (26 June 2019), p. 041017.

[277] Marcin Mierzejewski, Tomaž Prosen, and Peter Prelovšek. "Approximate conservation laws in perturbed integrable lattice models". *Physical Review B* 92.19 (26 Nov. 2015), p. 260601.

[278] Anushya Chandran, Isaac H. Kim, Guifre Vidal, and Dmitry A. Abanin. "Constructing local integrals of motion in the many-body localized phase". *Phys. Rev. B* 91 (8 Feb. 2015), p. 085425.

[279] Steven J. Thomson and Marco Schirò. "Local integrals of motion in quasiperiodic many-body localized systems". *SciPost Phys.* 14 (26 June 2023), p. 125.

[280] Sandipan Manna, Sthitadhi Roy, and GJ Sreejith. "Projected ensemble in a system with locally supported conserved charges". *Physical Review B* 111.14 (26 June 2025), p. 144302.

[281] Oriol Bohigas, Marie-Joya Giannoni, and Charles Schmit. "Characterization of chaotic quantum spectra and universality of level fluctuation laws". *Physical review letters* 52.1 (26 June 1984), p. 1.

[282] Michael Victor Berry and M. Tabor. "Level clustering in the regular spectrum". *Proceedings of the Royal Society of London. A. Mathematical and Physical Sciences* 356.1686 (26 June 1977), 375–394.

[283] Paul Erdős and Alfréd Rényi. "On random graphs I". *Publ. math. debrecen* 6.290-297 (26 June 1959), p. 18.

[284] Harry J Lipkin, N Meshkov, and AJ Glick. "Validity of many-body approximation methods for a solvable model:(I). Exact solutions and perturbation theory". *Nuclear Physics* 62.2 (26 June 1965), pp. 188–198.

[285] Paul Erdős and Alfréd Rényi. "On the evolution of random graphs". *Publ. Math. Inst. Hung. Acad. Sci.* 5 (26 June 1960), pp. 17–61.

[286] Francisco Barahona. "On the computational complexity of Ising spin glass models". *Journal of Physics A: Mathematical and General* 15.10 (26 June 1982), pp. 3241–3253.

[287] Andreas Elben, Steven T Flammia, Hsin-Yuan Huang, Richard Kueng, John Preskill, Benoît Vermersch, and Peter Zoller. "The randomized measurement toolbox". *Nature Reviews Physics* 5.1 (26 June 2023), pp. 9–24.

[288] Zhaoyang Chen, Guanzhong Li, and Lvzhou Li. "Implementation of a continuous-time quantum walk on a sparse graph". *Physical Review A* 110.5 (26 Nov. 2024), p. 260601.

[289] Diederik P. Kingma and Jimmy Ba. "Adam: A Method for Stochastic Optimization". *International Conference on Learning Representations (ICLR)*. Vol. 110. American Physical Society, June 2015, p. 260601.

[290] Amos Chan and Andrea De Luca. "Projected state ensemble of a generic model of many-body quantum chaos". *Journal of Physics A: Mathematical and Theoretical* 57.40 (26 June 2024), p. 405001.

[291] Matteo Ippoliti and Wen Wei Ho. "Solvable model of deep thermalization with distinct design times". *Quantum* 6 (26 June 2022), p. 886.

[292] Pieter W Claeys and Austen Lamacraft. "Emergent quantum state designs and biunitarity in dual-unitary circuit dynamics". *Quantum* 6 (26 June 2022), p. 738.

[293] Xie-Hang Yu, Wen Wei Ho, and Pavel Kos. "Mixed state deep thermalization". *arXiv preprint arXiv:2505.07795* 110 (26 June 2025), p. 260601.

[294] Chang Liu, Qi Camm Huang, and Wen Wei Ho. "Deep thermalization in Gaussian continuous-variable quantum systems". *Physical Review Letters* 133.26 (26 June 2024), p. 260401.

[295] Pavel Kos, Marko Ljubotina, and Toma ž Prosen. "Many-Body Quantum Chaos: Analytic Connection to Random Matrix Theory". *Phys. Rev. X* 8 (2 June 2018), p. 021062.

[296] Abhishodh Prakash, J. H. Pixley, and Manas Kulkarni. "Universal spectral form factor for many-body localization". *Phys. Rev. Res.* 3 (1 Feb. 2021), p. L012019.

[297] Bruno Bertini, Pavel Kos, and Toma ž Prosen. "Exact Spectral Form Factor in a Minimal Model of Many-Body Quantum Chaos". *Phys. Rev. Lett.* 121 (26 Dec. 2018), p. 264101.

[298] Curt W von Keyserlingk, Tibor Rakovszky, Frank Pollmann, and Shivaji Lal Sondhi. "Operator hydrodynamics, OTOCs, and entanglement growth in systems without conservation laws". *Physical Review X* 8.2 (26 June 2018), p. 021013.

[299] Zhiyang Tan and Piet W Brouwer. "Operator spreading in random unitary circuits with unitary-invariant gate distributions". *Physical Review B* 111.18 (26 June 2025), p. 184301.

[300] Vijay Balasubramanian, Pawel Caputa, Javier M Magan, and Qingyue Wu. "Quantum chaos and the complexity of spread of states". *Physical Review D* 106.4 (26 June 2022), p. 046007.

[301] E Rabinovici, A Sánchez-Garrido, R Shir, and J Sonner. "Operator complexity: a journey to the edge of Krylov space". *Journal of High Energy Physics* 2021.6 (26 June 2021), pp. 1–24.

[302] Fabian Ballar Trigueros and Cheng-Ju Lin. "Krylov complexity of many-body localization: Operator localization in Krylov basis". *SciPost Phys.* 13 (26 June 2022), p. 037.

[303] Aranya Bhattacharya, Pingal Pratyush Nath, and Himanshu Sahu. "Krylov complexity for nonlocal spin chains". *Physical Review D* 109.6 (26 June 2024), p. 066010.

[304] Pratik Nandy, Apollonas S Matsoukas-Roubeas, Pablo Martínez-Azcona, Anatoly Dymarsky, and Adolfo del Campo. "Quantum dynamics in Krylov space: Methods and applications". *Physics Reports* 1125 (26 June 2025), pp. 1–82.

[305] E Rabinovici, A Sánchez-Garrido, R Shir, and J Sonner. "Krylov complexity from integrability to chaos". *Journal of High Energy Physics* 2022.7 (26 June 2022), pp. 1–29.

[306] Haifeng Tang. "Operator Krylov complexity in random matrix theory". *arXiv preprint arXiv:2312.17416* 110 (26 June 2023), p. 260601.

[307] Alexander Avdoshkin, Anatoly Dymarsky, and Michael Smolkin. "Krylov complexity in quantum field theory, and beyond". *Journal of High Energy Physics* 2024.6 (26 June 2024), pp. 1–29.

[308] E Rabinovici, A Sánchez-Garrido, R Shir, and J Sonner. "Krylov localization and suppression of complexity". *Journal of High Energy Physics* 2022.3 (26 June 2022), pp. 1–42.

[309] Budhaditya Bhattacharjee, Xiangyu Cao, Pratik Nandy, and Tanay Pathak. "Krylov complexity in saddle-dominated scrambling". *Journal of High Energy Physics* 2022.5 (26 June 2022), pp. 1–27.

[310] Joonho Kim, Jeff Murugan, Jan Olle, and Dario Rosa. "Operator delocalization in quantum networks". *Phys. Rev. A* 105 (1 Jan. 2022), p. L010201.

[311] Saud Čindrak, Adrian Paschke, Lina Jaurigue, and Kathy Lüdge. "Measurable Krylov spaces and eigenenergy count in quantum state dynamics". *Journal of High Energy Physics* 2024.10 (26 Oct. 2024), p. 260601.

[312] Gene H. Golub and Charles F. Van Loan. *Matrix Computations*. 4th. Vol. 110. Baltimore, MD: Johns Hopkins University Press, June 2013, p. 260601.

[313] E B Mpemba and D G Osborne. "Cool?" *Physics Education* 4.3 (26 May 1969), p. 172.

[314] Zhiyue Lu and Oren Raz. "Nonequilibrium thermodynamics of the Markovian Mpemba effect and its inverse". *Proceedings of the National Academy of Sciences* 114.20 (26 May 2017), 5083–5088.

[315] Andrea Nava and Michele Fabrizio. "Lindblad dissipative dynamics in the presence of phase coexistence". *Phys. Rev. B* 100 (12 Sept. 2019), p. 125102.

[316] Federico Carollo, Antonio Lasanta, and Igor Lesanovsky. "Exponentially Accelerated Approach to Stationarity in Markovian Open Quantum Systems through the Mpemba Effect". *Phys. Rev. Lett.* 127 (6 Aug. 2021), p. 060401.

[317] Amit Kumar Chatterjee, Satoshi Takada, and Hisao Hayakawa. "Quantum Mpemba Effect in a Quantum Dot with Reservoirs". *Phys. Rev. Lett.* 131 (8 Aug. 2023), p. 080402.

[318] Jie Zhang, Gang Xia, Chun-Wang Wu, Ting Chen, Qian Zhang, Yi Xie, Wen-Bo Su, Wei Wu, Cheng-Wei Qiu, Ping-Xing Chen, et al. "Observation of quantum strong Mpemba effect". *Nature Communications* 16.1 (26 June 2025), p. 301.

[319] Filiberto Ares, Colin Rylands, and Pasquale Calabrese. "A simpler probe of the quantum Mpemba effect in closed systems". *arXiv preprint arXiv:2507.05946* 110 (26 June 2024), p. 260601.

[320] Colin Rylands, Katja Klobas, Filiberto Ares, Pasquale Calabrese, Sara Murciano, and Bruno Bertini. "Microscopic Origin of the Quantum Mpemba Effect in Integrable Systems". *Physical Review Letters* 133.1 (26 June 2024), p. 010401.

[321] Filiberto Ares, Pasquale Calabrese, and Sara Murciano. "The quantum Mpemba effects". *arXiv preprint arXiv:2502.08087* 110 (26 June 2025), p. 260601.

[322] Yuqi Zhu and Ching Hua Lee. "Quantum Mpemba Effects from Symmetry Perspectives". *arXiv preprint arXiv:2507.02301* 110 (26 June 2025), p. 260601.

[323] Tanmay Bhore, Lei Su, Ivar Martin, Aashish A. Clerk, and Zlatko Papić. "Quantum Mpemba effect without global symmetries". *arXiv preprint arXiv:2505.17181* 110 (26 June 2025), p. 260601.

[324] Shuo Liu, Hao-Kai Zhang, Shuai Yin, Shi-Xin Zhang, and Hong Yao. "Quantum Mpemba effects in many-body localization systems". *arXiv preprint arXiv:2408.07750* 110 (26 June 2024), p. 260601.

[325] Konstantinos Chalas, Filiberto Ares, Colin Rylands, and Pasquale Calabrese. "Multiple crossings during dynamical symmetry restoration and implications for the quantum Mpemba effect". *Journal of Statistical Mechanics: Theory and Experiment* 2024.10 (26 June 2024), p. 103101.

[326] Tomaž Prosen. "Matrix product solutions of boundary driven quantum chains". *Journal of Physics A: Mathematical and Theoretical* 48.37 (26 June 2015), p. 373001.

[327] Marco Cerezo, Andrew Arrasmith, Ryan Babbush, Simon C Benjamin, Suguru Endo, Keisuke Fujii, Jarrod R McClean, Kosuke Mitarai, Xiao Yuan, Lukasz Cincio, et al. "Variational quantum algorithms". *Nature Reviews Physics* 3.9 (26 June 2021), pp. 625–644.

[328] Kishor Bharti, Alba Cervera-Lierta, Thi Ha Kyaw, Tobias Haug, Sumner Alperin-Lea, Abhinav Anand, Matthias Degroote, Hermanni Heimonen, Jakob S Kottmann, Tim Menke, et al. "Noisy intermediate-scale quantum algorithms". *Reviews of Modern Physics* 94.1 (26 June 2022), p. 015004.